Growth and Characterization of InGaAsP Alloy Nanowires with Widely Tunable

Bandgaps for Optoelectronic Applications

by

Seyed Ebrahim Hashemi Amiri

A Dissertation Presented in Partial Fulfillment
of the Requirements for the Degree
Doctor of Philosophy

Approved November 2017 by the
Graduate Supervisory Committee:

Cun-Zheng Ning, Chair
William Petuskey
Hongbin Yu

ARIZONA STATE UNIVERSITY

May 2018

ABSTRACT

The larger tolerance to lattice mismatch in growth of semiconductor nanowires (NWs) offers much more flexibility for achieving a wide range of compositions and bandgaps via alloying within a single substrate. The bandgap of III-V InGaAsP alloy NWs can be tuned to cover a wide range of (0.4, 2.25) eV, appealing for various optoelectronic applications such as photodetectors, solar cells, Light Emitting Diodes (LEDs), lasers, etc., given the existing rich knowledge in device fabrication based on these materials.

This dissertation explores the growth of InGaAsP alloys using a low-cost method that could be potentially important especially for III-V NW-based solar cells. The NWs were grown by Vapor-Liquid-Solid (VLS) and Vapor-Solid (VS) mechanisms using a Low-Pressure Chemical Vapor Deposition (LPCVD) technique. The concept of supersaturation was employed to control the morphology of NWs through the interplay between VLS and VS growth mechanisms. Comprehensive optical and material characterizations were carried out to evaluate the quality of the grown materials.

The growth of exceptionally high quality III-V phosphide NWs of InP and GaP was studied with an emphasis on the effects of vastly different sublimation rates of the associated III and V elements. The incorporation of defects exerted by deviation from stoichiometry was examined for GaP NWs, with an aim towards maximization of bandedge-to-defect emission ratio. In addition, a VLS-VS assisted growth of highly stoichiometric InP thin films and nano-networks with a wide temperature window from

560°C to 720°C was demonstrated. Such growth is shown to be insensitive to the type of substrates such as silicon, InP, and fused quartz. The dual gradient method was exploited to grow composition-graded ternary alloy NWs of InGaP, InGaAs, and GaAsP with different bandgaps ranging from 0.6 eV to 2.2 eV, to be used for making laterally-arrayed multiple bandgap (LAMB) solar cells. Furthermore, a template-based growth of the NWs was attempted based on the Si/SiO2 substrate. Such platform can be used to grow a wide range of alloy nanopillar materials, without being limited by typical lattice mismatch, providing a low cost universal platform for future PV solar cells.

DEDICATION

To my lovely family;

my mother (Gohar) and father (Abolfazl),

and

my lovely sister (Leili) and brother (Akbar)

ACKNOWLEDGMENTS

TABLE OF CONTENTS

LIST OF TABLES

LIST OF FIGURES

LIST OF SYMBOLS

1D	One-Dimensional
CMOS	Complementary Metal-Oxide-Semiconductor
CW	Continuous Wave
EDS	Energy Dispersive Spectroscopy
EDXS	Energy Dispersive X-ray Spectroscopy
FCC	Face-Centered-Cubic
FWHM	Full Width at Half Maximum
GaAs	Gallium Arsenide
GaP	Gallium Phosphide
Ge	Germanium
HVPE	Hydride Vapor Phase Epitaxy
InAs	Indium Arsenide
InGaAsP	Indium Gallium Arsenide Phosphide
InP	Indium Phosphide
ITO	Indium Tin Oxide
IBE	Integrated Bandedge Emission
IDE	Integrated Defect Emission
LAMB	Laterally Arrayed Multiple Bandgap
LED	Light-Emitting Diode
LILO	Light-in
LILO	Light-In-Light-Out
LPCVD	Low Pressure Chemical Vapor Deposition

MOCVD	Metal-Organic Chemical Vapor Deposition
MIR	Mid-infrared
MBE	Molecular Beam Epitaxy
NP	Nano Pillar
NB	Nanobelt
NW	Nanowire
NIR	Near-infrared
PMT	Photo Multiplier Tube
PL	Photoluminescence
PR	Photoresist
PMMA	Polymethyl methacrylate
QD	Quantum Dot
SEM	Scanning Electron Microscope
Si	Silicon
TRPL	Time Resolved Photoluminescence
TCSPC	Time-Correlated-Single Photon-Counting
TEM	Transmission Electron Microscope
UV	Ultraviolet
VS	Vapor Solid
VLS	Vapor-Liquid-Solid
WZ	Wurtzite
XRD	X-Ray Diffraction
ZB	Zinc Blende

1 INTRODUCTION

1.1 Compound III-V Semiconductors

Semiconductors are materials with conductivity between metal and insulator which contain a relatively small concentration of current carries. The main difference between a metal and semiconductor is the magnitude their bandgap (E_g), which is a crucial term to determine the conductivity of material. Bandgap is referred as the minimum energy needed to excite an electron contributing into a bond between two atoms (valence band) to a free state (conduction band), where it can participate in conduction process. This process results in creation of mobile holes and electrons as the current carriers. The Figure 1 shows a section from the periodic table with the most common constituent elements of semiconductors that are highlighted in blue color. Group IV semiconductor elements such as Si, Ge, etc., with four valence electrons are crystalized in a face-centered cubic (FCC) crystal structure, such that each atom forms four covalent bonds with neighbor atoms in a tetrahedral arrangement.

Figure 1. Semiconductors in periodic table of elements. The most common constituent elements of semiconductors that are shown in blue color. The area marked by black solid line refers to InGaAsP material system, which is the interest of the current study [1].

Combination of isoelectronic elements with elemental silicon, in periodic table, forms binary compound III-V or II-VI semiconductors such as GaAs or ZnTe. As it can be inferred from the name, III-V compounds are made of a non-metal group V and a group III metallic element. III-V semiconductor compounds are of central importance among the others because of their known preferred material properties such as their high electron mobility and chemical stability compared to II-V materials.

1.2 Bandgap Engineering

The optoelectronics properties of semiconductors are primarily determined by their bandgap energy. Bandgap engineering is a powerful technique that allows for design of new semiconductor materials and devices for desired optoelectronic application. A precise control over the composition, size and doping concentration of semiconductors directly influences their emission wavelength, thereby the carrier transport properties. Bandgap of semiconductors can be tuned by altering variety of factors and variables as explained in the following;

1.2.1 Semiconductor Alloying

Alloying is the most common way for making semiconductors of various bandgaps with specific desired optical and electronic properties. Unlike other solid solutions, semiconductor alloying must result in formation of a second-phase-free and single crystal structure. This requires the semiconductors to be mixed perfectly within a single crystalline body. Semiconductor alloys of made of two or three types of single elemental semiconductors (e.g., Si, Ge) or binary compounds (e.g., GaAs, InP) can form a crystal structure within which the constituent elements are distributed in a periodic fashion.
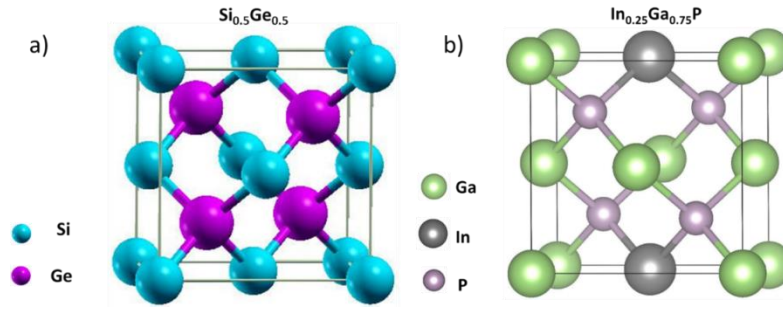
Figure 2. Crystal structure of semiconductor alloys; binary IV alloy of $Si_{0.5}Ge_{0.5}$ (a), ternary III-V alloy of $In_{0.25}Ga_{0.75}P$ (crystal structures are drawn by VISTA).

Unit cells of specific binary, ternary or quaternary alloys can be formed, each of which having a desired composition and bandgap value (Figure 2). Vegard's law is an empirical approximate rule used to correlate the composition with the most important characteristics of a semiconductor such as lattice constant of the crystal and energy bandgap for the alloyed semiconductor based on the concentration of constituent semiconductor (e.g., A and B) present in the structure. According to Vegard's law the bandgap values and lattice parameters of the semiconductor alloy can be determined based on a linear interpolation between those values for pure A and B. Sometimes there is a deviation between values obtained by experiments and linear estimation by Vegard's law, so that a quadratic coefficient called bowing parameter is introduced to compensate the deviation. However, the bowing parameter can usually be neglected in our calculations, depending on the alloy system. For example, the associated bandgap or other physical quantities such as lattice constant of a III-V ternary alloys of $A_xB_{1-x}C$ can be obtained by the formula below:

$$Q(A_xB_{1-x}C)= x.Q(AB)+ (1-x).Q(BC)-bx(1-x), \qquad (1.1)$$

where Q is the physical quatity, x is the fraction of AC semiconductor (1-x is the fraction of BC) in composition of ternary alloy, and b is the bowing parameter which describes the deviation from linearity.

1.2.2 Size Effect

By decreasing the size of the materials from three-dimensional (3D)-bulk structure down to 2D,1D or 0D, it is also possible to change the band structure of the semiconductor materials by altering the density of states (DOS) which is a key factor in band engineering of various semiconductors (Figure 3). DOS describes the number of available electronic states in a particular system which is essential for determining the carrier (e^- and h^+) concentration and the energy distribution of the carriers in a semiconductor with 0D, 1D, 2D and 3D structures.
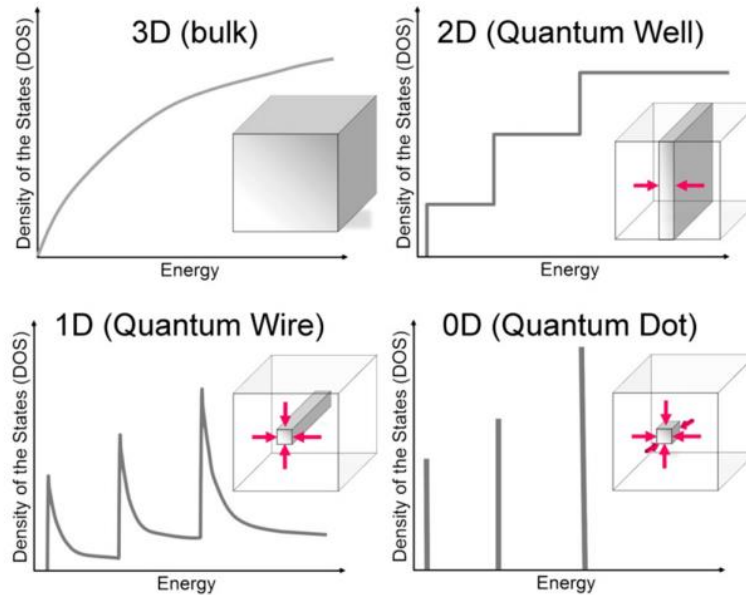
Figure 3. Electronic density of states of materials; for a 3D bulk crystalline material, a 2D quantum well a 1D nanowire, and a 0D quantum dot. The inset shows the confinement behavior of electrons in each case [2].

It is known that the 3D bulk semiconductors usually have fixed bandgap values owing to their continues band structure. For smaller dimensions such as the 0D quantum dots (QDs) (i.e., CdSe nanoparticles) with a size of 10s of nanometers (comparable to wavelength of the electrons) the motion of the randomly moving electrons is confined in all three directions. This is called quantum confinement effect which leads to a transition from continuous band to discrete energy levels and the bandgap to widen up under the energy quantization effect. This can enable us to change the bandgap energy simply by altering the size of the nanoparticles to achieve various emission wavelength of interest. One-dimensional (1D) semiconductor nanowires (NWs) with sufficiently small diameters can have different bandgap values than their 3D bulk value sizes, due to the confinement of electrons in two other dimensions.

1.2.3 Doping Dependence of Bandgap

Introducing a high density of dopants in both intrinsic and extrinsic semiconductors results in shrinking the bandgap. This effect is explained by the fact that the wavefunctions of the electrons bound to the impurity atoms start to overlap with their wavefunctions as the density of the impurities increase. For instance, at two different dopant densities of 10^{15} and 10^{17} cm^{-3}, the average distance between two impurities is different at each case. This overlap causes energy band to be formed rather than a discrete energy level (unlike the size reduction effect). Therefore, presence of very high concentration of impurity band can result in reduced energy band of the matrix/host semiconductor material [3].

1.3 Significance of III-V Nanowires Growth in a Wide Bandgap Range

III-V compound semiconductor NWs have attracted considerable attention during the past decades as the building block of next generation of optoelectronic devices such as solar cells, transistors, laser diodes, and light emitting diodes (LEDs) and many others. Their tunable direct bandgaps, high carrier mobility and excellent mechanical properties make them superior candidates to other semiconductor materials [4-5]. The challenging issue with epitaxial technology for growth of high quality thin film of semiconductors is mainly the lack of the lattice-matched single crystal substrate with respect to lattice matching requirement. This somewhat limits us in terms of bandgap engineering. Shown in Figure 4 is the bandgap versus lattice constant for various semiconductors. The red color dashed-line rectangular area illustrates such limitation with maximum tolerable lattice mismatch that is a quite small value. Alternatively, NWs because of the smaller cross section that they have, can accommodate larger lattice mismatches compared to thin films. For example if GaAs is chosen as the growth substrate, it is possible to grow materials of different bandgaps from 0.5 to 2.2 eV with up to ~10% tolerance to lattice mismatch [6]. Therefore, InGaAsP alloy nanopillars (NPs) with all the needed bandgaps can be potentially grown on GaAs substrate. The large range of achievable bandgap through NW growth with a such relax lattice mismatch requirement makes this process almost arbitrary alloying. However, for the epitaxial growth of NWs on a lattice-mismatched substrate there is a critical diameter below which the defect-free vertically aligned NWs are grown, and above this critical value NWs are not grown or have a high concentration of defects [7]. Therefore, heteroepitaxial growth of NWs with larger

diameter always remains a challenge due to high lattice mismatch and large thermal expansion coefficients for different semiconductors [8].

For solar cell applications, the NW layers of a few microns thickness absorb a much higher percentage of the incident light compared to the planar thin films of the same thickness for the same material [9]. Therefore, it is a great improvement to use NWs for the fabrication of highly efficient solar cells beyond the theoretical Shockley-Queisser limit under one-sun illumination [10].
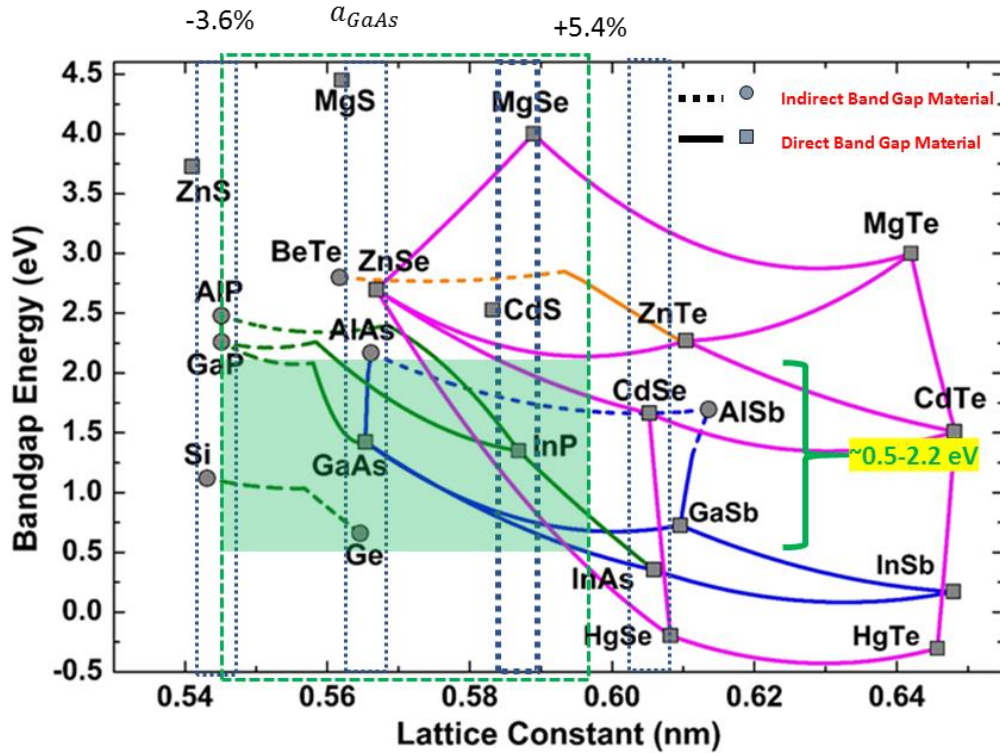
Figure 4 Bandgap versus lattice constant for different semiconductors. The red dashed-line rectangular area represents the maximum tolerable lattice mismatch in thin film (planar) growth for various single crystal substrate. The green rectangular area illustrates the relaxed lattice mismatch requirement in NW growth on single crystal GaAs substrate that allows for wide range of achievable bandgap within a given single substrate. [Figure adapted from ASU MBE Optoelectronic Group].

Fabrication of solar cell devices based on NWs has advantage of lower cost by both reduced amount of material being used compared to thin film, and eliminating the necessity for expensive single crystal substrates. Having direct bandgaps, most of the III-V NWs can be rationally designed and synthesized to cover a wide range of the bandgap energy by tuning the composition, on a single substrate or monolithically for variety of applications. Monolithic integration of semiconductor with different lattice constant on a single substrate has attracted great interest during the recent years making them appealing for new applications such as tunable lasers [11] and photodetectors [12] on a single chip, monolithic white laser [13], etc. Growth of composition graded semiconductor alloy NWs using the dual gradient method [14] has produced an interesting material platform for developing monolithic solar cells for dispersive concentration photovoltaic systems [15]. At the same time, such growth also provides a unique means to study semiconductor alloys in high quality single crystal form and in a wider composition range that is otherwise impossible to grow. Such growth and the resulting materials using ZnCdSSe in its full composition range have been studied in the past [14-16].

In the current work, it will be shown that how dual gradient method provides a combinatorial chemistry type of platform for growing the composition-graded ternary NW alloys of InGaAsP material system by tuning the supersaturation rate in an Au-catalyzed growth process on a single substrate. More specifically, the vapor phase growth of InGaAs, InGaP, GaAsP ternary alloys with emphasis on the effects of vastly different sublimation rates of the associated elements is studied using a facile vapor transport method. The dual gradient approach provides an especially effective tool for rapidly

identifying growth conditions in terms of adjusting the temperature and source element gradients. As a result, the bandgap gradually changes on a single substrate for different alloy systems. It is believed that growth of III-V NW alloys in a wide range of bandgaps within a single substrate can pave the way for fabrication of different types of new multifunctional optoelectronic devices such as multispectral photodetectors, broad band tunable LEDs and lasers on a single chip, and high-efficiency solar cells.

1.4 Vapor-Liquid-Solid Growth of Nanowires/ Nanobelts

Nanowires are generally produced by two main methods including "top-down" etching process [17] and "bottom-up" growth mechanisms. But the most commonly used approach to grow one-dimensional (1D) NWs is using chemical vapor deposition (CVD) via so called Vapor-Liquid-Solid (VLS) mechanism, hereafter called VLS which was first introduced for growth of silicon NWs by Wagner and Ellis [18].
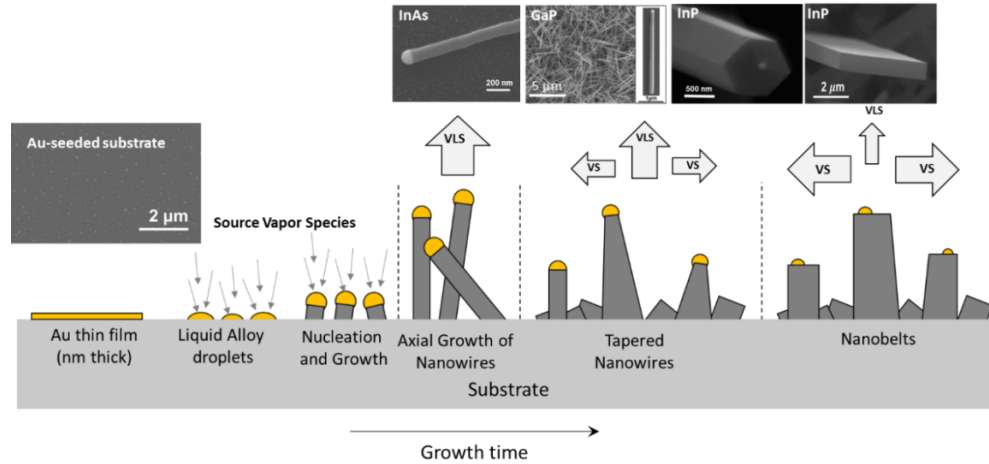
Figure 5. Schematic of VLS-VS growth mechanisms for various nanostructures.

A schematic of the VLS method for growth of NWs and NBs is shown in Figure 5.

In order to grow NWs via VLS approach, a metallic catalyst (usually noble metals such as Au or Ni, etc.) with a high melting point is used. In VLS mechanism, the metal catalyst forms a liquid alloy droplet (Au reservoir) at a high temperature by impingement of the vapor phase species into alloy droplet. When the concentration of the vapor components inside the liquid droplet is higher than equilibrium concentration, the nucleation of NW crystal occurs at the interface of solid-liquid (substrate and droplet). This is called supersaturation level which is required to be sustained for growth of NW to be continued in axial direction. A very important requirement for the axial NW growth is that the nanocluster catalyst should be a suitable catalyst, in terms of solubility of vapor phase species. This means the catalysts must form a liquid solution with the components of solid phase, which requires high solubility limit for catalyst in liquid than its solid form [19]. Thus, the most suitable metal clusters should be selected to use as a catalyst. Gold is found to be one the most commonly used catalysts for VLS growth of NWs. As it can be inferred from the schematic of VLS growth, the diameter and the areal density of the NWs are governed by size and position of the Au alloy droplet. If a thin layer of the Au film is used prior to growth, under Ostwald ripening at high temperatures, the large discrete Au droplets are formed on the surface of substrate at the expense of shrinking smaller Au droplets. However, depending on the growth condition the self-catalyzed growth of NWs occurs without requiring a pre-deposited Au catalyst. In self-catalyzed growth, the metallic source materials often can form metal seeds that play the role of catalyst. The autocatalytic growth requires the homogenous nucleation of the metal cluster on the surface of the flat substrate which is usually higher than energy barrier for incorporation of the vapor species into Au reservoir. it is required for the nucleated metal

clusters to exceed the critical diameter to be survived and not decompose at high temperatures. The advantage of catalyst-free growth is the minimized contamination caused by Au catalyst that may raise some concern for possible III-V contamination, even though there are systematic studies showing such concerns are not serious. Generally, the growth of NWs occurs through the Au alloys droplet. However, when the partial vapor pressure of the gas phase species that are introduced into the growth chamber is so high, the vapor-solid (VS) mode becomes activated. In VS growth, the direct nucleation and growth of crystals occur without mediation of liquid droplet. VS growth results in expansion of NWs in lateral direction. Various nanostructures such as tapered NWs and NBs can be grown via interplay between VLS and VS mechanisms. Radial core/shell heterostructures can be grown by favoring the growth condition for vapor-solid (VS) mechanism in conjunction with the proper compositional modulation to grow different NW architectures for device applications.

From thermodynamics point of view, the VLS growth should be energetically favored for nucleation and growth of NWs. To better understand this, the term chemical potential (μ), known as the partial molar free energy of species ($\mu_i = \frac{\partial G}{\partial n_i}$), needs to be explained first. Chemical potential is the potential energy that is released or absorbed in a chemical reaction or phase transition. In VLS growth, the chemical potential is the affinity of the vapor phase components to enter inside the liquid alloy droplet which must be sufficiently high to achieve the supersaturation.
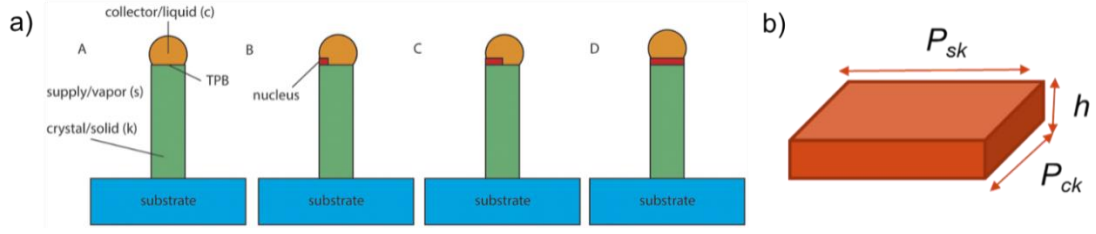
Figure 6. Schematic of the nanowire growth dynamics (a); (A) Three different phases of the vapor, solid and liquid during the nanowire growth. (B) nucleation at the TPB. (C) propagation of nucleated layer along the TPB. (D) Complete formation of first nucleated layer. b) A geometrical dimension of the nucleated layer at the TPB. Figure adapted from reference [20].

To better explain this, the VLS process is treated as a three-phase system with the supply (s), collector (c) and crystal (k) in the vapor, liquid and solid phase, respectively, as shown in Figure 6. The boundary between all three-phase (TPB) is where the nucleation occurs. Hence, by taking into account the chemical potential concept, the Gibbs free energy of nucleation at TPB can be expressed as follows

$$\Delta G_{TPB} = -n\Delta\mu_{sk} + P_{ck}h\sigma_{ck} + P_{sk}h\sigma_{sk}, \qquad (1.2)$$

where $\Delta\mu_{sk}$ is the chemical potential difference between the vapor (supply) and solid (crystal) phases, P_{ck} (P_{sk}) and σ_{ck} (σ_{sk}) are perimeter length and the interface energy of the collector/crystal (supply/crystal), n is number of atoms nucleated, and h is the growth height in this nucleation event [20]. The ΔG_{TPB} is obtained by difference of energy released from chemical potential (negative term) and energy needed for creation of the new interfaces (positive term). Apparently, it should be a negative value for the continuous layer by layer nucleation at the TPB which leads to NWs to grow longer.

1.5 Challenge with High Sublimation Rate of Group V Species in III-Vs

For III-V compounds such as InGaAsP, it has been experimentally proven that when the temperature is above the congruent sublimation temperature, T_{cs}, the sublimation rate

of the group V element is higher than that for group III elements [21-24]. Figure 7 shows

the partial vapor pressure of group V species above some of the III-V compounds and

their related alloys.
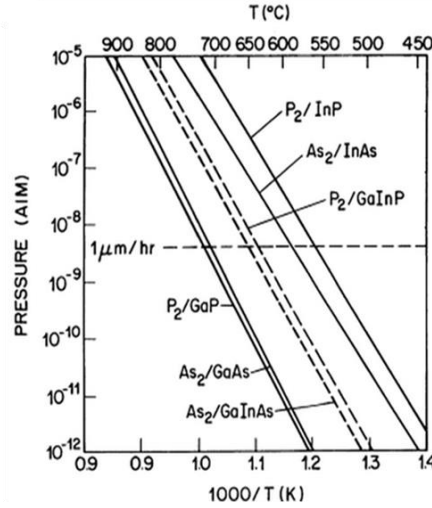
Figure 7. Partial vapor pressure group V species above the III-V compounds (Springer US, 1989. 267-277).

Therefore, for binary compounds with evaporation temperature of higher than T_{cs} , e.g.,

630 ◦C for GaAs [25] and 387 ◦C for InAs [21], the outcome is an early loss of

significant amount of As in very first few minutes of the growth due to higher

sublimation rate of As than In and Ga. Zi et al. have shown for InAs NWs grown via

vapor transport method, due to a significant decrease in arsenic vapor pressure after a few

minutes growth, this factor becomes the rate-limiting factor for the growth affecting the

kinetics of growth, thereby morphology of NWs [26]. Since above the T_{cs}, vapor pressure

of the III and V species leaving the surface are different, and technologically this is

important for determination of upper-bound of growth temperature in MBE growth of

stoichiometric III-V materials. It is also experimentally proved that T_{cs} can be directly

controlled by changing the group V flux [27].
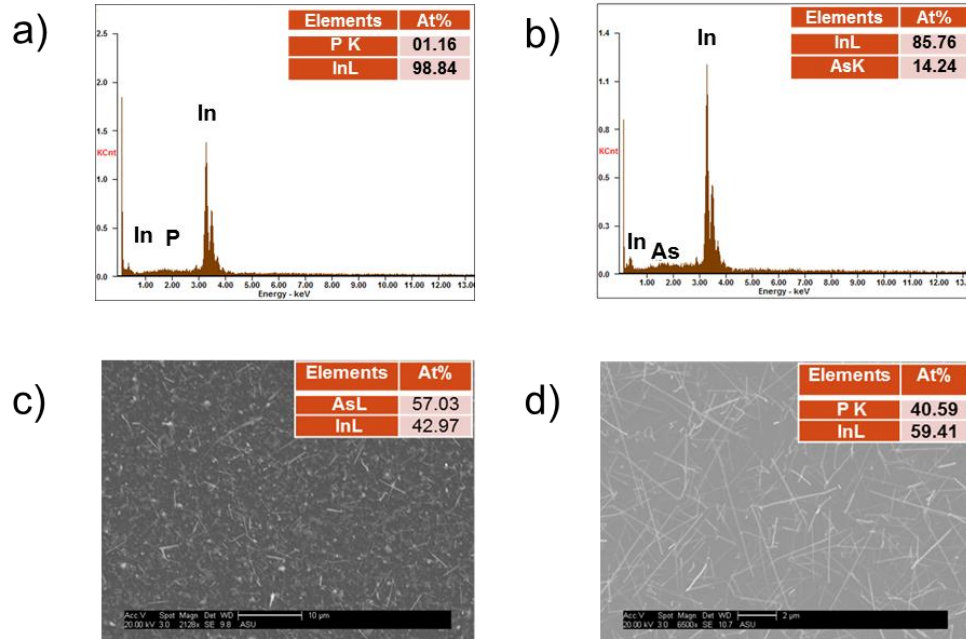
Figure 8. Quantitative elemental analysis of nanowires grown via vapor transport method; EDS analysis of a) InP precursor boat heated at =800° C for 10 min and total pressure of 3.3 Torr, b) InAs precursor boat heated at 840° C for 10 min and total pressure of 3.3 Torr, and EDS results of corresponding NWs obtained at the end of growth; c) InAs NWs grown at 650 ∘C, and d) InP NWs grown at 440 ∘C.

Due to the higher sublimation rates of As and P than those for In and Ga, the stoichiometry of the resulting alloys is greatly influenced, such that the EDS elemental analysis for as grown NWs shows significant deviation from perfect stoichiometric composition. Furthermore, the EDS analysis of remaining precursors from source materials boats of different growth experiment (Figure 8) confirmed the high sublimation rate of As and P from InAs and InP compounds, respectively. This is due to preferential evaporation of As and P from the surface leaving behind liquid group III metal with small amount of As or P dissolved. To address this issue, different growth strategies are experimented to compensate the deficiency of As and P which will be shown later.

1.6 Growth of InGaAsP Nanowire for Design of LAMB Solar Cells

To reduce the cost per watt ($/W) of photovoltaic solar cells, the current research and technology attempts to address both numerator and denominator by decreasing the cost and increasing the efficiency, respectively. Since 2002, the efficiency of solar PV has increased by ~0.9%, in average per year [28]. The highest efficiency for concentrated triple-junction (GaInP/GaAs/GaInAs) and four-Junction (GaInP/GaAs/GaInAsP/GaInAs) tandem solar cells that was ever reported is made by Sharp [29] and Fraunhofer ISE [30] with efficiencies of 44.4% and 46.0%, respectively. However, their application is practically limited by expensive fabrication costs, difficulties in adding the new junction and lattice-matching requirements. Monolithically Integrated Laterally Arrayed Multiple Bandgap (MILAMB) solar cells for making dispersive concentration PV solar cells has been demonstrated at C. Z. Ning's ASU Nanophotonics Group, recently [15, 31]. Design of such system based on an InGaAsP material platform requires growth of subcells of various bandgaps with a continuous spatial composition gradient over a single substrate. As illustrated in Figure 9a, the full composition InGaAsP alloys are able to cover a wide bandgap range spanning from InAs (0.35 eV) to GaP (2.26 eV). Figure 9b is a 2D plane representing all the possible compositions with the associated bandgap for InGaAsP alloy system. The four corners of the figure represent the four binaries, InAs, GaAs, InP, and GaP, while the four edges represent the corresponding four possible ternaries with varying composition, and each given (x, y) point in the interior represents a quaternary InGaAsP alloy of a given composition.

The bandgap distribution on each cell should be optimized to meet the current-matching constraint for integrating the manufactured MILAMB cells with a dispersive micro-optical array acting as prism. The spectral splitter used in such design divides the solar spectrum into different wavelengths, which will be absorbed by laterally arranged subcells with corresponding bandgap energy cells.
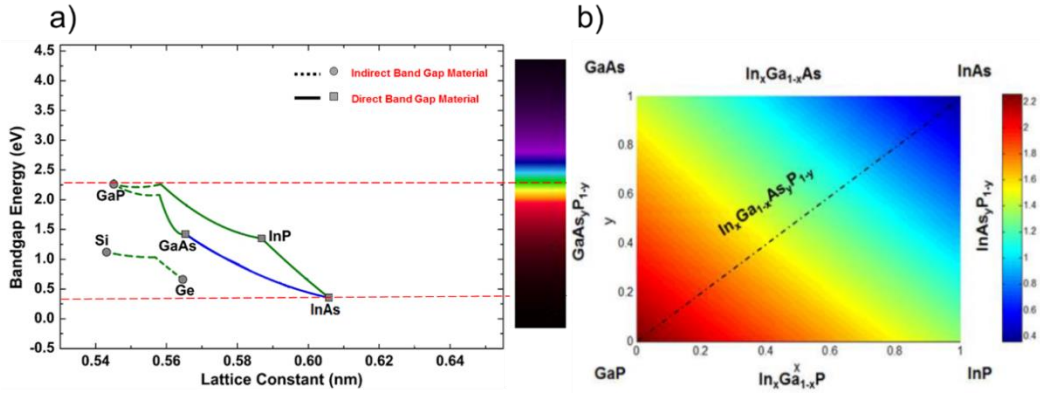
Figure 9. Bandgap of InGaAsP alloys; a) Bandgap vs. lattice constant for InGaAsP alloys covering the bandgap range of (0.35, 2.25) eV. b) bandgap contour plots in two-dimensional composition plane of InGaAsP alloying system

A home-made dual gradient system based on the low-pressure CVD is used to grow the LAMB subcells of InGaAsP alloy NPs with variable compositions on a single substrate. A schematic of solar cell design on a platform of LAMB cells is depicted in Figure 10. It is made of three p-i-n junction solar cells with the dielectric interlayer filling the gaps between NPs. An example of such subcell design would be C_1: InAsP (0.6-1.35 eV), C_2: InGaAs (1.35-1.8 eV), and C_3: InGaP (1.8-2.0 eV).

NW solar cells are believed to be potentially able to achieve higher efficiency than their counterpart planar thin film absorbers, if designed properly to efficiently trap the striking light onto the cell [9]. Our preliminary 3D optical-electronic simulation using the finite-difference time-domain (FDTD) method compares the Power Conversion Efficiency

(PCE) achieved based on 3-NP-LAMB cells with that from thin-film 3-LAMB cells by taking into account the potential recombination paths in bulk and surface (Figure 11). As can be seen from the figure, the entire cell is predicted to be able to deliver a PCE of higher than 50% under 400x concentrated sun illumination.
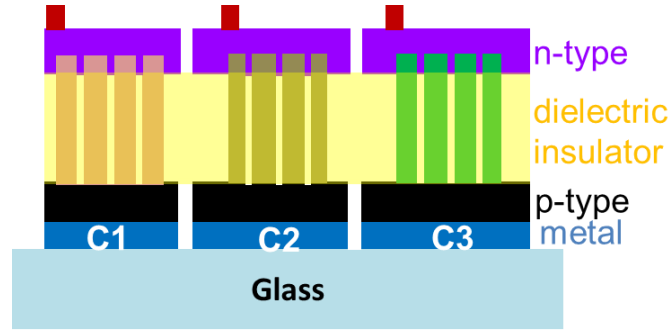
Figure 10. Schematic of a 3-subcell NP-LAMB cell structure based on InGaAsP

To obtain higher PCE, a semiconductor silicon platform must be integrated beneath this optical array system to capture diffused non-directional sunlight.
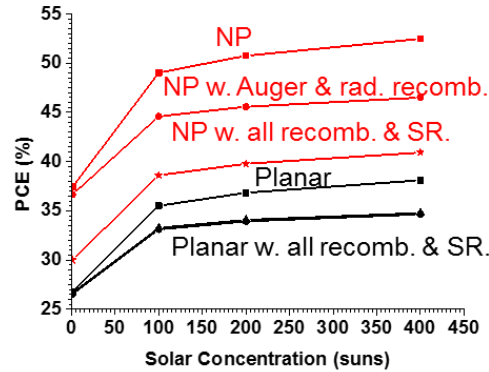
Figure 11. Power conversion efficiency (PCE) of 3-NP-LAMB cells predicted based on 3D optical-electronic simulation in comparison with thin-film 3-LAMB cells. SR: surface recombination.

Figure 12 shows the illustration obtained by simulation of a compact dispersive lens design, coupled with a 3-junction lateral solar cell, which is done by our collaborators at Massachusetts Institute of Technology (MIT).
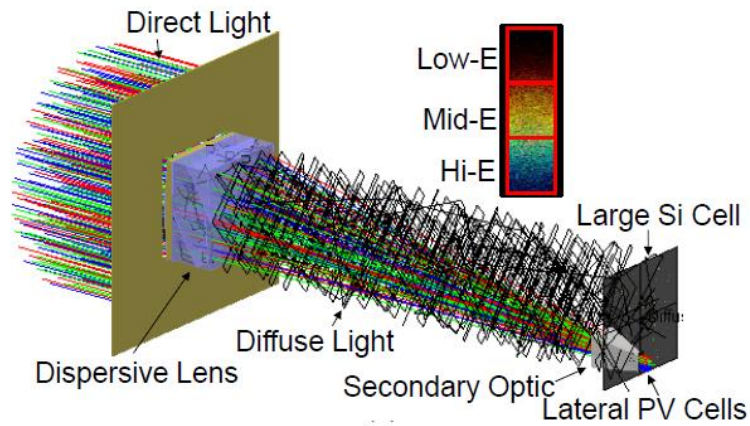
Figure 12. Preliminary baseline design model of LAMB solar cell that allows the co-design between dispersive lens system and lateral sub-cells to maximize overall conversion efficiency.

1.7 Summary

The current dissertation will be mostly devoted to the development of CVD growth of III-V InGaAsP alloy NWs for the design of a LAMB material platform for PV solar cells. In addition, a templated growth without use of an expensive single crystal substrate or precursor that can be a universal platform for growth of a wide range of alloys will be presented. It is strongly believed that composition-graded III-V subcells of various bandgap could be a potentially more suitable alternative to substitute multi-junction solar cells. Our proposed approach is expected to address the issue associated with the high cost and complexity in design, mostly by elimination of lattice-matching requirement for growth of stacked layers of various bandgap materials.

2 EXPERIMENTAL TECHNIQUES

2.1 Introduction

The current chapter will be mostly giving an introduction into experimental techniques including materials growth and processing techniques and characterization methods that are used throughout the entire work shown in the current dissertation. Given that, the high cost is one of the most critical issues in crystal growth of in semiconductor technology, it is important to reduce both preparation and precursor expenditure. The vapor transport-based chemical vapor deposition that is used in our work is advantageous compared to more expensive techniques such as molecular beam epitaxy (MBE) and metal organic chemical vapor deposition (MOCVD), given the high material quality that can be obtained. However, the lower growth rate rendered by those methods make them more suitable for growth of high quality thin films for applications including, for example, tandem solar cells, quantum-well laser diodes, where precise control over the thickness of grown layer in nanometer range is required. The entire growth of III-V binaries and ternary alloys are performed using a homemade-CVD setup with a hot wall horizontal reactor configuration. Therefore, a brief introduction into the principle and theory of vapor transport method is important to be discussed beforehand. Also, the template fabrication procedure as well as a solar cell device fabrication and characterization will be presented. The material characterization techniques that are utilized for structural and optical properties of the NWs and thin films are described in the current chapter to give an insight for the reader prior to moving into results and discussion section.

2.2 Materials Processing Techniques

2.2.1 Low Pressure Chemical Vapor Deposition

III-V Semiconductor materials are mostly grown by variety of techniques such as MBE, MOCVD, hydride vapor phase epitaxy (HVPVE), and liquid phase epitaxy. Single crystal high quality binary substrates can be also obtained by conventional methods such as Bridgman [32] or Czochralski [33] method. However, growth of III-V materials using all aforementioned methods is limited by more complexity, precursor chemistry and purity issue as well as potential incorporation of unwanted dopants such as carbon or chlorine in MOCVD or HVPE methods. These dopants are considered as the main cause of point defects that are required to be driven off during or after the growth via different post-growth treatment techniques. Vapor transport method has the advantage of minimized impurity level introduced by metalorganic precursors and so on. This growth technique relies on sublimation of the precursor, of either elemental reagents or binary powder, as the parent source material and the reaction of gaseous species occurring at the surface of the substrate forming a solid deposition. Low pressure chemical vapor deposition (LPCVD) with sub-atmospheric pressure range [34] is widely used to grow crystalline semiconductors at relatively high temperatures. The hot-wall horizontal tube configuration, with a parabolic temperature profile, with a maximum falling at the center of the CVD furnace enables us to achieve different temperatures along the tube axis. The total pressure of the CVD chamber affects the mean free path (MFP) of the gaseous species which is defined as the average distance traveled by a gas molecule before colliding with another, given by the formula:

$$\lambda = \frac{K_b T}{\sqrt{2}\,\pi P d^2} \tag{2.1}$$

, where P is the total pressure, d is the diameter of molecule, K_b is the Boltzmann constant and T is the temperature [35]. For the pressure range of below atmospheric value (760 Torr) and 1 Torr, the corresponding MFP of the molecules can be less than 100 micron range which is a very small λ value compared to ultra-high vacuum ($10^{-8} - 10^{-9}$ Torr) systems, such as MBE with a MFP in the order of several kilometers. Such small MFP in circular tubes with diameter of D, where $\lambda \ll$ D , results in a laminar flow regime, where the carrier gas undergoes a layer flux within the reaction medium until it reaches to the surface of the substrate. The flow regime at extremely low pressure or ultra-high vacuum condition turns to molecular flow, with molecules moving inside the tube with less intermolecular collisions in random directions ($\lambda \gg$ D) [35].

In the current work, the growth set up used to grow III-V alloy NWs was a hot wall system with a horizontal quartz tube embedded in a single zone CVD furnace (Lindberg/Blue M) extended along the tube axis with a maximum set temperature up to 1100°C. The technique simply relies on sublimation of solid source materials at upstream side which can migrate under the flow of inert carrier gas such as ultra-high-purity nitrogen (N_2) or Ar+5% H_2 towards the substrate placed at downstream the furnace. The main concept behind the growth of nanostructures is supersaturation which is defined as the ratio between the actual vapor pressure of species and the equilibrium vapor pressure of compounds. The driving force for crystal nucleation and growth is supersaturation which is the most important term by which the morphology and size of the grown crystals

are controlled. Growth of high quality epitaxial film requires low supersaturation that is equivalent to low growth rate, while polycrystalline and gas-phase nucleated powdery film are grown at extremely high supersaturation rates. Growth of NWs favors a low to medium supersaturation level [36]. By adjusting the supersaturation level under both Au- and self-catalyzed growth condition and taking into account the interplay between VLS and VS growth modes, various nanostructures can be obtained. In the current dissertation, it will be shown that by changing the superstation level nanostructures such as NWs, nanobelt (NBs), nano-network and polycrystalline thin film can be grown using the vapor transport method. This requires careful engineering of the growth condition to obtain the desired morphology only by adjusting the growth parameters such as the source material and substrate (growth) temperature, carrier gas flow rate, total system pressure, growth time, etc. In order to grow binary and ternary alloy NWs with different compositions the unique methodologies were introduced and developed. Growth of templated NPs was achieved using both VLS and phosphorization approaches. Composition-graded III-V alloy NWs with spatial composition variation across the single substrate were grown using the dual gradient method in a CVD system. These subcells with different bandgap ranges will be potentially used for making laterally arrayed multiple bandgap (LAMB) solar cells [15].

2.2.2 Langmuir-Blodgett Coating

The Langmuir-Blodgett technique is a well-established way of coating a single molecule thick film on a surface. Coating such thin a layer with proper control over the packing density of the molecules is carried out by immersion of a substrate of interest into a liquid

containing the molecules floating on top surface of liquid or solution. A thick layer of Langmuir-Blodgett film can be obtained by coating a multiple layer of molecules since the thickness of the monolayer is already known [37]. The substrate being used for the coating must be clean and sufficiently hydrophilic to avoid formation of defect in close-packed monolayer structure. In this research, this technique is used to coat the polystyrene (PS) microspheres of 0.5 to 1.0 μm size on the surface of SiO_2-coated silicon substrate. Figure 13 shows a schematic of how this refined technique works.
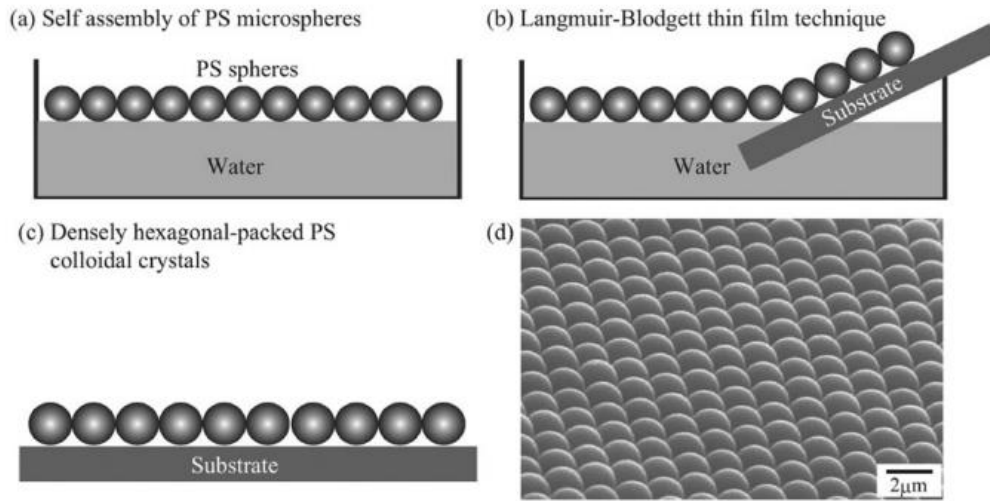
Figure 13. A schematic of Langmuir-Blodgett technique for the coating close-packed PS microspheres; the self-assembly of microspheres(a), the coating process by immersion of substrate into liquid(b), the close-packed PS spheres (c), the SEM image of colloidal film made of PS spheres (d) [38].

The PS-coated substrate is further processed by other fabrication steps to make a porous etched-through template that is used as a universal template for growth of NWs. The detailed procedure about fabrication of such template is discussed in chapter 7. The formation of monolayer is, in principle, based on (1) first immersion of the PS spheres inside water, and then (2) floating on the top surface of water that prevents them from sinking due to the high surface tension and the very close density value of PS spheres

(1.05 g/cm^3) to that of water [39]. The moving behavior of the PS spheres is dominated by Brownian motion rather than their gravity, thanks to the surface tension of water and the Brownian motion of the PS spheres helping them to make a close-packed monolayer film at the top surface.

2.2.3 Plasma-Enhanced Chemical Vapor Deposition (PECVD)

Plasma is often called the unique state of matter after gas, solid and liquid that is composed of ionized gas. Plasma-Enhanced Chemical Vapor Deposition (PECVD) is a process by which the thin films can be deposited in a plasma environment often created between two parallel electrodes (a grounded electrode and an RF-energized electrode as shown in Figure 14). Once the reactant gases are introduced into PECVD chamber, the capacitive coupling between two electrodes results in excitation of gaseous species (silane (SiH$_4$), etc.) into plasma. This will result in formation of solid thin film deposition on the ground electrode which has a temperature of as low as 100-400 ∘C, though that might be even higher for different models.
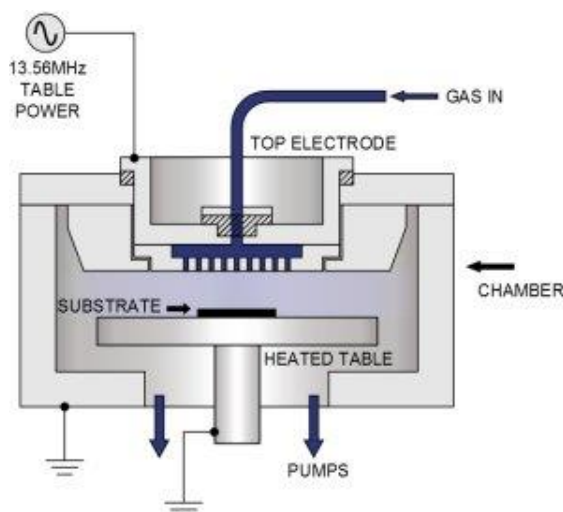
Figure 14. Schematic of PECVD setup

PECVD has an advantage of operation at low temperatures over thermally activated conventional CVD. It can be used for deposition of various materials such as SiO_x, SiN_x for wide range of applications such as photonic crystals, surface passivation and dielectric layers used in transistors, etc. In the current work, PECVD is utilized for various purposes such as a dielectric layer of SiO_2 of a few microns for fabrication of etched-through templates for nanopillar growth. It is also used for surface passivation of as-grown III-V nanostructures in solar cell fabrication. Depending on the functionality of the whole device architecture or the growth methods it will require to choose different deposition recipes, mostly with respect to deposition temperature. For example, to deposit a few hundred nanometers of silicon dioxide on indium thin film, which is pre-deposited using thermal evaporation, it is required to choose the PECVD growth temperature of below-melting point of indium (157 ∘C) to prevent formation of indium droplets at top surface.

2.2.4 Wet Etching

Wet etching is used to remove the unwanted layers such as oxide, residual thin film, etc. via the chemical reaction between liquid etchant and the material that is required to be removed from the surface of a wafer or as grown layer before or during the fabrication. Wet etching is usually an isotropic or multidirectional process with an almost equal etching rate in all directions. In general, the etching rate depends on the concentration of acidic or basic solutions, which is usually used in diluted form for controlled etching rate. Wet etching usually includes a sequence of steps as follows: a) transferring the etchant solution to the surface; b) waiting for a certain period (depending on the etching rate) and

let the reaction occurs between etchant molecules and material at surface moving to depth of thin film; 3) desorption of the reaction product; 4) rinsing the sample with deionized water (DI water) to remove the reaction product away from the surface. In this work, mostly the wet etching is applied either for substrate preparation prior to growth or during different steps of nanopillar solar cell fabrication. For instance, to remove native SiO_2 layer from the surface of silicon, a dilute HF (2-5%) solution is used. Since the etching rate of concentrated HF (49%) is too high, in order to decrease the etching rate, a buffer etchant solution made of a mixture of 35-40% NH_4F in DI water and 49% HF in DI with volume ratio of 6:1 is used to etch (modify) a few microns thick PECVD-grown SiO_2 that are etched through by dry etching techniques (described next). The oxide compounds such as $InPO_4$, In_2O_3, etc., formed on the surface of, for instance, InP, were removed using a dilute (5%) hydrochloric acid (HCl), prior to moving to the next step. On the contrary, concentrated (36-38%) HCl as a strong acid was used to remove metals such as Aluminum (Al) or Indium (In). It is already established, but important to mention that HCl: Glycerol with 1:1 volume ratio can be used as an efficient etchant to dissolve the Chromium (Cr) vigorously, which is important during the fabrication of templates for growth of NWs. Apparently, sonication in water bath and increasing the temperature can result in increasing the etching rate in some cases. To be able to achieve the controllable and reproducible results it is recommended to make a fresh etchant solution each time.

2.2.5 Dry Etching

Dry etching relies on gaseous species playing the role of etchants for removing the

unwanted material from the surface or etching through the micron thick films.It is one of the core processes that is necessary for fabrication of microelectronic devices. Unlike wet etching, the dry etching does not require using any liquid solution, so it does not damage the whole film but rather it has the advantage of the anisotropic (unidirectional) etching process.
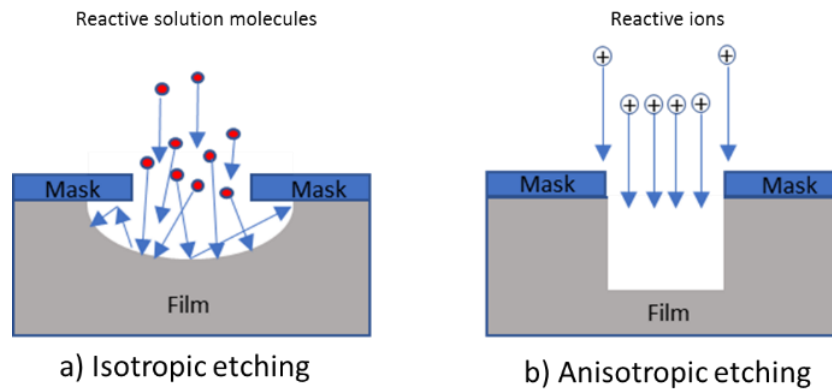
Figure 15. Schematic of etch-through process in wet and dry etching.

This helps us to vertically etch, for example, a thin layer of SiO_2 coated with a metal mask in a vertical direction regardless of the crystal structure or SiO_2 being amorphous material. Dry etching is based on plasma environment containing reactive ionic species that remove material under ion bombardment that diffuse to the surface and reacts with atoms at top surface. The most commonly used gas in dry etching for SiO_2 is a mixture of CHF_3 and O_2 that turns into free radical that are highly selective for SiO_2 in terms of high etching rate over Cr or photoresist that are used in fabrication of template. Directional etching in dry plasma etching is due to acceleration of the ions from plasma by high electric field. Figure 15 shows a schematic of the differences between isotropic wet etching and anisotropic plasma-based dry etching.

27

2.2.6 Metal Electroplating

To grow III-V NWs via a catalyst based VLS mechanism, it is required for the surface of the substrate to be seeded by nanoparticles of noble metals such as Au that turns into liquid when it makes alloy with other (usually metal) species that present inside the growth chamber. However, It is proposed that growth of NWs on lattice-mismatched substrate requires using a universal template that eliminates the necessity for using single crystal lattice-matched substrate. In chapter 7, it will be presented how such platform which is made of pore arrays created on a SiO_2- coated substrate is fabricated through inexpensive polystyrene nanosphere lithography. Once the template is fabricated, as the next step metal electroplating at the bottom of the pores will be performed by exploiting electrochemistry to embed small nanoparticles of Au acting as the catalyst at the bottom of the pores for subsequent VLS growth of NPs. The contamination of III-V materials caused by Au, which can adversely affect optoelectronic properties of the grown materials, must be prevented. In solving this, a new recipe has been developed for the successful electroplating of group III metals (In and Ga) which are no longer considered as a contamination sources for their parent III-V materials. The In or Ga plated inside the pores will be either used as the catalyst for VLS growth or it can be exposed by phosphorous or arsenic flow to grow III-V NPs.

2.3 Materials Characterization

2.3.1 Electron Microscopy

Electron microscopy is a useful technique for study of the nanostructures which can reveal information about the surface topography and crystallographic features of the

specimen of interest. The analysis is based on illumination of the surface of a nanostructure using an electron beam to create an enlarged image of the sample with a high magnification. The very high resolution of electron microscope compared to the regular optical microscope, often referred to as light microscope, is due to the much smaller wavelength of electron known as its de Broglie wavelength. For example, a photon with energy of 2 eV has a wavelength of 621 nm from $\lambda = hc/E_{ph}$, where h is the plank constant (6.625×10^{-34} m^2 kg/s), and c is the speed of light (3×10^8 m/s). While the wavelength of an electron with a kinetic energy of 2 eV is obtained to be 0.87 nm associated with the de Broglie wavelength ($\lambda = h/p$, where p is the momentum of an electron with a kinetic energy of k= $p^2/2m_e$; m_e= 9.1×10^{-31} kg) of the electron. Such high resolution offered by an electron microscope makes it an essential tool for the study of the morphology and atomic resolution structure of the semiconductor NWs. The resolution and detection capability of the electron microscope highly depends on both energy and the size of the electron beam which can be adjusted for various studies. In electron microscopy, the electron beam strikes the surface of the specimen and if it is sufficiently thin, it will pass through the sample in a so-called transmission process. Depending on the interaction of the electron with specimen different signals are generated. Figure 16 depicts a schematic illustration of various interactive events which might occur between electron beam and matter. Those electrons which are scattered from the surface of the sample either lose their primary energy, called back-scattered electrons, or experience an energy loss of those within the forward-scattering process that can be either an elastic or inelastic scattering. For an elastic scattering, both incident and scattered electron beam maintain their direction and energy, whereas for the inelastic

scattering, the primary electron undergoes a change in beam path, as well as a measurable loss in energy of electron. Some of the signals that are generated through an inelastic event are secondary electrons, Auger electrons, characteristics x-ray, cathodoluminescence and bremsstrahlung radiation.
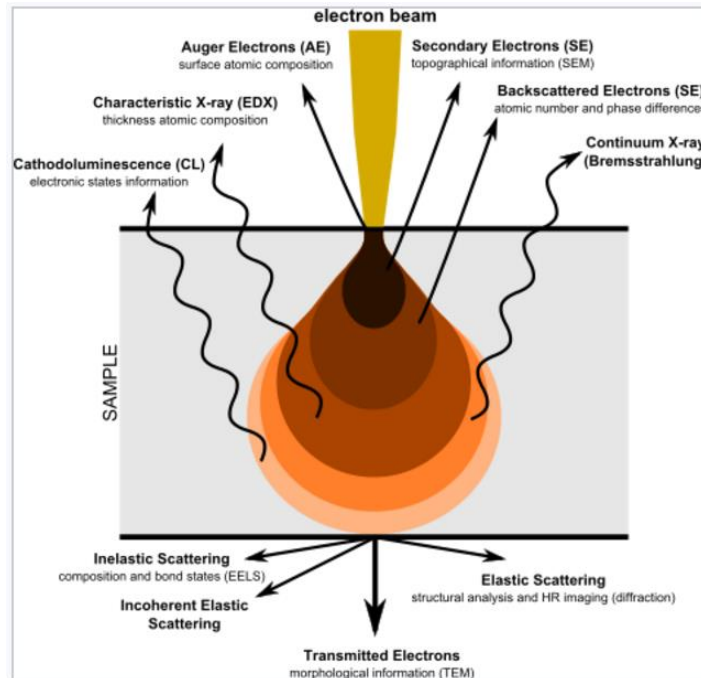
Figure 16. Schematic illustration of the interaction between highly energetic electron and matter [https://en.wikipedia.org/wiki/Electron_microscope].

All these generated signals provide useful information about the specimen. For example, Auger electrons are used to study the elemental composition of the surface of a given specimen. The characteristics X-ray that are emitted through the process of bombardment of inner shell electrons are used for identification of elemental composition of the sample using a commonly used technique, energy dispersive X-ray spectroscopy (EDS) which will be discussed in detail in the following sections. Among all the known electron

microscopy related techniques, transmission electron microscopy (TEM) and scanning electron microscopy (SEM) in combination with EDS or EDXS are utilized for the in-depth study of the morphology and structural properties as well as the composition of semiconductor nanostructures, which are synthesized in the current thesis.

2.3.1.1 Scanning Electron Microscopy (SEM)

SEM is the most essential technique for the study of the morphology and surface topology of the grown NWs (nanostructures). The technique relies on scanning of a relatively rough surface of the specimen using a very small focused probe (<10 nm) of electrons striking the sample.
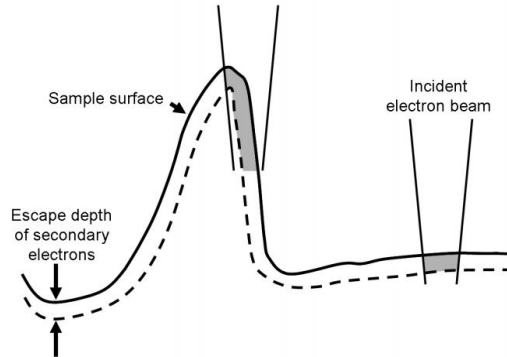
Figure 17. Schematic presentation of the escape depth and volume for the secondary electrons generated by incident electron beam in SEM. Dashed lines represents the depth and the shaded grey areas are the escape volume [41]

The secondary electrons (SEs) generated by bombardment of the specimen using a high-energy electron beam results in the ejection of outer-shell electrons of atoms exerted by kinetic energy of incident electrons. The collection of the low energy (less than 50 eV) secondary electrons escaping from the very near surface (depth of 5 to 50 nm) by a wide-field secondary electron detector results in formation of an image that displays the

topography of the surface. Figure 17 shows an illustrative image of escape depth and volume for secondary electrons. As can be seen for the protrusions (bumps) areas of the sample the escape volume is larger than that of the smooth surfaces that have normal direction parallel to incident electron beam. This phenomenon brings about the higher number of secondary electrons to be generated by protrusions which makes them appear brighter while being imaged in SEM [41]. Figure 18 depicts a schematic picture of a scanning electron microscope with multiple components. As it can be inferred from the vertical column of SEM there are different apertures and lenses that are responsible for better focusing of the incident electron beam onto the surface of the specimen. The condenser lenses are designed to control the spot size by demagnifying the electron beam generated by the gun. The objective lens is used to focus the electron beam to a small spot. After these secondary electrons are generated near the surface, they move towards the surface of a positively biased grid. The most commonly used detector for this purpose is the Everhart/Thornley type. As a result of the secondary electrons striking the surface (scintillator; a luminescent material) of the detector, the electrical energy is converted to a form of photons entering the photomultiplier tube. These photons are later changed back to the electrical energy and their amplified signal is projected onto the screen of a cathode ray tube. The backscatter electron (>50 eV) detector collects the electrons that bounce back after collision with the different atoms of the target specimen, providing the information about the distribution of different elements in the sample based on the well-known concept of Z-contrast. From the backscattering image, which is generally poorer than SE image, the atoms with high atomic number (Z) appear brighter due to greater elastic scattering from heavier atoms.
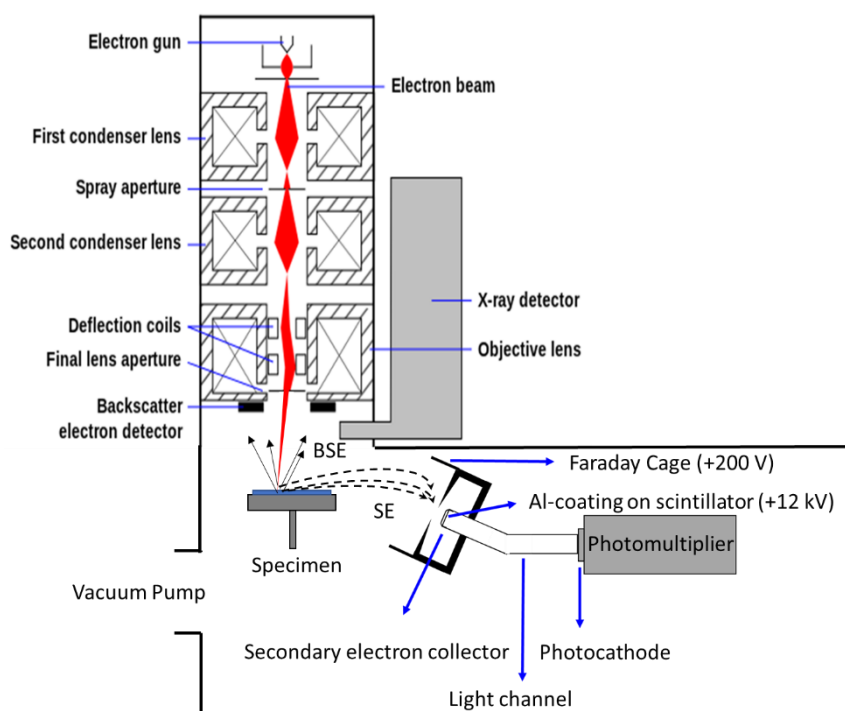
Figure 18. Schematic of SEM with a working principle of secondary electron detector [modified from https://en.wikipedia.org/wiki/Scanning_electron_microscope + https://cmrf.research.uiowa.edu/scanning-electron-microscopy].

In the current dissertation, a XL30 ESEM-FEG was utilized for imaging our different nanostructures mostly in secondary electron (SE) mode. The XL-30 SEM (Figure 19) employs a stable high brightness Schottky Field Emission electron gun (FEG) in an operating low vacuum level of 10^{-5} mbar. The spot size (1-10 nm) and energy of the beam (5-30 kV) was adjusted depending on different case of studies. To avoid surface charging of the samples that are transferred onto quartz glass through a contact printing method, the surface of the samples was coated via sputtering of a thin (<50 nm) layer of the Au-Pd. This is necessary to facilitate the sinking process of the electrons from the surface by creating a conductive layer on the top surface of the specimen.

33

Figure 19. XL-30 SEM at LeRoy Solid State Science Center (LSSSC) of ASU.

Together with EDS detector, the XL-30 SEM provides very important information about the morphology, dimension, growth direction and areal density of the nanostructure as well as the element composition of samples with various experimental and processing conditions.

2.3.1.2 Transmission Electron Microscopy (TEM)

TEM is a powerful technique for studying the crystallinity of nanostructures down to atomic levels. It requires a very thin electron transparent specimen (less than 100 nm) that allows for a very high energy beam to pass through the sample. TEM provides useful information about the crystal orientation, or rather called growth direction, and phase purity (ZB or WZ) of the nanostructure as well as the concentration of the planar defects such as stacking faults and dislocations in nanomaterials. A schematic diagram of the typical TEM column is shown in Fig. 20. TEM operation system consists of three main

sections: illumination, electron beam-specimen interaction and image formation from the top to down inside the column, respectively. First the high energy electrons are generated through an electron gun which is typically a filament or a field emission tip with a high accelerating voltage. The electrons pass through the condenser lens system which is used to focus the electron beam with smaller size. The condenser lenses control the intensity and convergence angle of the beam that is directed onto specimen. The incident electron beam on the specimen is transmitted and scattered, which passes through the objective lens, thereby forming an image of sample on back focal planes (intermediate image 1) object plane. In diffraction mode, the selected area electron diffraction (SAED) aperture must be inserted inside to be in front focal plane of the intermediate lens.
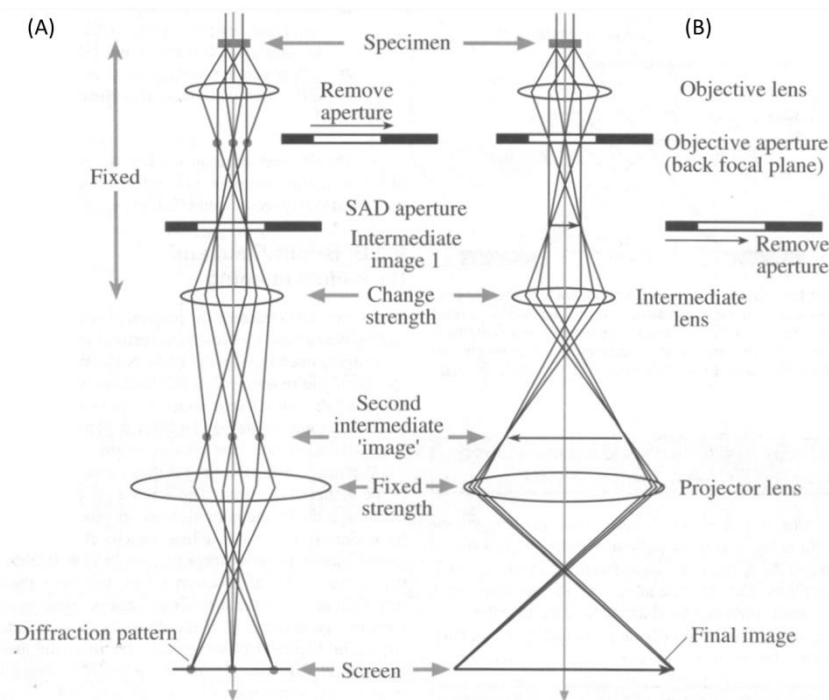
Figure 20. Ray diagram representing two basic operation modes of TEM. A) diffraction mode: the diffraction pattern is projected onto viewing screen B) imaging mode: the image is projected onto the viewing screen. The difference between the two modes is the strength of the intermediate lens which selects either image plane or the back focal plane of the objective lens as its object. [42]

The configuration of spots in diffraction pattern which is generated by elastically scattered electrons depends on interplanar spacing between atomic planes and the angle of incidence of electron beam onto the crystalline specimen. Each spot in diffraction pattern represents the interplanar distance of a specific set of planes from which the crystal structure and phase (ZB or WZ) can be determined. There are two types of imaging modes known as bright filed and dark field present in TEM. Bright field images are formed by the transmitted electron beam, whereas the dark field images are generated using the diffracted electron beam. More importantly, to obtain the high resolution TEM (HRTEM) image of the NWs the TEM NWs must be tilted to a required zone axis. In reciprocal space, the zone axis is a term used to specify the direction of the incident electron beam with respect to the crystal [43]. In this work, the nanostructures were analyzed using an aberration-corrected FEI Titan TEM operating at 300 kV (Fig. 21). The system is also equipped with an EDXS detector for elemental analysis of the NWs. As mentioned, it is important for the TEM specimen to be thin enough for the electron beam to pass through, thus it is required for the NWs to have a diameter of a few hundred nanometers. For the thicker wires, it is required to do sample preparation and thin them down via polishing and similar techniques. Herein, the NWs or NBs that are studied are mostly thin enough to be electron transparent. TEM samples were prepared by contact printing which is a direct mechanical transfer of NWs from the as-grown sample to another substrate. First the holey-carbon coated copper TEM grid is soaked in ethanol for a few second and blown off using an ultra-high purity nitrogen gun. Subsequently, by

gently sliding the grid on the as-grown substrate, the nanostructures are transferred onto the TEM grid. HRTEM imaging of the nanostructures along the required zone axis was performed to identify the crystal structure and study the twin planes and stacking faults in combination with SAED patterns.
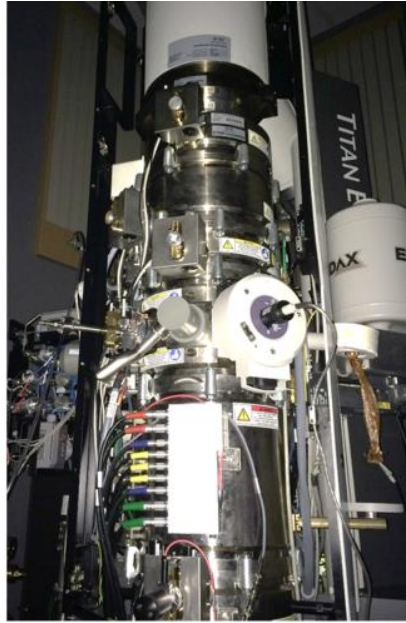
Figure 21. Titan 300/80 (FEI) [courtesy of Prof. Crozier, ASU]

2.3.2 Optical Characterization

2.3.2.1 Photoluminescence Spectroscopy (PL)

Photoluminescence (PL) is the widely used contactless and nondestructive technique for the study of the intrinsic and extrinsic optical and electronic properties of the semiconductors. In PL spectroscopy, photon with energy higher than the bandgap of the material is used to generate the photoexcited carriers through an optical pumping process. When the specimen is pumped with a high energy laser source, the electrons get excited

to the conduction band and leave behind the holes. The photo-generated electron-hole pairs can relax to a lower available energy levels through a radiative or non-radiative recombination process. The non-radiative recombination occurs when an electron in conduction band and a hole in valence band recombine and the excessive energy is released in the form of phonon (thermal energy) or lattice vibration in crystal lattice. Three major non-radiative recombination processes are Auger recombination, surface recombination and the recombination at defect centers such as dislocations and impurities. Direct or radiative recombination of an electron in a conduction band and a hole in valence band results in emitting the photons with a wavelength corresponding to the bandedge of the semiconductor material. The main optical processes associated with radiative recombinations are: absorption or gain, spontaneous emission and stimulated spontaneous emission. The schematic of the photon-matter interaction processes in a system with two levels of energy is shown in Fig. 22. The idea of stimulated emission was first realized by Einstein in 1916. E_1 and E_2 are the ground and excited state energy levels of atoms.
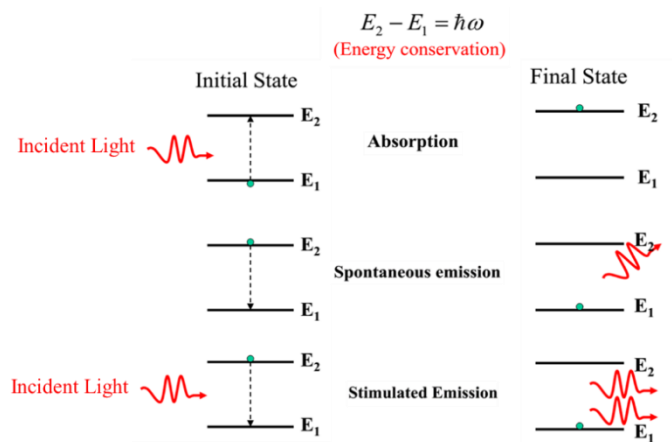
Figure 22. Light-matter interaction processes in a two-level system. Figure is from Nanophotonics course note by Prof. C.Z. Ning (ASU, Fall 2014)

When an electron is excited to a higher energy level under illumination of high energy light, it decays to a non-occupied lower energy level while emitting light with photon energy equal to the difference between ground and excited state. This is a well-known process called spontaneous emission which is taken into account for the identification of bandgap of material using PL spectroscopy. PL measurement is based on detecting the luminescent light produced by sample under optical pumping of high energy laser light. Stimulated emission is based on the interaction of incident light with an excited atom that results in decaying the electron to ground state. For a system under an equilibrium condition, the number of atoms in an excited state are much lower than those in ground state which means it is difficult for the rate of stimulated emission regime to exceed the absorption rate, unless there are much higher number of electrons in excited state. Provided that the optical gain medium (material) has much more gain (generation) of carriers than their loss (recombination), there will be an amplified spontaneous emission that is an essential condition for lasing to occur. By increasing the pumping power of the laser in a suitable resonant cavity, it is possible to achieve lasing under room temperature condition. This will be further discussed in the next chapter, where the lasing properties of InP nanostructures is studied. A detailed explanation of the PL spectroscopy can be found in a review paper by Gilliland [44]. Fig. 23 shows a schematic of a typical PL measurement setup. For each PL measurement setup, there are three main different components: excitation by laser light illumination (optical pumping), signal collection by an appropriately designed optics and detection of the light by spectrometer. A cryostat chamber was used for some of the low temperature measurements. Together with mirrors, lenses are used for directing the laser light onto the sample stage or the emitted

light after filtering of the laser light toward the spectrometer. The spectrometer consists of a diffraction grating-based monochromator and a detector that converts the light to PL signal.
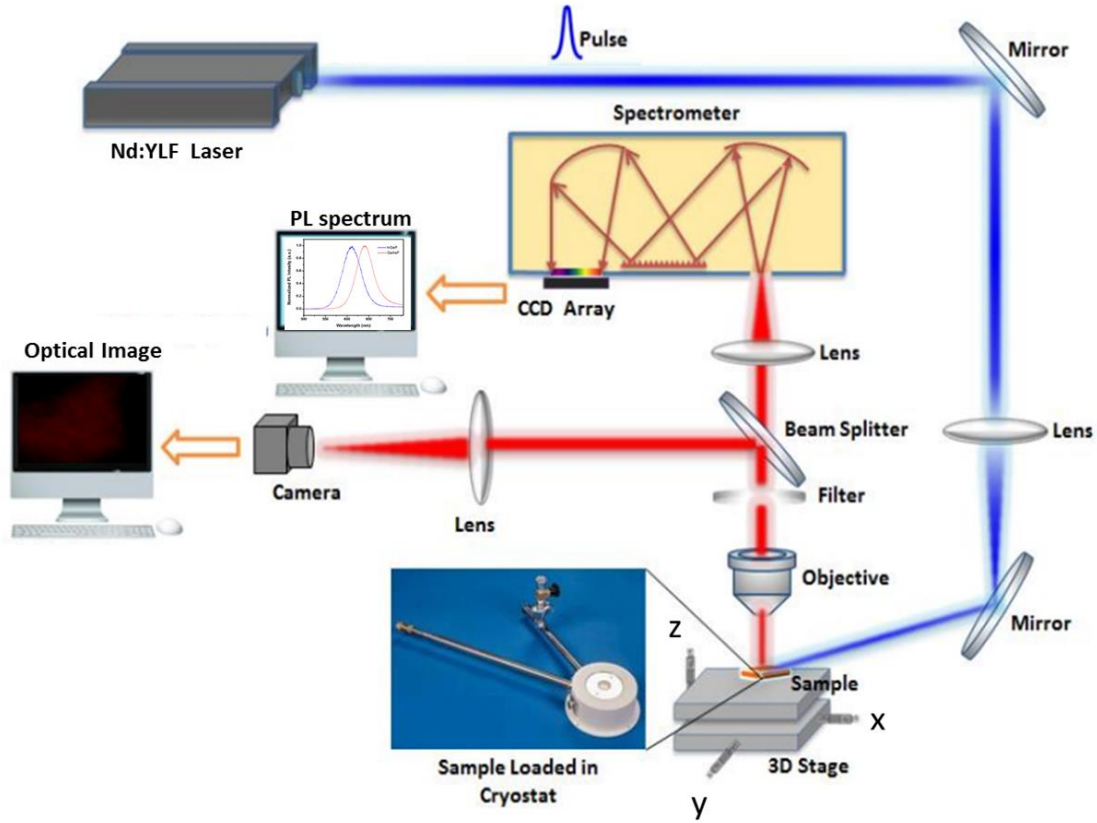
Figure 23. Schematic of typical PL setup in ASU Nanophotonic Lab. Figure modified from ref 45.

In the current research, depending on the materials of different bandgap and specific goal of study, different type of lasers are used as the excitation source such as Spectra-Physics Explorer 349nm pulsed Nd: YLF laser, Ti: Sapphire pulsed laser system (Tsunami) with λ=810 nm or a PDL 800-B PicoQuant pico-second pulsed diode laser delivering 405 nm laser pulses. All the measurements were performed at the optical lab of ASU Nanophotonics Group.

2.3.2.2 Time-Resolved Photoluminescence Spectroscopy

Excitation of the electrons in semiconductors leads to the generation of electron-hole pairs that can recombine either radiatively or non-radiatively depending on the carrier dynamics which is influenced by the crystal quality and the concentration of defects. The decay equation for a molecule from an excited state to the ground state can be expressed as;

$$I(t)=I_0 \exp(-\frac{t}{\tau_{eff}}), \tag{2.2}$$

where I_0 the fluorescence intensity upon excitation and and τ_{eff} is the effective lifetime which depends on both radiative and non-radiative events that are likely to occur in the material depending on the environment ($\frac{1}{\tau_{eff}} = \frac{1}{\tau_{Rad}} + \frac{1}{\tau_{NR}}$) [46]. PL emission is related to the radiative recombination of the carriers from excited states which have a finite lifetime. PL lifetime is the time that it takes for the carriers to recombine after the PL laser excitation is turned off. This process is not an instantaneous response and the decaying process of the carriers to the ground state occurs exponentially. By identifying the PL lifetime, the decay channels which increase the recombination rate of the material can be determined. Therefore, for the optoelectronic device applications such as solar cells, the lifetime measurement is very important task to be performed. Typically for the III-V semiconductors, PL lifetimes are in order of sub-nanoseconds to hundreds of nanoseconds.

In order to measure the fluorescence lifetime, the time-correlated single photon counting (TCSPC) measurement is used. In TCSPC, the single photon of a periodical light signal generated by a pulse laser is detected. In fact, the time between excitation of the sample

by pulse laser and the arrival time of the emitted photon to the detector is measured. For detection of the low-level light using the TSCPC system, the periodical light signal is divided into thousands of signals with a picosecond time resolution and the detected light is also synchronized to the periodical (pulsed laser) light as shown in Fig. 24.
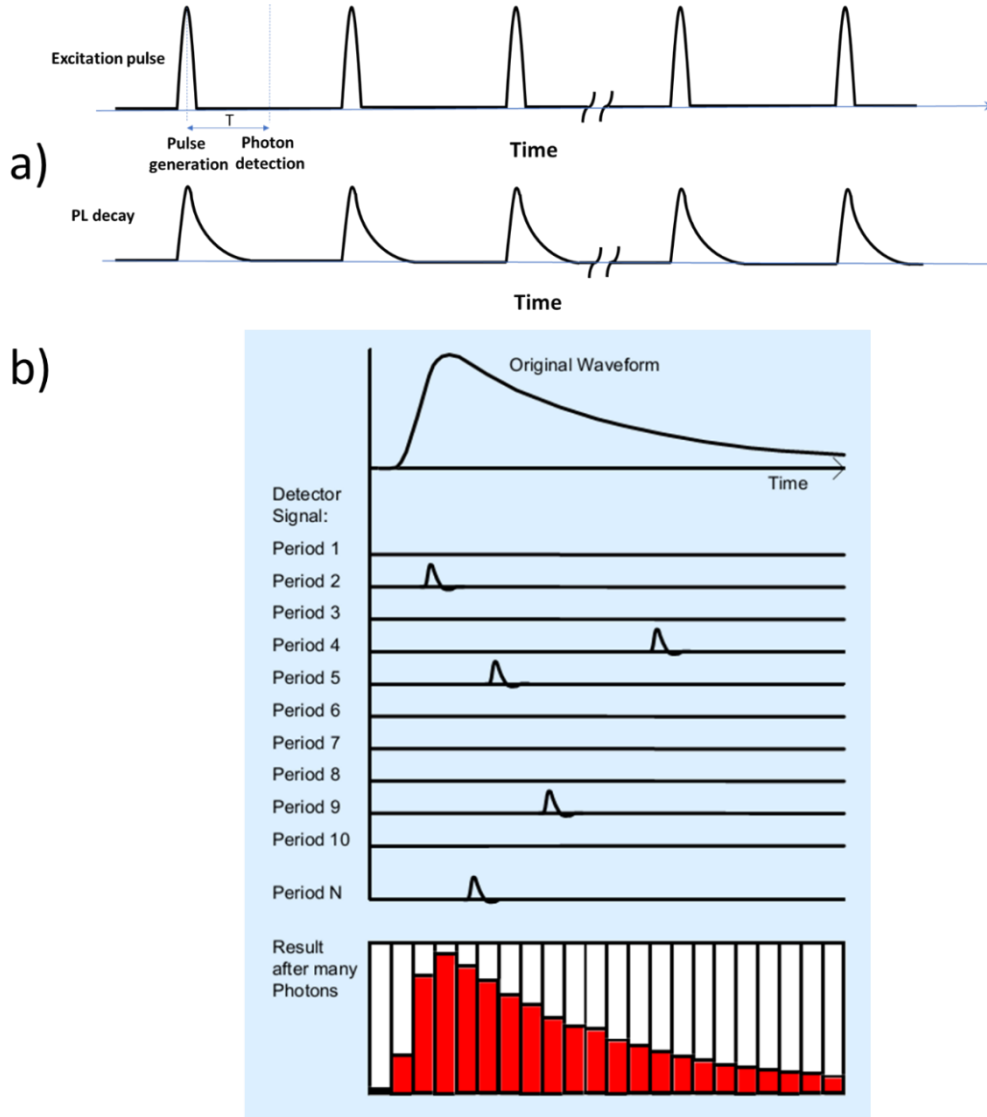
Figure 24. The time measurement in TCSPC. a) the PL decay is synchronized to excitation pulses. The time is measured between the excitation pulse and the detection of single photon. b) the waveform of the fluorescence gives information about the decay dynamic. The figure is adapted from Ref. 47 and 48, where the top long pulses indicate the actual PL signal and the small stripes (below) at indicate time channels.

As can be seen in Fig. 24a, each laser pulse can induce a PL decay that is completed before the next pulse (cycle) is started. It is required for the emitted photon to have detection probability of less than one. Therefore, the intensity of the emitted photons is kept low by adding the neutral density filter into the optical path of TCSPC system.

By summation of the detected single photons in various time channels (periods) after a long acquisition time the waveform of the fluorescence emission can be obtained from which the fluorescence lifetime can be measured (Fig. 24b.) A schematic of the TCSPC system used for lifetime measurement is shown in Fig. 25. The excitation source is a picosecond diode laser (405 nm pulsed laser) with the adjustable repetition rate between 2.5 MHz and 40 MHz. The excitation source is coupled to a PL system connected to a monochromator.
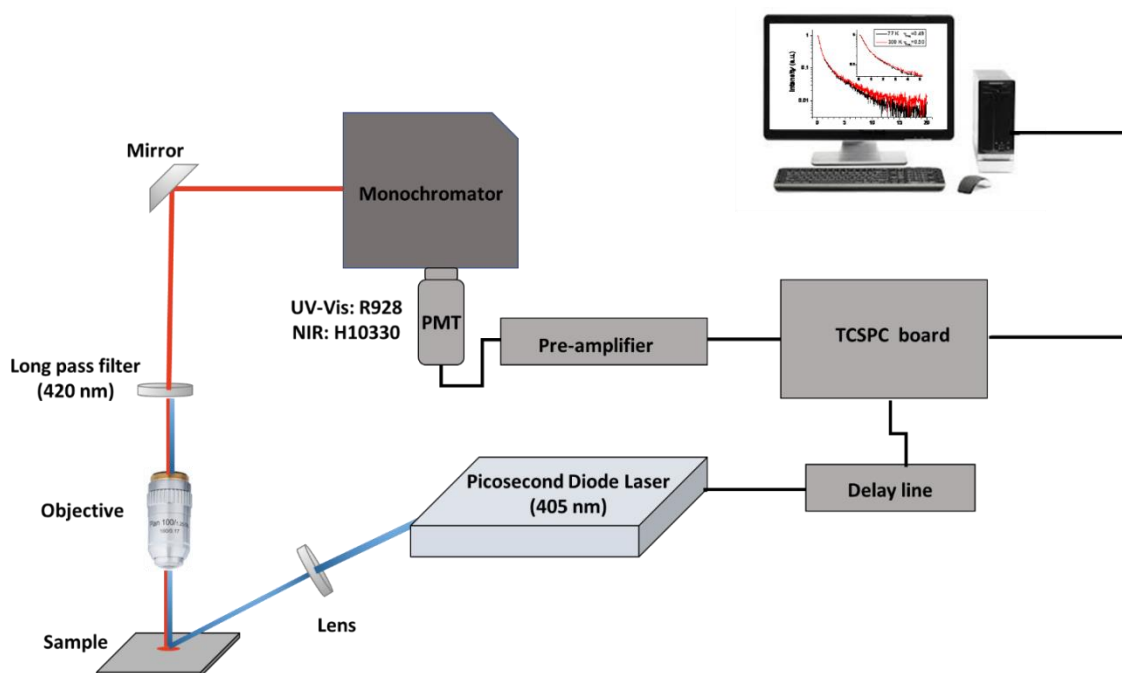
Figure 25. Schematic of PL lifetime measurement setup using TCSPC system

The detected signal by photo multiplier tube (PMT) is amplified by a preamplifier before reaching to the TCSPC board (B&H, SPC-130). Our available PMTs operate in in various wavelength range; Hamamatsu R928 for UV-VIS and H10330-75 for NIR. A digital delay line is used to compensate the time difference in optical path by delaying the synchronization signal. The result obtained by processing the PL and synchronization signal in TCSPC is used to construct the PL lifetime decay curve from which the carrier lifetime can be measured for the material of interest.

2.3.2.3 Raman Spectroscopy

Since Raman scattering was first discovered by C.V. Raman in 1920s [49], it has been widely used as one of the most instrumental analytical techniques to study the structural disorders attributed to non-stoichiometric defects that would disrupt the long-range ionic ordering in crystalline materials [50]. In Raman spectroscopy, the interaction of incident light which is often the monochromatic laser source with the molecular vibrations is studied in terms of the associated vibrational energy levels. When the sample is illuminated by laser light, a big portion of the light is scattered and re-emitted with the same frequency as absorbing photon, which is known as Rayleigh scattering. In Raman scattering, a very small portion of incident light is transferred to the molecular vibration which has energy frequency slightly different from that for the incident light. Raman effect which is based on an inelastic scattering of the incident light, causes a Raman shift (up or down) with respect to the wavelength of incident light. Fig. 26A illustrative a schematic picture of such phenomenon that results in Raman scattering.
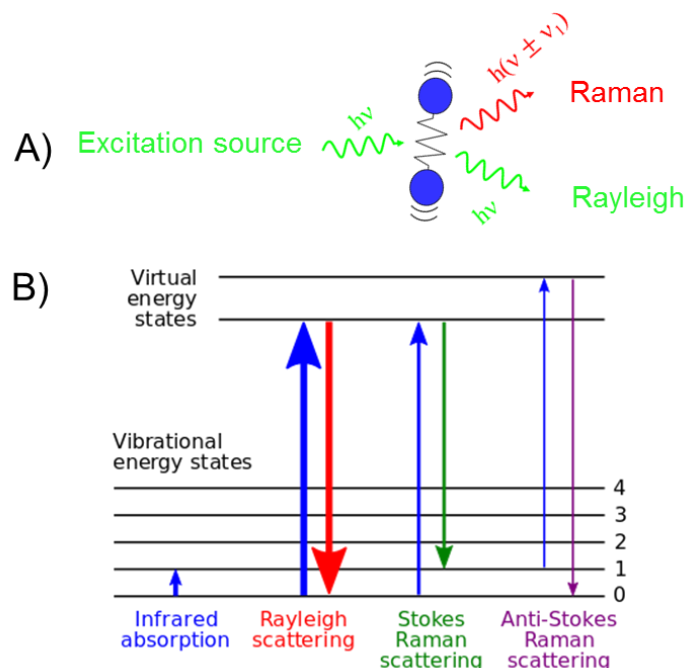
Figure 26. Schematic of Rayleigh and Raman scattering under excitation incident photon (A), Energy-level diagram showing the states involved in Raman spectra (B) [51].

If the frequency of the scattered photon is lower than that of incident light, it is called Stokes scattering, but if the frequency is shifted towards higher frequencies, it is called anti-Stokes scattering, as it is depicted in Fig. 26B. The experimental setup for Raman measurement is the same as PL with the exception that Raman signal is much weaker than signal detected by PL. Fig. 27 shows a schematic of typical Raman set up which is based on the detection of only the inelastically scattered light arising from molecular vibrations. A notch filter is used in optical path to filter the laser light before reaching to the spectrometer and being detected by CCD. The Raman spectrum is often plotted as a function of wavenumber shift which is defined as the energy difference between the excitation light and re-emitted photons. In order to convert the wavelength obtained by spectrum to Raman shift the following formula can be used;

45

$$\Delta\omega(cm^{-1}) = \left(\frac{1}{\lambda_0(nm)} - \frac{1}{\lambda_1(nm)}\right) \times \frac{(10^7 nm)}{(cm)}, \qquad (2.3)$$

where λ_0 is the wavelength of the laser, λ_1 is the wavelength of Raman spectrum, and $\Delta\omega$ is the Raman shift which is expressed by a wavenumber with a common unit of cm^{-1} [51].
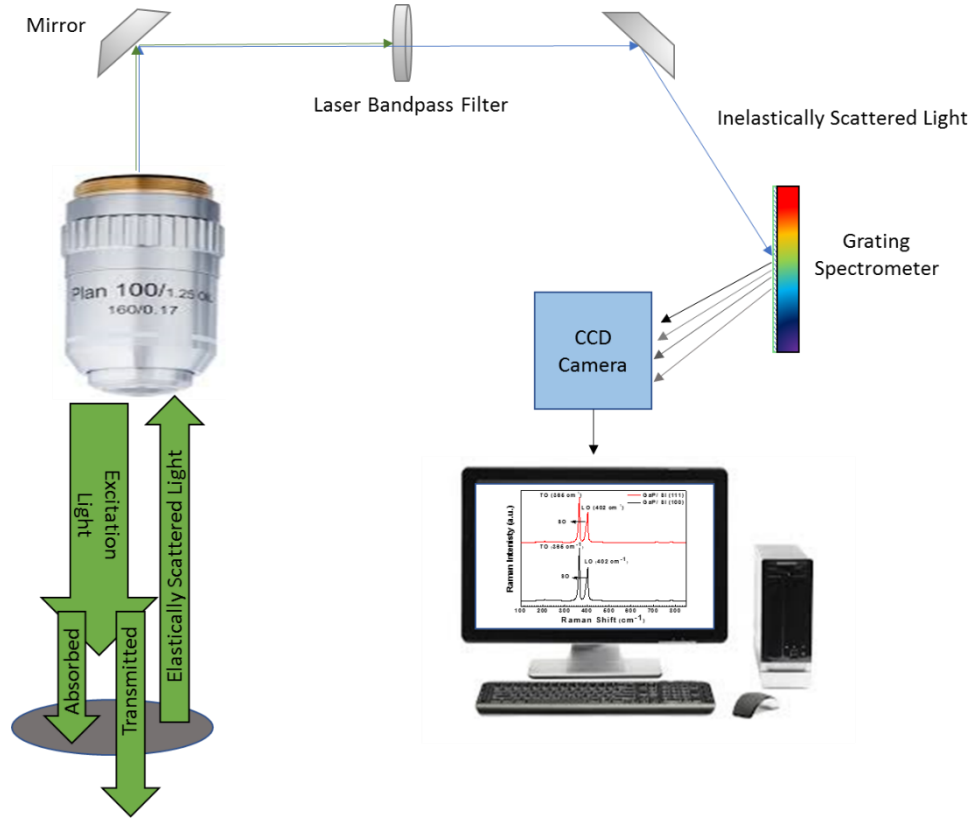
Figure 27. Schematic of the Raman measurement setup

In our work, we have collected Raman data using a custom-built Raman spectrometer in a 180° geometry. The excitation source is 150 mW Coherent Sapphire single frequency laser with a wavelength of 532 nm. The Raman signal is discriminated from the laser excitation using a Kaiser laser band pass filter followed by an ultranarrow-band notch filter and an edge filter. The data are collected using an Acton 300i spectrograph and a back thinned Princeton Instruments liquid nitrogen cooled CCD detector. The grating of

1800 g/mm was utilized for the measurement, resulting in a spectral resolution of less than 1 cm^{-1}.

2.3.3 Structural Characterization

2.3.3.1 X-Ray Diffraction (XRD)

XRD is one of the most convenient tools for determining the crystal quality of the materials. It is a non-destructive technique which also provides useful information about the strain/stress in thin film crystals as well as crystal orientation. XRD relies on existence of long-range order in a crystal due e to lattice periodicity which is formed by regular arrangement of atoms in a single crystal. Because of such periodic fashion in a crystalline material, a monochromatic x-ray beam striking the single crystal is diffracted in form of in-phase x-ray waves (Fig. 28). Such constrictive interference of x-ray is produced when the Bragg's law is satisfied as follows:

$$n\lambda = 2d\sin\theta, \qquad\qquad (2.4)$$

where n in an integer number representing the order of reflection, λ is the wavelength of the incident x-ray radiation, d is the interplanar spacing in the lattice, and θ is the diffraction angle. This means that the sample rotates through an angle of θ with a wide range of values, while the detector rotates simultaneously with a rotation angle of 2θ with respect to the incident x-ray beam.
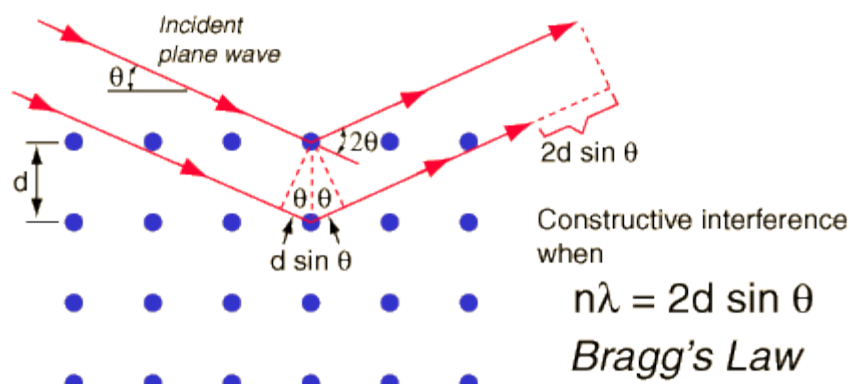
Figure 28. Principle of Bragg's law reflection [copied from
http://hyperphysics.phy-astr.gsu.edu/hbase/quantum/bragg.html]

The results obtained from XRD pattern are used to estimate the crystallite size, residual strain, and more importantly, the lattice constant for the grown NWs and thin films. For the alloy NWs, Vegard's law is applied to estimate the lattice constant for various ternary III-V alloys. Vegard's law is an approximation based on existence of a linear relationship between the lattice parameters of an alloy and the concentration of constituent components [52].

All the XRD data was acquired on a High-Resolution X-ray Diffractometer (PANalytical X' Pert Pro Materials Research XRD) equipped with copper K_α (λ= 0.15418 nm) in powder x-ray diffraction mode. The flexibility of the fixed divergence slits enables us to shrink the size of the x-ray beam in combination with beam masks down to desirable smaller sizes especially for the position dependent measurement of spatially composition-graded samples, where step size as small as below 1mm is needed to correlate the XRD data with those obtained by EDS and PL.

2.3.3.2 Energy-Dispersive Spectroscopy

 EDS coupled with SEM microscopes (EDXS in TEM) is an analytical technique for identification of elemntal composition of the nanostructues. As mentioned earlier in SEM section, the electron beam penetrating into the depth of the specimen brings about generation of charactersitcs x-ray with specific characterstics energy associated with each element. The main principle behind EDS measurments can be inferred from the difference between discrete energy level of inner shell electrons in an atom (Fig. 29).
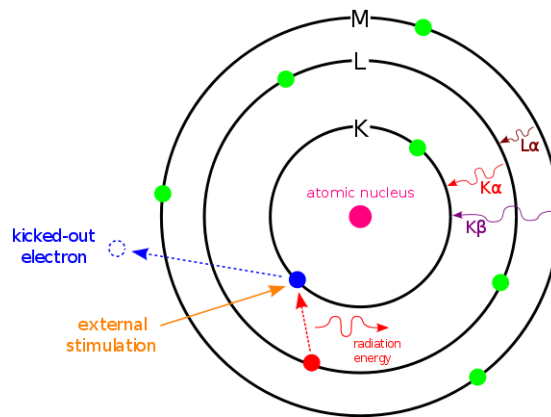
Figure 29. Characteristics x-ray energy; K, L and M are different electron shell around the nucleus [53].

As shown in figure, the x-rays are emitted by an atom when an excited electron by an external high energy source falls from an outer to the inner shells. Each different atom emits a photon of a specific characteristic energy corresponding to that transition in the element. These transitions are named according to their initial and final energy level. According to Mosely's law (depicted in Fig. 30), which is based on his emprical observation on relationship between atomic number of elements and magnitude of their charatertics x-ray energy, it is revealed that the outer electrons are repelled from the nucleus by all electrons closer to the nucleus [54].

49
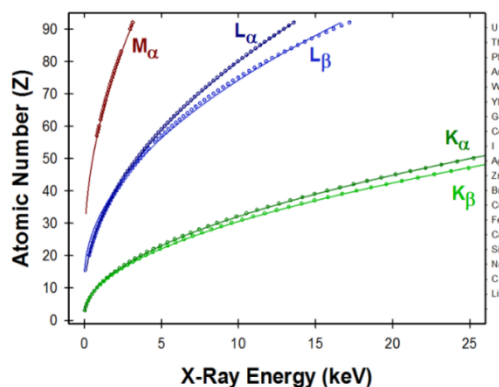
Figure 30. Moseley's law: relationship between characteristics
x-ray energy and atomic number(Z) [55].

This means for an element with specific atomic number, the X-ray characteristic energy value is larger for the transitions from the outer shells to nearest shell to the nucleus (K_α> L_α>M_α). The accumulation of the number of different x-rays counted by EDS detector is used to determine the EDS signal. EDS spot analysis mode in XL-30 SEM provides us with accurate elemental composition different materials with only limitation being incapable of detecting the elements with low atomic numbers (Z=1-5). To give an insight on precision of quantities data acquired by EDS; the small size of electron beam with a spot size of ~ 10 nm enable us to obtain a precise elemental composition profile along the length of a single NW. However, EDS results are subject to have errors up to 5-10% due to peak fitting, detector efficiency, background subtraction or sometimes overlap between the characteristics x-ray energy of two different elements with very close values [56].

2.3.4 Electrical Characterization

Evaluation of the electrical properties of the semiconductor materials are the indispensable task to perform prior to using them in making actual optoelectronic devices. For evaluation of a device or material in terms of performance and efficiency it

is required to examine some of its typical electrical properties. Those tests mainly include the measurement of resistivity and conductivity (type and magnitude) carried out on different semiconductor with various doping concentration, etc. The other important one is the study of the current vs. voltage (I-V) or resistance characteristics which is necessary to examine the performance of different devices such as LEDs, sensors and photovoltaic cells, etc.

2.3.4.1 Hot Probe Measurement

It is a very well-known technique used to determine the carrier type of semiconductor by diffusion of the carriers under a thermal energy (heat). The measurement is simply performed by using a multimeter while its positive terminal is heated by a soldering iron that causes the carriers (electrons in n-type and holes in p-type) to move towards the cold electrode (negative terminal) under diffusion at high elevated temperature.
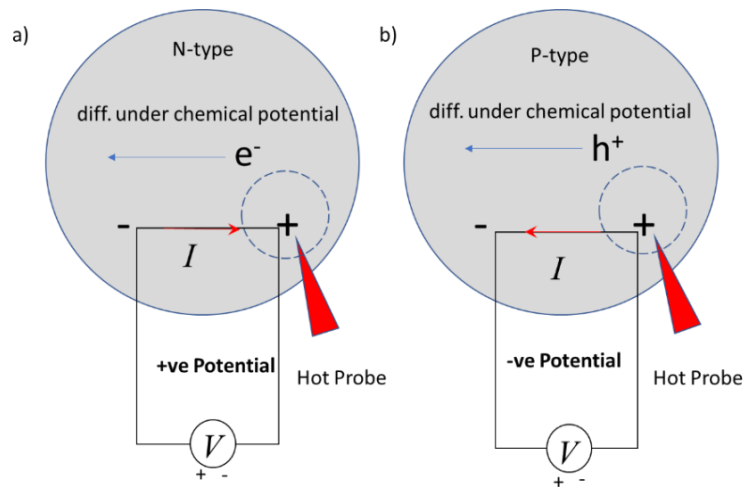
Figure 31. Schematic of hot-probe measurment.

Fig. 31 describes the experimental set up for the hot probe measurements. As it is shown in Fig. 31a, for an n-type semiconductor once the positive electrode is coupled with a hot

51

probe (red), the electrons start to move towards the negative electrode which makes the current to flow in a reverse direction. This is equivalent to forward bias, which means the voltmeter will be reading a positive voltage value. Similarly, for the p-type semiconductors, the value being read by the voltmeter will be negative (Fig. 31b). It is important to note that this method is not valid for the, grown layers on top of metals or semiconductor substrates such as silicon, etc.

2.3.4.2 Hall Measurement

Ever since Edwin Hall has discovered the "Hall Effect" in 1879 [57], it has been established as a powerful material characterization technique for the measurement of electron mobility of the semiconductors that are used in optoelectronic device manufacturing. Basically, for a bulk conductor, Hall measurements reveals how much of electrons or carriers flow through the crystal or in another word how much of current can be handled by a device. To observe the Hall effect the current pass through the semiconductor sample (slab with dimension given as l×w×t shown in Fig. 32), while it is exposed to a magnetic field under perpendicular direction to current direction. When a magnetic field is applied (in -z direction), these charge carriers (electrons or holes) experience a force, called the Lorentz force [58]. Thus, the magnetic field passing through the thin film sample deflect electrons inside the semiconductor causes the potential difference perpendicular to current flow. As shown schematically in Fig. 32a, for an n-type semiconductor the Lorentz force will be forcing the electrons toward the front face (right hand rule), where the accumulation of electrons and depletion in the back-face results in building a electric potential with a resulting electric field in that

52

forces the electrons in opposite direction to the Lorentz force. At some point where these two forces become equal and balance out each other, there will not be any further accumulation of electrons, hence this is called steady state.
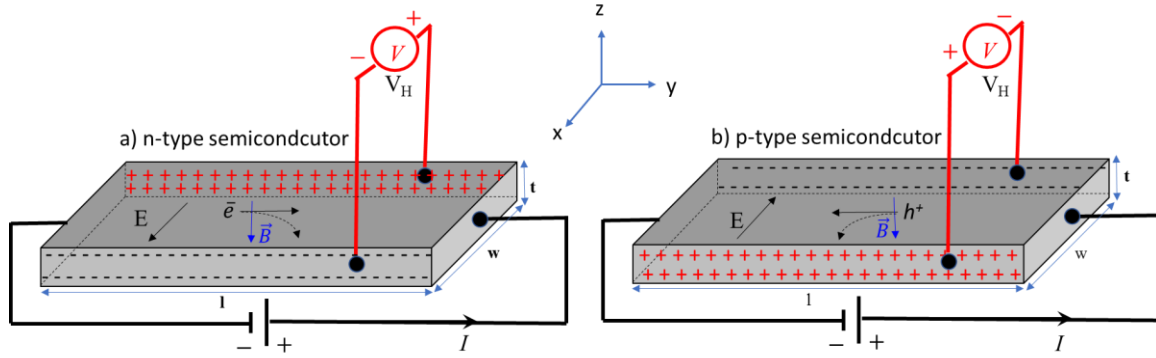
Figure 32. Schematic of Hall effect for a) n-type and b) p-type semiconductors

The corresponding developed potential difference in x-direction is known as Hall voltage (V_H). For the p-type material (Fig. 32b) with holes as the majority carriers, the direction of the electric field ($E_H = \frac{V_H}{w}$) will be reverse. The V_H read by a voltmeter will be negative for an n-type and positive for a p-type. The Hall coefficient can be driven as:

$$R_H = \frac{V_H t}{BI} , \qquad (2.5)$$

where B and I are magnetic field and current. The t value (sample thickness) is the width of the plane on which the charges are being accumulated. Hall mobility can be calculated using the formula below:

$$\mu_H = \sigma R_H = \frac{V_H t}{\rho BI} , \qquad (2.6)$$

where σ and ρ ($1/\sigma$) are conductivity and resistivity, respectively. It is also known that for a doped semiconductor resistivity can be obtained by:

$$\rho = \frac{1}{\mu n q} , \qquad (2.7)$$

where μ, n(p) and q are carrier mobility (cm2/V.s), concentration of carriers (cm^{-3}), and electron (hole) charge (C/cm^2), respectively. To measure the carrier concentration and mobility of our III-V film, a four-point probe measurement technique was used using indium metal contacts in a configuration schematically shown in Figure 33.
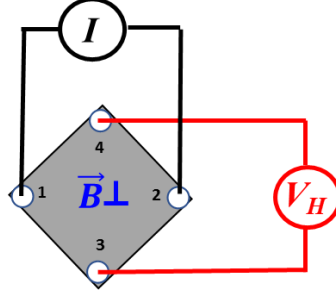
Figure 33. Schematic of four-point probe set up for Hall measurement. Figure adapted from ref. [59].

The applied magnetic field and current passing through the film with a known thickness and resistivity will help us to determine the Hall mobility and carrier type of the grown III-V sample.

2.3.4.3 I-V Measurement

I-V characteristic curves for solar cells show the current and voltage (I-V) characteristics of a phtovoltaic solar cell. The power conversion efficiency of a solar cell can be detrmined from the I-V measurments. To measure the performance of solar cells, I-V measurment is carried out by scanning an applied voltage across the fabricated solar and measuring the current response that is obtained from the cell. For the precise evaluation of the cell performance, a solar simulator is typically used. In this work, an LCS-100 solar simulator by ORIEL was used to create 1-sun condition for I-V measurement of solar cells. I-V curve is optained by plotting the current of solar cell versus applied. The term open-circuit voltage (V_{oc}) is defined as the maxium voltage across the cell, when the system is not connected to any load and the current is minimum (I=0). Also for a short circuit solar cell,

since the positive and negeative lead are connected together, the voltage across the cell becomes minumum (zero) while the short-circuit current (I_{sc}) is at its maximum state. Typically solar cells are made in p-n or p-i-n junction configuration, which allows for the carriers to be seperated and result in generation of a current upon exposure to light. The I-V curve for a solar cell is the superposition of the I-V curve in the dark condition with the photogenerated current [60]. As shown schematically in Fig. 34, when a solar cell is illuminated the dark I-V shifts down to fourth duadrant, where the product of curret and voltage is not zero and the power can be extracted since from the solar cell diode. The term illumination current (I_L) can be added to the p-n junction diode current and the result is expresed by;

$$I = I_0 \, (e^{\frac{qV}{kT}} - 1) - I_L, \tag{2.8}$$

where I is the net current passing through diode, I_0 is the leakage current density of diode in the absence of light, V is the applied potential across the terminals of diode, q is electron charge, k is Boltzmann constant, and T is the absolute temperature. From the I-V curve, the maximum power point (P_{max}) can be found as the point where the multiplication of current and voltage values is maximum ($V_{max} \cdot I_{max}$).

The fill factor (FF) is determined by a portion of area under I-V curve that is limited to rectangular area (yellow region) and it can be written as:

$$FF = \frac{V_{max} \cdot I_{max}}{V_{oc} \cdot I_{sc}} \tag{2.9}$$

At last, the power conversion efficiency (η) of solar cell can be determined using the formula below:

$$\eta = \frac{P_{out}}{P_{in}} = \frac{V_{oc} \cdot I_{sc} \cdot FF}{P_{in}}, \tag{2.10}$$
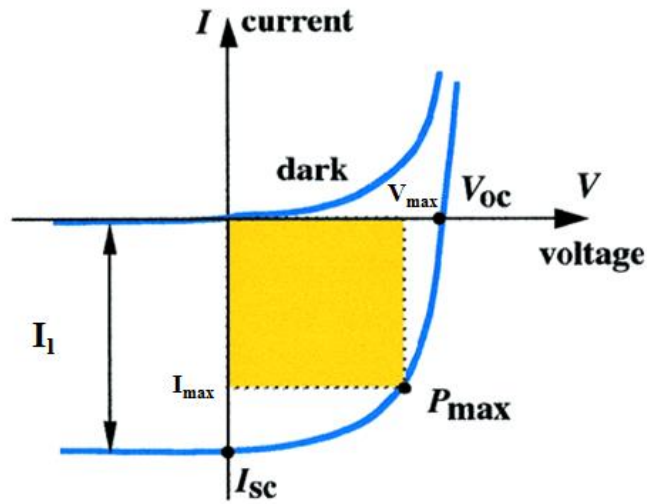
Figure 34. A typical I-V curve for solar cell devices
[https://www.ossila.com/products/iv-curve-measurement-system].

where P_{in} is the incident light power which is 100 mW/Cm^2 for 1 sun AM1.5 G spectrum.

In overall, evaluation of I-V characteristics of a solar cell during the course of fabrication

provides us with a better understanding of different steps that result in failure or very low

device efficiency which are required to be improved.

3 GROWTH OF InP NANOSTRUCTURES

3.1 Introduction

Indium Phosphide is one of the most important III-V semiconductors because of its direct bandgap and superior properties such as high electron mobility and low surface recombination velocity which makes it suitable for a variety of optoelectronic applications. So far, growth of highly crystalline InP NWs has only been demonstrated using MOCVD [8, 61] and MBE [62]. As shown in chapter 1, growth of InP NWs using vapor phase CVD system using InP source suffers from higher sublimation rate of P leading non-stoichiometric InP growth [63]. In this chapter, a low-cost growth methodology will be presented that not only resolves this issue, but also significantly extends the narrow window of growth temperature of InP to a broader range, while sustaining stoichiometric InP growth. InP NWs grown under such growth methodology based on vapor transport of elemental source material show less deviation from stoichiometric composition. Detailed growth dynamic and optical properties of synthesized NWs will be discussed in the following sections. Growth of Nanobelts (NBs) and microdisks of InP via interplay between VLS and VS mechanisms are also demonstrated.

3.2 Growth Procedure

InP NWs were synthesized using a chemical vapor deposition method in a hot wall CVD furnace. High purity Indium (In) metal sphere (1mm dia., 99.99% Alfa Aesar), red Phosphorous (P) (≥99.99% Sigma Aldrich) powder were supplied with controlled evaporation rates inside the separate amorphous quartz boats, each of which attached to a

57

long quartz rod for manipulation of source material using a magnet outside the furnace tube (Fig. 35a). The Si (100) substrate was etched using a 2% dilute solution of HF to remove the native silicon dioxide layer (1-2 nm), and subsequently washed with DI water. A thin layer (1-1.5 nm) of Au was sputtered on the surface of the H-terminated Si substrate and it was immediately placed, horizontally, at downstream end of the furnace on a rectangular quartz plate. The system was pumped down to a base pressure of 100 mTorr, and then flushed by purging Ar+5%H_2 carrier gas at a rate of 300 standard cubic centimeter per minute (sccm) for 30 min to evacuate the system form excessive oxygen and CO_2 molecules, prior to the growth. Afterwards, the furnace was heated up to 1000∘C, with ramp-up rate of 42∘C/min. During the growth process, the flow rate was reduced to 20 sccm, giving rise to a total pressure of 2 Torr. It is important to mention that In source was inside the furnace during the ramp-up time, but after the temperature ramp-up process, the red phosphorous boat was pushed to the edge of furnace, where the temperature is 400-450 ∘C. After a period of 1-60 min growth time, both In and P boats were pushed outside the furnace, where the temperature is low, and the system was naturally cooled down to room temperature. In some other set of experiments, pure InP was as the precursor loaded inside a quartz boat and evaporating at various pressure and temperature conditions. After experimenting different growth conditions, it was figured out that if binary InP powder is used as source material, the obtained NWs are very sparsely grown with a poor stoichiometry (Fig. 35b). On the contrary, using the single elemental In and P precursor results in growth of highly stoichiometric InP NWs (Fig. 35c). In another word, using binary source material for vapor transport CVD growth requires finding the optimum pressure-temperature for evaporation of source material that

leads to a stoichiometric product. In the other hand, using single elemental precursors is

very simple and provides more degrees of freedom for adjusting the vapor pressure of III

and V species, separately.
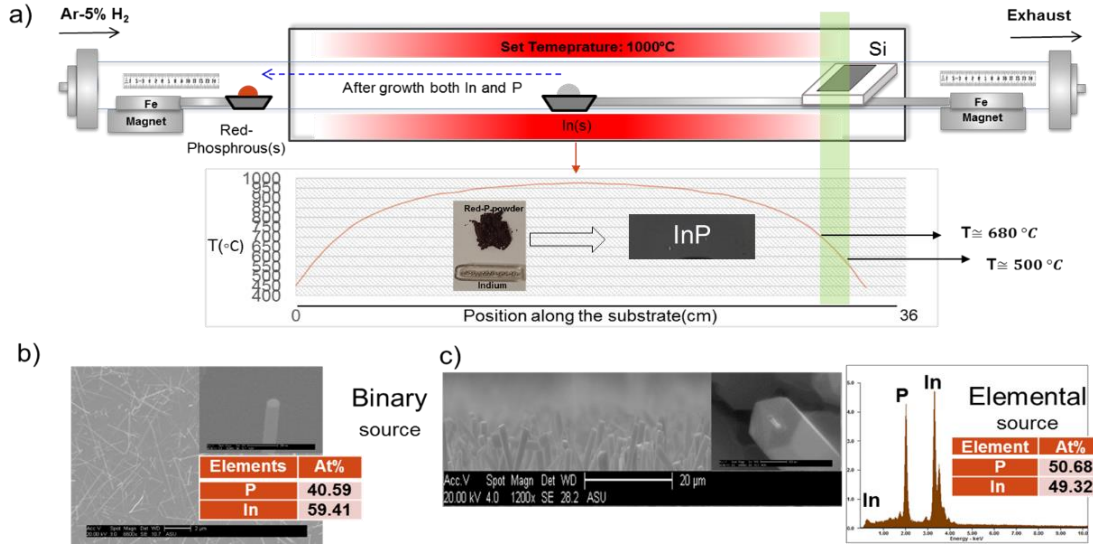
Figure 35. Schematic of the InP NW growth setup. Inset is the images of single elemental source and as grown sample. (a) SEM and EDS result for NWs grown at 440 ∘C using binary source material. (b) cross-section SEM image and EDS of InP NWs grown at 600 ∘C using single elemental precursor. Inset shows the SEM image of hexagonal NW with Au tip sticking out along the NW axis.

As can be seen from the SEM image of the InP NWs with longer growth time, they are

somewhat vertically aligned with respect to the surface of Si (100) substrate, and thick

with a hexagonal cross-section and gold tip sticking out. In tems of growth direction, it is

known that (111) planes have lower surface energy (γ) compared to other

crystallographic planes, due to smaller number of dangling bonds ($\gamma_{(111)} < \gamma_{(100)} <$

$\gamma_{(110)}$). It has been shown for III-V NWs using (111) substrate can lead to growth of

vertical NWs perpendicular to the surface of substrate. On the contrary, when (100) is

used, the low angle (35.3°) NWs are grown, still in (111) direction [64]. However, the

growth direction has been observed to vary presumably due to altering the surface energy by surface free energies, strain, etc [65, 66]. Krishnamachari et al. have demonstrated that the growth of defect free InP NW directly on (001) surfaces in [001] direction to be possible under certain circumstances such as avoided annealing of Au nanoparticles prior to growth [67]. Generally, it is reported that pretreatment of Au catalyst to have an impact on growth direction regime [68-70]. In our particular case, further exploration of the growth direction is required either by HRTEM study and further tuning the growth parameter by a single variable testing to pinpoint why such vertical growth from the surface of Si (100) substrate is observed.

3.3 Growth Dynamic of InP NWs

Growth mechanism of such syringe-like InP NWs using single elemental approach can be understood by their morphology. The underlying mechanism can be explained by interplay between catalyst-mediated VLS and VS growth mechanisms. It can be postulated that VLS growth is followed by a VS growth resulting in lateral expansion of NWs. First, the Au thin film sputtered on a substrate is annealed at 600 ∘C, and broken down to smaller nanoparticles. Subsequently, Au nanoparticles are alloyed with In prior to growth forming an In-Au droplet. NWs are nucleated under the supersaturation of vapor phase In and P species inside the Au alloy droplets giving rise to growth of long NWs with diameters close to those for In-Au-P droplets. The second step is where the VS mode becomes activated and the NWs start to get expanded through the sidewall growth. A set of time dependent growth carried out to prove our postulation by observing a frame by frame of the growth scenario. The Fig. 36 shows the SEM image of NWs grown at

60

600 °C with various growth times. As can be seen for sample grown for 1min, a very long and thin InP NWs are grown. For the sample grown at 10 min, it can be seen that how the cladding layer of InP is formed on the surface of axially grown InP NW. As the growth proceeds, the NW become thicker and axially grown NW is completely covered by the cladding layer.
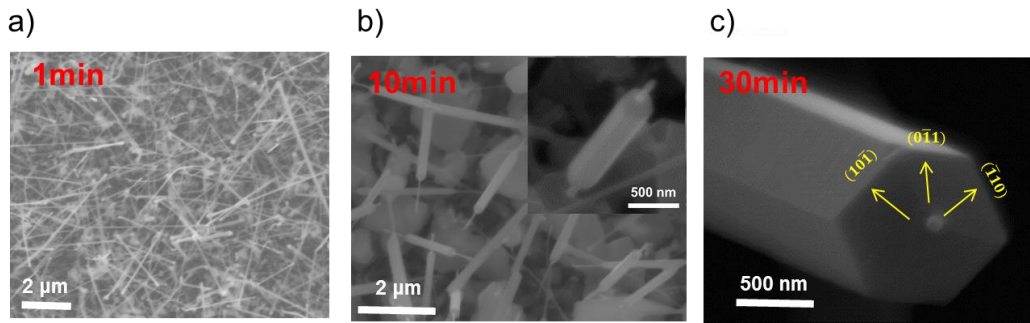
Figure 36. SEM images of time-dependent growth of InP: a) 1 min, b) 10 min, c) 30 min. The planar index of the hexagonal NW in c is by assuming that the NW is pure ZB.

The symmetric geometry along six different direction could be attributed to VS growth along the non-polar surface of the m- and a- planes in hexagonal wurtzite (WZ) along <0001> direction or corresponding planes along <111> direction of zinc blend(ZB). The Fig. 37 shows the atomic configuration of pure WZ and ZB structure along <111> and <0001> projections that can lead to formation of hexagonal NWs.
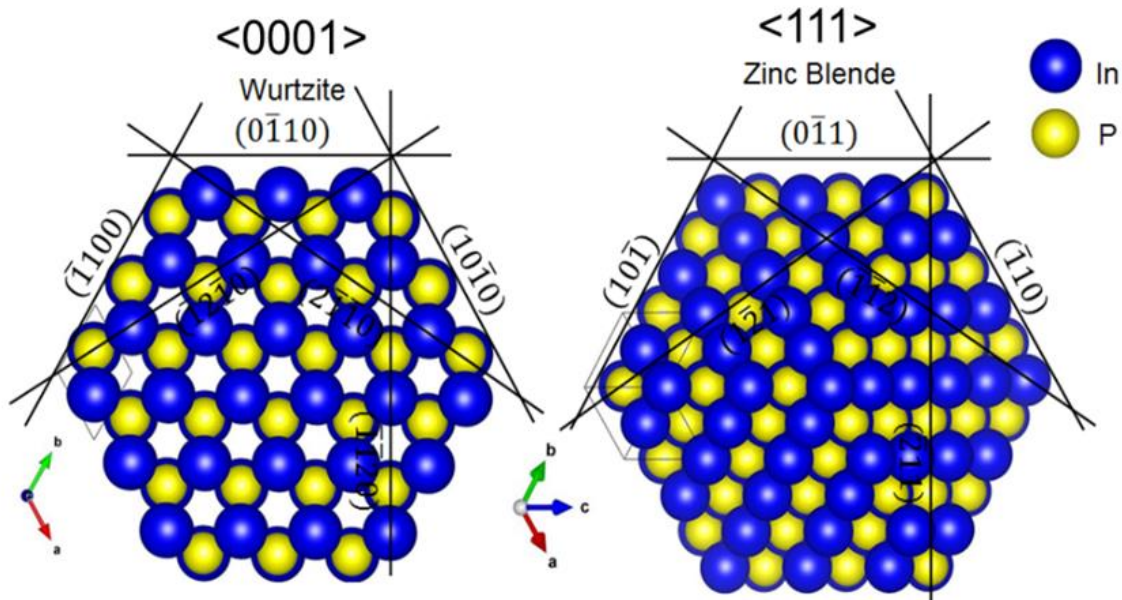
Figure 37. Atomic structure of wurtzite (left) and zinc blende (right) structures along <0001>, and <111> direction, respectively. The structures are drawn using VESTA software.

However, further TEM study is required to study the structural polytypism as well as the stacking faults and twin planes in grown NWs. Sample preparations for such NWs requires using complicated sample preparation methods since they are not thin enough to be electron transparent [71].
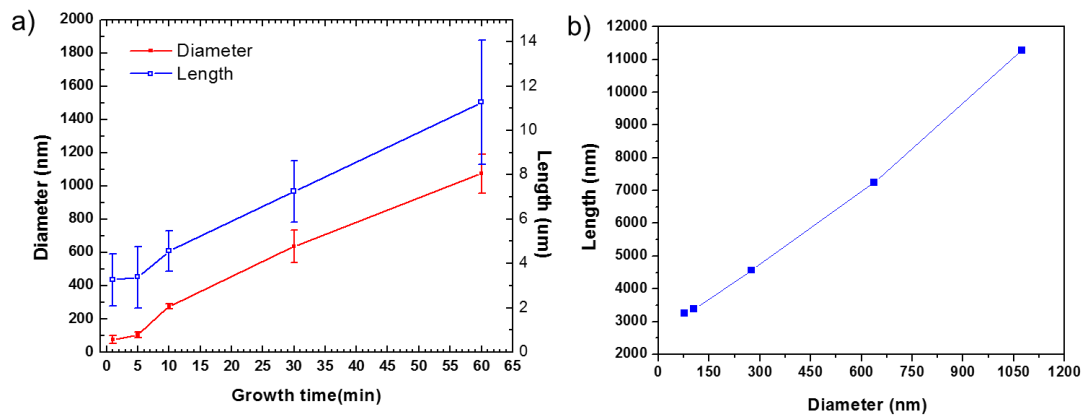
Figure 38. Relationship between growth time and length/diameter of InP NWs (a), Length versus diameter 2D plot obtained from samples with different growth times of 1 to 60 min (b).

In order to better understand the growth dynamic, a statistical study of simultaneous axial and radial growth of the NWs was carried out by measuring both diameter and length for 15-20 randomly selected NWs which are contact printed on a quartz substrate. The length of the NWs varies from 3.3 μm to 11.3 μm, while the diameter changes from 76 nm to 1074 nm for the growth time changing from 1 min to 60 min. The result of the study showed the slowest rate of axial and radial growth is for the first 5 min of the experiment and the highest growth rate is for the time interval between the 5 to10, where the VS mechanism becomes accelerated and diffusion of the adatoms onto surface of the wires occur during the longer growth than 5 min (Fig. 38a). Also, from the LD space plot (Fig. 38b) of the NWs, the axial and radial growth rates are very similar indicating that both impinging the atomic species onto the catalyst droplet and sidewall growth occur with the same rate. The lateral growth of wire can be explained by the fact that diffusion length of the In adatoms is not long enough to reach the Au tip. When the length of the NW exceeds the diffusion length of In, thus results in sidewall expansion of NWs [72].

3.4 Effect of III/V Ratio; Supersaturation Effect

It is known for III-V NWs that the input ratio of group III to V is a critical factor for growth. For instance, by changing the III/V ratio, growth of long NWs can become accelerated in one regime, VLS or VS. It can also be suppressed by growing kinked wires or not being grown due to change in kinetics of supersaturation (SS) or adataom diffusion onto either sidewall surface or Au catalyst [73]. On the contrary, a low III/V ratio results in formation of In droplet [74]. To elaborate on the effect of III/V ratio on the growth rate of InP NWs in both axial and radial direction, a set of experiments were carried out at

600°C (growth temperature) by altering the III/V ratio through changing the evaporation rate of In metal at various temperatures, while P source was kept at constant temperature range of 400-450°C. The results did not reveal any change in morphology, but the areal density of wires significantly deceased for the lower III/V ratio. A comparison of LD relationship between different SS levels showed that by changing the evaporation rate of the source materials by manipulation of T_{In}/T_P ratio for the growth experiments performed at temperature of 600 °C and pressure of 2 Torr, simultaneous VS and VLS growth mechanism were observed and well-faceted thick wires were obtained in all three different SS rates (Fig. 39a). In order to determine the predominant growth mechanism (VLS or VS) for each case, a statistical study of both length and diameter of up to 20-30 NWs for each sample was performed, and the result of the LD dependency on SS level (different T_{In}) showed that there is an unusual behavior for T_{In}=900 °C (Fig. 39b).
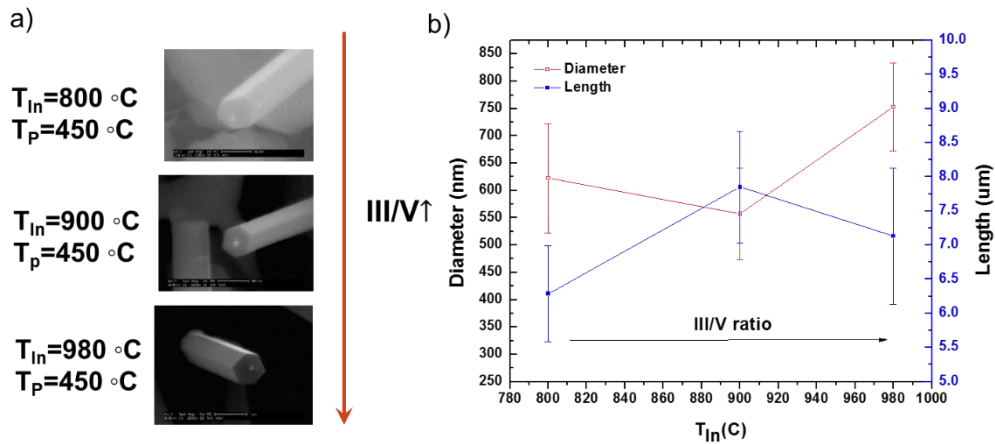
Figure 39. Effect of III/V ratio on a) morphology and b) dimension of the NWs grown at 600 °C.

As it was apparently found for this sample, the VLS mechanism dominated VS and the diameter of the wires decreased compared to the wire grown with T_{In}= 800 °00and 980 °C. This nonlinear behavior could be attributed to the change in chemistry of In-Au-P

alloying system increasing VLS growth rate. In addition, the length of the NWs showed a decrease for the sample with T_{In}= 980 ∘C compared to 900 ∘C. Despite the simplicity, this growth method enables us to alter the III/V ratio by changing the evaporation temperature of In (T_{In}) in our experiments.

3.5 Growth of InP Nanobelts and Nanodisks

Nanobelts (NBs), nanosheet and microdisks made of semiconductor materials are of great interest for making resonant microcavities that can be used as the nanolasers. Growth of such nanostructures with high quality have been reported for II-IV materials [75] and perovskites [76]. It was incidentally found that Au-catalyzed growth on Si (111) substrate promotes formation of NBs. As can be seen from the SEM image (Fig. 40a) for 30 min growth, the obtained NBs are up to ~100 μm long and some of them have the width of up to ~15-20 μm, which makes them a suitable cavity that can potentially lase under even relatively low optical pumping powers which will be shown later. The Fig. 40 shows a summary of substrate dependency of single elemental growth of InP. As can be seen for the pre-cleaned InP (100) substrate, hexagonal and rectangular shape NWs are grown with much higher vertical growth yield, compared to those grown on Si (100), apparently due to lattice matching. Growth of NBs can be explained via interplay between VLS and VS mechanisms using Au-catalyzed growth.
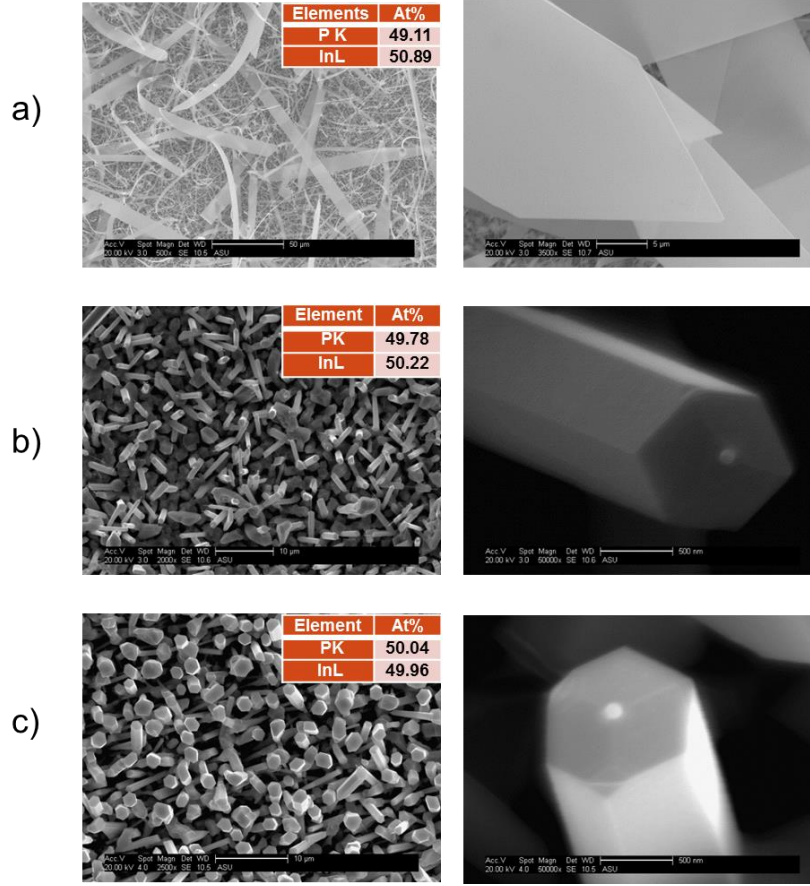
Figure 40. SEM image of Au-catalyzed InP nanostructures on different substrates: a) Nanobelts grown on Si (111), nanowires on b) Si(100) and c) InP (100) . EDS results are taken from a single nanostructure.

Further investigation is required for complete understanding the underlying growth mechanism. . HRTEM and the corresponding indexed selected-area electron diffraction (SAED) pattern of a single InP nanobelt is shown in Fig. 41 indicating that the NB has zinc blend structure with growth along $\langle\bar{1}10\rangle$ direction. It can be also concluded that the VLS-grown NW initially is grow along $\langle\bar{1}10\rangle$ direction and the VS mode becomes activated perpendicular to NB growth axis and the NB grows wider.
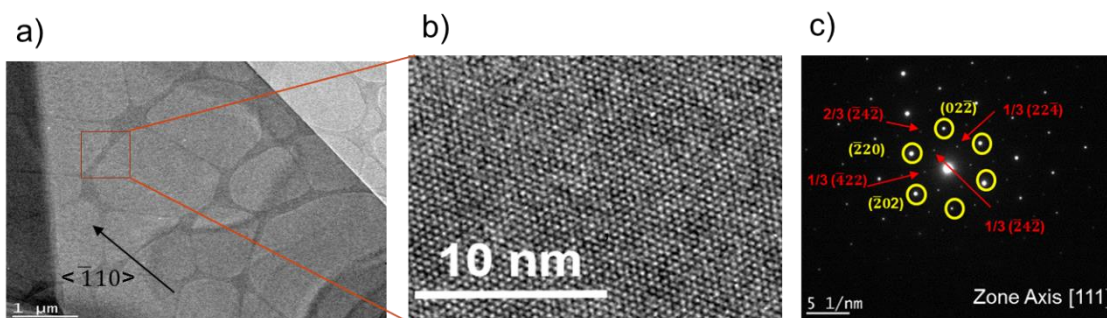
Figure 41. HRTEM study of an InP nanobelt grown under Au-catalyzed condition: a) bright field image of single NB. b) HRTEM image of NB. c) SAED pattern of InP NB along the [111] zone axis.

Using the same growth approach, but a self-(In-) catalyzed mechanism, the InP microdisks were grown on quartz (amorphous silica) substrate at a growth temperature of
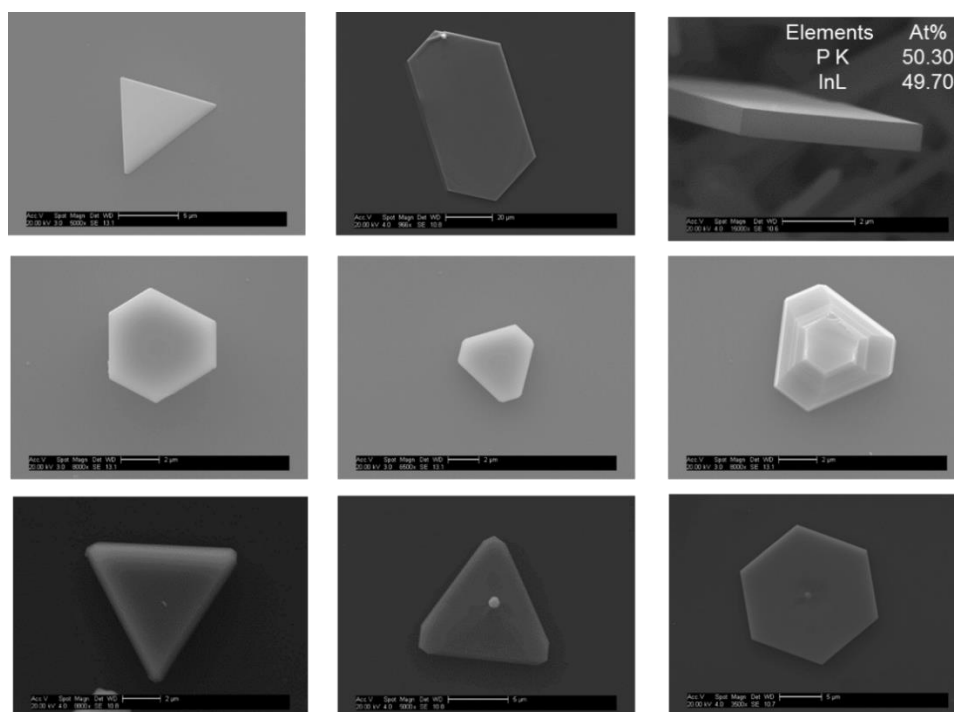
Figure 42. SEM image of self-(In-) catalyzed grown InP microdisks on amorphous quartz substrate. The top right cuboid structure is grown on silicon (111) with Au-catalyzed growth at 650 ∘C.

720 ∘C. Fig. 42 shows SEM image of some of the selected microdisks with interesting morphologies with a symmetric geometry. The underlying mechanism for growth of such nanostructures needs to be studied and well understood separately in the future. The

67

grown nanostructures were transferred from as-grown substrate using contact printing on quartz slides (optical glass) and observed under SEM. The structures have different geometries that will be utilized as suitable Fabry-Perot cavities for demonstration of lasing under optical pumping.

3.6 Lasing of InP Nanostructures

After demonstration of first optically pumped NW laser by Yan et al. in 2001, NW photonics has opened a new avenue in NWs research [77]. Semiconductor NWs (NBs or microdisks) lasers are typically dominated by mirror losses at their end facets due to transmission and scattering of light at the two ends of the resonator cavity. NWs with smaller diameter suffer from significant mirror loss preventing them to be practically used for photonic integrated device. As a result, lasing threshold of NWs strongly depend on their length and diameter;

$$\Gamma G_{th} = \alpha_s + \alpha_m \tag{3.1}$$

$$G_{th} = \frac{1}{L} ln \frac{1}{R}, \tag{3.2}$$

where α_s and α_m are scattering, and mirror losses, respectively. Γ is the confinement factor, and G_{th} is the material gain. In the second equation, L is the length of wire, and R is the laser power reflectivity. Taking all parameters into account, there is a trade-off between the diameter and optical loss in terms of integration density and threshold of NW based photonic devices [78]. Growth of InP wires with high surface quality can pave the way for on-chip photonic devices based IR lasers. The result of our studies showed that

as grown NWs/NBs and microdisks are high quality resonant cavities with flat end and sidewall facets that sustain lasing with minimal loss under high power optical pumping powers. The quantization effect is prohibited owing to large size (both length and diameter) of the wires that allows for fundamental bandgap emission. To study the NIR lasing of InP NWs/NBs they were first dispersed onto a glass substrate by contact printing and optically pumped at room temperature. A 349 nm Nd:YLF UV-laser was utilized to illuminate the nanostructures individually with high energy laser beam under confocal condition.
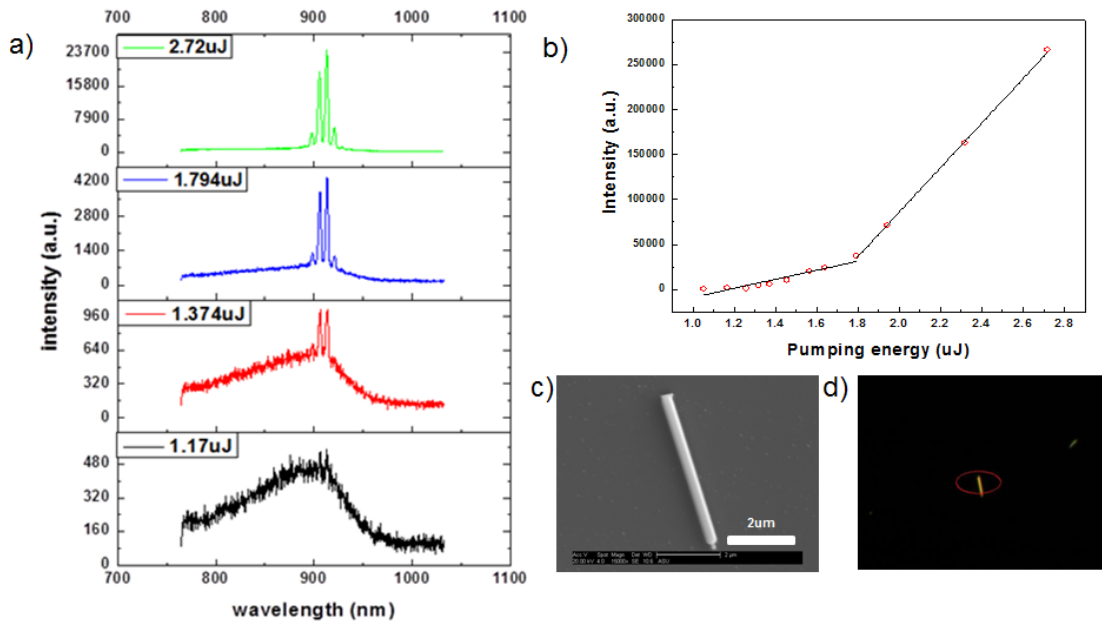
Figure 43. PL evolution of a single InP NWs at room temperature (a), Light-in–light-out curves of InP wire with multimode lasing behavior (b), SEM image of InP wire disperesed on glass (c), Dark field image of InP wire under confocal condition of optical microscope (d).

Fig. 43a shows the PL evolution of InP wires starting with a broad band spontaneous emission under a low pumping power. By increasing the laser power, initial lasing modes

appear to be red shifted with respect to the bandedge emission wavelength. Eventually the spontaneous emission becomes saturated, while the amplified spontaneous emission (ASE) with multimode lasing occurs with high emission intensities. Transition from linear to superlinear regime in typical Light in-Light out (L-L) curve is an evidence for threshold behavior (Fig. 43b). A precise study based on NW dimensions (length and diameter) is required to determine the critical dimension of wires, below which the lasing does not occur. Similarly, as can be seen for the triangular InP microdisk lasing was observed (Fig. 44a) with a very low lasing threshold under much lower pumping energy of the Nd:YLF laser. A top view and side view SEM image of the microcavity is shown in Fig. 44 b and 44c.
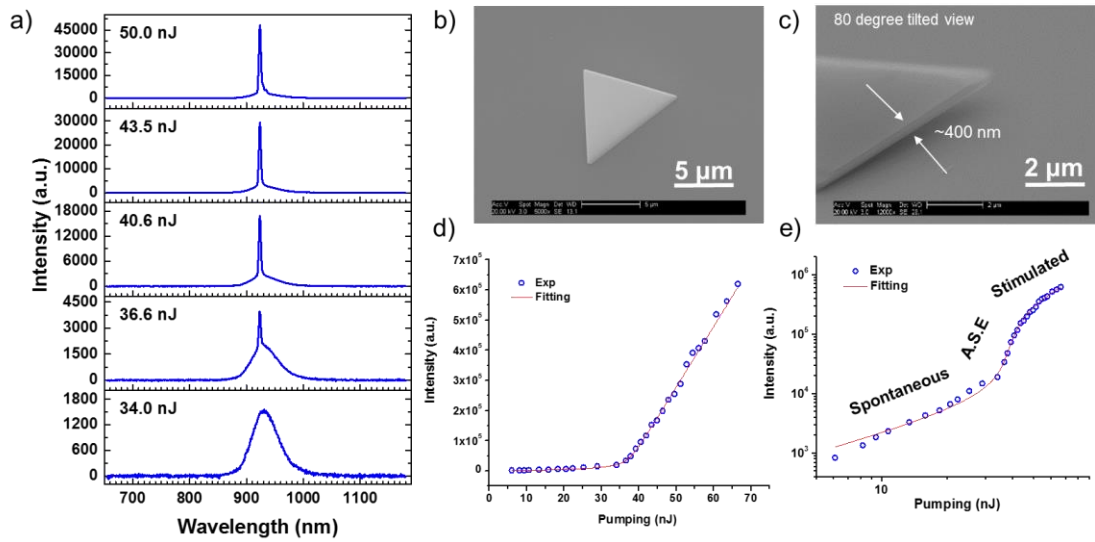
Figure 44. (a) PL evolution of equilateral triangular InP microdisk cavity with single mode lasing observed under optical pumping of Nd:YLF laser, (b and c) SEM images of InP microdisk with a thickness of ~ 400nm, (d) Light-in-Light-out (LILO) plot of optically pumped triangular cavity, (e) typical s-curve for lasing as the evidence for amplified spontaneous emission.

The spontaneous emission spectra prior to appearance of first lasing modes, shows a central wavelength of 921 nm, which is the typical emission wavelength for direct bandgap InP with ZB structure. There is not any deviation from fitting observed due to thermal effect at higher pumping level that consumes some of the carriers through a non-radiative recombination event. Single mode lasing with very dramatic transition slope was observed. Typical LILO and SS curve for lading is shown (Fig. 44d and 44e) as the evidence for amplified spontaneous emission.

3.7 Growth of Self-Catalyzed InAsP

To show the versatility of the single elemental growth, under the same condition as before, an extra boat containing small amount of InAs source powder (99.9999%, Alfa Aesar) was placed at 760 ∘C, upstream close to P- source boat. InAs has relatively a very high vapor pressure, compared to other binaries in InGaAsP material system. This results in an early loss of As at very early stage of the growth (as shown in chapter 1, Fig. 8), that is why the evaporation temperature of InAs is chosen to be slightly low. An epi-ready clean Si (100) was used to grow InAsP NWs. There was not any catalyst such as Au used, but instead the In seeding prior to growth was used to grow InAsP NWs under self-catalyzed condition. To do that, initially InAs and P boats were outside of the furnace, and they were pushed inside the furnace after 5 min after the furnace reached the set temperature of 1000 ∘C. The growth time was 25 counted after 5 min seeding, where the growth starts. The growth temperature was 650 ∘C under 20 sccm flow of Ar+5% H_2. The only variable in two set of experiments was the evaporation temperature of P which was 400-450 ∘C and 350-400 ∘C. For the latter, the P boat was 0.5 cm farther towards

upstream. A set of SEM images (Fig. 45) show that InAsP NWs are grown through self-catalyzed mechanism, but the shape of the tip and body of the NWs vary with change in P flow (evaporation rate). As can be seen for both cases, the InAsP NWs of up to 20 μm are obtained with a bulky tip which is different from the typical VLS-grown features.

a)

	NW1		NW2		NW3	
	Elements	At%	Elements	At%	Elements	At%
Tip	P K	43.93	P K	43.26	P K	44.04
	InL	45.72	InL	47.40	InL	46.20
	AsK	10.34	AsK	09.34	AsK	09.76
	Elements	At%	Elements	At%	Elements	At%
NW	P K	40.52	P K	40.20	P K	39.75
	InL	46.30	InL	47.25	InL	47.25
	AsK	13.18	AsK	12.55	AsK	13.00

b)

	NW1		NW2		NW3	
	Elements	At%	Elements	At%	Elements	At%
Tip	P K	37.95	P K	40.10	P K	38.26
	InL	48.84	InL	48.62	InL	47.24
	AsK	13.22	AsK	11.28	AsK	14.50
	Elements	At%	Elements	At%	Elements	At%
NW	P K	35.18	P K	37.40	P K	35.93
	InL	49.11	InL	48.67	InL	47.50
	AsK	15.72	AsK	13.94	AsK	16.57

Figure 45. SEM image of self-catalyzed InAsP NWs: a) Low P-flow, b) High P-flow. EDS analysis of three NWs and their tips from each sample are shown below each sample. The last image in each row is the contact printed sample on quartz substrate.

For the sample with high P content, a periodically twin zigzag morphology was observed. (Fig. 45a). Formation of such features in NWs has been widely reported due to formation of stacking faults and twining planes [79]. Formation of faceted catalyst is very similar to NW tip formed during vapor solid-solid (VSS) growth. However, here, in the

beginning the tip is in liquid form (150∘C, T_m for In) and at the end of the growth event, during the cooling stage, the tip also crystallizes to a faceted shape.

As can be seen (Fig. 45b) for sample with lower P flow (evaporation temperature) our aim was to grow the wires with higher As content, but it is difficult to tune the composition by manipulation of evaporation temperature InAs source due premature (congruent) sublimation of As. Lower P content available in vapor phase results in highly crystalline nail-like NWs without any sign of twining defects and zigzag morphology. EDS results also shows better stoichiometry. From EDS spot analysis of three random NWs for each sample as can be seen, the As content of tip for all NWs shows a decrease compared to body of NWs, while the P content is vice versa. This can be explained by decreased partial vapor pressure of As above InAs during the cooling process which might not be the case if single elemental As is used.

3.8 Summary

A simple, but successful strategy for growth of highly stoichiometric InP nanostructures was presented. Since non-stoichiometric materials are often accompanied by defect emission or less efficient bandedge emission, the presented method in chapter 3 for growth of InP could be potentially important for demonstration of the highly efficient InP-base photonic devices. The growth mechanism of InP NWs was explained by interplay between VLS and VS growth. The optical properties of InP nanostructures such as NWs, NBs and microdisks showed that all the as grown nanostructures support lasing under high optical pumping conditions.

4 VLS GROWTH OF GaP NANOWIRES

4.1 Introduction

Gallium Phosphide (GaP) NWs have attracted great deal of attention among III-V materials, due to the wide bandgap energy and emission in the visible spectrum and its role as an alloy partner with InP or GaAs for a wide range of applications in optoelectronics as light emission and solar cell applications. Growth of direct bandgap GaP NWs with wurtzite (WZ) structure has shown to be challenging. However, the indirect bandgap zinc blende (ZB) GaP alloyed with other binary compounds has been vastly utilized for fabrication of optoelectronic devices such as light emitting diodes (LEDs) [80], solar cells [81], photoelectrochemical cell [82], etc. Ternary GaP-based alloy compounds such as GaAsP [83] and InGaP [84,85] has shown to have a transition from indirect to a direct bandgap cross over that makes their applications appealing for the state-of-the-art electron based devices. GaP NWs has been synthesized using different methods such as laser ablation [86], metal organic vapor phase epitaxy (MOVPE) [87], Molecular beam epitaxy (MBE) [88], surfactant-free solution−liquid−solid (SLS) synthetic method [89] and thermal evaporation [90].

For applications where the low cost is more important such as solar cells, the simple chemical vapor deposition (CVD) with low-cost precursor materials is preferred to produce material of high crystal quality. However, growth of oxide-free GaP NWs via vapor phase transport method [91-93] has been difficult, mostly due to formation of stable oxide species such as Ga_2O_3, and $GaPO_4$ that are thermodynamically prone to incorporate into the structure of as-grown GaP resulting in poor optical quality [90]. There has been a lack of systematic study of parametric dependent growth study and

understanding. Moreover, the large difference in vapor pressure of P and Ga makes it challenging to GaP of highly stoichiometric. In binary semiconductors such as GaP, deviation from stoichiometry can cause a lattice disorder attributed to vacancies (V_{Ga}, V_P), antisites (P_{Ga}, Ga_P) and self-interstitials (P_i, Ga_i) affecting the crystal structure within the NWs which are found to be deleterious for device applications [94]. Formation of such intrinsic point defects in bulk GaP has been studied from both computational and experimental points of view [95-99]. The concentration of unintentionally formed native defects are very sensitive to the stoichiometry of grown GaP and also to the Fermi-level position and hence to the dopant concentration. Höglund et al. [99] have reported on the effect of stoichiometry on defect type and concentration. Presence of such defect-related deep levels near the bandedge has been previously reported in ZnO [100] and ZnSe [101] NWs, but there have been few reports [102] on origin of defect-induced red-band emission of GaP NWs.

In this chapter, an approach for the VLS-growth of GaP NWs will be introduced. The main objective of this study is to investigate the effects of growth conditions, substrates and precursors on stoichiometry of GaP NWs and to establish a link between stoichiometry to the intensity ratio of bandedge emission to defect emission. Our study involved systematic materials growth experiments under various conditions, optical and material characterizations. Such study allows the establishment of a growth strategy for producing high quality GaP NWs based on a simple, inexpensive approach. Our systematic growth study under various conditions shows that utilizing elemental P in addition to GaP source is necessary for replenishing the P deficiency exerted by

congruent sublimation of GaP to grow highly stoichiometric NWs. Our findings for the

grown GaP NWs under various condition shows that inclusion of defects introduces a

pronounced red-shifted deep defect emission (DE) peak at wavelength range of 690-720

nm next to bandedge emission (BE) at 556 nm, while the similar feature for single-crystal

bulk GaP is also observed at 730 nm that will be shown later. In particular, different

growth condition are examined to produce maximized BE to DE intensity ratio, both as

an important requirement for many photonic applications, and as a direct and simple

indication of stoichiometry and crystal quality of grown NWs. The comprehensive

structural and optical analyses were carried out to interpret this behavior that will be

presented below.

4.2 GaP Growth Procedure

Our growth experiment was carried out in a hot-wall horizontal low-pressure CVD setup.

Schematic illustration of growth set up and procedure is shown in Fig. 46. Silicon

substrates were cleaned ultrasonically in acetone, ethanol and DI water. Subsequently, the

substrates were immersed in a 2% HF for a few second to remove the native oxide prior

to introduction to growth chamber. GaP NWs were grown on Si substrates coated with a

nominal Au thickness of ~1-10 nm as the catalyst for VLS growth, via sputter deposition

at room temperature. The Au-coated substrate was placed at downstream side of a single

zone furnace where temperature ranges from 720°C to 800 °C. Growth at lower

temperatures than 720 °C is shown to have high oxygen content in NWs (Fig. 49). As the

source materials, ball milled high purity GaP (99.999% Alfa Aesar), Gallium metal and

red Phosphorous powder (≥99.99% Sigma Aldrich) were used inside separate amorphous

quartz boats. Ar+5% H_2 with flow rate of 40-45 sccm (standard cubic centimeter per minutes) was used as carrier gas and the pressure of the reactor was kept constant around ~5 Torr using a mechanical pump attached to the capacitance manometers. Prior to growth, the ball-milled GaP powder was placed in the middle of the furnace where temperature is maximum. A magnetic manipulator was utilized to position the red phosphorous, upstream from the GaP precursor, outside of the furnace heating zone (see Fig. 46a). In different experiments, Ga source was also placed in a separate boat upstream of the GaP boat (Fig. 46b). The system was purged for 1 hr under 300 sccm flow rate of carrier gas to purge excessive oxygen, CO_2 and water molecules inside the furnace tube. After the furnace reached the target temperature of 1000 ∘C with a ramp up rate of 42 ∘C/min, the red phosphorus boat was pushed inside the furnace using a magnetic manipulator where the temperature was 400-450 ∘C. After a certain period of growth time (7 to 45 min) the system was naturally cooled down to room temperature. To study the effects of various precursors, experiments were carried out with pure GaP, GaP with P, and GaP with Ga as the source materials.

4.3 Results and Discussion

Our choice of source materials is guided by simplicity, safety, low cost, and most importantly the ability to lead to high quality material. One of the greatest advantages of the low-cost CVD approach is to be able to use the same compound powder as source material to grow NWs of the same material.
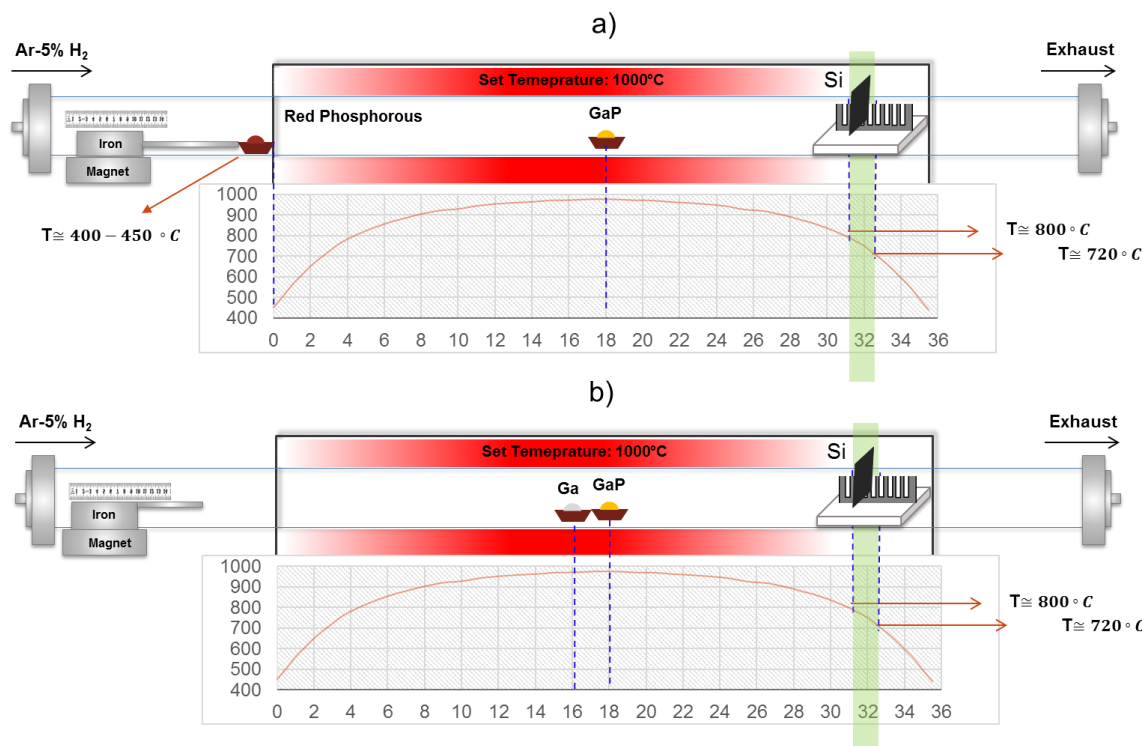
Figure 46. Schematic of set up GaP nanowire growth using GaP+P (a) and GaP+Ga as the source materials. The green bar indicates the growth temperature window of oxide-free GaP NWs.

Herein, a comparison between using different source materials including GaP, GaP+Ga, and GaP+ P as the growth precursor will be presented. As shown in Fig. 47a, our growth experiments using pure GaP source lead to GaP NWs with a poor stoichiometry, due to a much higher sublimation of P than Ga atoms and premature exhaustion of P. Initially such high P sublimation rate leads to excess P in gas phase and in the final grown NWs. But during the later stage of growth, the reduced availability of P in the source boat leads to less availability of P and eventually the deficiency of P in the grown NWs for longer time growth, as shown in Fig. 47. The EDS measurement after 45 min of growth left the source with a P to Ga ratio of ~11 to 59, with 29% of oxygen incorporation. To have a complete picture of the effects of source materials, Ga in addition to GaP as source material was introduced to the growth chamber. The EDS analysis after 15 min of growth

was shown in Fig. 48a and 48b. The addition of Ga apparently exacerbated the incongruent sublimation of Ga and P. The source boat P to Ga ratio was even more asymmetric in favoring a faster P sublimation. Interestingly, the NWs have a higher P (Ga/P=47.14/52.86) after the first 15 min growth due to the enhanced P availability in the initial stage of growth.

From growth-time dependent study using GaP source it was found that if grow long enough (e.g., 45 min), the GaP powder turns into a non-stoichiometric source which means only a few first min of the growth occurs in a stoichiometric ambient and for the remaining time, growth proceeds with a non-stoichiometric source that affects the stoichiometry of the grown NWs (Fig. 48a). It was also found that presence of a Ga metallic source boat placed at 980 °C in addition to pure GaP at 980 °C (2cm apart, upstream to the GaP source) results in quite faster sublimation of phosphorous. This could be explained as follows; assuming that the carrier gas flow rate is not low enough to let GaP and Ga reach the equilibrium, given the slightly higher vapor pressure of Ga above Ga source Ga(g)/Ga(s)) than that above GaP (Ga(g)/GaP(s)) [103] the chemical potential of Ga in gas phase increases. This results in faster sublimation rate of phosphorous due to a high affinity of P to Ga to react and form GaP. In fact, the excess Ga source here is used to balance the number of atomic Ga and P that are present in the growth chamber by almost doubling the partial pressure of Ga. This is why the NWs grown for 15 min under excess Ga source are still P-rich, while those grown using pure GaP are Ga-rich which was expected due to higher sublimation rate of P than Ga above

GaP that results in continuing the growth in a P-deficient environment using single source.
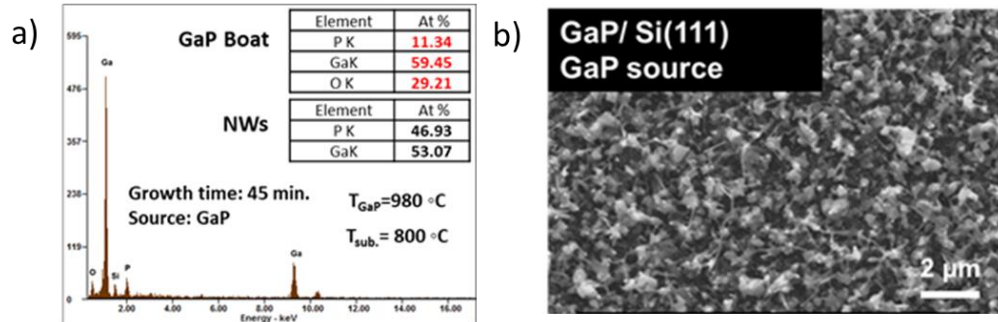
Figure 47. GaP NW grown using pure GaP source: EDS (a) and morphology (b) characterization of source boat and NWs grown using pure GaP source for 45 minutes.
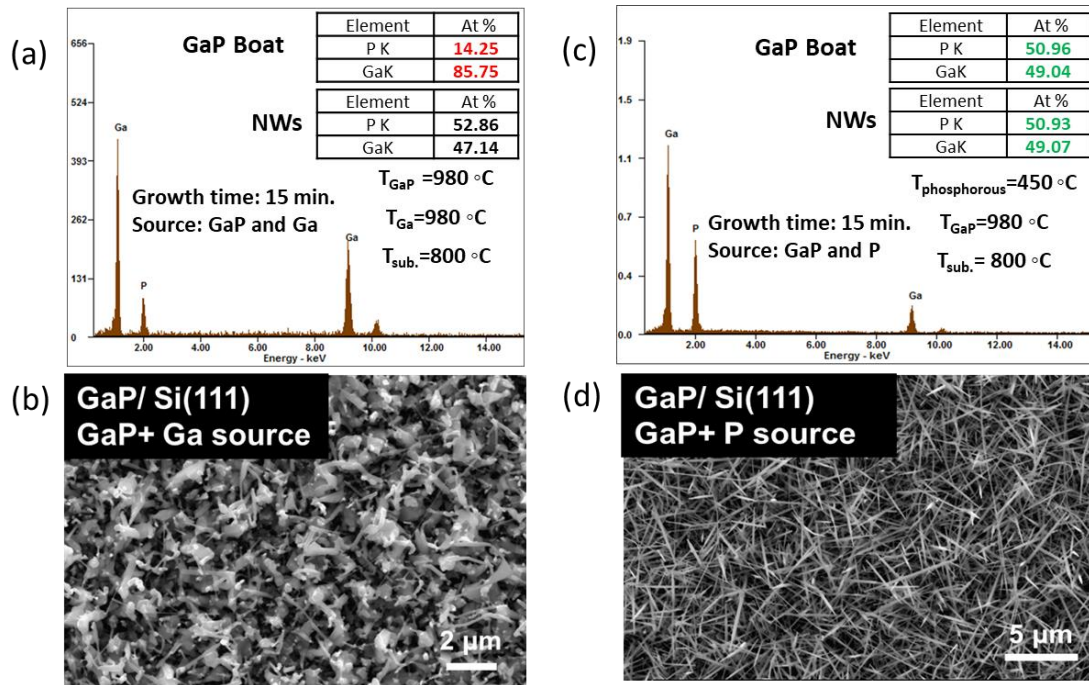
Figure 48. GaP nanowires grown using pure GaP+Ga and GaP+P source: EDS (a, c) and morphology (b, d) characterization of source boat and NWs grown with additional Ga (a, b) or P (c, d) in addition to GaP source after 15 minute growth.

These observations are consistent with growth under excess P source with the exception that the EDS results showed that in former case, with GaP+P source, the GaP source remains stoichiometric after growth (Fig. 48c), while in latter cases almost Ga metal with a small amount of dissolved P was left in the source boat. From EDS measurement of the remaining source material after 15 min growth, the amount of remaining P is ~14% for GaP with additional Ga, as shown in Fig. 48a.

4.3.1 Growth Using GaP and Excess P Source

GaP NWs growth performed under excess P condition at lower temperatures showed that incorporation of oxygen increases as the growth temperature varies further towards downstream from 700∘C to 560 ∘C (Fig. 49). It is worth noting that he growth temperature always can be determined using the temperature profile measured for the horizontal quartz tube furnace (Lindberg/Blue M). This observation corresponds to a
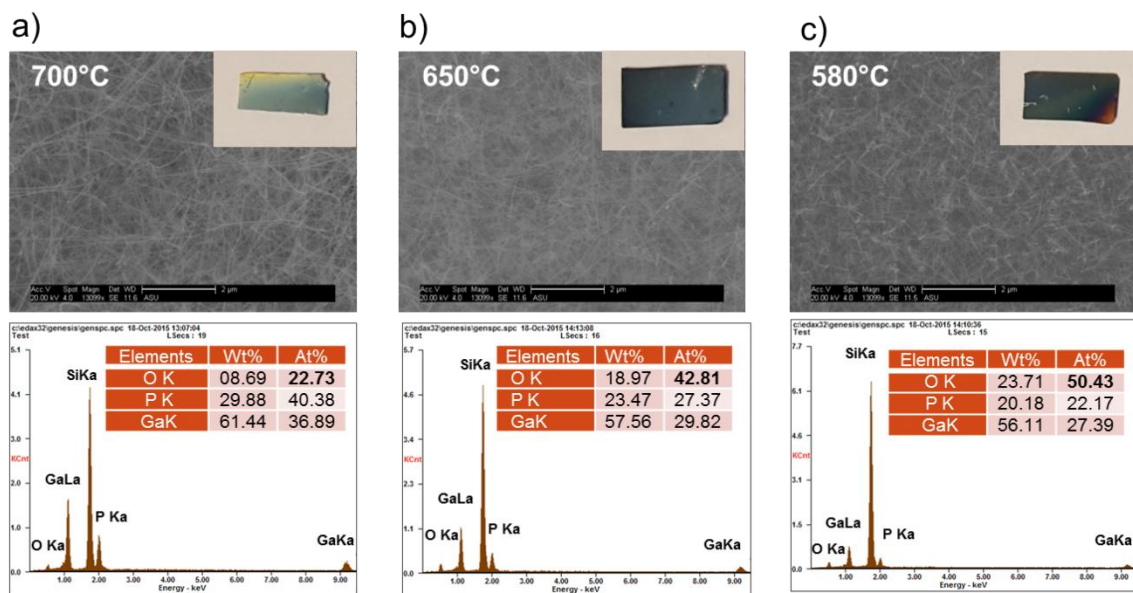
Figure 49. Effect of growth temperature on oxygen content of GaP NWs; SEM image of Ga-P-O nanowires grown at (a) 560 ∘C, (b) 650 ∘C and (c) 700 ∘C. The top right inset is the room-color picture of the as grown samples on silicon substrate. Second row represents the corresponding EDS spectra of nanowires grown at different temperatures.

decrease in activation energy of formation for Ga-P-O compounds such that increasing the growth temperature drives the oxygen off the nanostructure. A set of systematic growth experiments performed at various temperatures shows that using the current growth system, the ideal growth temperature window to achieve an oxide-free GaP is 720-800 °C. Experiments were performed to verify the above understanding with an additional elemental P added to the GaP precursor to replenish the deficiency of P after the initial phase of growth.
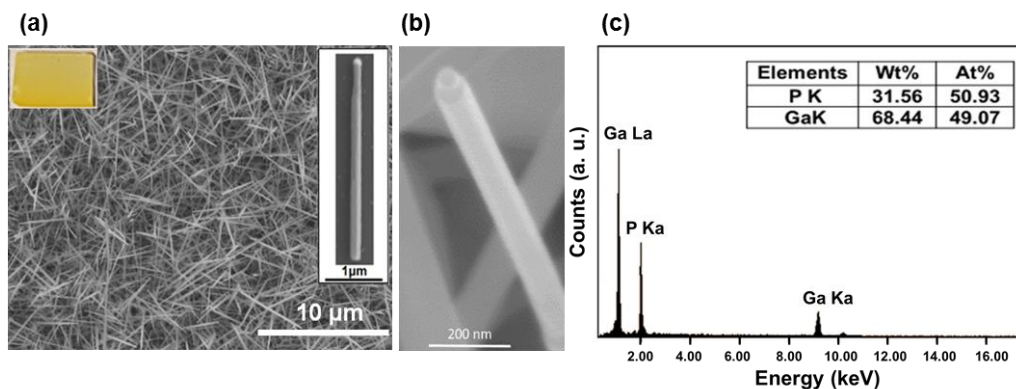
Figure 50. GaP nanowires grown under excess P condition: SEM micrograph of GaP NWs grown on Si (100) substrate; (insets are real color image of as grown sample (top left) and SEM image of a single NW with Au tip, dispersed on glass (top right)). (b) A well-faceted hexagonal GaP wire with Au catalyst. (c) A typical EDS spectrum of individual wires with quantitative elemental analysis of stoichiometric GaP.

Indeed, our examination of source boat and grown NWs after a 15-minute growth in the presence of additional elemental P shows a more congruent sublimation. Fig. 48c,d show highly stoichiometric NWs and remaining GaP in the boat in contrast to the growth with pure GaP source or with GaP and Ga source. More importantly, this approach also led to very congruent sublimation of GaP from the source boat and a stoichiometric GaP NWs for long time growth, as shown in Fig. 50c for a 45 min growth. A top view of representative SEM image of GaP NWs grown at 800 °C for 45 min using both red-P and

GaP source materials on a Si (100) substrate is shown in Fig. 50(a). Inset (right) of Fig. 50(a) shows a GaP NW dispersed on a glass with a uniform body and slight necking near the Au tip. The top left inset of Fig. 50(a) shows a photograph of the whole substrate under room lighting (yellow color), showing the large-scale uniformity over the substrate of 10 by 15 mm in size. A high magnification SEM image of NWs shows their faceted morphology (Fig. 50(b)). The energy-dispersive X-ray spectroscopy (EDS) analysis (Fig. 50(c)) on the body of GaP NWs grown using GaP+P source shows the Ga:P atomic ratio to be 1.00:1.02, with only ~2% deviation from stoichiometry. The extensive growth experiments established that the combined GaP and P source material combination is ideal for the growth of high quality and high stoichiometric GaP NWs.

4.3.2 Stoichiometric GaP Nanowires: Effects of Source Materials

To understand the situation, it is necessary to consider the difference in partial vapor pressures of Ga and P above GaP boat and how it relates to the chemical potential difference ($\Delta\mu$) between vapor and solid phases. It is known for many III-V compounds including GaP that above the congruent sublimation temperature ($T_{cs=}$ 571∘C for GaP), GaP loses phosphorous from the surface, preferentially over Ga [104]. For the sublimed GaP, the phosphorous dimers (P_2) and tetramers (P_4) are the common molecular compounds that have higher equilibrium partial pressure than that of the Ga element, above the T_{cs}[105,106]. In general, there are two ways to prevent the non-stoichiometric sublimation of group III and V species. One way is to determine the sublimation phase diagram in P-T space to maintain GaP source boat is always under congruent conditions.

This requires numerous experiments under different P-T combinations to determine such phase diagram and becomes impractical. Additionally, the likely required low sublimation rate would lead to extremely slow growth of NWs and become impractical for many low cost applications. The alternative way is to provide an additional phosphorous source to maintain a highly positive chemical potential for P in gas phase above source boat, whereas the chemical potential of P in gas phase is normally very low, if pure GaP is used. Since the growth process occurs under the constant carrier gas flow rate, total pressure of growth chamber and evaporation temperature are kept constant, thus the system is thermodynamically under quasi-equilibrium condition. The condition during the sublimation process under constant temperature and pressure is written as follows:

$$\text{GaP (solid)} \underset{\xrightarrow{\hspace{1cm}}}{\overset{equilibrium}{\xleftarrow{\hspace{1cm}}}} \text{Ga (liquid/gas)} + \uparrow \text{P (gas)} + \uparrow \text{GaP (gas)} \qquad (4.1)$$
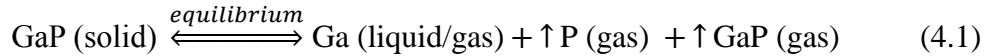
The sublimation reaction can be explained by different levels of chemical potential obtained at various growth conditions. Let μ_j^i be the chemical potential of species i in phase j, where i refer to P or Ga. Hence, $\Delta\mu = \mu_g^P - \mu_s^P$ is the difference in chemical potential of P in the gas and solid phase. The $\Delta\mu$ for the growth using pure GaP source compared with excess P source condition is given by;

$$\text{Pure GaP ;} \quad \mu_s^P > \mu_g^P \text{ , or } \Delta\mu < 0 \qquad (4.2)$$

$$\text{GaP and P ;} \quad \mu_g^P > \mu_s^P \text{ , or } \Delta\mu > 0 \qquad (4.3)$$

Therefore, by increasing the partial vapor pressure of phosphorous in the growth system by providing an additional P source $\Delta\mu$ becomes a positive term, leading to the inhibited sublimation of P from the source. Given the high stoichiometry of the GaP obtained from

84

GaP+P combination as the source materials, our study in the following will be focused on the growth under excess P condition.

4.3.4 Structural Characterization

In order to study the crystal structure of GaP NWs grown using GaP+P source, XRD measurements with X-ray source of Cu K_α were carried out. For both samples grown on Si (100) and Si (111) three main diffraction peaks were observed at 2θ values of 28.37°, 47.24°, and 55.79° corresponding to (111), (220), and (311) crystallographic planes of ZB GaP, respectively (Figure 51a).
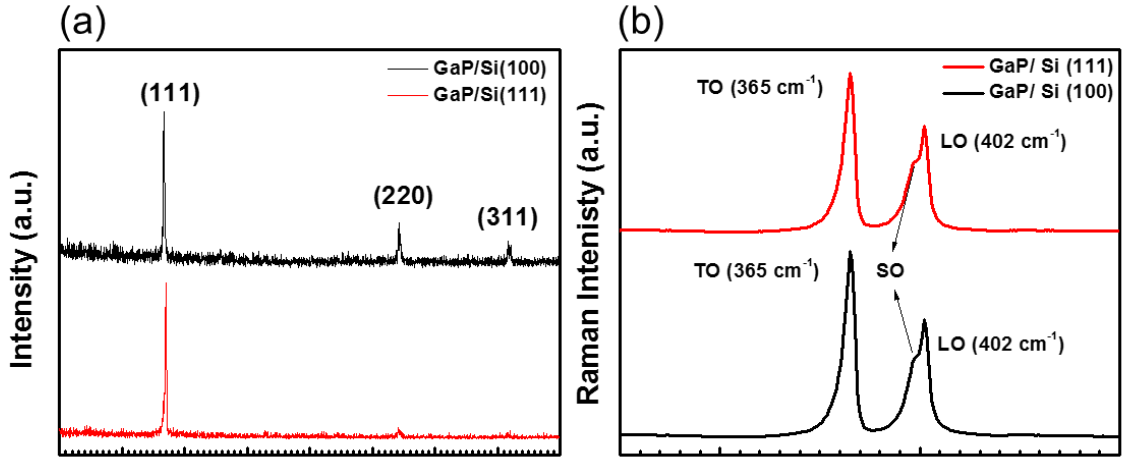
Figure 51. Powder XRD spectra for GaP samples grown on Si (111) and Si (100) under P-rich condition (a), and Raman spectra of GaP nanowires grown on Si (100) and (111) substrates (b).

From normalized XRD spectra both samples show a sharp (111) peak, where the GaP NWs grown on Si (111) show relatively better texturing along [111] direction. This can be inferred from relative intensity of peaks with respect to (111) peak. The cross-section view of the GaP NWs grown at 800 ∘C for 15 min on both Si (100) and (111) substrates are shown in Fig. 52. As it can be clearly seen, GaP NWs grown on Si (111) has more vertical yield, indicating (111) as the predominant growth direction which is in an agreement with XRD results.
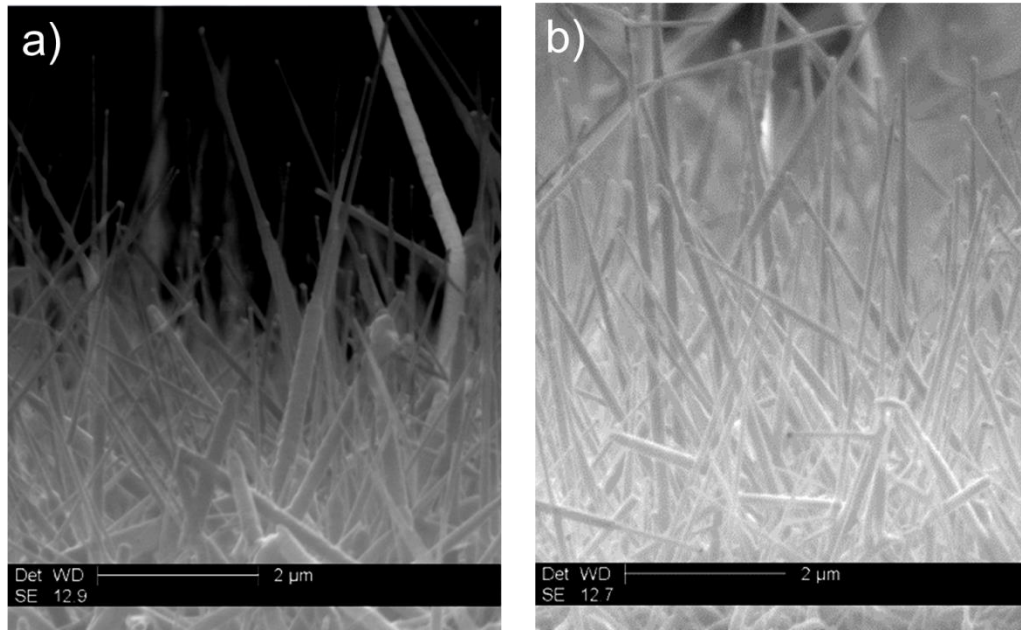
Figure 52. Cross-section SEM image of GaP nanowires grown (at 800C for 15 min) on (a) Si (100), and (b) Si(111)

Furthermore, the crystal quality of GaP NWs was further examined using Raman spectroscopy in which the inelastic scattering of the incident laser light leads to Raman shift, revealing the structural information in terms of energy of vibrational transitions in crystal lattice [107]. The sample was excited using a 150 mW Coherent Sapphire single frequency laser with a wavelength of 532 nm. The laser power was controlled using a neutral density filters wheel and an initial laser power of 100mW. Raman spectra for GaP NWs were collected using a low laser power of 1.3 mW on a single GaP NW. The Raman scattering spectra of the GaP NWs are presented in Fig. 51b. The results obtained at room temperature for two different samples grown on Si (111) and Si (100) exhibit two phonon modes: the transverse optical phonon (TO), and the longitudinal optical phonon

86

(LO) with the corresponding peaks appearing at around 365 and 402 cm^{-1}, respectively. These values are in good agreement with the reported bulk values for GaP [108] and also the numbers obtained for single crystal GaP wafers. The FWHM of TO mode is 6.04 and 5.98 cm^{-1} for GaP NWs grown on Si (100) and (111), and the linewidth for LO mode is 4.39 and 4.01 cm^{-1}, respectively (Table 1).

Table 1. Raman peak position and FWHM obtained by Lorentzian two and three peak fitting for GaP nanowires and wafer.

Raman Mode	TO(cm^{-1})		SO(cm^{-1})		LO(cm^{-1})	
Sample	Peak	FWHM	Peak	FWHM	Peak	FWHM
GaP on Si (111)	364.57	5.98	396.61	8.32	402.32	4.01
GaP on Si (100)	364.68	6.04	396.84	8.35	402.44	4.39
Wafer	365.19	7.88	N.A.	N.A.	402.95	5.29

For comparison, the linewidth of single crystal GaP wafer was also measured. The FWHM for TO and LO mode are 7.88 cm^{-1} and 5.29 cm^{-1}, respectively. These Raman linewidths indicate a very good crystal quality for NWs and slightly better crystallinity for the sample grown on Si (111). The slight downshift of both TO and LO modes might be because of an excess of phosphorus (as interstitial or antisites) in the GaP resulting in slight lattice distortion [109, 110]. The TO/LO intensity ratio for NWs grown on Si (100) and Si (111) is 1.55 and 1.48, respectively. It is known that TO/LO intensity ratio is directly correlated with the concentration of defects [111]. This slight difference is presumably due to different concentration of intrinsic point defects in two samples. For the single crystal GaP wafer this ratio is below 1 which is indicative of smaller concentration of defects. The shoulder on the LO peak of GaP for both samples is related to surface optical (SO) phonons due to existence of a surface or an interface of

amorphous surface oxide in core-shell GaP NWs [112]. The SO modes in NWs appear due to extremely large surface of GaP NWs compared to bulk GaP [113-116], which is not observed for GaP bulk as shown in Fig. 53. The absence of SO mode for wafer indicated that the physics behind Raman scattering of one-dimensional nanostructures such as NWs can be different from that of bulk which is due to the fact that Raman feature in NWs are angular dependent due to their highly anisotropic shape [117].
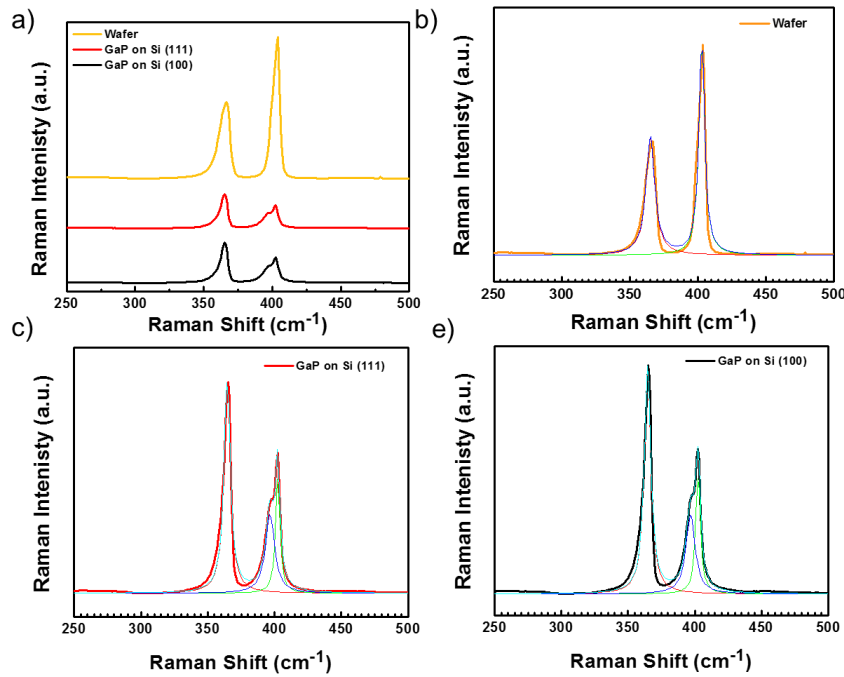
Figure 53. Raman spectra of GaP wafer in comparison with nanowires grown on Si (100) and Si (111) (a). double peak fitting of GaP wafer for both TO and LO modes (b). Three peak fitting for TO, SO and LO modes of GaP NWs grown on c) Si (111) and d) Si (100).

The bright-field (BF) TEM images of a typical VLS-grown GaP NW grown on Si (111) substrate (under P-rich condition) are shown in Fig. 54a and 54b. Presence of an amorphous layer outside of both NW body and Au-Ga-P alloy droplet is due to existence of Ga-P-O compounds such as $GaPO_4$ and Ga_2O_3 that are formed during the transfer of

the NWs onto TEM grid (Fig. 54c). Formation of segments of different contrast (Fig. 54a
) is attributed to coherent twinning super lattices (TSLs) that are formed by incorporation
of rotational twins. HRTEM of an individual NW showed a high density of stacking
faults (SF) and twinning defect (Fig. 54d). Shown in right side of Fig. 54d are the
selected-area electron diffraction (SAED) pattern taken from two adjacent segments
separated with a thin multi atomic layer of microtwins (MTs) making a rotation angle of
141∘ when viewed from $<\bar{1}10>$ zone axis (Fig. 54f). From the interplanar spacing
between parallel lattice fringes the lattice constant is calculated to be 0.314 nm which
corresponds well to the (111) interlayer spacing of bulk ZB GaP, thus confirming <111>
as the growth direction. Indexed characteristic double-spot superimposed pattern obtained
by fast Fourier transform (FFT) is for zinc blende TSL of GaP that is shown in Fig. 54e.
Both patterns have a 2-fold symmetry along $<\bar{1}10>$ zone axis that have a rotation of $\sim70^{\circ}$
(or 110°) with respect to each other. Formation of such quasiperiodic twinning segments
within entire body of NW corresponds to intermittent rotational twins introduced by
stacking faults along <111> growth direction. The exact mechanism of formation of
TSLs across which the set of stacked (111) family of planes undergo 180° rotation along
the [111] axis, is not still fully understood. However, their dependency on growth
temperature and diameter of NW and dopants has been studied [118,119]. It has been
reported that periodic array of twin boundaries in TSLs can result in formation of mini
bands due to periodic electron scattering [120]. The PL emission characteristics of our
GaP NWs will be later discussed, in the context of optical properties, to study the defect-
mediated electronic transitions.
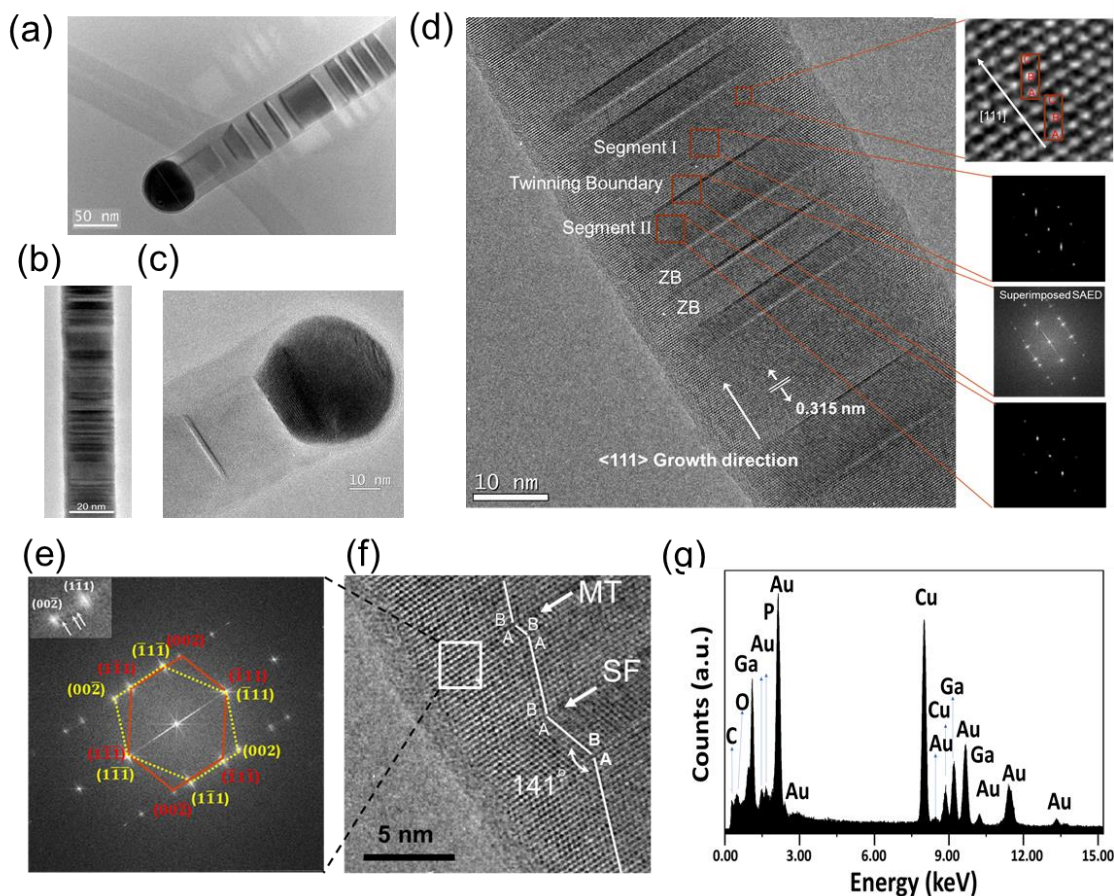
Figure 54. TEM study of GaP NWs grown under excess P condition. (a) Bright field TEM image taken from the NW of 50 nm diameter with evident TSL onset showing transition from single-crystal growth to coherent twinning growth. (b) Formation of planar defects such as stacking faults and twin-planes within entire body of a GaP NW with the observed smallest diameter of 20 nm. (c) Amorphous layer outside of both NW body and Au-Ga-P alloy droplet is due to formation of Ga-P-O compounds such as $GaPO_4$ and Ga_2O_3. (d) high-resolution (HRTEM) image of quasiperiodic TSL along $[\bar{1}10]$ zone axis with ABCABC stacking, for each segment, attributed to the normal ZB planar sequence with [111] growth direction. The associated FFT images are taken from two adjacent segments and twin boundary, in which the diffraction spots correspond to the (111) planes perpendicular to the growth direction. (e) Indexed double spot FFT pattern (two superimposed pattern) along $[\bar{1}10]$ zone axis pattern. Inset with some white arrows represents some of the spots diffracted from the TSL. (f) HRTEM image of twin segments with SFs and MTs formed at the boundaries. (g) The energy dispersive X-ray spectrum (EDXS) spectrum obtained from Au tip. The C and Cu peaks are from the holey carbon grid.

Fig. 54g shows an energy dispersive X-Ray spectroscopy (EDXS) spectrum with the resolved quantitative elemental analysis of tip for NW with 21.15%, 38.00%, 40.84% for P, Ga and Au, respectively. However, the composition of tip of NW grown at 800 ◦C

which is based on a gradual cooling path for an unknown liquid composition in Au-Ga-P phase diagram [121], does not match with stoichiometric GaP. The EDXS point measurement of composition for the crystallized alloy droplet (fringes in Fig. 54c) is $Au_{0.52}Ga_{0.48}$ with a significant Ga content compared to P, which is indicative of the fact that above congruent transition temperature of GaP during the cooling process the number of cationic and anionic gas phase atomic species leaving GaP boat are not equal, while the P-flux at the low temperature downstream is completely interrupted. The stepwise non-uniformity in diameter of NWs occurs during the cooling stage where the depletion of Au reservoir occurs while the introduction of gas phase species into Au droplet is also terminated. This is in an agreement with the similar phenomenon observed by Harman et al. [122], and Persson et al. [123] on MBE-grown GaAs NWs. As the impingement rate of vapor species decreases, the reservoir is purged under lower P flux, resulting in a constriction corresponding to diminution of the volume of reservoir. This phenomenon is caused by non-identical vapor pressure of P and Ga adatoms that brings about two different incidents as follows: tapering of wire near the Au tip by decreasing the size of the catalyst during the cooling process resulting in decreased number of nucleation sites at the interface of Au and GaP crystal. Neck formation below the Au seed is due to decreased supersaturation rate and complete depletion of reservoir during the cooling down process.

4.3.5 Optical Characterization

Following the structural studies, optical characterization of the GaP NWs was carried out. From PL measurement using an Nd:YLF UV-laser (349 nm) as the excitation source, the optical emission properties of NWs were investigated. Room temperature PL spectra of as-grown GaP NWs showed (Fig. 55) that there are two dominant characteristics peaks; a narrow bandedge (BE) emission at 556 nm attributed to indirect transition of Γ_V-to-X_C and a broad band defect emission (DE) peak at a range of 690-720 nm, possibly related to deep defect recombination centers. To examine the emission features of NWs, pump-power dependent PL measurements are performed, as shown in Fig. 55a. As we see there, the relative emission intensities change with decrease in defect emission (DE) and increase in BE, consistent with the assignment of 690-720 nm range as the DE band. Due to the smaller density of states in DE band, the DE band is quickly filled up with the increase in pumping, resulting more population of BE states. To relate the material quality with relative BE-DE intensities, PL from sample grown using pure GaP source and that grown using the combined GaP and P sources were compared, as shown in Fig. 55b. It is clear that the less stoichiometric NWs grown in the former case show much stronger DE emission than the stoichiometric NWs of latter case. This further validates our proposed approach of using a combined GaP and P sources as precursors for the growth of high quality NWs. Presence of such native defect was also observed in PL spectrum obtained from single-crystal GaP wafer, despite their high crystal quality which will be shown later in comparison with the as grown NW samples. The integrated BE to DE (IBE/IDE) ratio to is the more precise way to gauge how much the BE predominates

over DE and will be examined more in the following. This is because IBE/IDE takes into account the bandwidth (FWHM), in addition to taking the maximum intensities into consideration. The IBE/IDE ratio shows a ~3 fold increase for growth with additional P (from 0.37 with pure GaP source to 1.13 with GaP and P sources). This comparison shows that the P-deficiency contributes significantly to the DE. Quantitatively, the 3-fold increase of IBE/IDE ratio corresponds to an improvement of stoichiometry of about 5.5% (from 6.15% to 0.66%).

In order to establish a correlation between the stoichiometry and IBE/IDE intensity ratio the PL for GaP NW samples grown under various experimental conditions including two different orientations of Si substrate, growth temperature, growth time, etc. was measured, and the results are summarized in Fig. 56 and in Table 2.
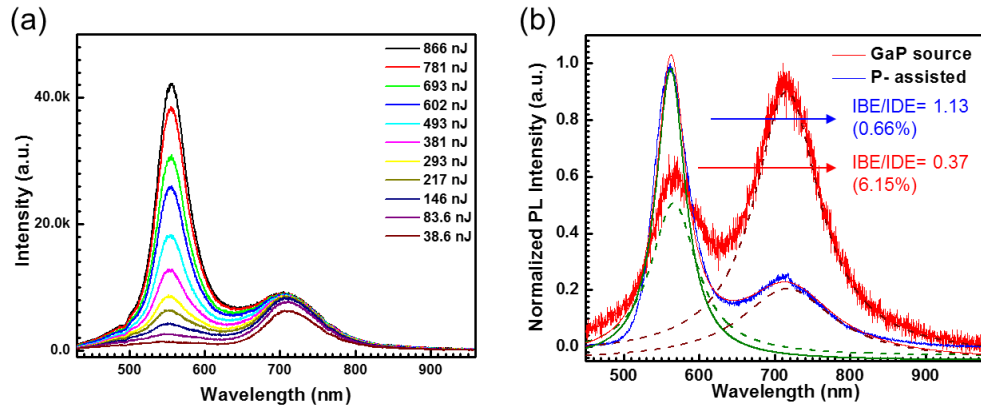
Figure 55. Photoluminescence measurement of GaP nanowires with different growth conditions. (a) Evolution of PL spectra for GaP NWs grown at 800 ◦C on Si (111) for 45 min with Au thickness of 1-1.5 nm. Enhancement of IBE/IDE intensity ratio under high optical pumping power reveals the saturation of shallow donor-acceptor levels (b) Comparison of normalized PL spectra at pumping energy of 493 nJ for NWs grown using pure GaP source and under excess P condition (both at 800 ◦C for 45 min, 1-1.5 nm Au) shows a ~3-fold increase in IBE/IDE intensity ratio. The numbers below the ratios show the deviation from stoichiometry (%).

Table 2. The correlation between stoichiometry and BE/DE ratio for different GaP samples grown under different conditions.

Sample	1	2	3	4	5	6	7	8	9
Growth Condition	1-1.5 nm Au Si(111) 45min 800°C	1-1.5 nm Au Si(100) 45min 800°C	2-3 nm Au Si(111) 45min 800°C	6-9 nm Au Si(111) 45min 800°C	6-9 nm Au Si(100) 45min 800°C	1-1.5 nm Au Si(111) 15min 800°C	1-1.5 nm Au Si(100) 15min 800°C	Same as Sample 1 with Pure GaP Source	1-1.5 nm Au Si(100) 45min 720°C
P (%)	50.52	49.17	52.48	53.85	52.59	50.36	51.74	49.56	53.55
Ga (%)	49.48	50.83	47.52	46.15	47.41	49.64	48.26	50.44	46.45
P (%)	49.71	51.5	51.84	53.45	53.71	51.03	50.51	49.48	52.91
Ga (%)	50.29	48.5	48.16	46.55	46.29	48.97	49.49	50.52	47.09
P (%)	51.00	50.01	52.81	53.52	51.58	50.47	50.68	48.79	51.13
Ga (%)	49.00	49.99	47.97	46.48	48.42	49.53	49.32	50.88	48.87
P (%)	50.39	50.8	50.48	52.66	52.75	50.1	50.76	49.76	52.02
Ga (%)	49.61	49.2	49.52	47.34	47.25	49.9	49.24	50.24	48.7
P (%)	51.18	51.17	52.84	53.57	51.92	50.35	48.91	42.85	52.39
Ga (%)	48.82	48.83	47.16	46.43	48.08	49.65	51.09	57.15	47.61
P (%)	49.19	50.90	50.66	53.69	53.000	49.58	50.93	41.12	48.60
Ga (%)	50.81	49.10	49.34	46.31	47.00	50.42	49.07	58.88	51.40
P (%)-Avg.	50.33	50.59	51.85	53.46	52.59	50.32	50.59	46.93	51.77
Ga (%)-Avg.	49.67	49.41	48.15	46.54	47.41	49.69	49.41	53.07	48.23
Standard deviation	0.71	0.91	2.19	0.97	1.40	0.62	0.81	7.83	1.83
Devotion from stoichiometry(%)	0.66	1.18	3.70	6.91	5.18	0.63	1.18	6.15	3.53
DE peak position(nm)	718	718	718	719	716	720	719	720	690
Max(BE)/ Max(DE) ratio at pumping current of 493 nJ	4.34	3.93	2.15	0.80	0.94	5.07	5.00	0.67	1.92
Integrated intensity ratio (IBE)/(IDE) ratio at pumping current of 493 nJ	1.134037	1.152394	0.846042	0.318927	0.384189	2.437564	2.529399	0.374862	2.129038

The comparison of IBE to EDE ratio (IBE/IDE) for 9 different samples shown in Fig. 56 is based on measurement of PL on as-grown samples at the equal pumping energy of 493 nJ. The PL spectra of all the samples are shown in Fig. 57. First the Lorentzian fitting was performed for both BE (in the range of 460-650 nm) and DE (in the wavelength range of 550-850 nm), respectively. As measure of stoichiometry, P/Ga ratio was obtained from EDS results of all samples, transferred via contact printing [13] from the original substrates onto fresh quartz substrate (Table 2). To measure uniformity, 6 NWs were measured from each of 9 samples, as presented by 6 data points along each horizontal line in Fig. 56. Since PL measurement was performed on as-grown samples with a micron-size resolution, all 6 SEM measurements from a given sample corresponds

to a single IBE/IDE ratio. In Fig. 56, 9 samples are divided into 3 groups based on growth temperature and time. A few observations can be made from Fig. 56: First, NWs with high stoichiometric symmetry (P/Ga~1) shows higher IBE/IDE ratio. The best examples are samples 6 and 7, showing the highest IBE/IDE ratio of larger than 2.5. Second, samples grown for shorter time (15 mins, samples 6 and 7) have higher IBE/IDE ratio than longer time (45 mins, samples 1 and 2) under the same growth conditions. This is likely due to the fact that smaller wires grown for shorter time are less likely to incorporate into defects.
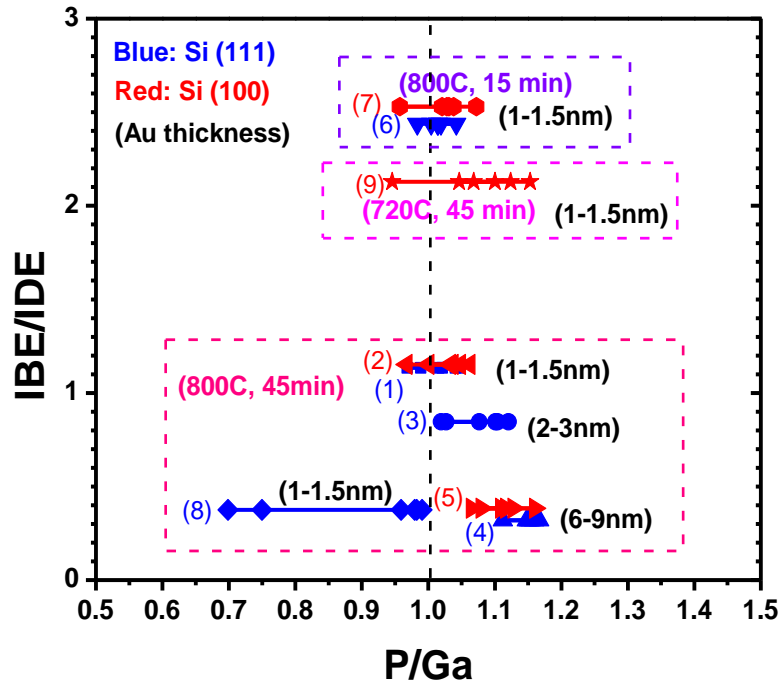
Figure 56. Relationship between IBE/IDE ratio and stoichiometry and IBE/IDE for various GaP samples grown under different conditions. Deviation from stoichiometry (P/Ga=1) is determined from EDS analysis of single NWs/spots. The IBE/IDE intensity ratios are obtained based on integration of Lorentzian fitting of PL spectra (under identical PL pumping energy of 493 nJ) within identical range of 460-650 nm for BE and 550-850 nm for DE peaks, respectively. Samples are divided into 3 groups based on the growth conditions (dashed boxes). The numbers in the parenthesis in front of data set indicate the samples numbers used in Table 2. The black numbers with unit of nm indicates the thickness of Au catalyst before the growth. All samples were grown using GaP+P as recipe except sample 8, which was grown using GaP only.
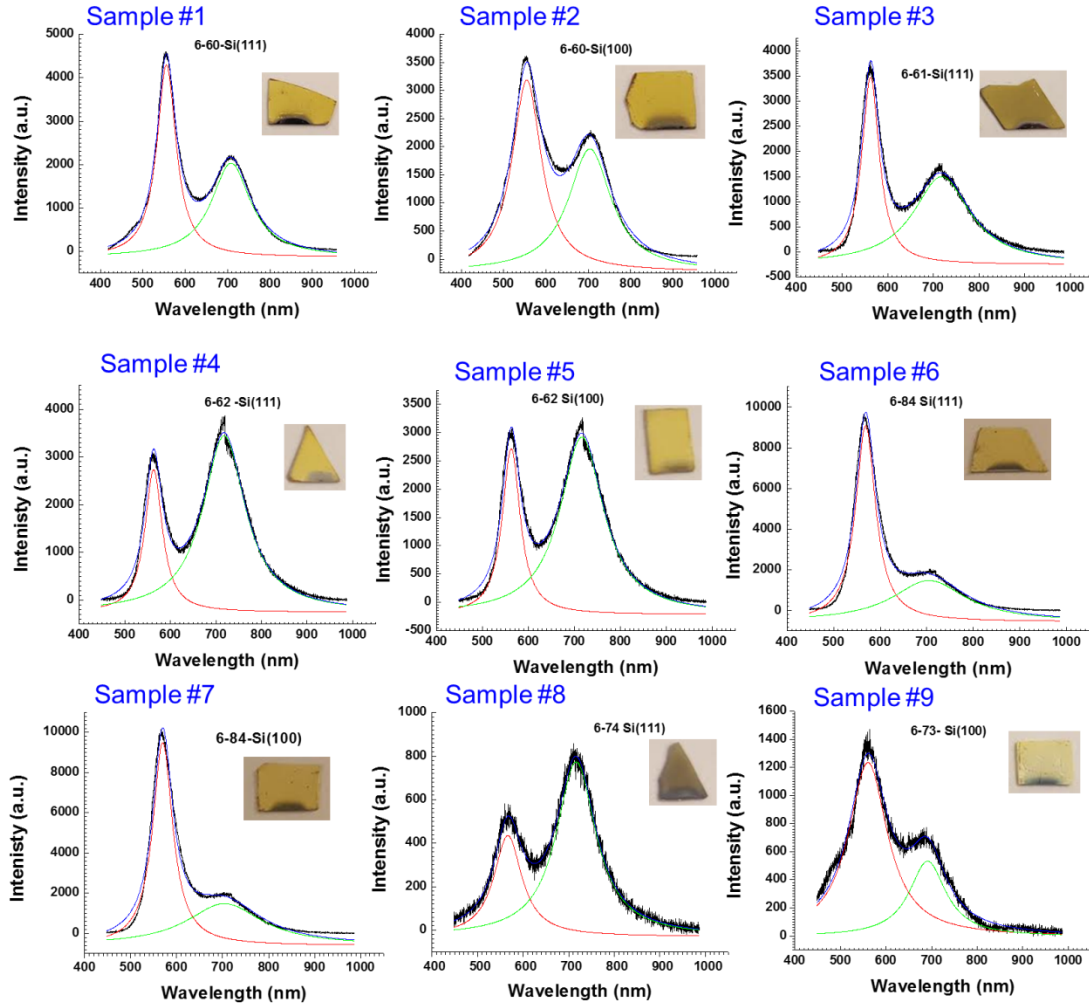
Figure 57. PL spectra of GaP samples grown under different condition. PL is acquired at identical 493 nJ Pumping of Nd-YLF lasers. An image of each as-grown sample under room lighting is embedded on corresponding PL plot.

It is also interesting to note that there is no apparent difference in stoichiometry between the two groups of wires. Therefore, the additional defects incorporated into samples 1 and 2 are likely to be stoichiometric. Third, NWs grown with thinner layer of Au are more stoichiometric and have stronger BE (higher IBE/IDE ratio), as can be clearly seen by comparing samples 1 through 5, as Au is increased from 1-1.5 nm, 2-3 nm, to 6-9 nm. Another observation is that there is little difference between substrate orientations (Si

(100) vs. Si (111)) in terms of stoichiometry or IBE/IDE ratio. It was found that in general, higher growth temperature leads to better stoichiometry and better BE. The ideal growth window of temperature is in the range of 720-800 ◦C. Within the ideal temperature window, higher temperature does not necessarily lead to better material quality. An example is provided by comparing sample 9 grown at 720 ◦C with sample 2 grown at 800 ◦C, where lower temperature gives higher IBE/IDE ratio. It is also worth noting that there is a change of DE central wavelength from 690 nm at 720 ◦C to 718 nm at 800 ◦C (see Table 2 and Fig. 57). Another exception to the above observations is sample 8, which was grown under otherwise the same conditions as sample 1. The poor stoichiometry and low IBE/IDE ratio are results of growth with pure GaP source without additional P, while all other 8 samples were all grown with GaP+P source materials. This further verifies the key result of this paper that GaP together with P provides an ideal source combination. It is believed that such systematic understanding could be utilized to guide the growth of high quality GaP NWs.

To gain more quantitative information about the spectroscopic features of NWs, we examined pumping power dependence of IBE, IDE, IBE/IDE ratio, and linewidths of BE and DE of two of our samples grown on Si (100) and Si (111) and compared such features with those of commercial GaP wafer, as shown in Fig. 58 for two of our samples (samples 6 and 7 shown in Fig. 56). The three samples (sample 6, 7 and wafer) were pumped with pumping energy from 217 nJ to 866 nJ and their PL spectra are shown in Fig. 59a-c. The details of Lorentzian fitting are shown in Fig. 59d-f and in Table 3.
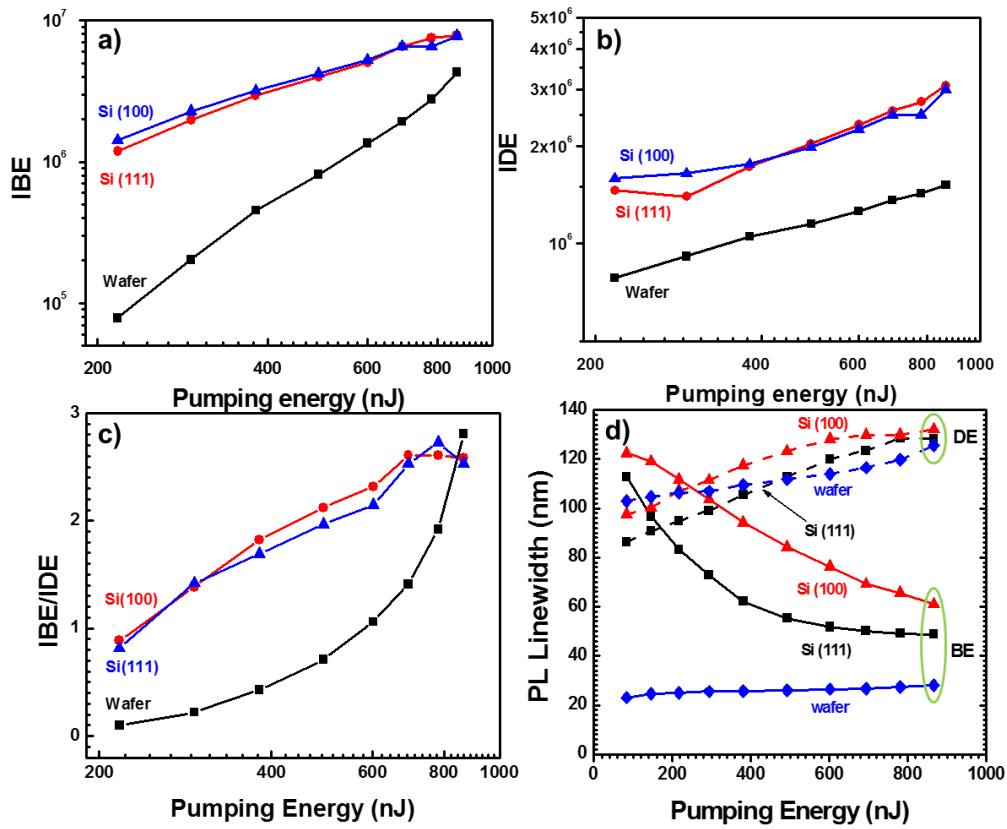
Figure 58. Comparison of optical characteristics of GaP wafers and nanowires grown on Si (111) and (100) (both at 800 ∘C for 15 min and 1-1.5 nm Au catalyst) and single crystal GaP under different laser pumping levels. (a): IBE, (b): IDE, (c) IBE/IDE ratio; and the linewidths of PL peaks (d).

For this comparison, it is important to note that the reflection from NWs at the surface of NW samples is very different from the flat GaP wafer. The reflectivity of the GaP wafer was estimated to be R=51.15% from Fresnel's equation for an incident laser light angle of 30∘. The pumping intensity of GaP wafer was therefore scaled by (1-R).

Such difference while affecting an absolute comparison between the wafer and NW samples, it does not affect the slopes of quantities that we plot on log-log scale in Fig. 58a-c.
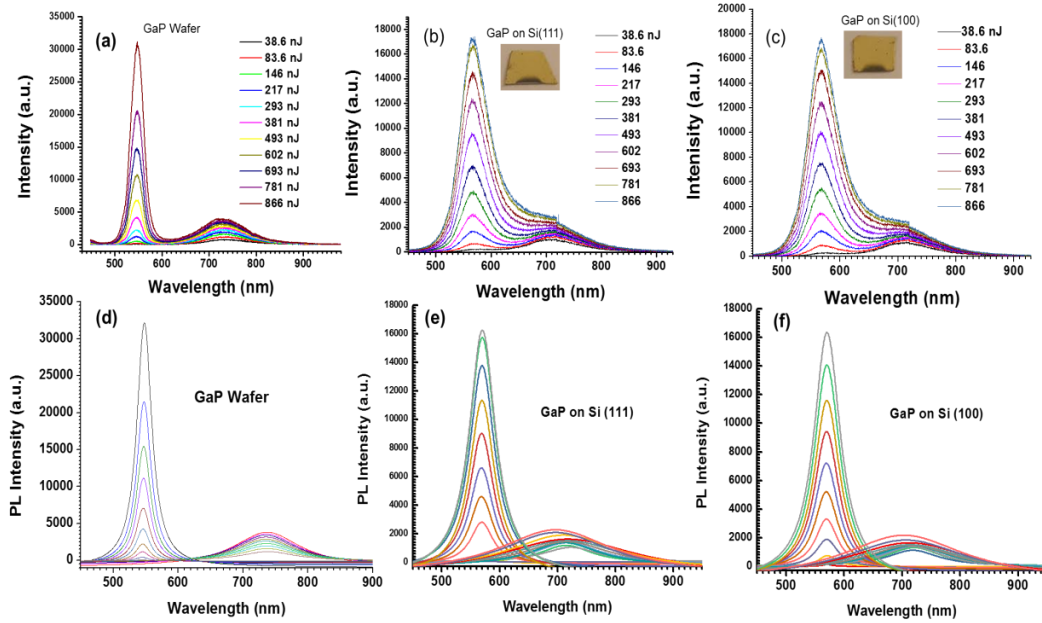
Figure 59. PL evolution spectra for different GaP samples with their corresponding double peak Lorentzian fitting; GaP wafer (a and d), GaP NWs grown on Si (111) (sample 7) (b and e), GaP NWs grown on Si (100) (sample 6) (c and f).

First, we notice that the IBE of GaP wafer shows a strongly super-linear increase (with a scaling index larger than 2) with pumping, mostly as a result of increased penetration depth of pumping beam into a very thick wafer. The IBE from both NW samples shows a slightly sublinear increase with a scaling index close to but smaller than 1. The DE for all three samples show the same sub-linear increase, as the DE bands are filled up with increasing pump. The IBE/IDE ratio reflects mostly the behavior of IBE, since IDE is similar for all of them. The linewidth comparison shown in Fig. 58d is more interesting. The linewidths for all DE bands increase with pumping, while linewidths for BE of NWs decrease and that for the wafer stays practically constant. The increase of DE linewidth is

a result of filling of DE states of wider range as pumping increase. The absence of

linewidth increase for wafer is an indication that there are little shallow defect states as a

result of high quality wafer.

Table 3. The integrated intensity values for BE and DE obtained from Lorentzian double peak fitting for GaP NWs grown at 800 ◦C for 15 min (sample 6 and 7) and single-crystal GaP. Integration was based on identical range of 460-650 nm and 550-850 nm for BE and DE peaks, respectively.

Pumping Energy (nJ)	Wafer IBE	Wafer IDE	Wafer IBE/IDE	GaP/Si(100) IBE	GaP/Si(100) IDE	GaP/Si(100) IBE/IDE	GaP/Si(111) IBE	GaP/Si(111) IDE	GaP/Si(111) IBE/IDE
217	78575.04187	784449.4886	0.10	1.42E+06	1.59E+06	0.888545	1.19E+06	1.46E+06	0.816489
293	202973.9707	912907.1129	0.22	2.28E+06	1.65E+06	1.385676	1.99E+06	1.40E+06	1.420848
381	453639.7566	1.05E+06	0.43	3.21E+06	1.76E+06	1.822182	2.93E+06	1.73E+06	1.691236
493	810467.4545	1.15E+06	0.71	4.21E+06	1.99E+06	2.121193	4.00E+06	2.04E+06	1.967312
602	1.35E+06	1.26E+06	1.06	5.25E+06	2.26E+06	2.317588	5.01E+06	2.33E+06	2.146938
693	1.92E+06	1.36E+06	1.41	6.52E+06	2.50E+06	2.610848	6.52E+06	2.57E+06	2.53183
781	2.76E+06	1.43E+06	1.92	6.52E+06	2.50E+06	2.610848	7.48E+06	2.74E+06	2.727809
866	4.28E+06	1.52E+06	2.81	7.76E+06	3.00E+06	2.583795	7.81E+06	3.09E+06	2.530909

 The decrease of BE linewidth for NW samples indicates a saturation of shallow defect

states in NWs with pumping, as the excited carriers populate increasingly more and more

states in the continuum bands. The larger BE linewidth of NWs than that of wafer

indicates existence of shallow defect states, most likely related to the surface states and

other twinning defects as seen in the HRTEM analysis. Thus, the linewidth approaches

the more intrinsic linewidth determined by the band structure, as in the case of wafer. The

defect peak observed in PL spectrum for GaP is often attributed to structural defects such

as stacking faults, twins [124, 125], and non-stoichiometric point defects [126,127], that

introduce deep electronic levels within the bandgap. The density functional theory (DFT)

calculation by Höglund et al. [99] for local density approximation of native defect states

in GaP has shown that the stable charge states which have neither electron in conduction

band nor holes in valence band are primarily vacancies and antisites rather than

interstitial species, mostly due to their relatively lower formation energy [99,128].

Formation of localized energy levels within the bandgap associated with point defects that combine to form donor-acceptor pairs seems to be responsible for electronic transition of 1.7-1.75 eV for GaP NWs. It is reported in GaP, the intrinsic point defects introduced during the growth under excess P condition, are predominantly P_{Ga}^{+2} and V_{Ga}^{-3} [99]. However, the DE at 690-720 nm was observed for all the samples grown near stoichiometric concentration using vapor phase method using Ga, GaP+Ga and GaP+P source reagents. Formation of these DE levels could be attributed to the shallow acceptor level of V_{Ga} (at E_c-1.7 eV) or donor level of P_{Ga} (at E_c-0.6 eV) [129]. The location of Fermi-level strongly depends on the concentration of native defects that results in slight variation in DE peak position.

4.4 Growth of GaAsP and InGaP Nanowires Using Vapor Transport Method

To show the versatility of this growth method, by taking into account the composition dependency of the bandgap, InGaP and GaAsP alloy NWs were rationally synthesized. This is achieved through the precise control over the composition of the ternary alloys simply by adding the elemental As or In into GaP growth chamber. For instance, GaAsP NWs were grown in a similar condition to GaP NW growth at 800 ∘C and total pressure of ~3 Torr. As the source material ball-milled GaP powder was used with a mixture of As+P with 1:1 atomic ratio of As:P assuming that As and Red-P have very close vapor pressure (slightly higher vapor pressure for As). Shown in right inset of Fig. 60a is the SEM image of the Tapered- shape GaAsP NWs. Similarly pellets by providing indium pellets at upstream side of the furnace where evaporation temperature is 800 ∘C, single composition InGaP alloy NWs were grown. Further experiments are required to adjust

the growth parameter for bandgap tuning across the entire composition for $Ga_xAs_{1-x}P$ and $In_xGa_{1-x}P$. A representative PL spectrum for single composition-tunable GaAsP and InGaP NWs with a direct bandgap red-emitting wavelength is shown in Fig. 60b.
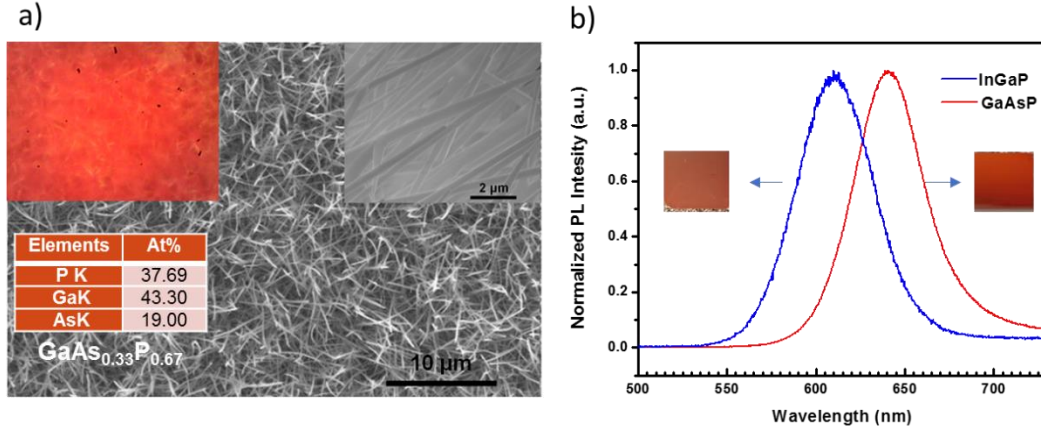
Figure 60. Growth of GaAsP and InGaP nanowires: a) SEM image of $Ga_{0.33}As_{0.67}P$ nanowires (a). Insets are the bright field optical image of sample pumped using Nd:YLF (λ=349nm) laser (top left) and the zoomed image of the sample from side view. B) PL spectra for InGaP and GaAsP with emission wavelength of 610 nm 640 nm. (Embedded pictures are for the real color images of as grown samples)

The narrow width of the PL emission spectra for both alloys without any surface-passivation corresponds to the high optical quality of the as grown NWs, apparently due to good surface properties and fewer intrinsic defects. Growth of alloys of GaP using such low-cost method is promising in terms of application for making LEDs, solar cells, etc., despite the simplicity of growth method while rendering high material quality.

4.5 Summary

In summary, an Au-catalyzed VLS strategy for the growth of highly stoichiometric GaP NWs on Si substrates with a simple low-cost CVD method was presented. It was found that excess phosphorous precursor is necessary to inhibit the incongruent sublimation of P and Ga and to restore the chemical balance. As a result, highly

stoichiometric GaP NWs are grown with less defects and more bandedge emission. The sublimation behavior of these precursors was explained using the concept of chemical potential. This strategy and the associated understanding are established through a systematic growth study and characterization by comparing three sets of precursors: pure GaP, GaP+Ga and GaP+P. From the structural study of NWs grown under P-rich condition the formation of coherent twin planes or TSLs as the structural defects in body of VLS-grown NWs was also noticed. The effect of growth parameters such as time, type of silicon substrate, growth temperature, etc., on suppression of DE caused by intrinsic crystal imperfections was demonstrated. Our comprehensive growth and characterization study allowed us to relate the growth conditions and growth precursors to stoichiometry of NWs and the latter in turn to the existence and degree of deep defect states and band edge emission. Since types and concentration of defects are important as well as the relative intensity of bandage emission for optoelectronic devices, it is therefore imperative to study the crucial roles of growth parameters and conditions and to develop a growth strategy to minimize defect bands and maximize band edge emission. It is believed that such a growth strategy is not only important for GaP, but also for other III-V compounds. However, there are more aspects of such growth yet to be explored for the eventual optimization of material properties and maximization of bandedge emission. In addition, the versatility of the GaP growth was shown by bandgap tuning of its alloy partners such as InGaP and GaAsP NWs, simply by adding the As or In source into the growth medium.

5 GROWTH OF InP THIN FILMS AND NANO-NETWORKS

5.1 Introduction

InP is one of the important semiconductors for solar cell applications [130-132], either as an important alloy partner with GaP to produce wide-gap junctions [133,134] or as an independent material for single junction [130,131] cells with almost ideal bandgap. Its superior properties include high electron mobility of 5400 cm^2/V.s [135,136] close to that of other III-V semiconductors such as GaAs (8500 cm^2/V.s) [137], and low surface recombination velocity (SRV) of $\sim 10^3$ cm s^{-1} [138,139] compared to GaAs with extremely high SRV of $\sim 10^6$ cm s^{-1} [140-142] that can be combined to define a figure of merit for solar application. Having high absorption coefficient [143,144], a thin layer InP with a direct bandgap can absorb the incoming sun light, efficiently that can reach the theoretical Shockley-Queisser limit of $\sim$ 33% under AM1.5G illumination [145]. It is reported that a 2 μm thick layer of InP can generate more than 95% of the maximum photocurrent efficiency produced by a layer with thickness of infinite, while a 100μ thick layer of Si is required to achieve the same ratio [146]. So far, growth of high quality InP thin film has mostly been demonstrated by more expensive MOCVD [147] or MBE [148] techniques, with some exceptions being the recently demonstrated In phosphorization [149] and closed space sublimation (CSS) [150] approaches. Despite the large grain size of InP obtained by phosphorization approach, using molybdenum metal substrate as the nucleation promoter and thermally evaporated SiO_x-capped In exposed by P flux makes this approach somewhat complicated. It has been shown that presence of e-beam evaporated SiO_x capping layer prior to phosphorization is crucial to prevent dewetting of

In thin film from the substrate [149]. Growth of InP via CSS is also limited by using the metal substrate of choice with a film growth temperature window of 600-700 ◦C and as-received high purity InP powder as source material [150]. Hence, the extremely high precursor and preparation cost together with complexity of processes is still problematic for manufacturing the low-cost commercial InP solar cells. It is known that the mismatches in lattice parameters and coefficient of thermal expansion make the heteroepitaxy of high quality InP challenging. In fact, growth on non-epitaxial substrate leads to polycrystalline film with large concentration of recombination centers exerted by grain boundaries reducing the density of photogenerated minority carriers. In order to decrease the grain boundaries, it is important to grow InP with larger grain size in a controllable manner which is crucial for high performance solar cells. It is also essential for InP to be grown with largely independency to the growth on single crystal substrate. Growth of InP thin film using the typical low-pressure vapor transport method has advantage of low cost over other more expensive techniques. However, vapor phase CVD growth of InP using precursors such as solid source InP compound directly suffers from large difference in sublimation rate of In and P as shown in chapter 3. In the current chapter, a low cost VLS-VS assisted growth technique of high quality InP thin film or network. The growth approach is based on using single elemental precursor similar to InP NW growth which was presented in chapter 3. It will be shown here that the current approach which is believed to be the most direct approach for InP growth that leads to growth of highly stoichiometric InP in a wide growth temperature window. In addition, this approach enables us to control the film thickness and size of the grains by changing the growth parameters. The growth mechanism is explained in terms of interplay between

VLS and VS mechanisms for both Au-catalyzed and self-catalyzed to shed light on the key role that Au catalyst plays on promotion of nucleation leading to growth of coalesced nano-network structures. More importantly, the current method is independent of the growth substrate such as silicon, InP, fused amorphous quartz, etc. This growth strategy provides a simpler, lower cost way towards producing high quality InP thin film that is scalable to high-volume manufacturing of solar cells given the fact that it requires the thin film-like processing steps after growth. Extensive material and optical characterization as well as device application will be described in detail in following sections.

5.2 Growth Method

A schematic of basic growth setup is shown in Fig. 61. Prior to growth, all substrates were first immersed in acetone and ethanol and DI water, respectively and sonicated for 5 min during each step to remove organic contaminations from their surface. Subsequently, the native oxide was removed for Si substrate by soaking them in a dilute 5% HF solution for 2 min, and then they were rinsed with DI water and blown with ultra-high purity nitrogen gas to avoid re-oxidation. The InP substrate only was soaked in a 5% HCl bath for 5 min (instead of HF solution) to remove the oxide completely. A thin 1-1.5 nm layer of Au film was deposited as catalyst on various substrates such as Si, InP, amorphous quartz via physical sputtering. The pre-deposited substrate was placed downstream in a vertical configuration facing the flow direction. As the source material, the high purity Indium spheres (1mm dia.) (99.99% Alfa Aesar) and red phosphorous (≥99.99% Sigma Aldrich) were placed inside a 4 feet long horizontal $34 \times 38\ mm$ (I.D.×O.D.) quartz tube

embedded in a single zone furnace (Lindberg/Blue M) at corresponding temperature of 980 °C and 450 °C, respectively. The system was purged for 1 hr under 300 sccm flow rate of Ar+5% H_2 carrier gas to evacuate the reactor from excessive oxygen, CO_2 and water molecules inside the furnace tube. The set temperature of the furnace at the center was 980 °C that was achieved in a 24 min ramp-up time and the growth time is defined by elapsed time after the temperature reaches to the set value. As shown in Fig. 61, two separate magnetic manipulators made of quartz rods were used to control the locations (and thus the temperatures or evaporation rates) of source materials. It is important to
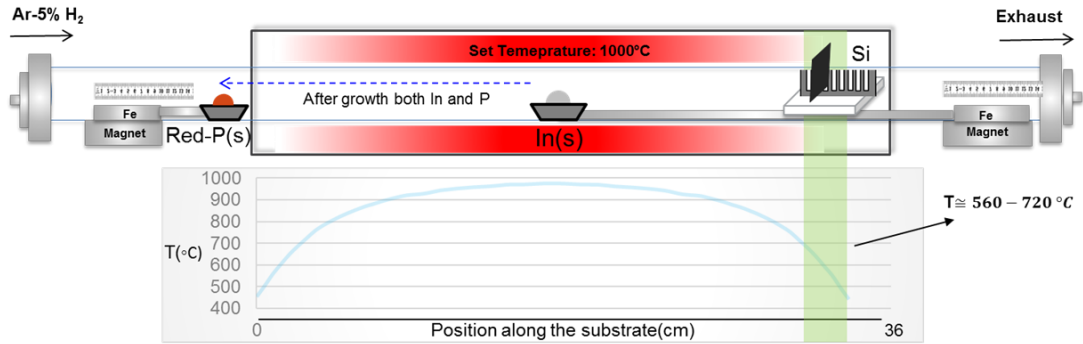
Figure 61. Schematic of growth set up for single elemental VLS-InP

notice that the P source material was outside of the heat zones during the temperature ramp-up time and only pushed to the desired location after the set temperature is reached, while In source was at the center of the heating zone from the beginning of the ramp-up time. InP crystals were grown under 20 sccm carrier gas flow on Au-deposited substrates positioned inside the furnace at downstream, where the substrate or growth temperature varies from 500 °C to 720 °C. Growth times were 2-60 min and total pressure range was ~2 Torr.

5.3 Growth Mechanism

Fig. 62 shows the SEM images of Au-catalyzed InP films for a series of growth studies with various growth times at total pressure of 2 Torr and temperatures of of 600 ◦C (Fig. 62a) and 650 ◦C (Fig. 62b). As can be seen from the 2 min growth at 600 ◦C on Au-deposited silicon substrate, VLS-growth of short NWs with diameter of less than 200 nm are initiated predominantly. The white dots are the Au nanoparticles formed from the original 1-1.5 nm thick Au film under Ostwald ripening at high temperature. By increasing the growth time, VS growth mode leads to more growth transverse to the original NWs, as can be seen clearly from the zoomed-in image for the growth time of 7 minutes. With the further increase of growth time, the size of grains increases which leads to the merging of grains and eventually forming a film with minimal voids and gaps or interconnected network depending on the growth time and other parameters such as temperature, as can be seen in the images for 15 mins and 1 hr growth times. The grown InP film is polycrystalline with randomly oriented facets. Comparatively, growth at higher temperature of 650 ◦C gave qualitatively similar results. The key difference is to be the number of initial nucleation sites and sizes of Au particles, as can be understood by comparing the two images for the growth time of 15 mins. Larger and smaller number of grains are seen at 650 ◦C than those formed at 600 ◦C. In addition, the VS growth at 650 ◦C seems to be more active than at 600 ◦C, resulting less voids and more continuous film in the latter case. Details of spatial filling of the films will be further discussed later.
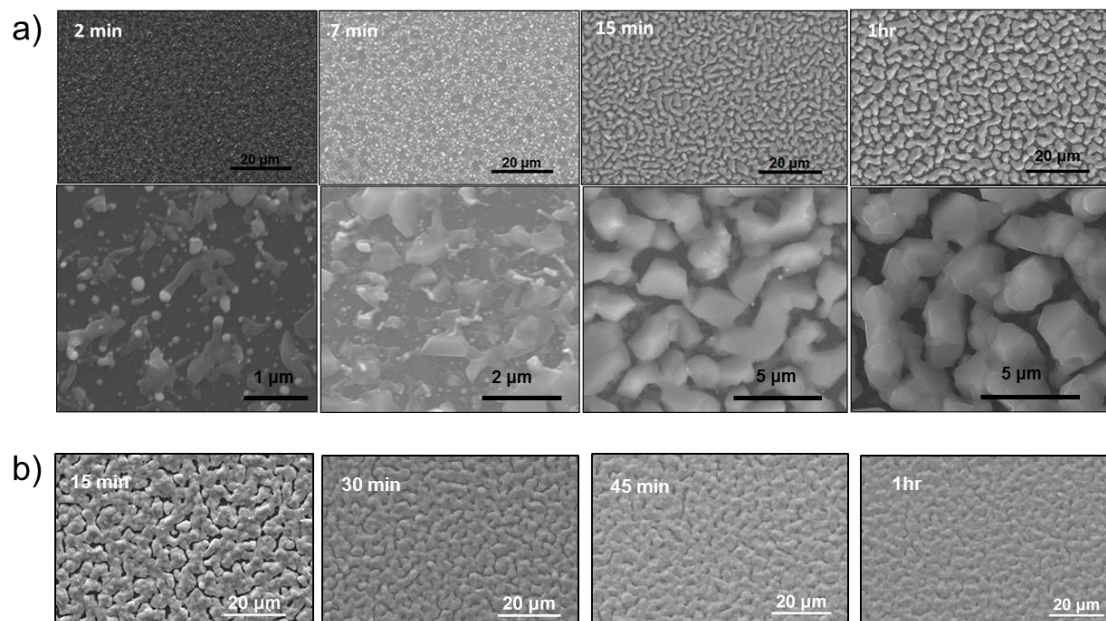
Figure 62. SEM images for a series of growth studies for different lengths of growth times on Si (100) substrate at growth temperature of 600 °C (row a) and 650 °C (row b). The corresponding zoomed-in SEM images of samples grown at 600 °C are also shown.

The difference between NW growth shown in chapter 3 and film growth is mainly the supersaturation levels of the second step after VLS nucleation and thereafter. If the supersaturation is purposely tuned to be high enough, it grows into film.

5.4 Effect of Growth Temperature

In order to understand and eventually be able to control the growth of films vs. NWs, the growth at different temperatures was experimented. At low pressure of 2 Torr, there is wide range of growth temperatures from 560 °C to 720 °C where InP films can be grown. At lower temperature of 500 °C, the growth of NWs was predominantly via the VLS mechanism (Fig. 63).
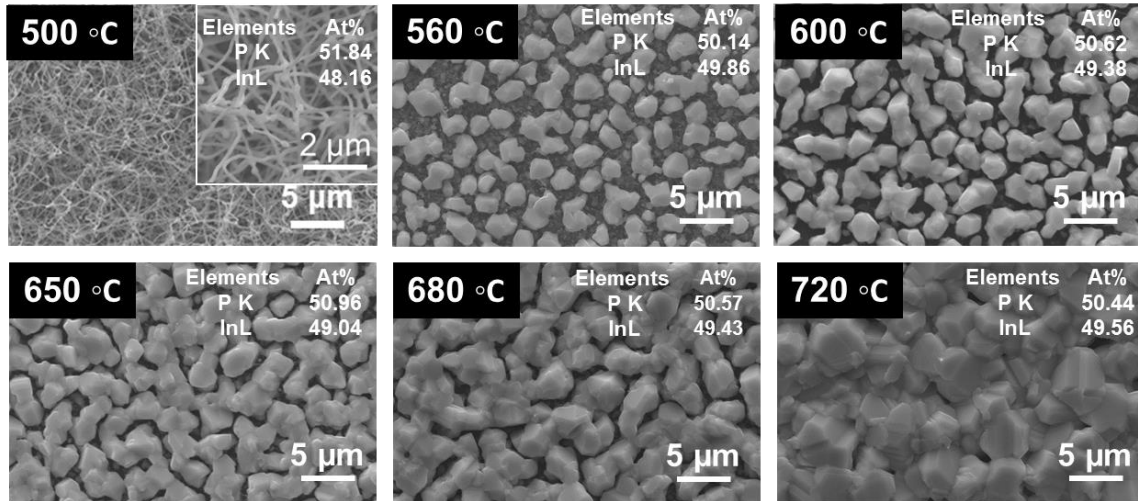
Figure 63. SEM images of InP grown at wide temperature window of 220 ∘C. VLS-thin film polycrystalline InP are grown at range of 560 to 720 ∘C. Inset in top right of 500 ∘C growth is the high magnification image of VLS-grown InP NWs. Quantitative EDS elemental composition results show high stoichiometry of grown InP.

The fact that growth at higher temperatures lead to more active VS growth mode than low temperature can be explained by kinetic of the growth using r=Aexp(-E_a/kT) equation, where r is the growth rate, E_a is the activation energy, k is the Boltzmann constant and T is the temperature. According to the growth rate equation, it is expected to observe higher growth rate at higher temperatures. This is equivalent to the higher reaction rate between In and P atomic species. Peiman et al. have reported growth of highly tapered short wires or island of InP by increasing the temperature and V/III ratio which accounts for the differences in In diffusion length [151]. From the SEM images, it can be clearly seen that the growth at higher temperatures results in larger grain sizes and less voids which leads to formation of more continuous film.

To quantify the continuity of the film or the spatial filling of grains, image processing is performed on SEM image acquired from four different samples (all adjusted to the same level of brightness and contrast) grown at temperature range of 600 to 720 °C, where the gray scale of images is digitized in the range of [0, 255], with 0 representing the silicon substrate as background. To properly represent the voids distribution, visual comparison of original images (Fig. 64a) and those overlaid with various threshold levels (marked as white in Fig. 64b).
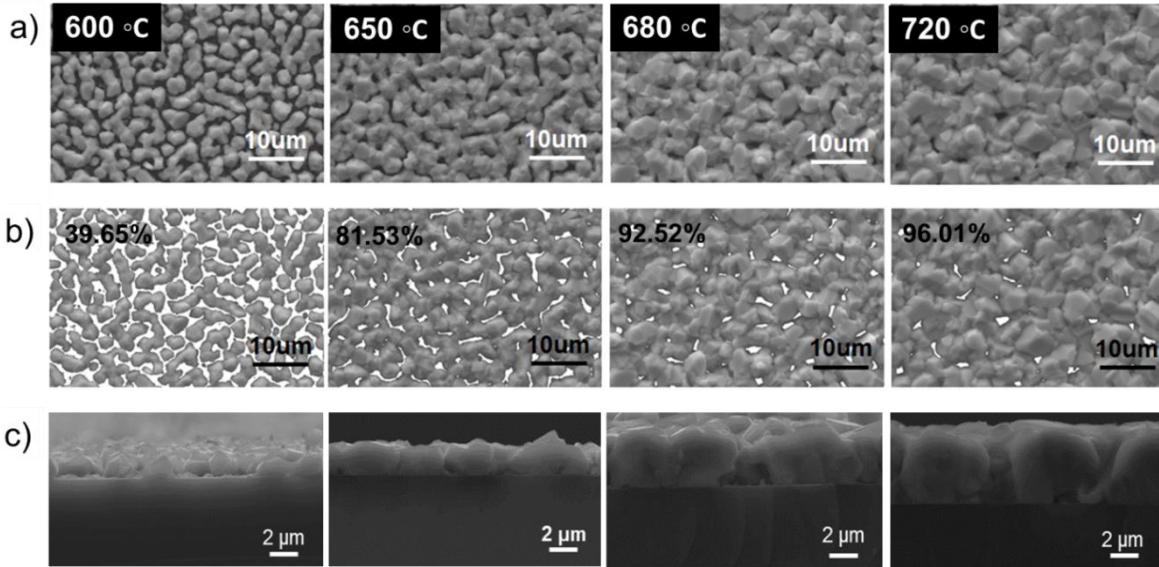
Figure 64. SEM study of temperature effects on growth of InP film with Au catalyst . The top via SEM images of the InP films grown at temperatures of 600, 650, 680 and 720°C from left to right (a). Processed images shown in row "a" with various spatial filling ratios (b). The white areas represent voids as obtained by the image processing (see text for more explanation). The numbers on top left are the spatial pore filling given by %. The side view corresponding SEM images of samples in row a showing the thickness of fils (c).

A best threshold value of 70 was determined this way. Gray levels below 70 are considered voids without growth and are marked in white in Fig. 64b. The spatial filling ratio is then defined as the percentage of the areas over 70 to the total area. This ratio is plotted as a function of growth temperature in Fig. 65a. As can be seen, there is a monotonous increase of spatial filling with growth temperature, correlated with an

111

increase of grain sizes. The maximum filling ratio of ~96% is achieved at 720∘C for 1 hr growth. The thickness of the InP film can also be estimated from the cross-section image of the samples (Fig. 64c), ranging from 1.6 μm to 5.5 μm in the temperature from 600∘C to 720∘C. The thickness of InP thin film vs. growth temperature is shown in Fig. 65b.
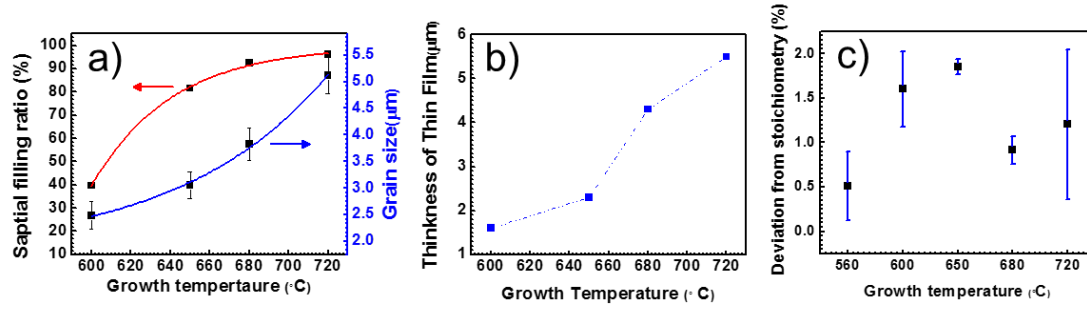
Figure 65. Quantitative measurements on temperature effects on the growth of InP film with Au catalyst. a) plots of spatial pore filling ratio (red) and average grain size (blue) vs. growth temperatures. Curves are obtained by exponential fitting in Origin, b) plot of thickness vs. growth temperature. c) Deviation from perfect stoichiometry based on EDS elemental analysis.

The mean value of the grain size ranges from ~2.5 μm to 5.1 μm for the growth temperature varying from 600∘C to 720∘C (Fig. 65a). The estimated lateral grain size (G) and the spatial filling (SF) are both fitted for the temperature (T) dependence (blue and red curves, respectively), as shown in Fig 65a.

Table 4. EDS elemental composition obtained from multiple spots for the samples grown at different temperatures.

Growth Temperature (∘ C)	560	600	650	680	720
In (%)	49.86	49.38	49.04	49.43	49.56
P (%)	50.14	50.62	50.96	50.57	50.44
In (%)	49.47	48.91	49.14	49.58	49.48
P (%)	50.53	51.09	50.86	50.42	50.52
In (%)	49.91	49.33	49.07	49.55	48.79
P (%)	50.11	50.67	50.93	50.45	51.21
In (%)	49.78	49.18	49.05	49.61	49.76
P (%)	50.24	50.82	50.95	50.39	50.24
In (%)-Avg.	49.755	49.2	49.075	49.5425	49.3975
P (%)-Avg.	50.255	50.8	50.925	50.4575	50.6025
Standard Deviation	0.383144881	0.422374242	0.090184995	0.157797338	0.843544111
Devition from Stoichiometry(%)	0.51	1.60	1.85	0.91	1.20

The best exponential fits (obtained by ExpGrow1 function in origin) are given by $G \approx 1.78 + 2.41 \times 10^{-4} \, Exp \, (T/75.50)$ and $SF \approx 99.71 - 1.58 \, Exp(-T/40.58)$, respectively. EDS measurements were performed on multiple points on the samples grown at different temperatures, as presented in Table 4, where the average and calculated deviation from perfect stoichiometry are shown. The deviation from stoichiometry (%) for p-rich InP is calculated by $(P(\%)-50)*2$ formula. This deviation is plotted as a function of temperature in Fig 65c. As one can see, our growth in the wide range of growth temperature window of 160 °C only results in less than 2% deviation from perfect stoichiometry.

The difference between the temperature dependent-average grain size and film thickness values for the same growth temperature window is indicative of the unequal lateral and vertical growth rate. Also, by taking the direct relationship between growth temperature and grain size and pore filling ratio into account, it was attempted to grow a void-free continuous polycrystalline film by further optimizing the growth temperature (Fig. 66).
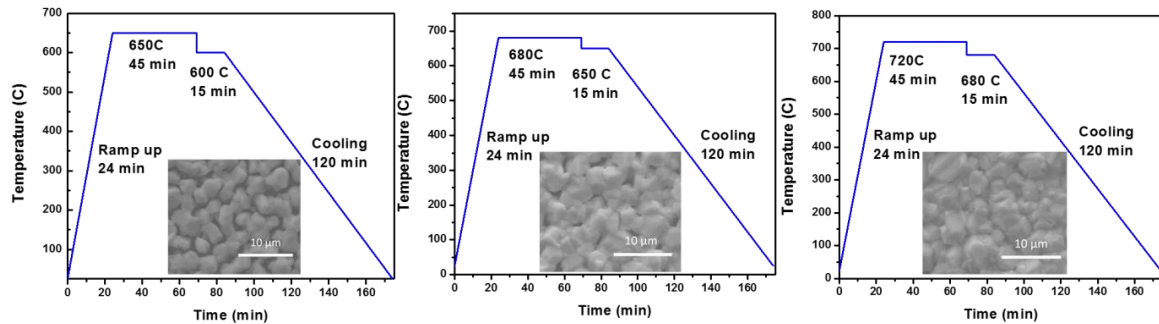
Figure 66. Schematic time-temperature diagram for two-step growth at a) 45 min @ 650°C followed by 15 min growth @ 600°C, (b) 45 min @ 680°C followed by 15 min growth @ 650°C min, and (c)45 min @ 720°C followed by 15 min growth @ 680°C (c). Corresponding SEM images are embedded in each plot.

It is important to know that during the growth there is always a trade-off between adsorption and desorption of atomic species which becomes rate-limiting factor of the growth. This suggests that a two-step growth at higher temperature followed by a relatively lower temperature might reduce the desorption rate of atoms from the crystals at last stage of the growth. Continuous polycrystalline film (Fig. 66c) was achieved by a growth at 720◦C for 45 min followed by 15 min growth at 680◦C. However, grains are not homogenous in size compared to sample grown at 720◦C for 1hr.

5.5 Effects of Growth Substrates

To substantiate the non-epitaxial nature and versatility of our growth mechanism, InP films were obtained on various substrate such as Si (100) and (111), InP (100) and fused amorphous quartz. Quality of VLS-VS assisted growth of InP thin film is largely independent of type of the substrate; SEM images of samples grown on the three different samples for an hour at 720◦C are shown in Fig. 67. It is seen that the polycrystalline InP with multi-facets (Fig. 67a) are grown on Si and fused quartz, whereas the film grown on InP (100) substrate has facets parallel to surface (Fig. 67b) of substrate indicating the [100] as the growth direction. It is known that misorientation of grains relative to the substrate results in formation of multi-facets depending on the misorienation angle and direction [152]. This is reflected by surface topography of the grown samples, as can be clearly seen on samples grown on silicon and amorphous quartz substrate. This is observed in self-catalyzed growth as well as will be shown later.
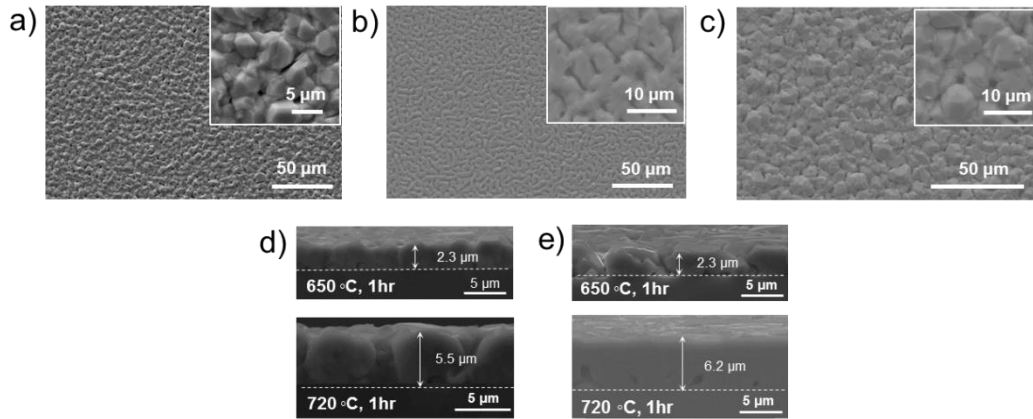
Figure 67. InP films grown on various substrates. a) Au-catalyzed InP on Si (100), b) Au-catalyzed InP on InP (100), c) self-catalyzed InP on fused amorphous quartz. All three samples are grown at 720°C for an hour. Comparison of temperature dependent thickness of InP film grown on Si (100) (d) and InP (100) (e) at two different temperatures of 650 °C and 720 °C.

From a comparison between thickness of InP grown on InP (100) and Si (100) substrates, it can be clearly distinguished that the non-epitaxial growth rate on Si substrate (5.5 µmh-1) is lower than that of homoepitaxy (6.2 µmh-1) at higher growth temperature of 720°C, while the growth speed is the same (2.3 µmh-1) at 650°C for 1 hour (Fig. 67d and 67e). Incidentally, it was noticed that, due to the mismatch in thermal expansion coefficients between InP (4.75 10^{-6}/K), Si (2.60 10^{-6}/K) and fused silica (0.55 10^{-6}/K) [153], thermal-induced stresses during the cooling process following the growth leads to the peeling-off of the film of 4-5 µm thick from the substrates. This might be an interesting approach towards removable and transferable InP film onto other substrates for making solar cells, etc.

5.6 Au-Catalyzed vs. Self-Catalyzed Growth

As it was discussed, Au-catalyzed growth promotes the formation of InP network and eventually highly coalesced polycrystalline InP film. However, to better understand the

growth mechanism it is required to also study the self (In-)-catalyzed growth explicitly in this case. Ideally it is preferred to avoid using external catalyst and try to use the vaporized precursor that contributes as reagent species in nucleation and growth of NWs. It is known that the use of metal catalyst such as Au in the VLS growth can cause Au contamination associated with formation of deep level traps in the grown materials, detrimental for device performance [154]. Therefore, the self-catalyzed approach is preferred where the metal element of a III-V compounds (such as In in the case of InP) is used as the catalyst without introducing foreign metal elements. It has been reported that self (In-)-catalyzed growth gives rise to broader size distribution of NWs than when pre-existing Au catalyst is used, due to a continuing nucleation of the In droplets during the growth [155]. In order to understand the difference between Au-seeded and In metal-catalyzed growth, additional self-catalyzed experiments were carried out. In metal was pre-seeded during the initial temperature ramp-up stage of 24 minutes, with In source placed at the location with temperature $\sim$ 980 $\circ$C and no P was introduced. After the ramp-up, P was then introduced with all the other conditions and growth time being the same as for the Au-catalyzed growth. The SEM images obtained for two samples grown on silicon substrate at 600 $\circ$C for 1 hr under Au- and self-catalyzed growth conditions a are shown in Fig 68 (top row of Fig. 68a and 68b). By precise looking, some major differences between can be observed from the two cases: from the processing of both images using ImageJ software by thresholding each one in gray scale between 53-255 via binary watershed processing mode, the number of grains per the same area ($\sim$47*26 μm^2) of self-catalyzed sample is greater value than that for Au-catalyzed sample. (449 vs. 159).

116
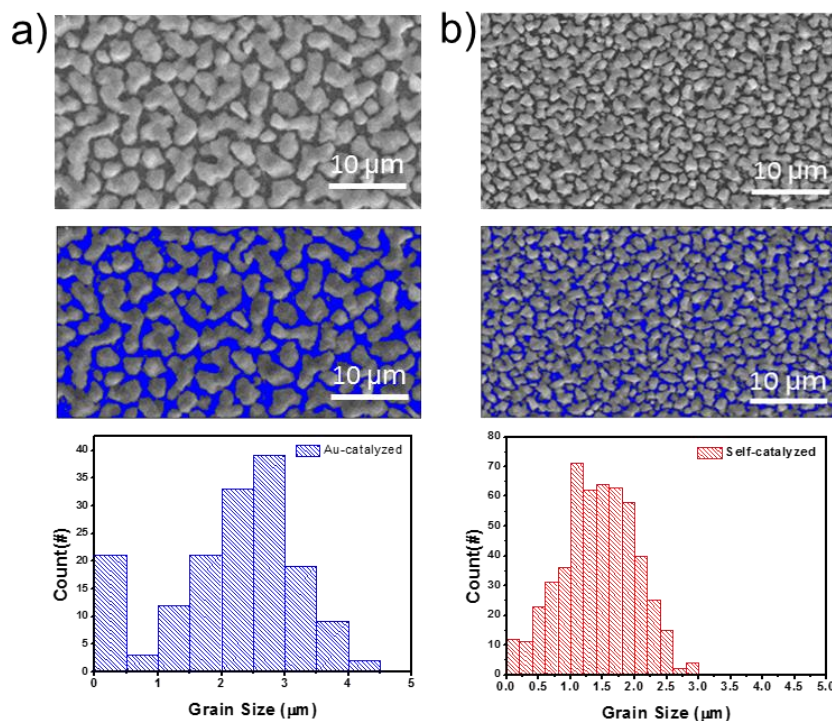
Figure 68.. Self-catalyzed vs. Au-catalyzed InP: Image processing results for comparison between SEM micrographs of samples grown InP grown at 600 ∘C for 1 hr under two different condition: a) Au-catalyzed, and b) self-catalyzed. The middle image in each column is obtained based on the gray scale thresholding between 53 and 255 via binary watershed processing mode using ImageJ software. The histogram for grain size distribution of each sample is shown at the bottom.

Gray levels below 53 are considered voids without any grain and are marked in blue (middle row images in Fig. 68). The histogram of grain size distribution for both samples is plotted in the bottom row of Fig. 68. As can be clearly seen from the original and processed images, the self-catalyzed growth leads to more symmetric bell-shape distribution of grains. However, Au-catalyzed growth also leads to broader grain size distribution up to 4.5 μm, while the same value for self-catalyzed is up to 3 μm. It is worth noting that the center-size distribution for the Au-catalyzed shows a value of ~2-3 μm vs. 1-2 μm for self-catalyzed. For the self-catalyzed growth at high temperatures the continuous nucleation of In is less observed and as a result the grains are more uniform as can be seen from a comparison between In-catalyzed growth at 650 ∘C and 720 ∘C (Fig. 69a and 69b).
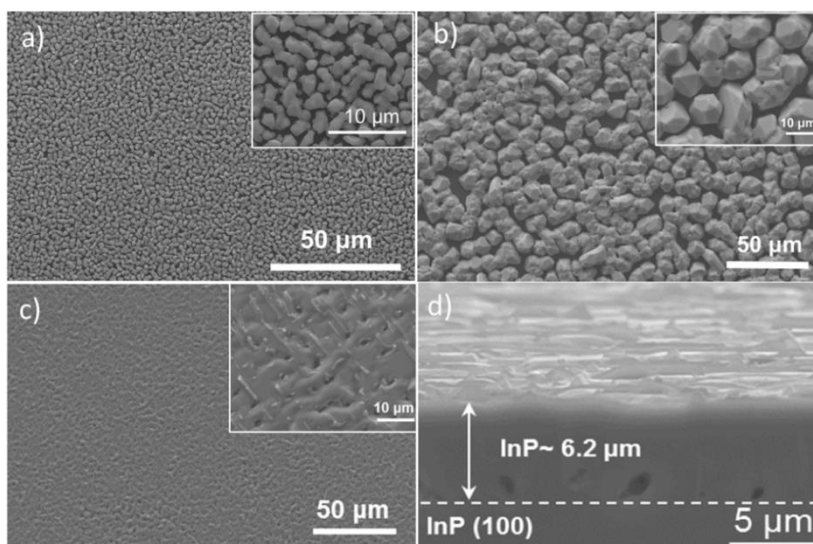
Figure 69. SEM image of the InP films grown under self-catalyzed condition; a) on Si (100) at 650 ◦C, b) on Si (100) at 720 ◦C, c) on InP (100) substrate at 720 ◦C. Growth time for all three samples is 1 hour. Insets on the top right of each figure are the magnified view from the corresponding images. Figure d) shows the cross-section image of the film shown in Figure c.

It is worthy to mention that, for self-catalyzed InP grown at 720 ◦C, polycrystals with grain size of greater than 10 μm was also obtained in form of InP islands that are less coalesced. The self-catalyzed growth on InP (100) substrate at 720 ◦C also shows formation of a very flat (parallel to the surface) and coalesced film, apparently due zero lattice mismatch.

5.7 Structural Characterization

Energy dispersive X-ray spectroscopy (EDS), X-ray diffraction (XRD), and Raman measurement were carried out to evaluate material quality of grown samples. EDS results were shown in connection with temperature dependent study in Fig. 65c.The XRD measurement of a sample grown on Si (100) at 600◦C revealed the absence of any obvious In peak present in diffraction pattern showing complete reaction between In and P. All peaks match with zinc blende (ZB) structure (JCPDS card 00–010-0216) [156]. As

shown in Fig. 70, the (111) peak in XRD pattern is disproportionally stronger compared to the XRD pattern of a single crystal InP than (200) and (220) peaks. This indicates that the polycrystal grains have larger dimensions along [111] direction. This is consistent with the smaller surface energy of (111) planes and the preferred growth direction along [111].
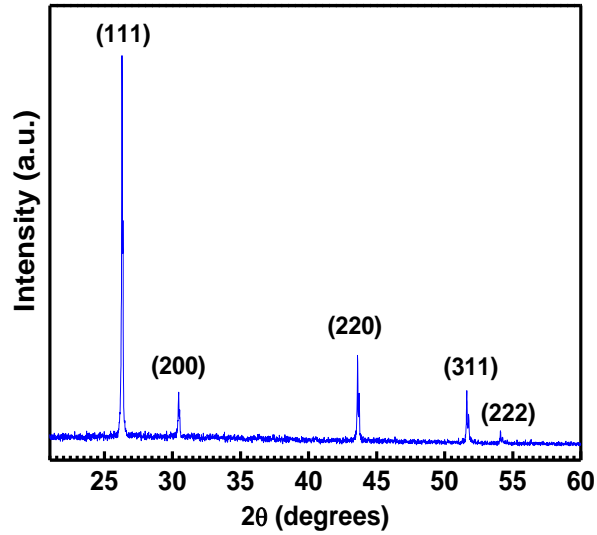
Figure 70. XRD spectrum of InP polycrystalline film grown on Si (100) at 600 ∘C for 1 hr.

Furthermore, the Raman measurement of polycrystalline InP was performed. Raman can reveal some subtle crystal imperfections that we are not able to obtain from XRD or TEM. Room Temperature micro-Raman measurement of InP grown at different temperatures were carried out using an unpolarized laser as the excitation source with wavelength of 532 nm and low laser power of 6.0 mW at the surface of the sample.
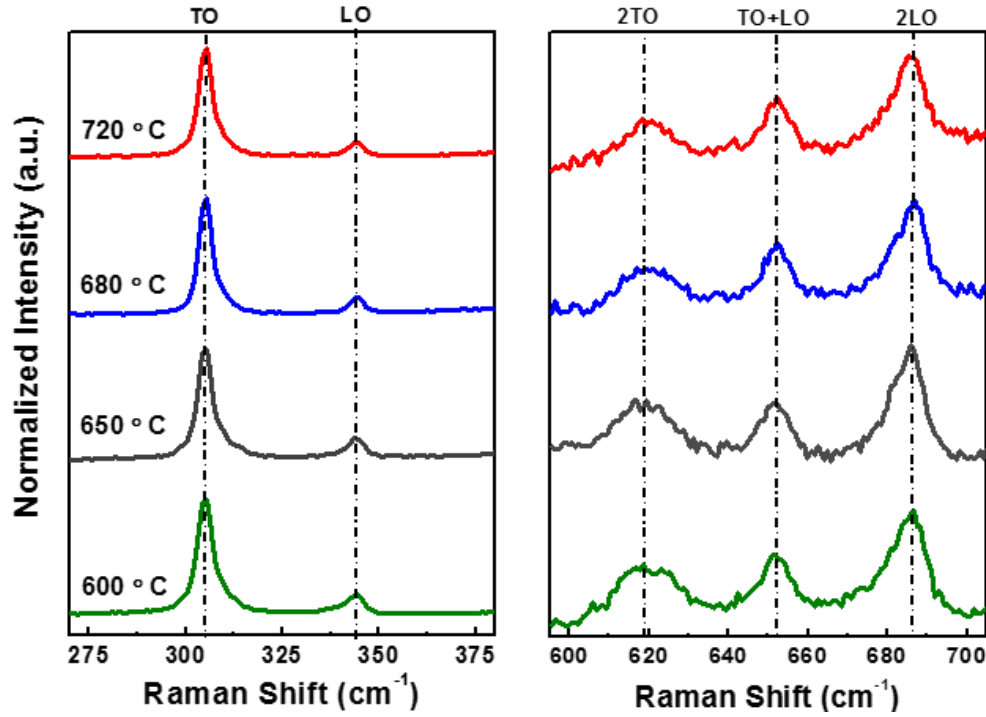
Figure 71. Raman spectra of InP thin film grown at different temperatures for 1hr. The intensity scale of all spectra has been normalized to the TO peak and the results match up to second order with the reference values obtained from single crystal InP wafer. The right plot represents the second order peaks, 2TO, TO+LO, and 2LO from left to right. The intensities for the right graph are 12X.

The Raman spectra shown in Fig. 71 match up to second order with the reference values obtained from single crystalline InP [157]. The anti-Stokes transverse optical phonon (TO), and the longitudinal optical phonon (LO) peaks are observed at around 305.3 cm^{-1} and 344.6 cm^{-1}, respectively. Second-order peaks of 2TO (~617 cm^{-1}), LO+TO (~652 cm^{-1}) and 2TO (~686 cm^{-1}) are also shown with a trend of intensity enhancement towards the higher frequencies. All the peaks are normalized to TO phonon peak intensity as the strongest peak and they are all in close agreement with previous reports [157,158]. It is known from the selection rules for zinc blende structure the TO mode is allowed in Raman backscattering only from (110) and (111) surfaces, whereas the LO modes are observed in backscattering from (100) and (111) surfaces [117]. The fact that both TO

and LO appear in Raman spectra is indicative of texturing of the grains along (111) planes regardless of (100) orientation of silicon substrate. This has been also observed in MOCVD grown polycrystalline InP grown on molybdenum substrate [147].

5.8 Optical and Electrical Properties

Room temperature PL measurement under optical pumping of Ti-sapphire CW laser (λ=810 nm) showed a symmetric band-to-band emission peak at 925 nm (1.34 eV) for the ZB InP grown on Si (100) and Si (111) (Fig. 72a). The PL characteristics of coalesced InP samples grown at 600 ∘C was also compared with that of an undoped (intrinsically n-type, $(1\sim10)E15$ cm^{-3}) InP single-crystal wafer. From PL measurements for the reference and our InP samples by taking into account reflectivity of the wafer (42.80%, calculated from Fresnel's equation for an incident light angle of 45∘) the peak positions are nearly identical (@ 925 nm), but the full-width-at-half-maximum (FWHM) is slightly broader (34 nm vs. 29 nm or 49 meV vs.41 meV) for coalesced polycrystalline InP samples on both Si (100) and (111) substrates. Broader emission bandwidth might be caused by higher concentration of carriers in grown InP. Also, to show the thickness uniformity of the grown InP across entire surface of the substrate, PL was measured PL for 12 different points in an s-shape scanning path (Fig. 72b). The examined PL intensity obtained from self- and Au- catalyzed samples grown at the same condition (T_g= 600∘C, 1 hr) showed that the average PL emission intensity of Au-catalyzed sample is higher than that of self-catalyzed sample and there was ~ 32% and 20% variation between two points with minimum and maximum intensities for self- and Au- catalyzed, respectively. This is due to the formation of grains of various size in self-catalyzed growth that are relatively

smaller than those grown under Au-catalyzed condition as shown in Fig. 68. To shed further light on optical quality of the grown InP, a systematic PL measurement is performed on our sample in comparison with single-crystal InP wafer. Taking reflectivity of the wafer as the reference into account, the PL emission characteristics of InP grown on Si (100) and Si (111) under different laser pumping power are evaluated. From the pumping power-dependent PL spectra for grown InP samples and single crystal InP, it can be seen the enhancement in PL emission follows the same trend.
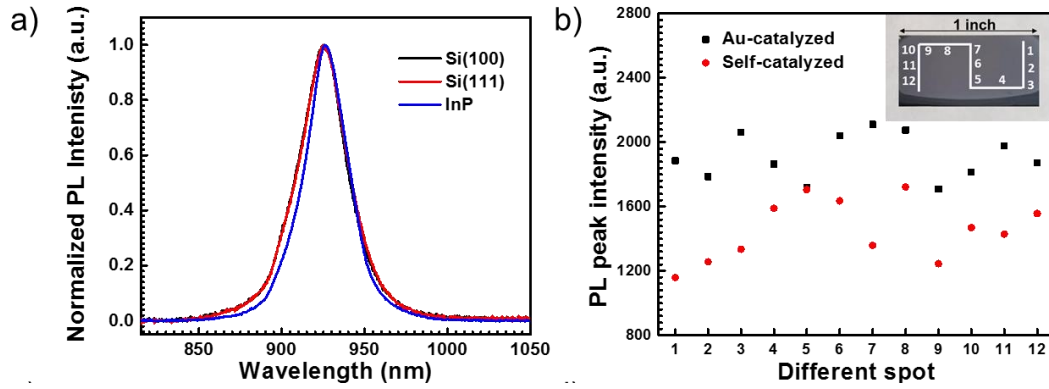
Figure 72. Optical characterization of InP film; a) Room temperature PL spectra of VLS- grown InP on silicon (100) and (111) substrates in comparison with an undoped single crystal wafer as a reference (blue line)., b) position dependent PL taken from different spots in a s-shape scanning path for self- and Au- catalyzed, respectively (inset is the real-color photo of as grown Au-catalyzed sample).

The normalized PL spectra for all samples (inset of Fig. 73a-c) indicates that band-edge transition is predominant and FWHM is not a function of pumping power. This is another strong reason on low density of electronic defect states in grown InP sample.

To identify the underlying recombination process by which the electronic transition occurs, we have further analyzed the integrated PL emission intensity-dependence on the excitation power. PL emission intensity is expressed as $I_{PL} = cI_{ex}^k$, where I_{PL} is the

integrated PL emission intensity, c is the proportionality constant, I_{ex} is the laser excitation power and k is an exponent related to the recombination type.
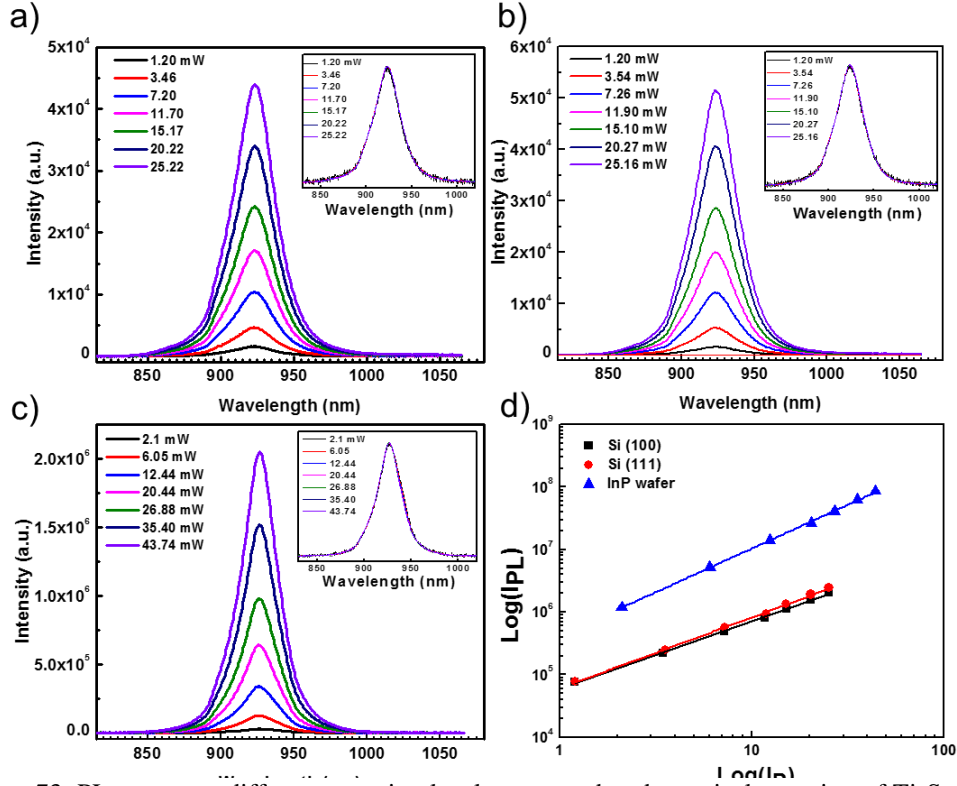
Figure 73. PL spectra at different pumping levels measured under optical pumping of Ti-Sapphire laser (λ=810nm), with taken into account the reflectivity of wafer, for a) InP grown on Si (100), b) InP grown on Si (111), c) Undoped InP (100) wafer, d) The log-log plot of the integrated PL intensity versus excitation power with linearly fitted data showing the k value for different samples.

Generally, for excitation laser light with an energy higher than the bandgap of material, k value is between 1 and 2 for the free- and bound-exciton emission, k < 1 for free-to-bound and donor-acceptor pair recombination. k around 1 means excitonic radiative recombination is more dominant than defect-involved (non-radiative) recombination processes [159]. From a linear fitting of the plot for grown InP on Si (100) and (111) k value is obtained to be 1.082 $\pm$ 0.018 and 1.134 $\pm$ 0.016 which is indicative of the

predominant band to band electronic transition of the carriers and high crystal quality of our samples (Fig. 73d). For the InP film grown in InP substrate, a somewhat larger index of 1.398 ± 0.015 was obtained. The larger scaling index is mainly due to the increasing penetration into the InP substrate as pump power is increased.

5.9 Hall Mobility Measurement

The room-temperature Hall measurement was carried out to determine the carrier concentration and mobility of Au-catalyzed InP grown at 720 °C on quartz substrate (for 1hr). Measurement of mobility on a substrate that has low resistivity (InP, our lightly doped Si) makes it difficult to measure the mobility as it will be influence the result that we get for the film. That requires the as grown film to be peeled off from low resistive substrate prior to Hall measurement. The grown InP is found to be n-type with unintentional bulk doping concentration of 1.7×10^{18} cm^{-3} and electron mobility of 13.25 cm^2/V.s. P-rich InP has shown to have higher net carrier concentration compared to stoichiometric and In-rich InP [160,161]. However, the low electron mobility value of the grown InP samples here can be attributed to the grain size effect [162], doping concentration or compensation ratio [163].

5.10 Time-Resolved Photoluminescence Lifetime

The time-resolved photoluminescence (TRPL) lifetime was measured for the InP grown at various temperatures. As the excitation source, a 405nm pulsed laser diode was used in combination with a time-correlated single photon counting (TCSPC) detector. The PL lifetime of all samples are below 0.7 ns for Au-catalyzed samples grown at temperature range of 560°C to 720°C (Fig. 74a).

124
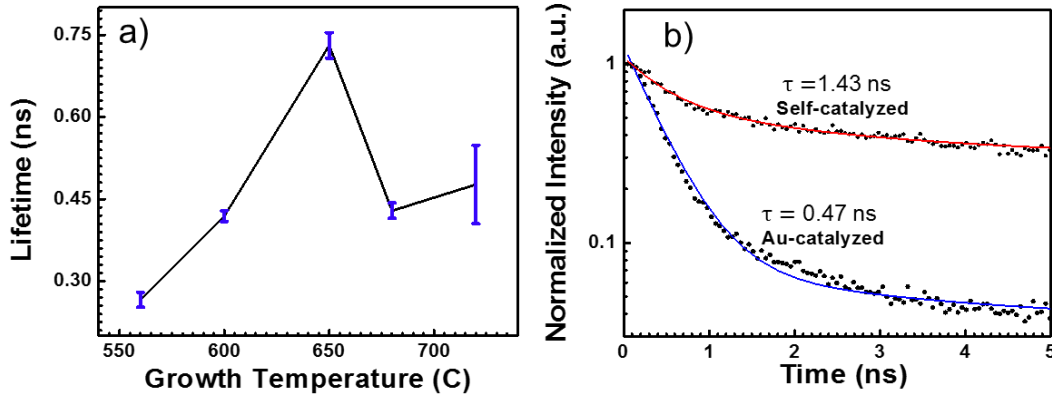
Figure 74. Lifetime measurements of InP film: a) Average time-resolved photoluminescence (TRPL) lifetime as a function of growth temperature. b) Comparison of TRPL lifetime for two different samples grown at 720∘C under self- and Au-catalyzed condition.

It is generally expected to have a higher minority carrier lifetime for the sample grown at higher temperatures due to reduced concentration of point defects such as interstitials and vacancies [149]. However, the highest lifetime that we observed is for polycrystalline InP grown at temperature of 650∘C and then start to decrease beyond 650 ∘C. It is known that the grain size and boundaries play an important role in carrier dynamics of polycrystalline crystals by reducing the diffusion length of the carriers due to increased concentration of defects such as impurities, dangling bonds and dislocations [160-162]. As shown in Fig. 64, the size of the grains increases by growth time which corresponds to longer lifetime. The decrease in lifetime for growth temperature higher than 650∘C might be due to diffusion of Au atoms into InP forming a shallow donor level [164] that contributes into the non-radiative recombination. Therefore, it is of particular importance to determine the difference in minority carrier lifetime between InP synthesized using the Au-catalyzed and self-assisted growth. Suitability of Au-catalyzed VLS grown NWs for optoelectronic application in terms of minority carrier lifetime has been examined [165,166]. This is under debate whether the residual atomic Au have significant impact

on optoelectronic properties of as grown materials, even though, there are systematic studies showing concerns over the effect of Au contamination on device quality [167]. As shown in Fig. 74b comparison between TRPL lifetime measured for two different samples grown at 720∘C under self- and Au-catalyzed condition showed about three times increase in lifetime of InP in the absence of Au catalyst. This result strengthens the hypothesis of diffusion of Au atoms into the crystal structure, thereby reducing the lifetime. To summarize key material characteristics of grown InP; table 5 represent the quantitative data obtained from our grown InP films in comparison with previously reported works.

Table 5. Comparison of material quality and optoelectronic properties for InP grown using various techniques.

Method	Deviation from Stoichiometry (%)	Grain size	Void density (spatial filling)	Mobility $cm^2/V\cdot s$	PL linewidth	Lifetime (ns)	Growth temperature window (∘C)	Reference
Phosphorized SiO_x- capped In	-----	Very large (no number)	- ---------	- ------	39 nm Vs. 34 nm for wafer	--------	600	[168]
CSS	-----	5 µm	100 % in a three step growth	-------	41 nm vs. 31 nm for wafer	0.89	600-700	[150]
HVPE	2.4	< 3 µm	-----------	-------	InP on InP ; 22 nm	--------	550 – 610	[169]
Flash evaporation	6%	4.2 nm	100 %	------	1.5 eV emission	--------	Room temperature	[170]
Pulsed laser deposition	----	60 nm	100 %	------	---------	--------	200	[171]
RF magnetron sputtering	3.8 %	< 500 nm	100 %	36	-------	-------	175	[172]
Spray pyrolysis	----	10.6 nm	----------	51.55	-------	--------	450-525	[173]
Phosphorized SiO_x- capped In	------	10-100 µm	100 %	500	37 nm vs. 29 for wafer	~ 2	400-800	[149]
MOCVD	------	10 µm	discontinuous film	-------	26 nm vs. 28 nm for wafer	------	445-545	[147]
Our work	< 2%	5-10 µm	96% single run 100% two step growth	13.2	34nm Vs. 29 nm for wafer	1.43	560-720	-

5.11 Device Application: Solar Cell

A p-n heterojunction solar cell based on InP NPs was demonstrated. The detailed Schematic of fabrication process flow is shown in Fig. 75. To fabricate the InP NP-solar cell, first InP was grown (at 650 ∘C) on low resistivity (0.001-0.005 Ω cm) p-type silicon.
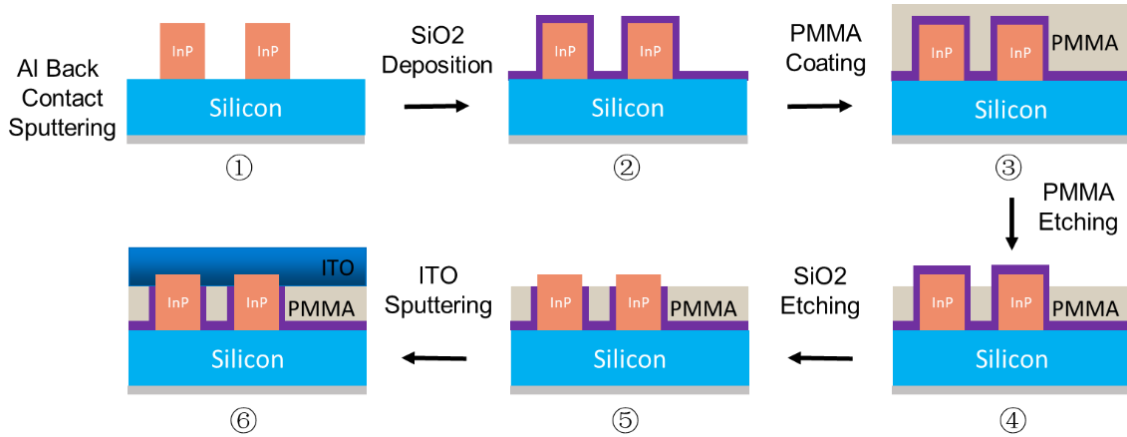
Figure 75. The process flow for fabrication ITO/ InP/ Si solar cells

An Aluminum back contact was sputtered on silicon after growth. The NPs then were etched with a dilute (5%) HCl solution to remove the native oxide and clean the NPs sidewalls. A thin (~50 nm) layer of SiO_2 was immediately grown by PECVD to passivate the surface of InP absorbers. Different interlayer dielectric (e.g., SOG, SU8, PMMA) were examined to fill the gaps between pillars by spin-coating. The spin-coated sample was polished using an Allied High-Tech MultiPrep Polishing System with a diamond lapping film, 0.1 micron to planarize the surface. Fig. 76 shows a representative image of fabrication steps before and after spin-coating of SOG followed by polishing and deposition of ITO and n-contact. For the sample that is demonstrated as the best working device, PMMA was used as the interlayer dielectric.

127

After PMMA spin-coating, an O_2 reactive ion etching (RIE) was used to etch back the extra PMMA on the top to open the NP tips. Then buffered HF (20:1 BOE:DI-H_2O) was used to remove the SiO_2 on the open tips before sputtering of the indium-tin-oxide (ITO) transparent conductive layer. Finally, the Au or Ag contacts are deposited via evaporation (Fig. 76d). The patterned cells are in square shape with 1×1 mm dimension. is known that NPs can result in suppressed reflectance and better light trapping in solar cells [174]. SiO_2 is expected to increase the PL lifetime by surface passivation of dangling bonds [175]. Also, it can result in enhanced light absorption [176].
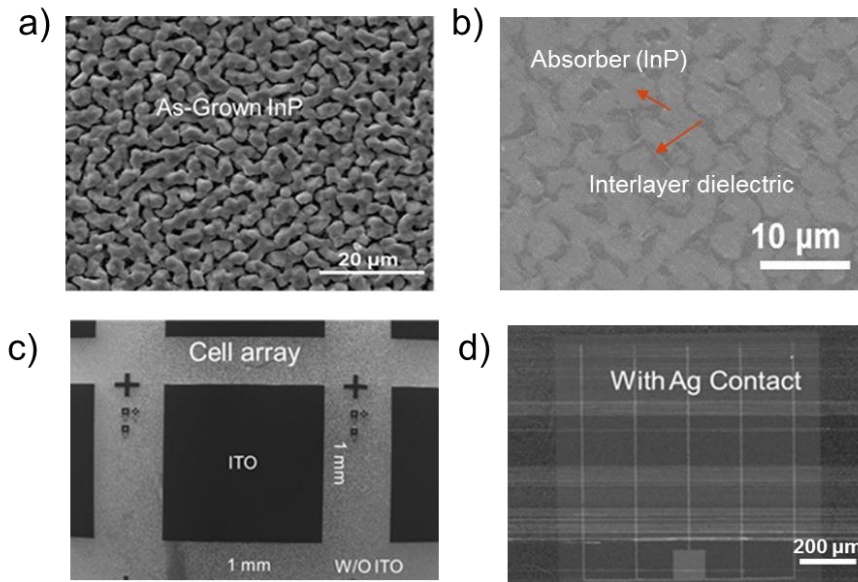
Figure 76. SEM images representing the interlayer dielectric filling; a) as grown InP pillars, b) a NP cell with spin coated dielectric layer SOG and polished, c) cell array before deposition of ITO (n-layer), d) solar cell after deposition of Ag (n-contact)

The absorptivity of naturally textured InP NP grown on quartz (reference) is compared with InP film. ITO is also included in such measurement performed by integrating sphere, since it is used as the window layer that light must pass through and reach the absorber layers (see Fig. 77).
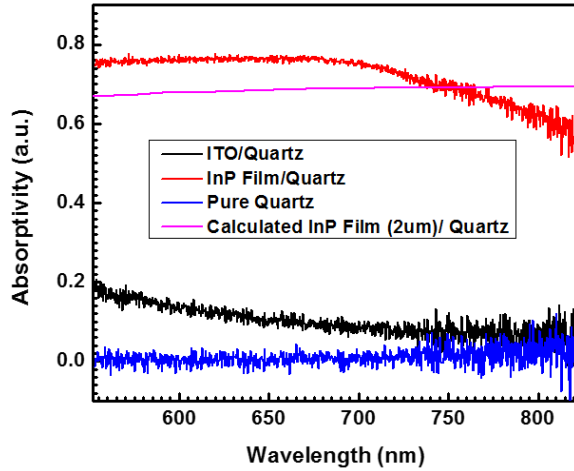
Figure 77. Absorptivity measured with integration spheres for self-textured InP film network grown at 600 °C for 1hr on quartz.

A representative top view SEM image of starting as grown InP sample and solar cell after deposition of ITO is shown in Fig. 78.
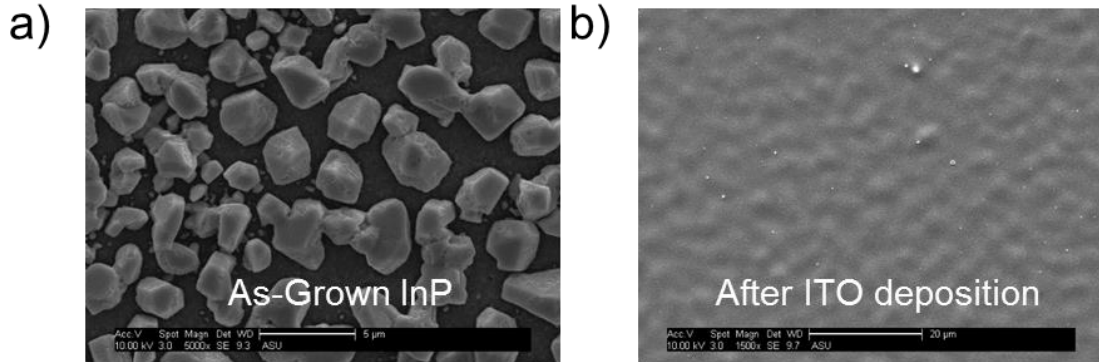
Figure 78. SEM image from solar cell fabrication steps; a) as grown InP pillars, b) a NP cell with spin coated dielectric layer (PMMA) and deposited ITO.

The schematic of the optimum cell architecture as well as the I-V characteristics of the best working device is show in Fig. 79. The NP solar cell based on Thin-film VLS InP absorber exhibit 5.29% efficiency with an open-circuit voltage (V_{oc}) of 529 mV, a short-circuit current density (J_{sc}) of 25.36 mA/cm^2, and a fill factor (FF) of 39.41% under AM1.5G solar illumination at 1-sun intensity.
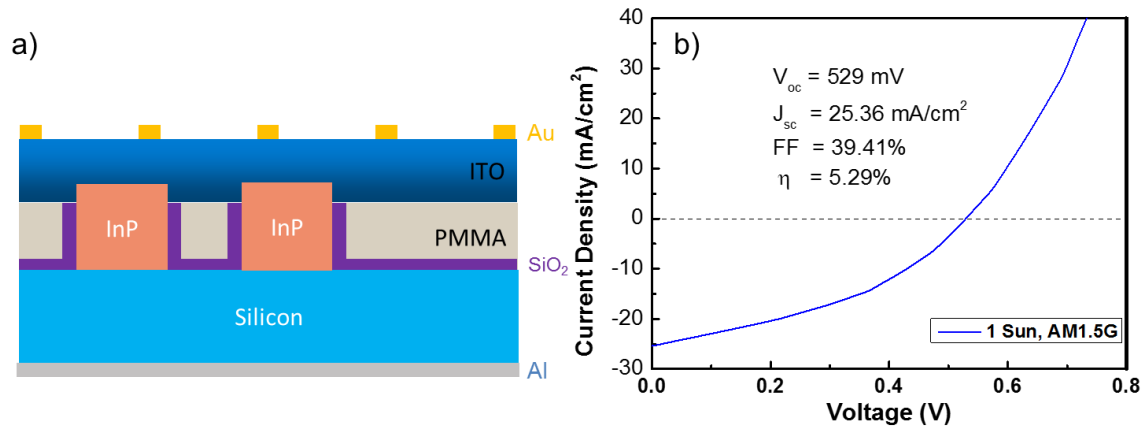
Figure 79. a) Schematic of NP-cell architecture, and b) representative J-V characteristics of best InP pillar-based solar cells with interlayer dielectric and cell configuration of ITO/n-InP/p-Si.

Although the preliminary solar cell devices based on the InP pillars on silicon substrate are demonstrated, further optimization is needed for the performance and low-cost fabrication. Especially, the improvement of the quality of ITO layer and its conformity covering all the InP pillars is needed to obtain a solar cell with a higher efficiency.

Table 6. Comparison of InP solar cell performance parameters with previous work

Device structure	V_{oc} (mV)	J_{sc} (mA/cm²)	FF (%)	Efficiency (%)	Description	Reference
ITO/InP	545	24.6	73.6	9.9	Heterojunction on InP wafer	Yin, Xingtian, et al. (2014)
ITO/TiO2/InP	785	30.8	80.1	19.2	Heterojunction on InP wafer	Yin, Xingtian, et al. (2014)
Axial InP NW	779	24.6	72.4	13.8	InP pillars, PIN homojunction on InP wafer	Wallentin, Jesper, et al. (2013)
ITO/InP/Si	529	25.3	39.4	~5.3	InP pillars, heterojunction on Si wafer	Current work

A comparison of device performance between our work and previous InP solar cells (Table 6) reveals that there is plenty of room to improve the efficiency of our solar cell. In addition, this can be achieved by further minimizing the fill factor losses and grain engineering [177] in material growth given the low cost and faster growth approach that leads to a reduced energy payback time for the final module [177, 178].

5.12 Summary

Growth of high quality III-V such as InP films using the inexpensive approaches is critical in lowering the cost of solar energy. So far, InP films have been produced mostly using the high-cost precursors using the single-crystal substrates in the case of epitaxial growth. In chapter 5, a low-cost growth of high quality polycrystalline InP thin film and nano-networks using a direct co-evaporation of single elemental In and P precursors via a chemical vapor deposition technique was demonstrated for solar cell applications. A very small deviation from the perfect stoichiometry for the films grown at a wide temperature range of 560 ∘C to 720 ∘C was observed. The proposed method was shown to be largely independent of type of substrate for both Au and self- (In-) catalyzed growth indicating the versatility of the growth approach. The underlying growth mechanism of nano-networks and coalesced thin films was explained via interplay between VLS and VS regimes. The key role that Au catalyst plays in the promotion of transverse growth was well defined. The grains size and spatial pore filling as well as the thickness of InP film was shown to be controllable by changing the growth parameters. Structural, optical and electrical properties of the grown films were investigated and eventually the preliminary solar cell devices were fabricated on a p-type silicon with an ITO contact layer. It is believed that our growth strategy provides a simpler approach for producing the high quality InP thin films to be used for fabrication of high efficiency solar cells, while lowering the cost for both precursors and growth substrate.

6 COMPOSITION-GRADED InGaAsP TERNARY ALLOY NANOWIRES

6.1 Introduction

The substrate insensitivity of NWs has led to epitaxial growth of device-quality materials on inexpensive silicon platform regardless of a large lattice mismatch [179]. More importantly, this relaxed requirement on substrate of choice for NWs allows for growth of alloys of new compositions that are not accessible by planar growth technique [11]. This flexibility provides new design space using semiconductor alloys with unprecedented access to new bandgap ranges. However, their bandgap tunability in a widely controllable wavelength range has been the main obstacle for developing novel optoelectronic devices such as tunable lasers [11], photodetectors on a single chip [12] and monolithic solar cells for dispersive concentration photovoltaics [15]. Rational design and synthesis of semiconductor alloys, monolithically [13] or on a single substrate [180], requires different concentration of source reagent and growth temperature for various alloy composition. Dual gradient method (DGM) [14] provides a unique means for growth of composition graded semiconductor alloy NWs. Combinatorial chemistry employed in DGM allows for simultaneous synthesis of materials of various composition with different enthalpy of formation. This method combines both temperature gradient and spatial source reagent gradient methods enabling us to cover a wide range of composition within a single substrate that are otherwise impossible to grow. Such growth strategy with a large range of composition control has been extensively implemented on II-VI materials [14-16]. Because of superior electrical and optical properties and existing rich knowledge in device fabrication based on III-V materials, it is of great interest to study similar possibility for III-V alloys which are largely unexplored so far. Thus far,

bandgap tuning of full composition range InGaAs [181], GaAsP [182] InGaP [84] alloy NWs has been reported. These results comprise the NWs of single compositions obtained by multiple growth runs for various alloys over the entire range between two binary compounds. In a most recent work, Kuykendall et al. have demonstrated composition-graded $In_xGa_{1-x}N$ on a single substrate over the entire range from the near-ultraviolet to the near-infrared region [180]. Composition-graded III-V subcells of various bandgap could be potentially better alternative to substitute tandem solar cells which are practically limited by expensive fabrication cost, complexity in adding the new junction and lattice-matching requirement. Full composition range of InGaAsP alloy system is able to cover a large range of bandgaps from InAs (0.35 eV) to GaP (2.25 eV), appealing for many applications such as full light-spectrum solar cells, multi spectral detector and widely tunable lasers. In the current chapter, growth and characterization of spatially composition-graded of $In_xGa_{1-x}P$, $In_xGa_{1-x}As$ and $GaAs_xP_{1-x}$ ternary alloy NWs using DMG on a single substrate will be presented in detail. It will be shown that the dual gradient approach plays an important role as an effective tool for rapidly identifying the growth parameters in terms of adjusting the temperature and source reagents gradients.

6.2 Growth of Composition-Graded InGaP

Growth of InP and GaP NWs via a facile vapor transport CVD method were presented in chapter 3 and 4, respectively. Full composition range of InGaP alloys between two III-phosphide binaries can cover a wide range of bandgaps of (1.35, 2.25) eV which can be used as a wide-bandgap subcell to design a monolithically integrated laterally arrayed multiple bandgap (MILAMB) solar cells for spectrum-splitting photovoltaic systems [15,

31, 183]. However, InGaP alloy NWs have been grown using MOCVD method, on III-V single crystalline substrate, with composition-dependent luminescence in various ranges of 755-871 nm [184], 590-760 nm [185], 574-867 nm [186]. Kornienko et al. have recently reported solution phase synthesis of InGaP in full composition range from 550 to 920 nm [84], but there is no report on integrated bandgaps of InGaP in a wide range from a single substrate. In this part, growth of composition-graded ternary InGaP alloys in a single growth run using Au-catalyzed VLS growth on a single Si substrate is presented. Here, a relatively wide range of PL emission from 580-780 nm from a monolithic single substrate is demonstrated. InGaP alloys are grown using a vapor transport method. A schematic of the growth setup is shown in Fig. 80a. As the source reagents, the high purity Indium spheres (1mm dia., 99.99% Alfa Aesar), red Phosphorous ($\geq$99.99% Sigma Aldrich) powder, ball-milled Gallium Phosphide (99.999% Alfa Aesar) powder were loaded inside two different inner mini tubes embedded inside the larger diameter quartz tube separately, giving rise to the material spatial dispersion (source gradient). A piece of silicon (111) substrate with dimension of 0.7 by 1.2 cm pre-deposited with a thin (2-3 nm) layer of Au film acting as the catalyst of VLS growth was placed at downstream side of the furnace. The substarte was in a vertical configuration facing the end of minitubes with slight tilting (0.5-1 cm) along the tube axis, such that it covered wide range of temperature from 680 ∘C to 800 ∘C (temperature gradient). The tube furnace was heated up to set temperature of 1000 ∘C and the growth was maintained for 15 min under a 50 sccm (standard centimeter cubic per minutes) flow of Ar+5% H_2 carrier gas with a
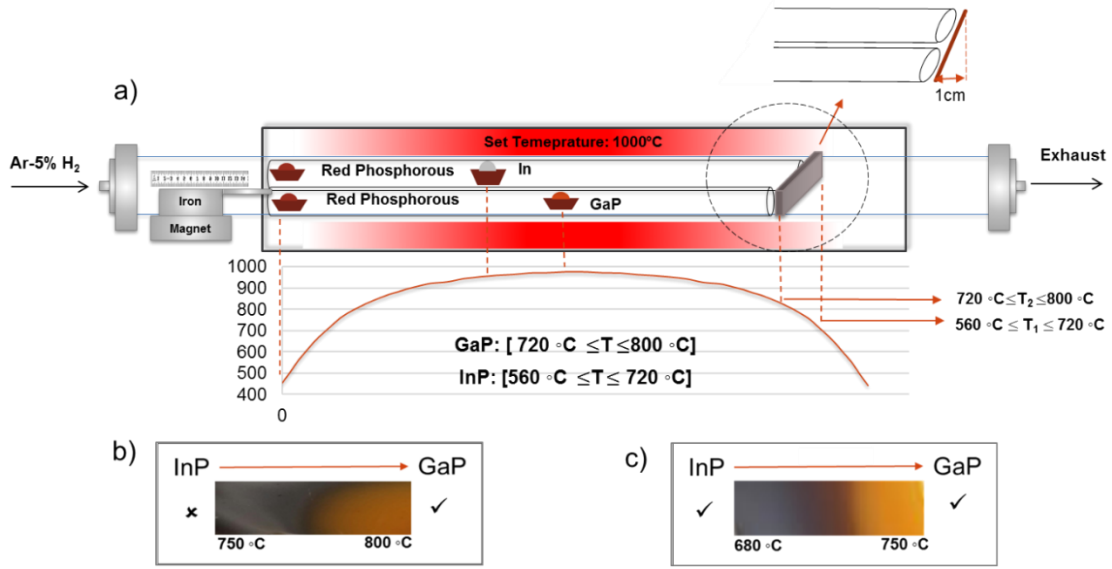
Figure 80. A schematic of growth se up for composition-graded $In_xGa_{1-x}P$ ternary alloy. The top view of the minitubes with cut out shape at a 45 ° angle is also shown. Room-color photograph of sample grown in temperature range of 750 to 800 °C (b) and 680 to 750 °C.

total growth pressure of 2.8 Torr. Excess red phosphorus boat was used to replenish the phosphorus lost from GaP source with emphasis on the effects of vastly different sublimation rates of the associated III and V elements above the congruent sublimation temperature of binary III-V (e.g., T_{cs} for InP and GaP is reported to be 571 and 268 °C) [21, 104]. After growth, the sample was kept inside the furnace to naturally cool down to room temperature. It was seen in chapter 3 that using single elemental In and P leads to growth highly stoichiometric InP with atomic percentage of close to 1:1 ([P%] =49.32 and for [In%] =50.68), while using binary InP compound results in non-stoichiometric InP with In-rich source material (97.10% In) after 15 min evaporation at 880 °C which becomes rate-limiting factor of the growth. To give an insight on importance of tempertaure optimization in such methodology for growth of InGaP, it is first required to

find the ideal growth tempretaure range for each of binary compunds of InP and GaP using vapor transport CVD method. In chapter 5, the ideal growth window for thin film-VLS InP with polycrystalline structure to be from 560 to 720 ∘C, while this range value is obtained to be 720 to 800 ∘C for VLS-grown GaP (see chapter 4). To achieve success, an overlap in growth windows of binaries is required. Hence, the right growth temperature must be selected to ensure both growths at InP- and GaP-rich sides are taking place. For instance, changing the substrate temperature range from 750 ∘C to 800 ∘C with a 0.5 cm tilting along the tube axis leads to almost no crystal growth in InP-rich region which is shown in Fig. 80b that above 750 ∘C InP is no longer stable. To successfully achieve a wide range of InGaP alloys, the sample was tilted 1cm along the tube axis rendering 70 ∘C temperature gradient from 680 ∘C (InP-rich side) to750 ∘C (GaP-rich side) As seen from the real-color image of as-grown InGaP sample (shown in Fig. 80c), the color gradually changes from grey (InP-rich region) to red, orange and eventually yellow corresponding to GaP-rich region. The temperature gradient together with material dispersion obtained by minitubes of carrying different source reagents favors different levels of formation enthalpy for alloy compositions with all needed bandgap from InP- to GaP-rich sides. Fig. 81a shows the SEM images taken from 12 representative points (marked from left to right) of composition-graded sample along the length of the sample (1.2 cm) showing the morphology changing from polycrystalline to NW (up to 10-15 μm in length) as we move from InP-rich to GaP-rich side.
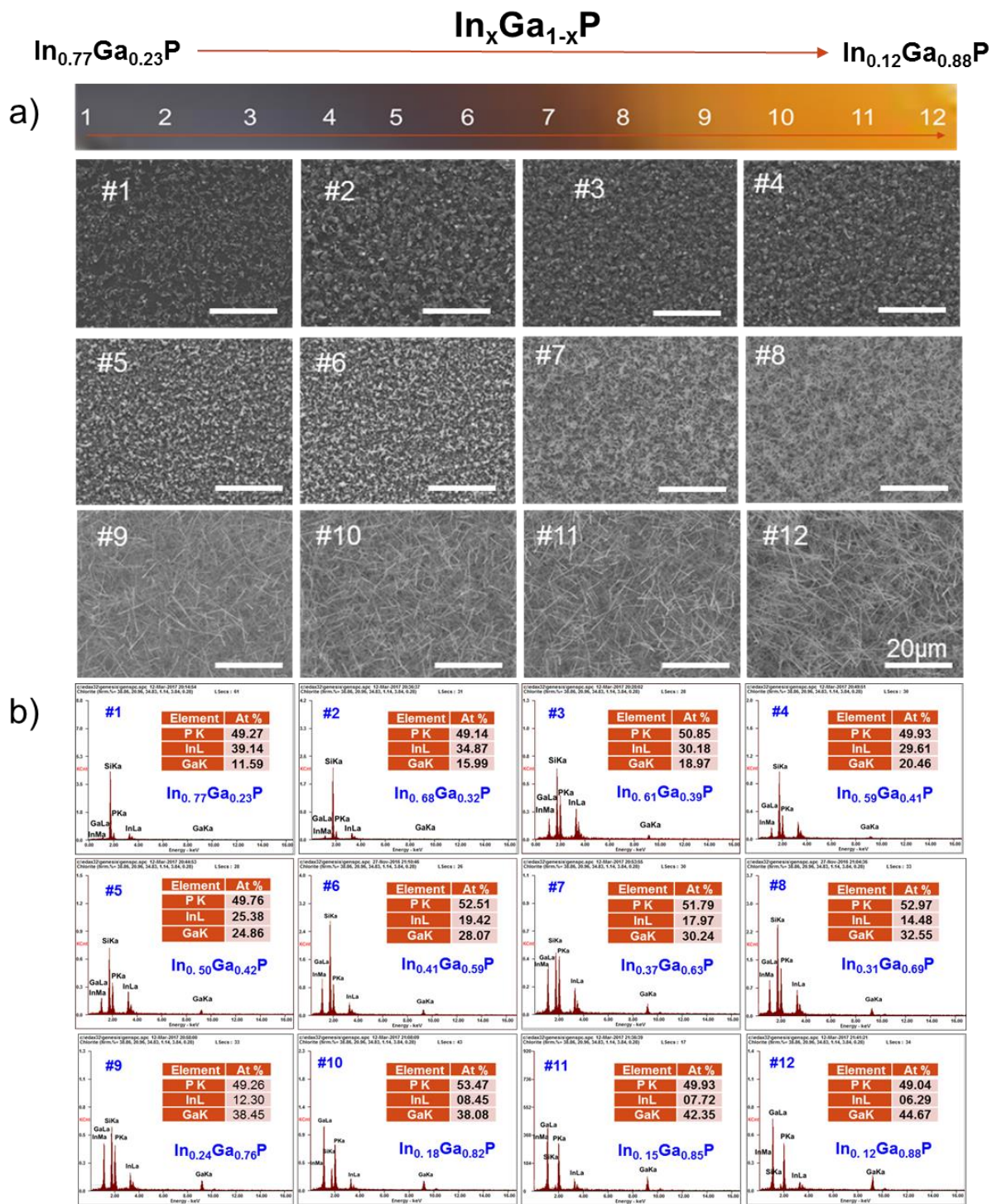
Figure 81. Position-dependent SEM and EDS of composition-graded InGaP: (a) Real color photograph of as-grown sample with color changing from grey (InP-rich) to yellow (GaP-rich) side. The SEM images are taken from the corresponding data points of In-rich (1) towards Ga-rich (12). (b) EDS elemental analysis of InxGa1-xP taken from 12 spots along the length of the substrate with indium content varying from x= 0.12 to 0.77.

The change in growth morphology indicates different growth kinetics mainly due to different level of supersaturation achieved by evaporation rate of the source reagents with different vapor pressures. It has been seen that during VLS growth the change in supersaturation level can affect the morphology of the obtained nanostructures [63,187]. Here, the lower supersaturation or vapor pressure obtained by lower evaporation rate of GaP source favors NW growth, while indium and phosphorous with a much higher evaporation rate of results in formation of polycrystalline In-rich InGaP. Likewise, the position-dependent energy-dispersive X-ray spectroscopy (EDS) spot analysis of corresponding regions reveals that In content varies from x= 0.12 to 0.77 (Fig. 81b).

6.2.1 Position-Dependent PL

To examine the optical quality of sample, an Nd: YLF laser (Spectra Physics, $\lambda = 349$ nm, repetition rate of 10 Hz, pulse width of 5 ns) with a beam spot size of ~ 100 μm was used as the optical pumping source for photoluminescence (PL) data acquisition at room temperature. From the refined PL measurement of different points along the length of the sample a strong emission with a gradual variation in wavelength from 578 nm composition, to 781 nm was observed (Fig. 82a). The width of PL peak or FWHM (full width at half maximum) is often indicative of the crystal quality of optical material. Broadening of PL linewidth might be due to existence of defects or possible inhomogeneity of alloy composition. Continuous PL mapping along the length of the sample also showed presence of broad peaks for In-rich intermediate compositions. As seen from normalized PL spectra, the narrow peaks at the two ends indicate high alloy quality. In addition, the red-shifted peaks at Ga-rich ends are due to known defect band emission. In order to understand the composition dependency of PL characterstics or

other physical quantities such as lattice constant, etc., the Vegard's law is used to calculate the composition of InGaP using below formula;

$$Q(In_xGa_{1-x}P) = x.Q(InP) + (1-x).Q(GaP) - bx(1-x) \qquad (6.1)$$

,where Q is the physical quatity, x is the fraction of x in composition of ternary alloy, and b is the quadratic coefficient called bowing parameter which describes the deviation from linearity. The wavelength values obtained from the central PL peak position and those from linear bandgap interpolation (b≅ 0) using EDS results by Vegard's law show a good overall agreement (Fig. 82b).
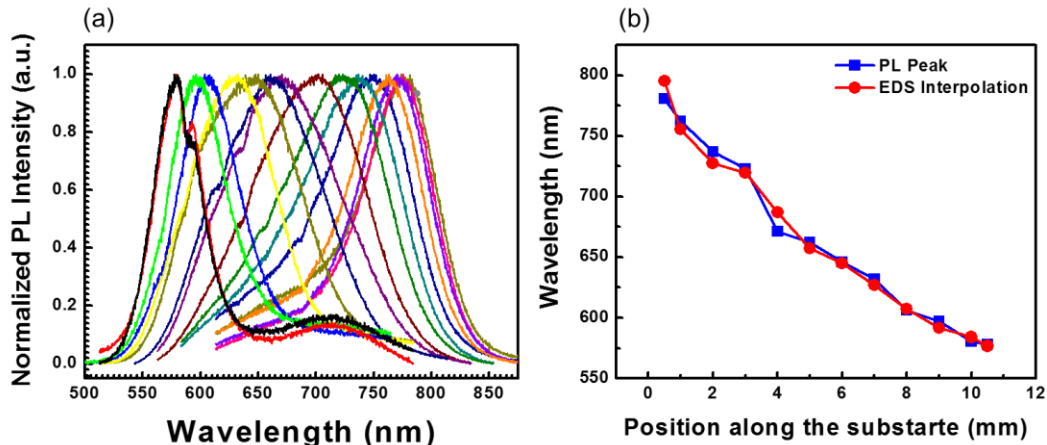
Figure 82. a) Normalized position-dependent PL spectra along the grading direction of InxGa1-xP with increase in indium content with central wavelength ranging from 578 to 781 nm. b) position-dependent PL peak wavelength (blue squares) and wavelength values obtained from interpolated EDS compositions (red circles).

6.2.2 Position-Dependent XRD

In order to determine the crystal quality/structure of as grown alloys across the entire length of the sample, the selected-small area high resolution X-ray diffraction (XRD) was utilized. For the precise measurement, a 1/16° narrow slit was used to shrink the size of

the striking x-ray beam to ~20 μm (spatial resolution), which was smaller than the beam

size of laser (~ 100 μm) used for PL measurement. All the XRD patterns shown in Fig.

83 are obtained by a point to point mapping along the length of the sample which match

with the cubic zinc blende(ZB) structure with (111) diffraction peak representing the

main crystallographic plane of InP and GaP. From InP-rich to GaP-rich end, the (111)

peak gradually shifts towards larger values of diffraction angle (2θ) indicating the

formation of intermediate InGaP alloys with decreased lattice constant. Presense of the

double peaks as we move towards InP-rich side is regarded as an indicator of phase
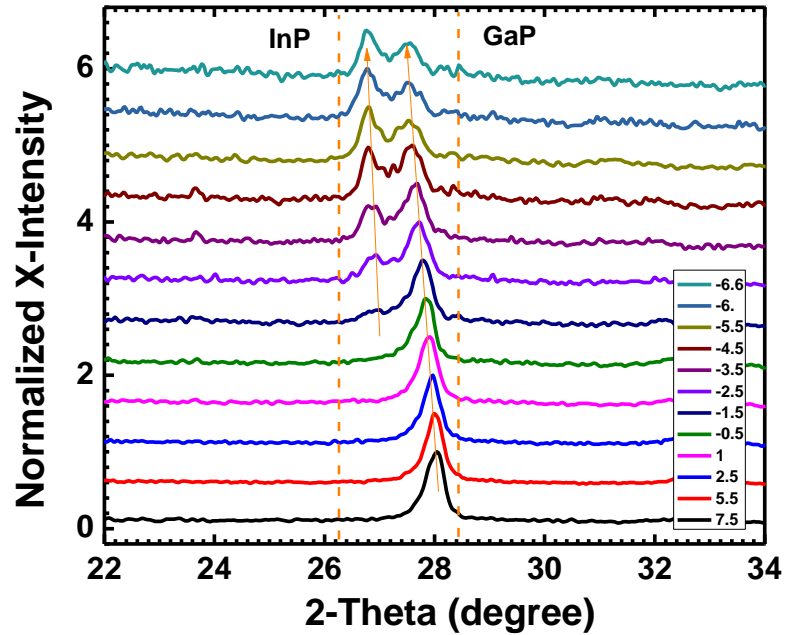
Figure 83. Position-dependent full range XRD patterns of composition-graded In$_x$Ga$_{1-x}$P obtained by mapping across the length of the 1.2 cm sample. Resolved (111) peaks showing a gradual peak shifting form InP- to GaP-rich. All the XRD patterns are normalized between 0 and 1. The legend shows the position of the corresponding points in mm across the length of the substrate.

segregation of InGaP alloys. Observation of phase separation for a wide range of

composition is due to the large differences in lattice constants of InP (5.8687 Å) and GaP

140

(5.4505 Å) which can result in separation of InGaP alloys into different phase domains caused by an internal lattice strain. The majority of III-V alloys are predicted to show phase seperation at relatively low growth temperatures [188, 189]. Among them, for pseudobinary $In_xGa_{1-x}P$ alloy system it is shown that the immiscibility occurs slightly below 650 ◦C [189, 190], while our growth temperature range is from 680 ◦C to 750 ◦C, it is not expected to see such phase sepration at low growth temepartures. Phase separation in III-V NWs have been also extensively reported in form of core-shell ternanry alloy NWs that are enriched in group-III elements (In, Ga, Al, etc.). Formation of such nanostructures are attributed to role that Au catalyst plays under different precursor flow rate or difference in diffusion lengths for the different growth species [191-193]. Nicholas et al. showed that the rapid cooling immediately after the growth can lead to a high-quality uniform alloy while unassisted natural cooling leads to the formation of axial or core−shell heterostructures, containing segments of different phases [194]. Therefore, it seems to be essential for the as grown sample to be quenched rapidly to the room temperature to obtain a homogenous, single phase $In_xGa_{1-x}P$ alloy. Since phase segregation of the alloys leads to formation of multiple domains with different compositions, the lattice constant and composition of each phase associated with two adjacent peaks was determined.

6.2.3 XRD Two-Peak Fitting

A Gaussian function was used for a two-peak fitting by Origin to define the center and FWHM of the peaks. Fig. 84 displays the fitted double peaks in a magnified scale. The corresponding (111) peaks to the In-rich and Ga-rich are referred to as InP-like and GaP-like alloys. The composition of each component (x_1 and x_2 is calculated using Vegard's law by taking the relative intensity of InP and GaP into account. From Bragg's law using the intensity of resolved InP-like and GaP-like (111) peaks, the cubic zincblend lattice constant (a) is calculated to be varying from 5.5048 to 5.7444 Å from GaP- to InP-rich side with a corrosponding In content changing from x=0.13 to x=0.70 obtained from interpolation using Vegard's law approximation.

Figure 84. Double peak fitting of XRD patterns taken from different points of the composition graded InGaP sample with the magnified scaled InP- and GaP-like (111) peaks. The (blue) pattern is fitted using Gaussian function. The red line represents the sum of the resolved black peaks. The weighted average of In-composition is given by the black numbers (top right). The composition of each (separated) phase is written above the corresponding peak.

In order to precisely detremine the weighted In content, the composition and fraction (relative intesity) of both peaks were used to estimate the composition of each spot . Detailed calculation and data processing is explained as follows;

142

Interplanar spacing for (111) planes in cubic zinc blende structure and lattice constant can be obtained from the formula below:

$$\text{From Bragg's law: } n\lambda = 2d\sin\theta \tag{6.1}$$

$$d_{(hkl)} = \frac{a}{\sqrt{h^2 + k^2 + l^2}} = \frac{a}{\sqrt{3}} \tag{6.2}$$

$$a = \frac{1.541874 \times \sqrt{3}}{2\sin(\theta(°) \times \frac{\pi}{180})} \tag{6.3}$$

By using the Vegard's law and known lattice constant values of 5.8687 and 5.4505 (Å) for InP and GaP with relative intensity ratio (RIR) of 14.09 and 8.31, respectively, the lattice constant of alloys can be obtained from XRD spectra.

Table 7. Resolved single and double peak obtained from position dependent XRD spectra.

Spectrum #	Single peaks			
	(111) Peak Position	d-spacing (Å)	a(Å)	Composition (In%)
1	Double	Double	Double	Double
2	Double	Double	Double	Double
3	Double	Double	Double	Double
4	Double	Double	Double	Double
5	Double	Double	Double	Double
6	Double	Double	Double	Double
7	Double	Double	Double	Double
8	Double	Double	Double	Double
9	27.85	3.203540228	5.548694439	23%
10	27.94	3.19342534	5.531174939	19%
11	28.02	3.184489445	5.515697515	16%
12	28.08	3.177821288	5.504147928	13%

The results are summarized in table 7 for both single and double peaks: The In content (%) for the single peaks can be estimated simply by obtaining the lattice constant from

Bragg's law and subsequent Vegard's law interpolation. The peak position and corrosponding lattice constant of double peaks are summarzaized in table 8.

Table 8. Peak position and lattice constant for InP- and GaP-like peaks.

Spectrum #	Double peaks			
	InP peak position	GaP peak position	Lattice constant based on InP peak	Lattice constant based on GaP peak
1	27.079	27.76	5.70359977	5.566328718
2	26.9299	27.712	5.734589968	5.575780986
3	26.845	27.6597	5.752391609	5.586117749
4	26.8062	27.5709	5.76056501	5.603759245
5	26.7796	27.5424	5.766182239	5.60944557
6	26.7211	27.3848	5.778575639	5.641105807
7	26.7153	27.3423	5.779807372	5.649706735
8	26.7034	27.3299	5.782336239	5.652221274

For double peaks, the relative intensity ratio (RIR) should be taken into account for the quantitative analysis of each phase based on weight fraction of each phase. This means after determining the composition for each peak with InP- or GaP-like characteristics, both intensity and composition should be normalized with respect to the RIR of InP and GaP.

$$\text{For InP-like peak (peak 1): } I_1^R = x_1 * 14.09 + (1 - x_1) * 8.3 \qquad (6.4)$$

$$\text{For GaP-like peak (peak 2): } I_2^R = x_1 * 14.09 + (1 - x_1) * 8.31 \qquad (6.5)$$

Modified Intensities can be obtained from the raw intensity with respect to RIR of each peak (see table 9) as follows;

$$\text{For InP-like peak (peak 1): } I_1^m = \frac{I_1}{I_1^R} \qquad (6.6)$$

$$\text{For GaP-like peak (peak 2): } I_2^m = \frac{I_2}{I_1^R}, \qquad (6.7)$$

where I_1 and I_2 are the intensity of InP-like and GaP-like peaks from XRD spectrum, respectively.

Table 9. Modified relative and raw intensities for InP- and GaP-like peaks.

InP-like peak		GaP-like peak		InP-like peak		GaP-like peak	
In % from VL (X1)	Converted RIR (I_1^R)	In % from VL (X2)	Converted RIR (I_2^R)	In. from spectrum (I_1)	Modified Intensity (I_1^m)	In. from spectrum (I_2)	Modified Intensity (I_2^m)
0.605212267	11.8081269	0.276969676	9.910884726	32.9	2.786216668	194.3	19.60470789
0.67931604	12.23644671	0.299571941	10.04152582	41.04	3.353914823	172.81	17.20953599
0.721883332	12.48248566	0.324289214	10.18439166	46.71	3.742043154	96.72	9.496885359
0.74142757	12.59545135	0.366473565	10.4282172	48.56	3.855360053	96.76	9.27867133
0.75485949	12.67308785	0.380070709	10.5068087	50.304	3.969356212	37.45	3.56435537
0.784494593	12.84437875	0.455776678	10.9443892	903.9	70.37319732	950.3	86.82987993
0.787439913	12.8614027	0.476343222	11.06326382	596.7	46.39462849	463.6	41.90445129
0.793486941	12.89635452	0.482355988	11.09801761	307.5	23.84394749	108.6	9.785531418

The next step is to apply the Vegard's law on the modified intenisty ratios to obtain the weighted value of In content for each set of double peaks, as shown below:

$$\text{Modied intensity ratio: } R_m = \frac{I_2^m}{I_2^m + I_1^m} \tag{6.8}$$

$$\text{Vegard's law: weighted In content: } x = x_1 * R_m + (1 - R_m) * x_2 \tag{6.9}$$

The final weighted values obtained from last 8 peaks are summarized in table 10. The trend of In content obtained from the resolved XRD peaks (x=0.13 to 0.70) fairly matches with EDS and PL.

Table 10. Weighted indium content from XRD two-peak fitting

Spectrum #	Intensity ratio(Ga/In)	Overall composition	a(Å)
1	0.875564912	0.317814571	5.583410054
2	0.836899222	0.361508499	5.601682854
3	0.717345467	0.436670993	5.633115809
4	0.706460268	0.476537463	5.649787967
5	0.473120763	0.577539136	5.692026867
6	0.552342113	0.602929845	5.702645261
7	0.474574043	0.639801498	5.718064987
8	0.290980763	0.702953819	5.744475287

6.2.4 PL Two-Peak Fitting

To further analyze the composition of segregated phases, the broad PL peaks was also resolved using a Gaussian function into two peaks similar to XRD peak treatments (Fig. 85).
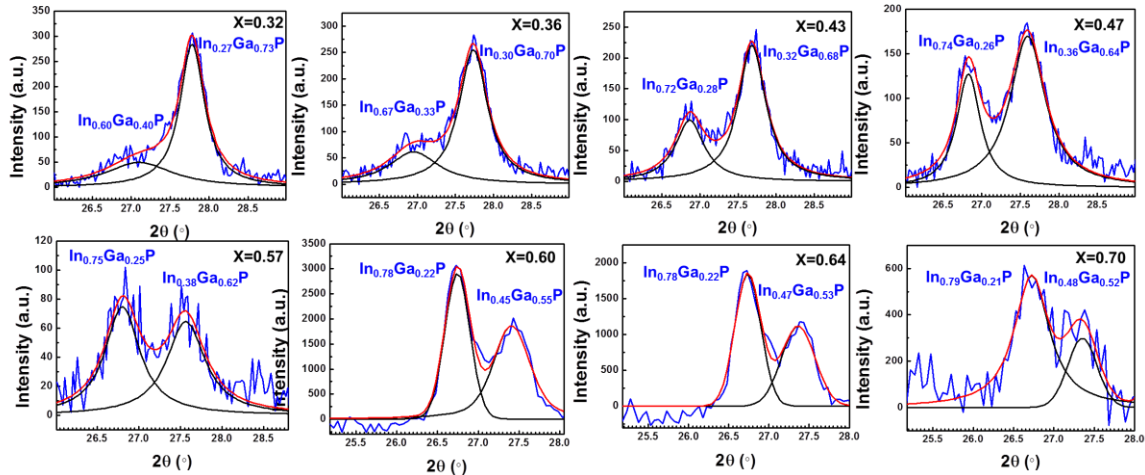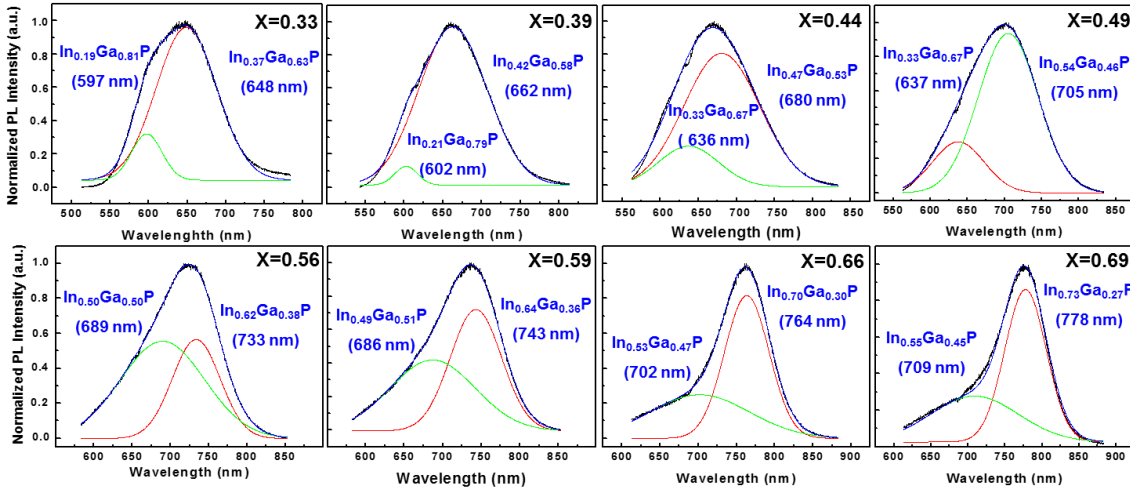

Figure 85. Double peak fitting of PL spectra taken from different points of the composition graded InGaP sample with the InP-like and GaP-like phase emission peaks. The blue line represents the sum of the resolved black peaks. The weighted average of In-composition is given by the black numbers (top right). All the peaks are fitted using a Gaussian function. The composition and interpolated emission wavelength (using Vagard's law) of each phase is written above the corresponding peak.

Composition of each InP- and GaP-like peak with calculated corresponding emission wavelength using the Vegards's law is shown next to the fitted green and red peaks.

More details of the calculation to obtain the weighted average of In-composition (black numbers at the top right of each spectrum) using two peak fitting for PL spectra with intermediate compositions are shown below in table 11. The weighted In content values are obtained from $\lambda_{ave} = \lambda_1 * I_1 + \lambda_2 * I_2$, where λ_{ave} is obtained from the normalized intensity of the InP- and GaP-like peaks. However, the beam size of X-ray was around 20 μm vs.

50-100 μm for Nd-YLF laser beam and ~10 nm electron beam size used for EDS acquisition.

Table 11. Weighted indium content from PL two-peak fitting

Spectrum #	GaP-like peak position (λ_1)	FWHM (nm)	x1 (In content)	normalized Intensity (I_1)	InP-like peak position (λ_2)	FWHM (nm)	x2 (In content)	normalized Intensity (I_2)	λ_{ave} (nm)	Weighted In Content
1	597	39	0.19	0.25	648	78	0.37	0.75	635.25	0.33
2	602	29	0.21	0.12	662	88	0.42	0.88	654.91	0.4
3	636	77	0.33	0.22	680	99	0.47	0.78	670.36	0.44
4	637	69	0.34	0.24	705	80	0.55	0.76	688.55	0.5
5	689	68	0.5	0.5	733	74	0.62	0.5	711.2	0.56
6	686	109	0.49	0.37	743	66	0.65	0.63	722	0.59
7	701.81	130	0.54	0.24	763.95	58	0.7	0.76	749.29	0.66
8	708.74	119	0.56	0.24	777.6	56	0.73	0.76	760.78	0.69

This means the probed areas for each technique are not the same and more specifically for the XRD and PL, the data is not obtained from the same number of NWs. For better matching between XRD and PL/EDS results, the Synchrotron XRD (micro XRD) measurement is needed.
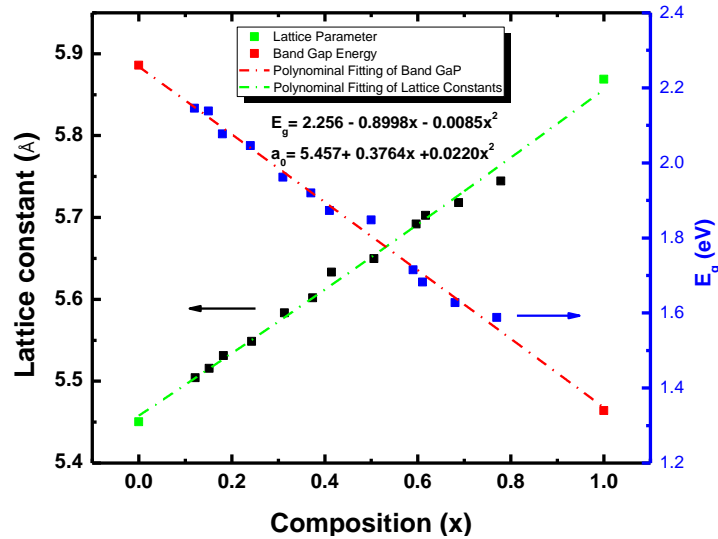
Figure 86. The lattice constant and bandgap energy of InGaP alloys obtained from Vegards's law. Black and blue squares are obtained from interpolation of PL and XRD results. The red and green dashed-lines are the curves obtained by polynominal fitting.

147

All the interpolated values for In contents averaged out from XRD lattice constant and PL emission wavelength (λ_{ave}) value that are obtained by considering the fact that there is not much of deviation from linear interpolation using the Vegard's law. Fig. 86 describes such dependency clearly in accordance with the Vegard's law. The fitted polynomial equations show values of 0.0085 and 0.0220 as the estimated bowing parameters for the bandgap and lattice constant obtained by interpolation, respectively. The fitted curves indicate that both lattice parameters and bandgap of ternary alloys $In_xGa_{1-x}P$ almost matches with the linear interpolation obtained by Vegard's law.

6.3 Growth of Composition-Graded InGaAs

As an important III-V ternary alloy semiconductor, full composition InGaAs with tunable bandgap ranging from 0.35 eV (InAs) to 1.42 eV (GaAs) can cover the near-infrared (NIR) to mid-infrared (MIR) wavelength region (~870 to 3550 nm) . Their high electron mobility has made them of particular interest to optoelectronic research for different applications such as IR photodetectors and lasers, III-V transistors, and photovoltaic solar cells. Growth of InGaAs NWs has been numerously reported via MOCVD [195, 196] and MBE [197, 198]. There are also a few reports on successful vapor phase growth of InGaAs, NWs, but among them the full-composition InGaAs has been only reported for single compositions obtained on different substrates [181, 199]. Here, an unprecedented successful growth of $In_xGa_{1-x}As$ covering a wide bandgap ranging from ~930 to 1980 nm emitting wavelengths will be presented. The detailed experimental growth procedure as well as characterization of the as grown sample is described below.

6.3.1 Growth Procedure

A rectangular piece of Si (100) substrate coated with 1-3 nm Au film as the catalyst for VLS growth. The schematic reprenstative diagram of growth set up for dual gradient growth is shown in Fig. 87. For growth of composition-graded $In_xGa_{1-x}As$ alloys first two quartz minitubes with 0.5 inch diameter were placed horizontally inside a 1.5 inch diameter furnace tube for transporting the source materials vapor to reaction zone. Prior to growth, the minitubes were loaded with high-purity InAs and GaAs (Alfa Aesar 99.999%) with excessive As powder (Sigma Aldrich, 99.999%), separately, for spatial dispersion of the materials (source gradient). Then the Au-sputtered substrate was placed in a vertical configuration facing the end of minitubes with slight tilting (0.5-1 cm) along the tube axis such that it covered wide range of temperature (650-680∘C)(temperature gradient) . Ar+5% H_2 with flow rate of 45 sccm (standard cubic centimeter per minutes) was used as carrier gas and the pressure of the reactor was kept constant around 3 Torr After the furnace reached the target temperature of 1000 ∘C with a ramp-up rate of 42∘C/min, the source minitubes were pushed inside the furnace using a magnetic manipulator where evaporation temperature of GaAs , InAs was 980 and 840 ∘C, respectively. After growth for 30 min the system was naturally cooled down to room temperature.
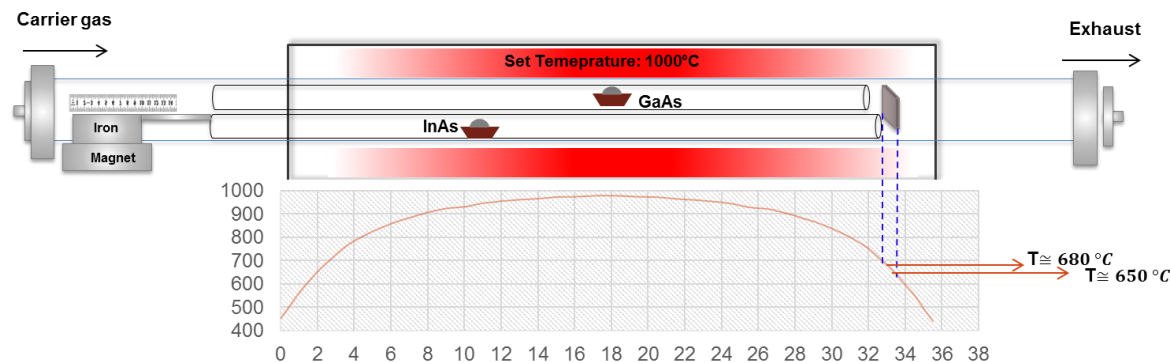
Figure 87. Schematic of dual gradient growth setup for composition graded InGaAs alloy nanowires with tube configuration and temperature profile of CVD reactor.

6.3.2 Result and Discussion

Fig. 88a shows the real-color photograph of the as-grown composition-graded InGaAs sample with a color changing from black (on the GaAs side) to gery (on the InAs side). Scanning Electron Microscopy (SEM) images taken from five representative points from GaAs-rich to InAs-rich along the length of the sample showed that NWs were grown in several tens of microns and diameter of 200-300 nanometers with Au tip as an evident sign of Au-catalyzed growth. The morphology of the wires are almost uniform for entire sample with lower density of NWs on the InAs-rich side (Fig. 88b). Fig. 88c shows the quantitative Energy Dispersive Spectroscopy (EDS) results of single NWs reavealing an obvious change in In content from GaAs-rich (x=0.07) to InAs-rich (x=0.84) side of the substrate indicating material dispersion along the substrate. This can be visually inferred from EDS spectra aquired from some of selected point of sample (indicated by high-energy Nd:YAG laser beam cut) with an obvious change in In peak intensity dominatly over Ga by moving from left to the right. Si peak in EDS spectrum originates from the substarte.
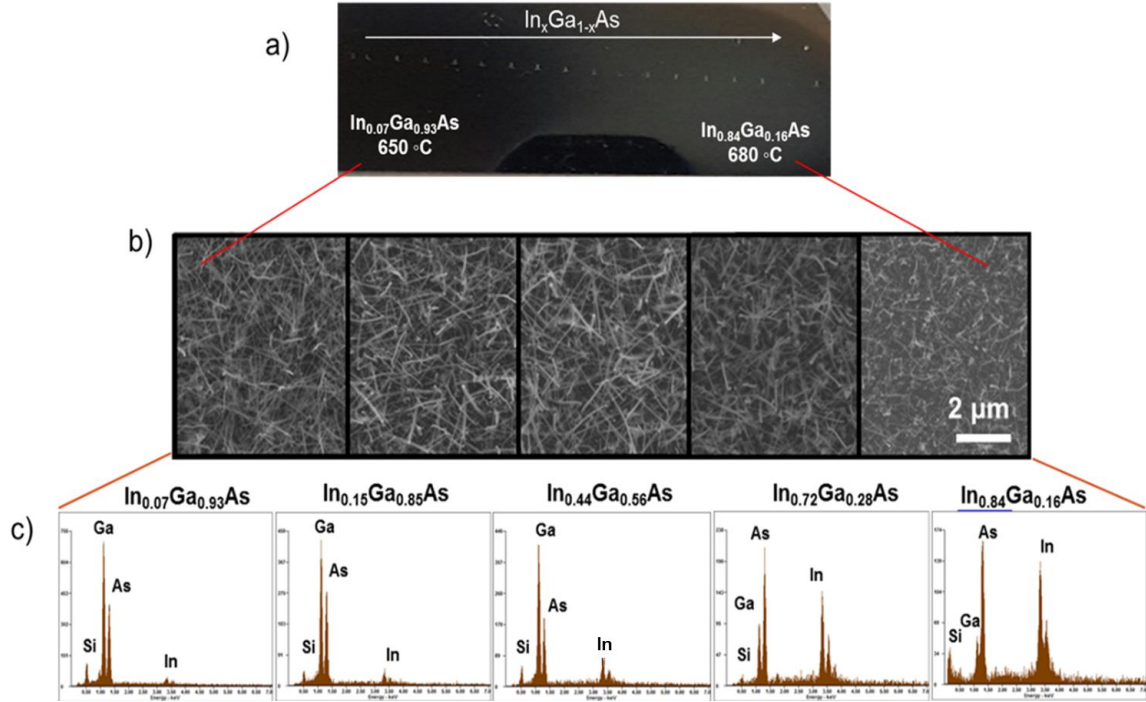
Figure 88. Position-dependent SEM and EDS of composition-graded InGaAs: Real-color photograph of as-grown sample (a), SEM micrographs taken from five representative points from GaAs-rich towards InAs-rich InGaAs alloy NWs (b), position-dependent representative EDS spectra along the grading direction of $In_xGa_{1-x}As$ with increase in In content ($0.7 \leq x \leq 0.84$).

Fig. 89 shows a representative SEM image of each sport showing the upside-down T-mark (Fig. 89b) on each point marked with a step size of 2 mm using Nd:YAG laser . EDS spot analysis was performed on A and B spots and the numbers were averaged out, representing the composition of each spot (Fig. 89c). Selected-area high resolution XRD with a beam size of a few micron was utilized to determine the crystal quality across the entire length of the sample. For the precise measurement a narrow,$1/16°$, slit was used to shrink the size of striking x-ray beam to a comparable scale with the size of the laser-marked spots. The XRD patterns obtained from diffrenet spots, matches with the cubic zinc blende (ZB) structure with three mean peaks corrosponding to (111), (220) and (311) crystallographic planes of GaAs and InAs (Fig. 90a).
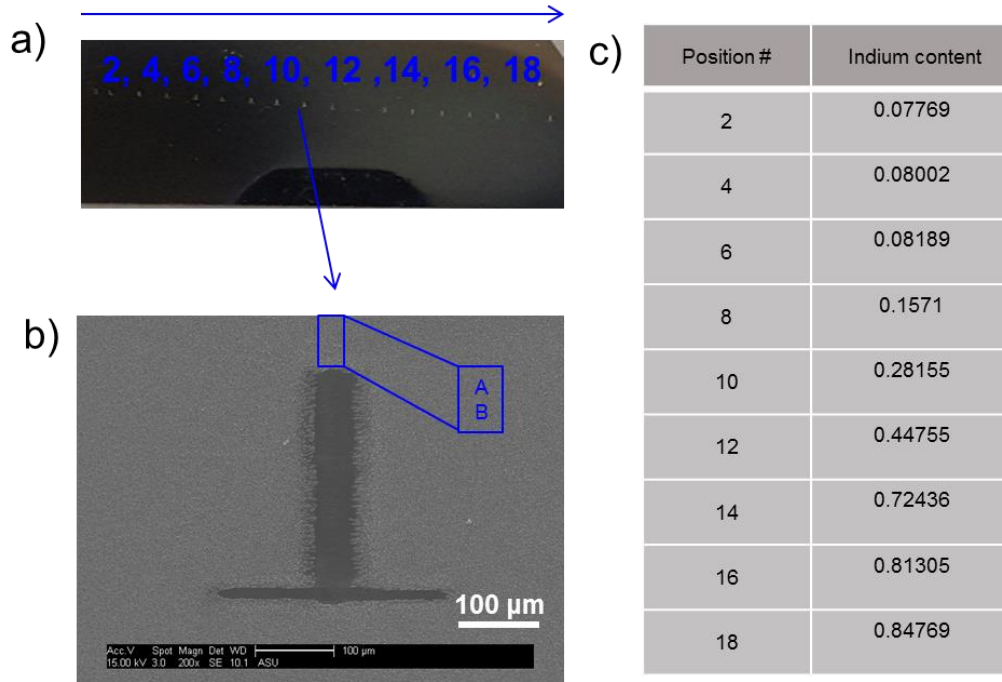
Figure 89. SEM and EDS data acquisition: A photograph of the as grown sample that is marked with step size of 2 mm using Nd:YAG laser (a). SEM image of each spot shows the upside-down T-mark on each point. EDS spot analysis was performed on A and B spots and the numbers were averaged out represent in the composition of each spot (c).

All of the peaks gradually shift towards higher value of diffraction angle, 2θ, by decreasing the In content, apparently due to a decrease in lattice constant. This results are consistent with those reported by Jung et al. [181]. From bragg's law using the main resolved (111) peak (Fig. 90b) the cubic lattice constanct (a) is calculated to be varing from 5.68 to 5.97 Å from GaAs- to InAs-rich side. From the linear interpolation between the lattice constant of pure InAs and GaAs using the Vegards's law approximation the In content in ternary $In_xGa_{1-x}As$ alloys wa calculated to be varying from x=0.06 to x=0.78. In order to investigate the optical quality of the NWs PL measurements was performed at room temperature using a Ti-Sapphire laser (Spectra Physics, Tsunami, , $\lambda = 810$ nm, 150

fs pulse duration) as an excitation source for NIR wavelength range. The position-dependent normalized photoluminescnce (PL) spectra (Fig. 91a) of $In_xGa_{1-x}As$ NWs along the length of the sample showed that every spot has different emission wavelength which is broadly tuned from GaAs-rich (~930) to the InAs-rich (1980 nm) region.
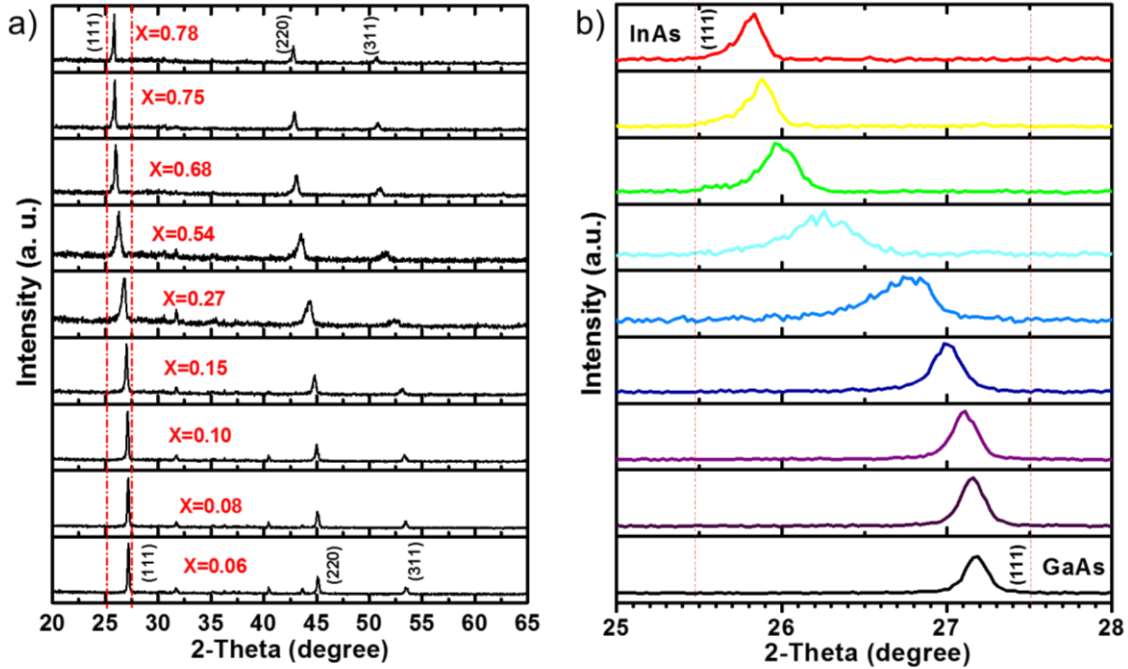
Figure 90. Position-dependent full range XRD pattern taken from composition-graded InxGa1-xAs (x=0.05 to x=0.78) obtained by mapping across the length of the sample with a step size of 2mm(a), Resolved (111) peaks showing a gradual peak shifting form InAs- to GaAs-rich (b)

The broad band emission can be described by poor surface quality of the arsenide-based NWs [200,201]. The existance of a large density of chemisorbed oxygen on the surface or other surface native defects such as dangling bonds are known to be responsible for such detrimental impact on optical and electronic properties of NWs. Sun et al. studied the removal of surface states and recovery of weak band-edge emission for InAs NWs by chemical surface passivation. They observed a quite dramatic change in linewidth

153

narrowing by such treatment [202]. Thus, similar passivation might help for improving the PL emission properties of our InGaAs alloy NWs.
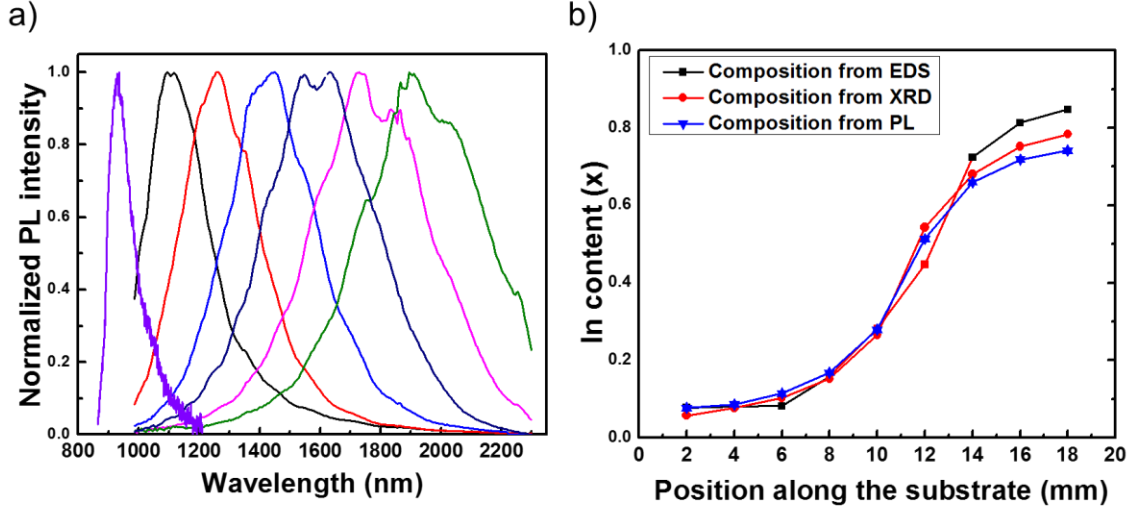
Figure 91. Normalized position-dependent PL spectra acquired from different points across the length of the composition-graded InGaAs (a), ternary alloy composition obtained using linear interpolation by Vegard's law for both PL and XRD which are in close agreement with EDS results; broadly tuned emission wavelength range (~930-1980 nm) obtained by PL mapping (b).

In order to understand the composition dependency of PL characterstics or other physical quantities such as lattice constant, etc., Vegard's law is used to calculate the composition of InGaAs using formula below

$$Q(In_xGa_{1-x}As)= x.Q(InAs)+ (1-x).Q(GaAs), \qquad (6.10)$$

where Q is the physical quatity and x is the fraction of x in composition of ternary alloy. The results obtained by PL and XRD are in a very close agreement with EDS elemntal analysis result (Fig. 91b) with the exception of last EDS elemntal mapping data point showing slightly (~6%) higher In content than the value obtained by XRD lattice constant obeying the Vegard's law. This might be due to phase segregation of indium in In-rich InGaAs alloys occuring during the cooling down process at room temperature or the fact

that acquisition area from ensemble of NWs for PL and XRD is differet from due to diffrenece in spot size of the x-ray and laser beam (in order of micron range) with electron beam (nanometer size).

6.4 Growth of Composition-Graded GaAsP

In continuation of our focus on growth of subcells of variable composition for design of LAMB solar cell successful growth of composition graded $GaAs_xP_{1-x}$ alloy NWs on a single substrate was also demonstrated. GaAs and GaP have both shown to have similar low vapor pressure that makes the growth of such composition graded alloys difficult. As the source material ball milled GaP and GaAs were loaded inside the separate minitubes with excess P and As with evaporation temperature of 400 ∘C and 300 ∘C, respectively. The evaporation temperature of GaAs and GaP were 980 ∘C. By a 0.5 cm tilting of substrate corresponding to 20 ∘C (780 to 800 ∘C), an emission wavelength variation from 685nm (at the GaP side) to 750nm (at the GaAs side) is achieved (Fig. 92a and 92b). Photoluminescence (PL) mapping on as-grown alloy NWs were performed at room temperature. Position-dependent PL of the $GaAs_xP_{1-x}$ shows better optical characteristics (narrower linewidth) compared to $In_xGa_{1-x}As$ alloys, possibly due to improved surface quality and reduced surface states by incorporation of GaP into alloy system. Fig. 93 shows the position-dependent SEM and EDS taken from five different representative points across the sample from GaAs- to GaP-rich (1 to 5).
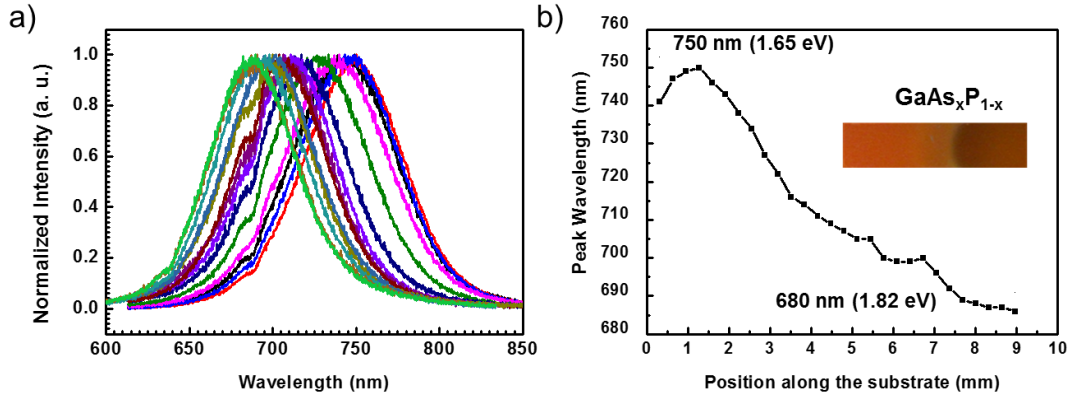
Figure 92. Normalized position-dependent PL spectra along the grading direction of GaAsP alloy nanowires under Nd-YLF laser pumping with wavelength variation from 685nm (at the GaP side) to 750nm (at the GaAs side) (a). PL peak wavelengths as a function of substrate length coordinate with an embedded real color photograph of as-grown sample with color changing from orange (GaAs side) to brown (GaP side) (b)

The size of the NWs is larger for the GaAs-rich side (2μm) than the GaP-rich side (10μm) that is because of the slightly lower vapor pressure of GaAs compared to GaP (Fig. 93a).
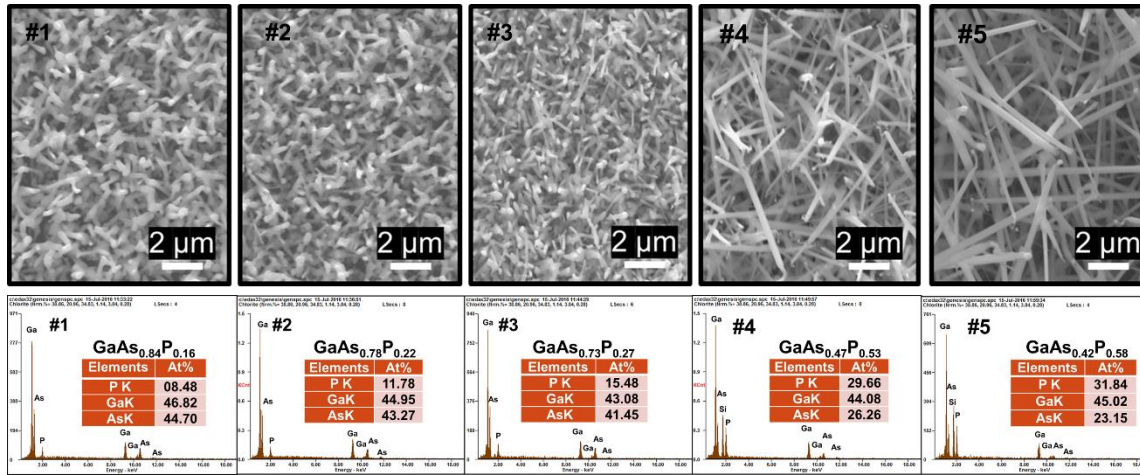
Figure 93. Position-dependent SEM and EDS of GaAsP alloys from five different representative points of composition-graded $GaAs_xP_{1-x}$ ($0.42 \leq x \leq 0.84$)

From the real color image of the as grown sample, the reason that (in spite of our expectation) the GaP side looks darker than GaAs rich side is due to the fact that GaP rich side is denser and able to trap the light better. This can be referred as higher VLS

156

growth rate of GaP compared to the GaAs. Further control over the spatial composition grading, temperature gradient, configuration of minitubes and evaporation rate and can result in improved crystal quality and more refined composition-bandgap grading.

6.5 Summary

In this chapter, growth of spatially composition-graded InGaAsP alloy NWs with a widely tunable bandgap on the single substrate was shown. The low-cost dual gradient method in combination with metal-catalyzed VLS approach was utilized to provide both source material dispersion and temperature gradient across the length of the substrate to grow InGaP, InGaAs, and GaAsP alloys with spatially-graded bandgaps. A series of different growth experiments were performed in our homemade CVD setup to find the optimum growth parameters and more specifically the growth window of such materials. Further extension of the range of achievable alloy composition and the associated alloy uniformity is the goal of future investigation. Such unique material capability provides a III-V platform for application in a wide range of novel devices from full spectrum solar cells, multispectral detector, tunable nanolasers, and spectrometer on a chip.

7 TEMPLATED NANOWIRE GROWTH

7.1 Introduction

Ever since the nanowire research has become the center of attention for optoelectronic application, a good control over the size, position, growth directional of NWs using bottom-up VLS growth has been extensively investigated [203-205]. But, when a large throughput is required, especially for solar cell applications, such methods are not realistically useful, mostly due to lattice-matched substrate requirement for epitaxial growth of vertical NWs. As shown in previous chapters, a successful growth of the high quality InGaAsP alloy NWs on lattice-mismatched substrates was demonstrated. However, for design of NP-LAMB cells, given the large differences in bandgaps (and therefore lattice constants) among the lateral cells, no single substrate of a given lattice constants can be used for the epitaxial growth of nano-pillar arrays. Therefore, fabrication of templates is a key step that could be used to grow NPs of different lattice parameters and bandgaps for the development of NP-LAMB cells. Furthermore, such templates could be used as a universal template for the growths beyond the NPs if successfully developed. So far, the traditional anodized aluminum oxide (AAO) template approach has been vastly employed to synthesize uniform NWs of Si [206-209], II-VI semiconductors [210-212], and perovskite [213] In the other hand, metal -assisted chemical etching has been recently introduced as an efficient way of fabrication of etched-through templates as well as vertically aligned nanopillars [214]. Recently, the low cost nanosphere lithography have shown to be as an effective approach for controllable fabrication of NW arrays which allows for engineering of the areal density

diameter of NWs. In fact, the pattern can be created by uniform distribution of a close-packed polystyrene or silica spheres which acts as a mask resulting in top-down fabrication of nanopillar array or making etched-through uniform pore arrays similar to AAO template that can be Au-impregnated and subsequently used for VLS growth of NWs [215]. Templated growth of III-V NWs have been earlier reported using different methods such as templated liquid phase (TLP) [216], and Template-assisted selective epitaxy (TASE) [217]. Despite the high quality of III-V materials, these methods are not economically viable in large scale due to complexity of approach. In the current chapter, the initial fabrication of pore arrays for this purpose will be presented. Systematic efforts are made to increase the yield of templates fabrication, to deposit metals such as Au, In and Ga as growth catalysts at the bottom of the pore, and subsequently grow NP arrays from such templates.

7.2 Template Fabrication

The process flow of fabrication of the templates is shown in Fig. 94. From the schematic of process flow, the first step to find a way to obtain a monolayer close-packed Polystyrene (PS) spheres from colloidal solution containing PS spheres. The refined Langmuir-Blodgett technique (explained in chapter 2) was developed to coat a monolayer of PS spheres more uniformly, on large pieces of substrates. A Langmuir–Blodgett film contains one or more monolayers of an organic material, which is usually deposited from the surface of a liquid onto a solid substrate by immersing the substrate into the liquid. PS spheres with three different size of 0.50, 0.75 and 1.0 μm (Polysterene latex

microspheres, 2.5 wt% dispersion in water, Alfa Aesar) were used to float on surface of the water with gradual injection using a syringe tip as shown schematically Fig. 95.
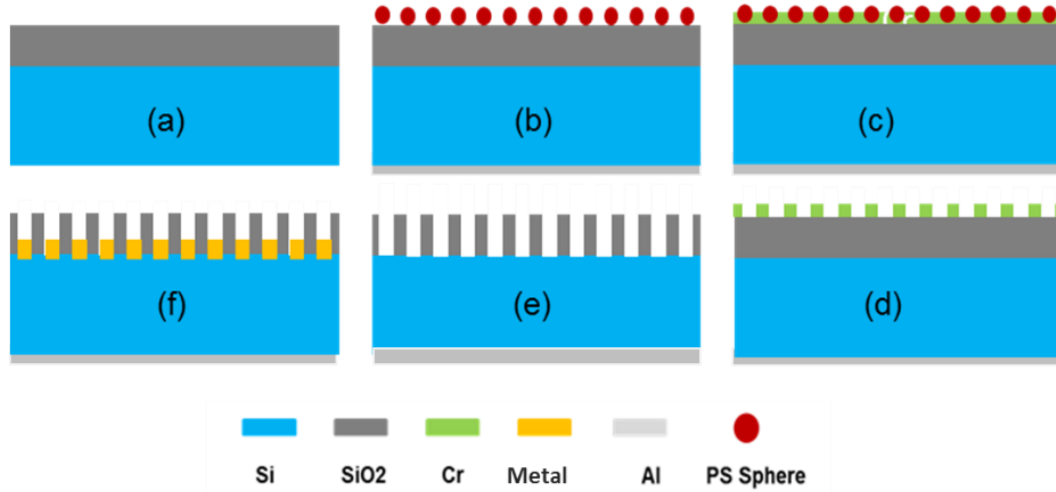
Figure 94. Schematic of optimized template fabrication process: (a): SiO2 deposition on p+ -Si substrate; (b): coating of polystyrene (PS) spheres of appropriate diameters and then thinning down by oxygen plasma to control the size of PS spheres; (c): metal deposition as hard mask; (d): removal of PS spheres; (e): dry etching to create pores; (f): electroplating of metal catalysts.

The surface of a p^+-Si substrate is first treated with acetone, ethanol and DI water and then piranha solution (a 3:1 mixture of concentrated sulfuric acid (H_2SO_4) with hydrogen peroxide (H_2O_2)) for 1hr and NH_4OH: DI water:H_2O_2 (1:5:1) for 30 min. These two steps are part of the cleaning process prior to deposition of SiO_2 film, as the main constituent of the walls of pore arrays. A 1-2 μm thick layer of SiO_2 was deposited using PECVD at 350 ∘C. Thereafter, a 300 nm thin layer of Aluminum (Al) was deposited using the e-beam evaporation on the back surface of Si as the ohmic contact. The top surface of SiO_2 was treated under oxygen (O_2) Plasma for 30 min for two main purposes; To remove any stains/organic contamination, and making the surface hydrophilic to facilitate the uniform dispersion of PS spheres. The as-received colloidal solution of PS spheres was mixed with ethanol in a 1:1 volume ratio and transferred to a syringe

attached to a fine micropipette tip. A 4" diameter petri dish was carefully washed and cleaned using acetone and ethanol and DI water. Then, it was filled with DI water up to a certain level. Subsequently the pre-cleaned/treated substrate was soaked into the water until it is placed at the bottom of the petri dish. Two glass slides were used as the baffles at two ends of the petri dish; one to block the flow of PS spheres at the surface and the other one as a stage on which a small piece of quartz was leaning with a sloping position.
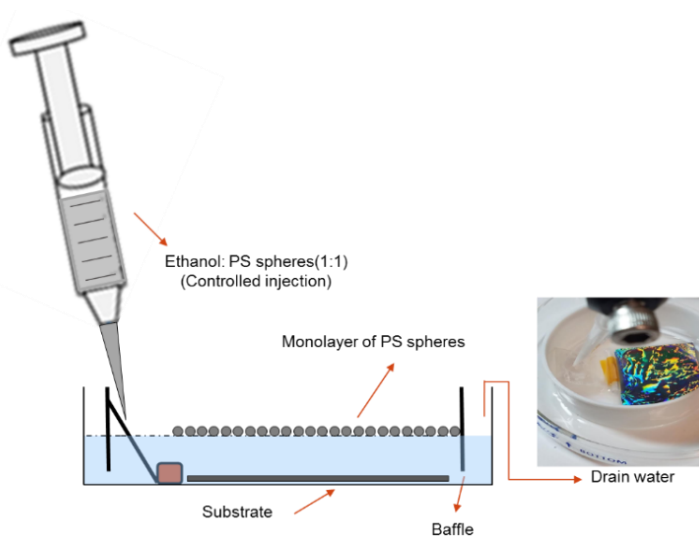
Figure 95. Schematic of Langmuir-Blodgett technique

The PS spheres were gently, with a constant rate, injected onto the surface of the inclined glass. The PS spheres moved readily toward the surface of the water while the agitation of the surface is minimized to not to rupture the surface tension otherwise the experiment will fail. Therefore, the microspheres float at the surface of water until their accumulation is forms a continuous film with a mixed rainbow color. After a uniform multi-color layer of film is formed at top surface of water, 1-2 drop of 2% Sodium Dodecyl (Lauryl) Sulfate (SDS, $NaC_{12}H_{25}SO_4$) solution (dissolved in DI water above 25 °C) is added to the

161

surface to break the surface tension and push the PS spheres more toward the baffle (as shown in the picture; Fig. 95). Next, the excess water is drained gradually, and a close-packed structure is formed, as can be seen from the picture taken from the sample which is dried overnight in the air. The rainbow color of PS-coated substrate is due to a phenomenon called iridescence that is the result of light diffraction from the small PS spheres. Afterwards, Oxygen plasma etching was used to reduce the size of the PS spheres to a desired diameter. Chromium (Cr) mask (50 nm) was deposited at top surface Cr deposition: a 50 nm layer using thermal evaporation (Fig. 94c). After removal of the
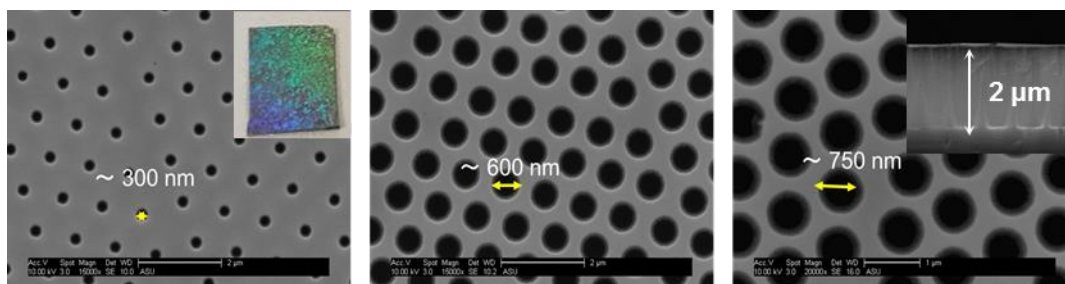
Figure 96. SEM images of templates with pore arrays fabricated by nanosphere lithography with different pore size of a) 300 nm, b) 600 nm and c) 750 nm. The insets in (a) is the real color image of fabricated template, and (c) is the cross- section image of the template with pore depth of ~ 2 µm.

PS spheres by sonication in isopropyl alcohol (IPA), dry etching was performed for 60-90min under presence of CHF_3 and O_2 mixture to create an etched-through SiO_2 film with pore arrays. The Cr at top surface was removed using a mixture of HCl: Glycerol with 1:1 volume ratio at 50 ∘C for 5-10 min. The substrate was sonicated in DI water for 10 min to remove all the residual glycerol from inside the pores. Fig. 96 shows the SEM image of some of the templates with different pore diameters before metal plating at the bottom of the pores. Pore array with distances as large as 1.0 µm can be obtained. The pore size can be adjusted by changing the O_2 plasma etching time that not only changes

the size of final pores, but also the lateral distance of the pores which is crucial for designing the light trapping behavior of the NP-solar cell.

7.3 Electroplating of Au Catalyst

After making the etched-through templates with a pore array, it is required to develop an electroplating method to embed the Au catalyst at the bottom of SiO_2/Si template for the subsequent growth of NPs. Electrodeposition of Au on the surface of a semiconductor requires a less resistive ohmic contact ohmic contact which is necessary for the electrochemical reaction. The process involves the exchange of electrons between the cathode and anode electrodes resulting in deposition of Au on the surface of Si. Electroplating of gold is of great importance for MEMS applications, because of its excellent physicochemical stability and low electrical resistivity [218]. The main problem with electroplating of Au on Si is its low adhesion. However, Fujita et al. have developed a two-step process for electrodeposition of Au on Si, which requires an annealing process at 250 ∘C between the two steps. They have used the commonly used cyan-type plating solution of K-24EA10 at pH of 4.0, and temperature of 40 ∘C [219]. They have also observed differences in plating results obtained for the n- and p-type Si. For electroplating with a low current density on a p-type Si, since the electron density is low, therefore the electron current density that is required to be supplied to the surface is low, thus there is not significant growth of Au film. In order to supply mobile electrons in p-type Si, they have exposed UV light to the surface of the Si which is in contact with solution. Hence, the resistivity and the type of conductivity type, are crucial factors to be considered before plating. Also, it is required to remove the native silicon dioxide via

dilute HF or BOE prior to electrodeposition to ensure the surface of the semiconductor Si substrate is conducting. For our application, it is required to perform electroplating preferably at room temperature and a cyanide-free environment (less toxic), which is more available and easy to use. Generally, two different methods for electroplating of Au on silicon was used as follows: electroplating from colloidal gold nanoparticle bath and electroplating from au plating solution.

7.3.1 Electroplating from Colloidal Gold Nanoparticle Bath

This method is based on electrodeposition of gold colloidal nanoparticles on a Si wafer under a uniform electric field. The negatively-charged gold nanoparticles get physically attached (physisorbed) to the surface under the electric field, similar to the study reported by Buttard et al. [220]. Typically, the experiment involves monitoring the current (I) versus time (t) at a constant voltage (V), between the surface of silicon (anode) and the inert platinum counter-electrode (cathode). A dilute solution containing citrate stabilized Au nanoparticles with a size of of 100 nm (Ted Pella Inc.) were used to plate the gold on the surface of bare silicon through electromigration of negatively charged gold nanoparticles. A piece of highly doped n-type silicon (0.001-0.005 ohm.cm) was cleaned according to the standard protocol (acetone, ethanol, DI-H_2O, 2% HF, DI-H_2O). A schematic of experiment set up is shown in Fig. 97. The resist (PMMA, etc.) at the back surface of silicon above the ohmic contact layer (Al) is to prevent deposition of Au at the back side.

A set of different conditions was experimented at room temperature and fixed concentration of colloidal gold mixed with DI water.
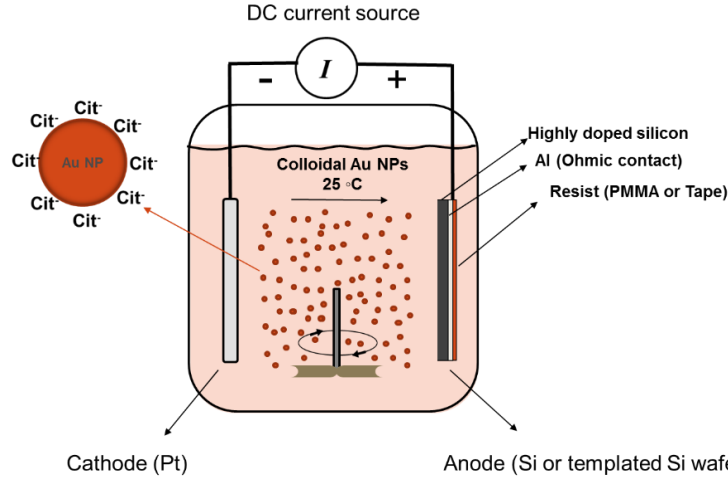
Figure 97. Schematic of experimental setup for electrodeposition of colloidal gold. The magnified picture illustrates the citrate-stabilized Au nanoparticles

The Si as the anode (positive terminal) accepts the negatively charged Au NPs forming a thin film layer of Au. Fig. 98 shows the SEM image of different samples obtained at two constant voltages of 1 and 5 volts with different deposition times ranging from 30 seconds to 1 min.
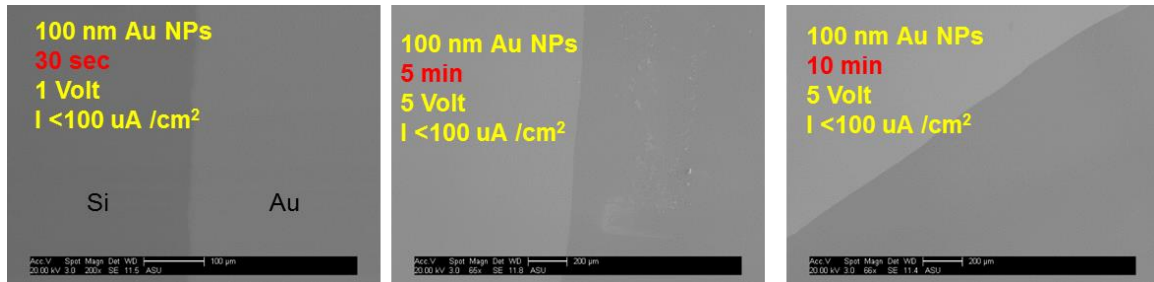
Figure 98. SEM images of electrodeposited colloidal Au nanoparticles (on n-type Si) with diameter of 100 nm under constant voltage of 1V and 5V with deposition time changing from 30 sec. to 10 min.

The current density for all the samples was less than 100 μm/cm^2 measured by a DC microamp meter. This approach requires to be studied more systematically as it turned

out from our preliminary results, to be slightly difficult to optimize and not promising for our purpose.

7.3.2 Electroplating from Au Plating Solution

Electrodeposition from the solution containing Au^{3+} ion through a reduction process is the most convenient way for electroplating of Au. A diluted Gold Chloroauric acid ($HAuCl_4.3H_2O$, 0.082 molar (M)) was used as the electroplating bath solution in an electrochemical cell. Different concentration of dilute plating bath was prepared for electroplating to find the optimum condition. The experimental setup consists of:

a) Au solution (cyanide free solutions are preferred)

b) Platinum electrode as anode where the oxidation reaction takes place

c) DC current source

d) Doped n- or p-type silicon substrate with low electrical resistivity which acts as the cathode, where the reduction reaction ($Au^{3+}+3\bar{e} \rightarrow Au^{0}$) takes place. Native oxide must be removed using HF or BOE.

Shown in Fig. 99 is the schematic of electroplating setup which was used. The stirrer (or magnet) at the bottom is to homogenize the solution during the electrochemical reaction. As seen, the back surface of the p- (or n-) type silicon substrate (ρ= 0.001-0.005 ohm.cm) is coated with an ohmic contact such as Al, In, etc. followed by deposition a thin layer of resist (e.g., PMMA). As the preliminary experiment two pieces of n- and p- type silicon (ρ= 0.001-0.005 ohm.cm) were tested.
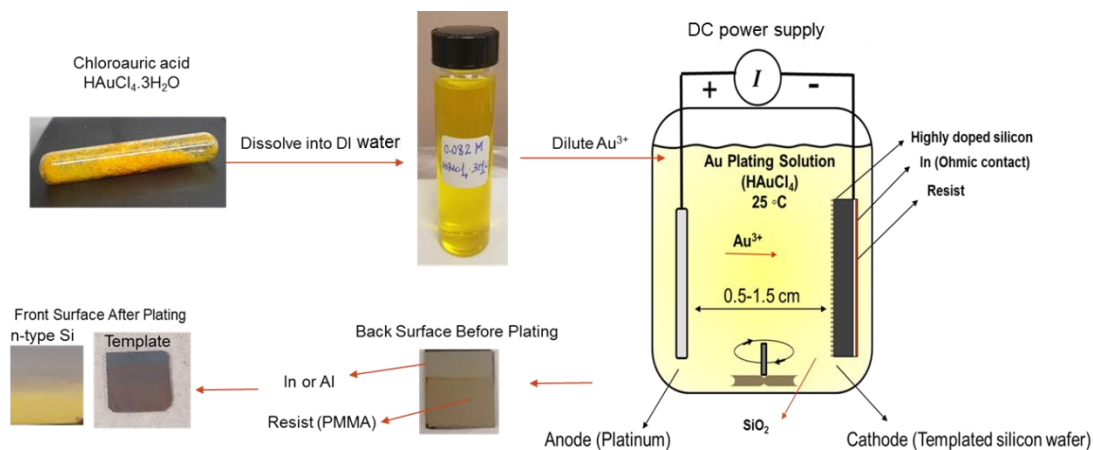
Figure 99. Schematic of experimental setup for electroplating of gold with real color image of plated samples (Si substrate and etched-through SiO_2/Si template).

The concentration of the gold bath was $4.1*10^{-3}$ M and the experiment was performed at constant voltage of 1V for 5 min. As seen from the picture of electroplated sample, the golden yellow color on the surface indicates successful deposition of Au film. SEM image in Fig. 100 shows that NPs with average particle size of ~100 nm and the Au film obtained on n-type silicon has relatively larger filling ratio of the surface under the same condition. This is because p-type Si has low electron density compared to n-type substrate. The same strategy was implemented on the fabricated templates, which was shown earlier (see 7.1), to embed the Au nanoparticles at the bottom of the pores via electroplating to be used for a subsequent VLS growth of NPs. For this purpose, the back surface of Al (or In) deposited template is similarly coated with a thin layer of resist (PMMA or adhesive tape). It was then connected to the negative terminal (cathode) of a DC current source. It is necessary to remove the native oxide (via sonication in dilute HF or BOE) that grows over the time (in the meantime between template fabrication and electroplating process) since it can decrease the affinity of ionic Au^{3+} species to be reduced into Au^0 clusters at the bottom of the pores.
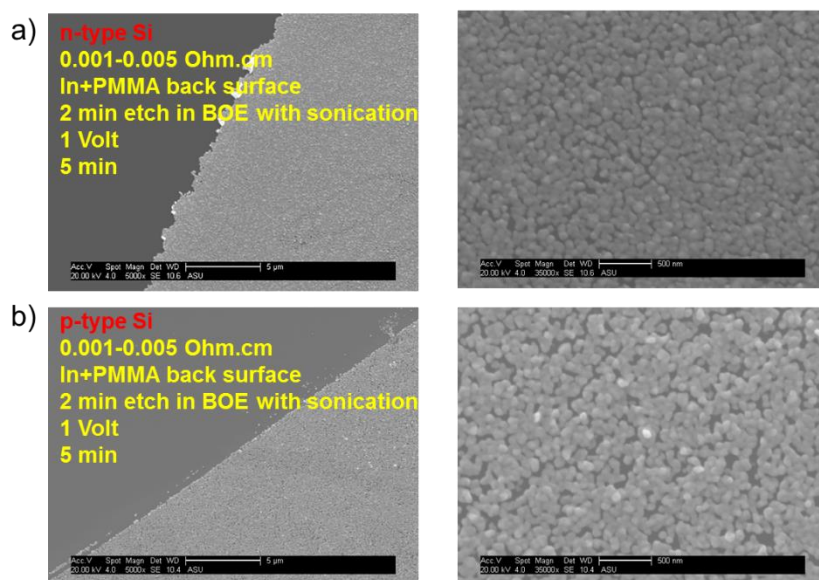
Figure 100. SEM image of the Au-plated Si substrates under similar condition for a) n-type Si, b) p-type Si. The right-hand side image shows the magnified image for two samples.

It is required to test different variables such as plating time, constant voltage, distance between electrodes influencing the current, concentration of bath, and temperature (if required). It is also expected to see slight differences between optimized parameters for bare silicon and the etched-through template since the conducting area of the substrate surface is reduced and the top of the pores are less accessible by ionic species in the bath. Fig. 101 shows an example of successful plating of Au into template with pore size of 500 nm diameter. The SEM image taken from large area of the sample shows uniform plating across the entire template with more than 90% coverage. The real color image of Au-plated template looks reddish brown.
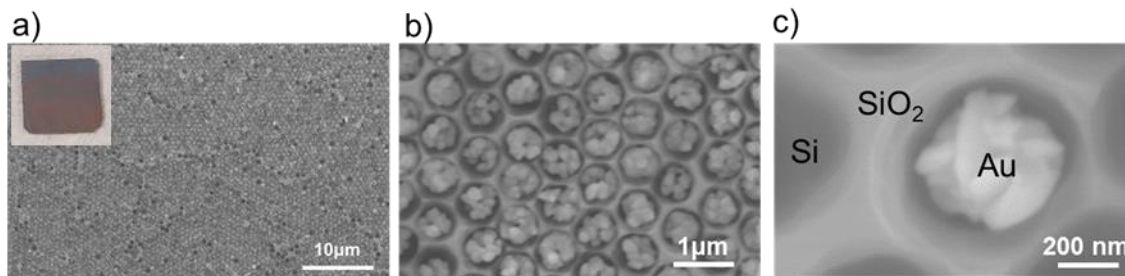
Figure 101. SEM image of electroplated Au onto templated p-type Si: a) image taken from large area of sample shown in inset, b) magnified image from a selected area, c) single pore with Au cluster grown under constant voltage of 1V for 10 min.

Apparently, increasing the voltage results in an increase in current density delivered by the cell that affects the size of Au nanocrystals. Filling factor and uniformity pretty much depend on fabrication of the template that must deliver a non-defective pore array without any crack on the walls. More importantly, all the pores must be uniformly etch-through by optimizing the dry etching time to make sure there is no residual SiO_2 at the bottom of the pores that prevents the electrons to reach to the surface. This can preclude the pore from receiving the Au deposition due to lack of conductivity. Fig. 102 shows some examples of such undesired plating results from templates of various batches that are processed consistently, but there are some fluctuations observed, most likely due to non-uniform dry etching. From the comparison between three samples, it can be seen that the template electroplated under voltage of 5V for 10 min (a) is receiving less gold than the other two (b and c) with less current density which is contradictory. Also, for sample c with 5 min plating compared to 10 min plating at 1V, the size of the clusters is not the same that can be different amount of residual oxide at the bottom of pores.
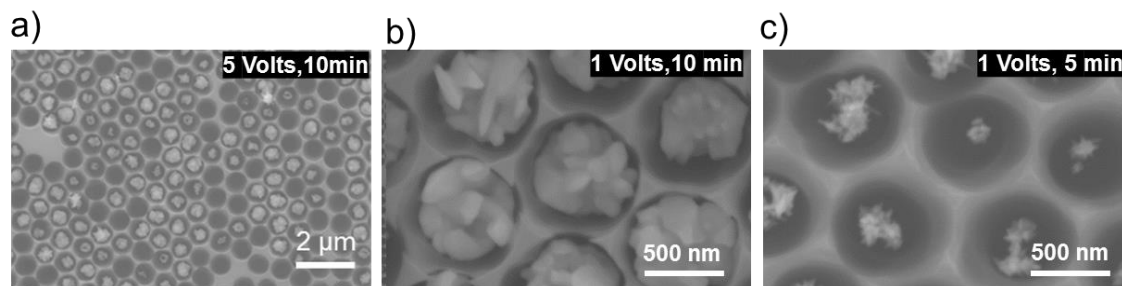
Figure 102. SEM image of variation in electroplating with non-uniform distribution of Au clusters across entire template.

Sometimes, formation of ring-shape Au pattern inside the pores rather than a cluster was observed. As shown in SEM images (Fig. 103), it seems to be due the fact that template is over-etched at the cross section between Si and SiO_2, thereby no reduction center to contribute into the Au^{3+} to Au^0 reaction.
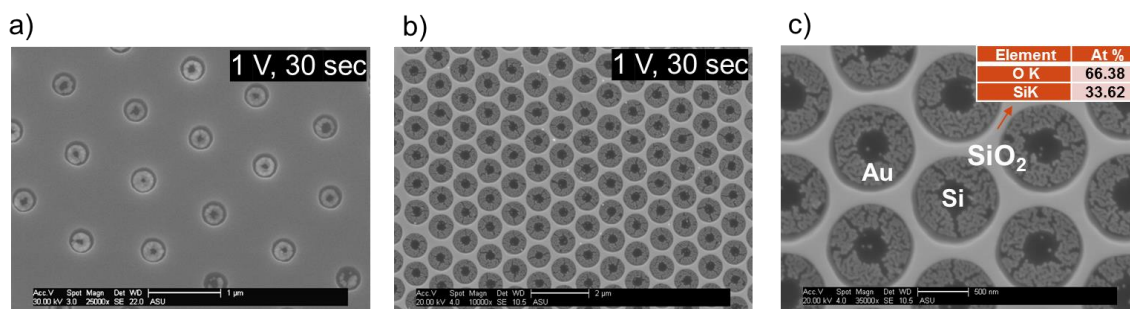
Figure 103. SEM images showing the formation of ring-shape Au pattern inside the pores of etched-through SiO2/Si template with pore sizes of a) ~300nm, b) ~750 nm. c) Magnified SEM image of sample (b). EDS spot analysis of the wall is shown for better distinction between three parts.

7.4 Growth of Au-Catalyzed InP Pillars

The typical VLS growth methodology shown in previous chapters for growth of III-V NP alloys will be implemented on the Au-plated templates. So far, the growth of composition-graded III-V subcells with all needed bandgaps for fabrication of the LAMB architecture with 3 lateral cells is demonstrated. The corresponding alloys can be grown

using the current templated approach, with flexibility around those bandgap values for optimization of the overall system efficiency. However, extensive studies should be conducted to optimize such process with an aim towards improving the uniformity of NPs. As the first step, we have tried to grow InP using VLS approach based on Au-catalyst seeded inside the pores of template. Similar to growth of InP NWs and thin film (chapter 3 and 5), here also we use the same growth parameters with a slight change in evaporation rate of In source as the rate limiting factor for growth. The evaporation temperature of In is optimized to be around 900 ∘C and that for red-phosphorous is ~450 ∘C. The growth temperature is chosen to be 680 ∘C and that is equivalent to relatively high supersaturation (highly active VS-mode). The growth pressure was kept 2 Torr for all of the templated growth of InP. The growth duration varies based on the size of the pores and depth of the SiO_2 pores which is equal to the time that it takes for the pores to be filled up to above the SiO_2 surface. The p^+-type Si-template was electroplated with Au seeds in constant voltage of 1V and the plating time was adjusted based on the size of the pores. SEM images reveal that post-electroplating growth for InP works successfully. Although there are some parameters that are required to be changed including the size of the pores, as a result the Au particle sizes to achieve will change. Fig. 104 shows an example of the VLS growth of NP array from the Au-plated templates. An Allied Polishing System was used to polish the as-grown sample with a fine lapping film (0.1 micron) to take off the surface artifacts, including excessive SiO_2 and features grown on top.
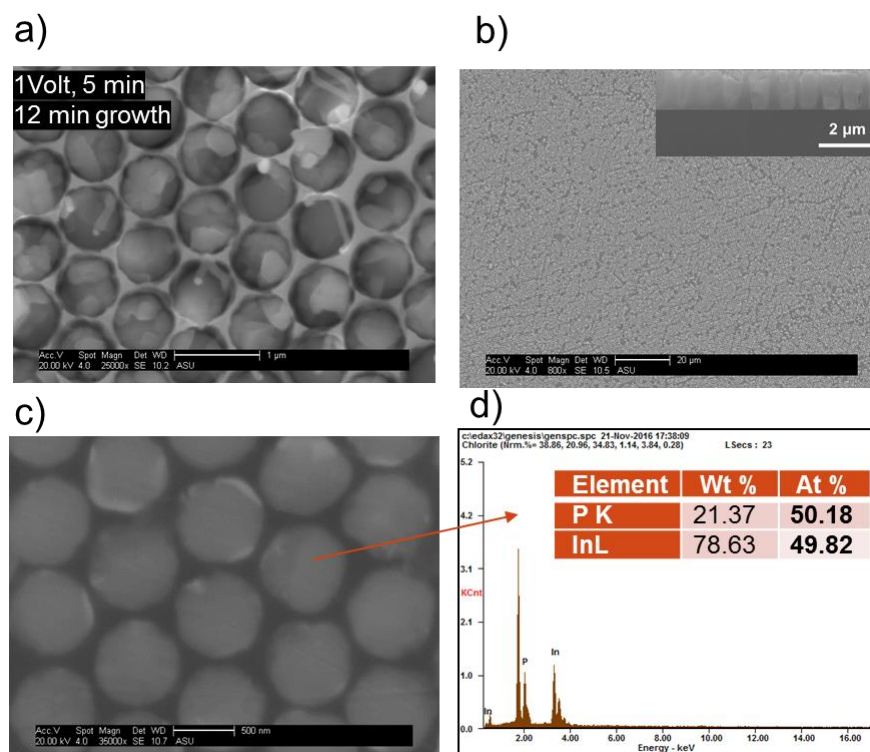
Figure 104. SEM image of templated grown InP with 1 V and 5 min plating parameters and 12 min growth (a), polished sample (large area) with ~ 100% pillar growth coverage. Inset is the cross section of the cleaved substrate (b), high magnification InP pillars (c) and their corresponding EDS result.

The surface of polished sample becomes artifact-free and clean. Fig. 104b shows the uniform ~ 100% pillar growth-coverage over the entire substrate. The EDS analysis indicates the high stoichiometry of as-grown InP pillars with diameter of ~700 nm. One of the most efficient ways to prevent formation of excessive features is to further reduce the evaporation temperature of In, but this might require longer growth times which is not desired. The cross-section image taken from a cleaved as-grown template indicates that there is a direct contact between InP and bottom substrate, which makes the current design highly suitable for making solar cells.
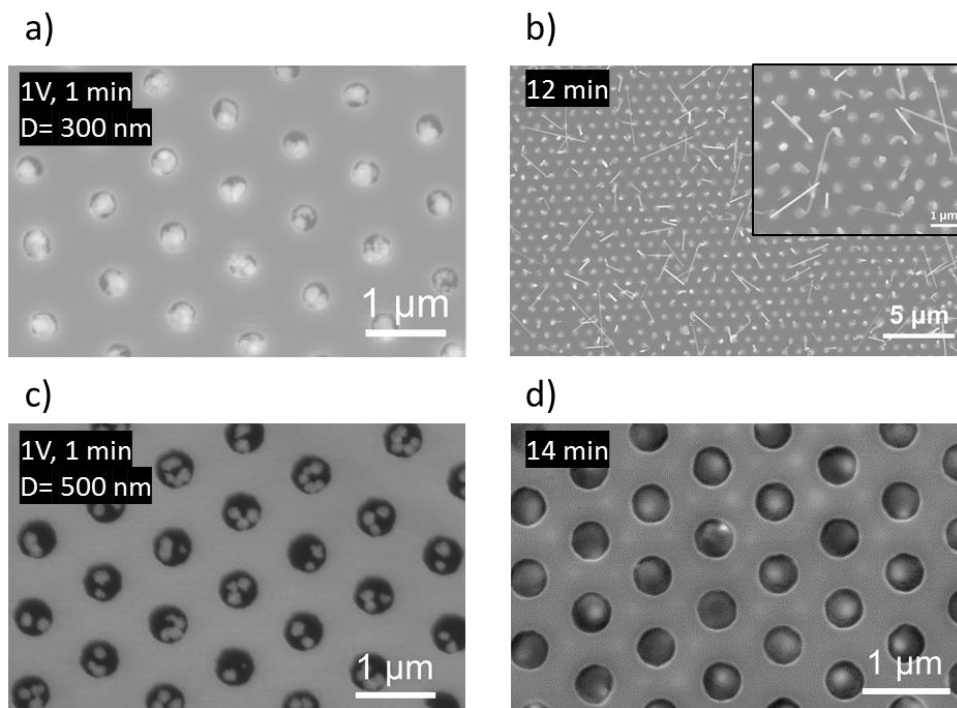
Figure 105. SEM image of templated growth InP: before and after plating: a) 1V and 1 min and D=300 nm, b) 1V and 1 min and D=500 nm and after growth: c) 12 min growth (inset is the magnified image) (d) 14 min growth.

In order to further improve the templated growth, it was realized that modification of the plating parameters (time and current, etc.) results in a growth of smaller and more uniform Au nanoparticles. Therefore, it is expected to obtain a better growth and a high uniformity of pillars, as can be seen in Fig. 105b and 105d. The NPs grown on a template with pore size of D =300 nm shows more active VLS growth. The sample grown on a template with pore size of D =500 nm does not show any significant surface artifacts which is highly preferred as such sample does not require a post growth polishing.

7.5 In-Ga plating

7.5.1 Indium Plating

Au is typically used as the catalyst for growth of NPs, but there are some concerns for possible III-V contamination, even though there are systematic studies showing such concerns are not serious. As an alternative to Au, a new plating recipe for In and Ga was developed, so that Au-free catalysts was successfully obtained at the bottom of the pores. For growth of InGAsP, In and Ga metals as the catalysts are especially interesting and important, since the III-V NPs already contain In and Ga elements. Such catalysts could potentially allow for self-catalyzed growth of NPs, without any concern of Au diffusion into NPs. For Au-plated templates, vapor-liquid-solid (VLS) growth is the standard approach. For In and Ga plated templates, phosphorization or arsenidation could be alternative to the VLS growth. It is believed both approaches can provide high quality pillars. The proposed method is based on an initial electroplating of In, Ga or combination of both on a pre-cleaned conductive or semiconducting substrate such as ITO-coated fused silica or silicon (p- or n-type). The electrochemical cell for this purpose is composed of an electrolyte solution containing the chloride-based bath of dilute $InCl_3$ or $GaCl_3$ that are highly soluble in water. The cathode is made of the prospective substrate and anode can be either In, Ga or Pt where the oxidation reaction occurs. To be able to reduce the In^{3+} or Ga^{3+} ions at the cathode which is connected to the negative end of the DC current source, it is necessary to provide ample voltage corresponding to reduction potential of the metallic elements (M) as follows;

$$M^{n+} + n\bar{e} \rightarrow M^0; \; E = E_M^0 + \frac{RT}{nF} \ln[M^{n+}], \qquad (7.1)$$
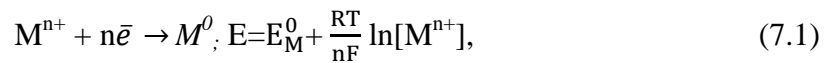
where E is the equilibrium potential of the electrode with respect to the standard hydrogen electrode and E_M^0 is the standard electrode potential of M element. R and F are the molar constant and Faraday's constant equal to 8.314 J.mol^{-1}. K^{-1} and 96,485 C/mol, respectively. Similarly, for In and Ga we have [221],

$$In^{3+} + 3\bar{e} \rightarrow In^0; E=E_{In}^0+\frac{RT}{3F}\ln[In^{3+}] = -0.342 + 0.0197 \log [In^{3+}] \qquad (7.2)$$

$$Ga^{3+} + 3\bar{e} \rightarrow Ga^0; E=E_{In}^0+\frac{RT}{3F}\ln[In^{3+}] = -0.529 + 0.0197 \log [Ga^{3+}] \qquad (7.3)$$

The concentration of the bath containing the prospective ions plays a crucial role in deposition rate, since the voltage is constant while the deposition is being driven through an electrical current. The thickness and uniformity of the film can be tuned by deposition time and voltage. Lobaccaro et al. have reported electrodeposition of In on molybdenum (Mo) foil, below room temperature with their electrochemical setup with a counter electrode of soluble In as the anode that helps for replenishing the In^{3+} ions that are being reduced on the cathode [222]. They have subsequently deposited a thin layer of SiO$_x$ as capping layer on top of electrodeposited In film. Afterwards, by exposing the substrate into P flow they have obtained a high quality thin-film InP with an epi-like quality. As the first step, preliminary electrodeposition of In on p$^+$-Si substrate was performed. As the counter electrode (anode) In and Platinum (Pt) were tested at room temperature. The schematic of electrodeposition setup is very similar to what was observed for Au-plating. As the plating-bath, a dilute InCl$_3$ (0.028 M) solution was prepared by dissolving 0.25 g of solid InCl$_3$ (anhydrous, 99.995%), a highly hygroscopic compound, in 40 ml DI-water. The SEM images of two different samples are shown in Fig. 106a and 106b. As seen for 30 sec electrodepositions, the plating rate on the sample with Pt as the anode is much

175

higher even at lower constant voltage of 5V vs. 10V compared to that obtained for sample with soluble In as the anode. An EDS analysis of the plated In shows that there is no residual chlorine inside the bulk of the deposited surface (Fig. 106c).
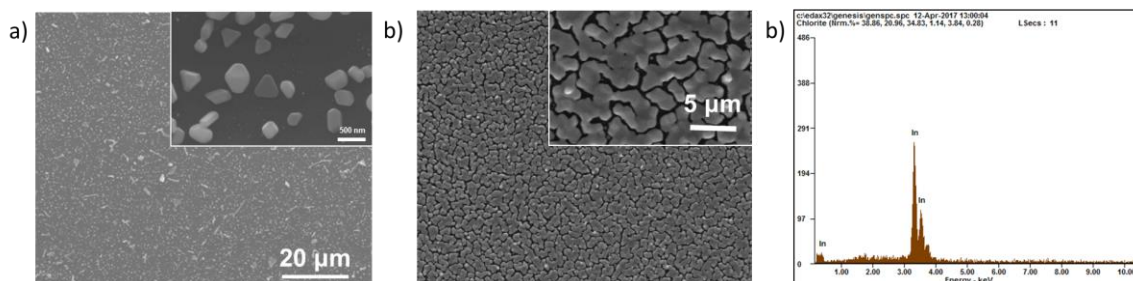
Figure 106. SEM micrograph of electrodeposited Indium thin film samples on P^+-Si in presence of different counter electrode as anode: a) Indium electrode 10 V, 30 sec., b) Pt electrode, 5V, 30 sec., c) EDS of electrodeposited In from $InCl_3$ bath for sample shown in Fig b.

A systematic study on time-dependent of In electrodeposition on p^+-Si with Pt electrode as the anode indicates the uniformity of the thin layer (white part in inset of Fig. 107c) with a thickness of $\sim$ 3µm obtained at 5V and 5 min. (Fig. 107 (a-d)).

By taking into account all these parameters that we have examined for electroplating of In, now we can move forward with electroplating of In into pores of template, either as the catalyst or for subsequent phosphorization process to grow InP. As can be seen from SEM image shown in Fig. 108 for a p^+- Si template, all the pores are uniformly filled with faceted In crystals. A cross section image for a plating time of 20 sec (b) also reveals that In is grown at the interface of silicon where there is no residual oxide. The time dependency of the fraction of pore depth that is filled with In crystal grown by plating is plotted in Fig. 108c.
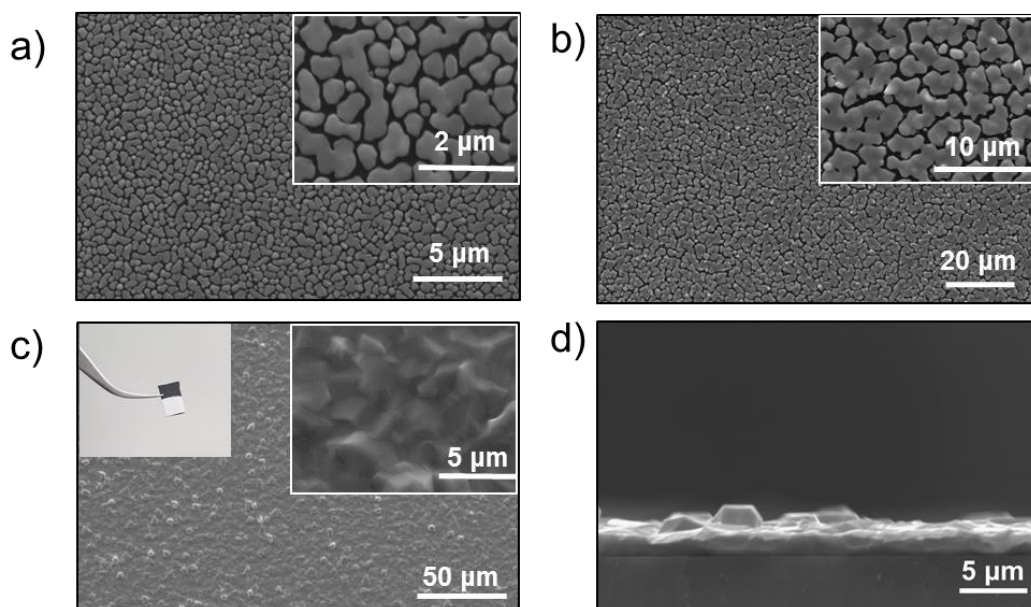
Figure 107. SEM micrograph of time-dependent electrodeposited indium on P$^+$-Si using DC current source with constant applied voltage and Pt as the counter electrode (anode) ; a) 5V, 5sec, b) 5 V, 30 sec, c) 5V, 5 min. insets are the magnified images from a selected area of each sample. d) cross-section image of sample c with an indium film thickness of ~3 μm.
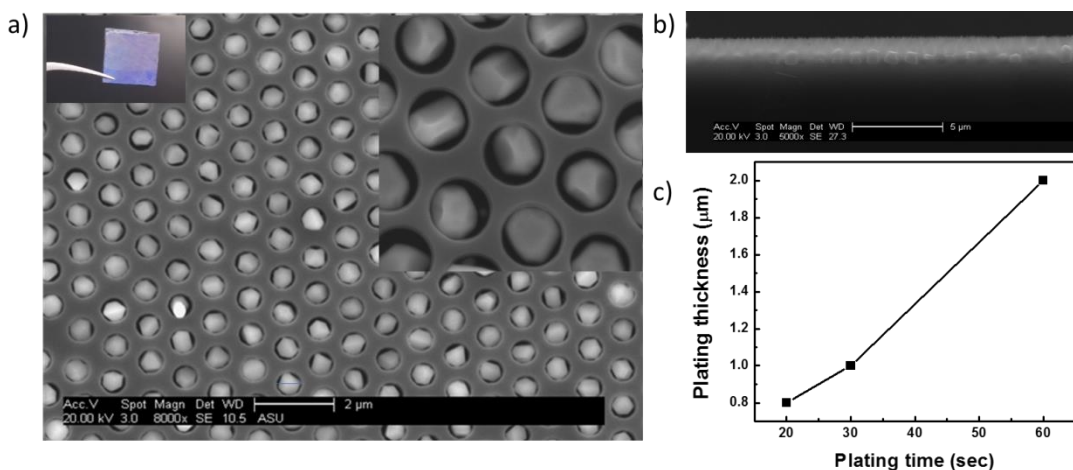
Figure 108. SEM image of the indium plated template at 5V for 1min with a pore size of ~ 625 nm. inset is the picture of electroplated piece template (a). cross-section SEM image of the template (D=750 nm) with a half-filled pore with indium crystals done at 5V for 20 sec(b) Plot of plated indium thickness vs. electroplating time. All three samples are done at 5V for a template with D=750 nm(c)

7.5.2 Gallium Plating

Similarly, a dilute $GaCl_3$ (0.52 gr $GaCl_3$ dissolved in 30 ml DI water) bath was used for electrodeposition of metallic gallium. Since the standard reduction potential of Ga^{3+} is more negative compared to In^{3+}, it is expected for the gallium solution with almost the same concentration to be reduced at higher voltage. A voltage of ~ 4V was recorded as the so-called threshold voltage for deposition for gallium, where a thin white layer of sparsely grown small Ga nanoparticles was observed. However, to get thicker (white and shiny) deposition of Ga (inset of Fig. 109a) a 10V DC current was applied. Formation of spherical Ga particles as large as up to 20 μm can be seen from the SEM image shown in Fig. 109a. It was first postulated that this might be due to the exothermic nature of reduction reaction ($Ga^{3+}+3\bar{e} \rightarrow Ga^{0}$) that brings about dewetting of gallium (contact angle is more than 90∘) to form Ga microspheres which tend to have a smaller surface energy. Progress in highly competitive $2H^{+}+2\bar{e} \rightarrow H_2$ reduction reaction by consumption of most of the cathodic electrons can be also a reason to form such morphology due to releasing H_2 gas that leaves the surface of the substrate [222]. Plating at low temperature deposition-bath was also examined, which is known to affect many of the activated processes during electrodeposition including adatom surface diffusion rate and interfacial binding energy [223]. The temperature of the bath is decreased using an ice bath which is controlled by a thermometer. Our results showed that plating at 8 ∘C leads to formation of smaller gallium spheres with more uniform surface coverage (Fig. 109b).
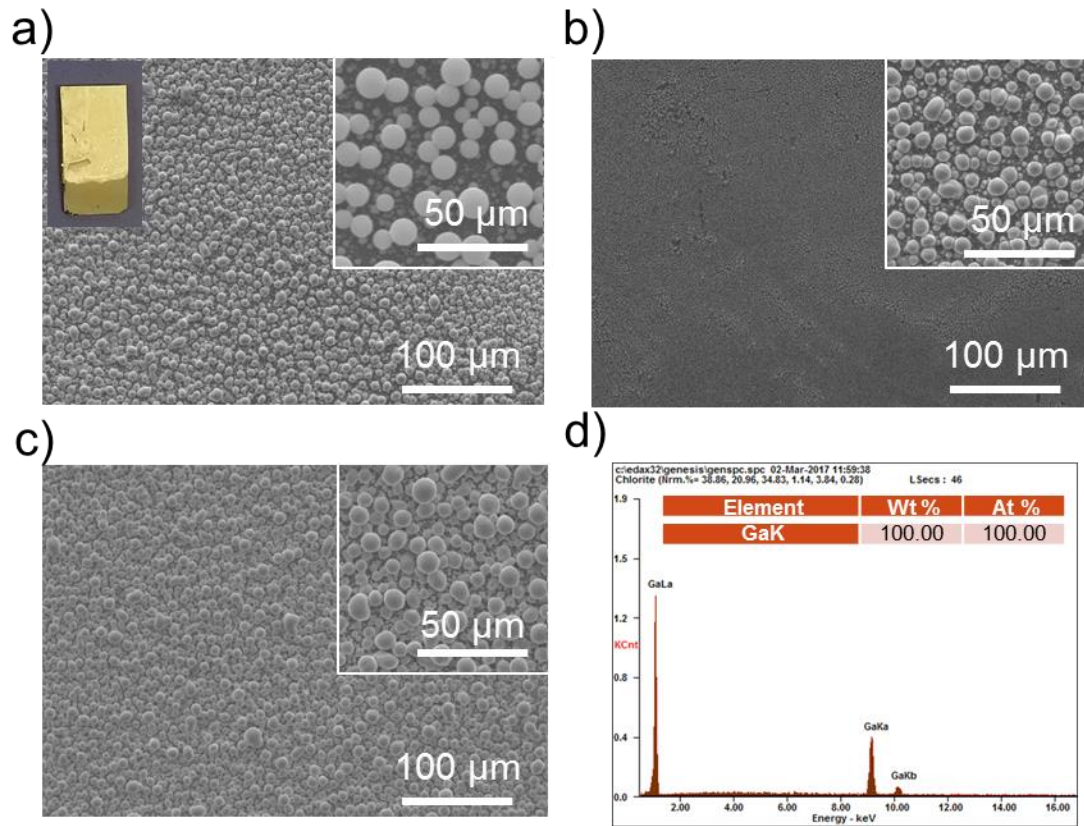
Figure 109. SEM image of the electrodeposited Ga on n$^+$-Si at 10V for 1min at various temperatures: a) 3 ◦C, b) 8 ◦C, c) 20 ◦C. insets are the magnified images. Top left in (c) is the picture of Ga elelctrodeposited sample. d) EDS analysis of sample in c.

7.5.3 Indium-Gallium Plating

In and Ga are the main constituent parts of semiconductor alloys such as Indium-Gallium Nitride (InGaN) or Copper Indium Gallium Selenide (CIGS). For example, solar cells of made of CuIn$_x$Ga$_{1-x}$Se$_2$ ($0 \leq x \leq 1$) covers a bandgap range of 1.0 eV (for CuInS$_2$) to about 1.7 eV (for CuGaSe$_2$). Electroplating can be used as an effective, low-cost and straightforward route towards making solar cells based on CIGS [224] or InGaAsP. In general, for III-V materials the current proposed approach relies on a very inexpensive electrodeposition technique for group III metallic alloys in composite or solid solution

179

form followed by a short time reaction with a hot flux of group V elements (P, As, N, etc.). The proposed method is highly suitable for producing high quality thin-film materials with epi-like quality. Hence, it is required to develop the electroplating process that can provide all the requirements of semiconductor alloying similar to other expensive techniques such as MOCVD or MBE. The most crucial factor is the ability to control the composition precisely by adjusting the In to Ga molar ratio in electroplated film. So far, the electroplating for pure In and Ga was optimized, but rational design of precursors as the constituent part of the electroplating bath for engineering the composition of In_xGa_{1-x} is quite challenging because the reduction potential of the In^{3+} and Ga^{3+} are not the same. This means by simply adjusting the molar ratio between In and Ga precursors, we cannot obtain the desired composition. A set of preliminary experiments were carried out which are required to be further developed as a promising future work. Given the different reduction rate of the In and Ga, there are different ways to engineer the composition(x) if In_xGa_{1-x} by varying the reduction potential. It is generally required to decrease the deposition rate of In since it has less negative reduction potential. This can be manipulated by different proposed ways:

a) Effect of concentration of precursor (bath): from the reduction potential equation that was shown earlier the effect of concentration does not seem to be very significant since its impact reduced under log scale (Log [In^{3+} or Ga^{3+}]).

b) Effect of temperature: changing the temperature affects both thermodynamics and kinetics. Decreasing the deposition-bath temperature leads to a reduction in kinetic of deposition for both In and Ga and this means the applied voltage

becomes very important in determining the deposition rate. Therefore, increasing the plating temperate can result in increasing the deposition rate of In and Ga.

c) Making a more stable compound with In ions using a complexing agent to increase the reduction potential in a controlled manner. Hence, it will be thermodynamically prohibited to be deposited easily.

From the preliminary results that we have obtained for In-Ga plating on silicon substrates, as can be seen from the SEM images, presence of high concentration of Ga in composition of the electrodeposited film results in formation of spherical features on tope surface. The SEM image shown in Fig. 110 is for the sample electrodeposited from a mix bath with $InCl_3$ to $GaCl_3$ molar ration of 0.01M to o.05M at voltage of 10V for 1 min. The EDS spot analysis shows that the selected spherical feature has ~87% Ga which is indicative of the fact that the concentration of Ga in electrodeposited film is directly proportional to the molar ratio of available ionic Ga species in the bath. There is no peak showing presence of chlorine or oxygen.
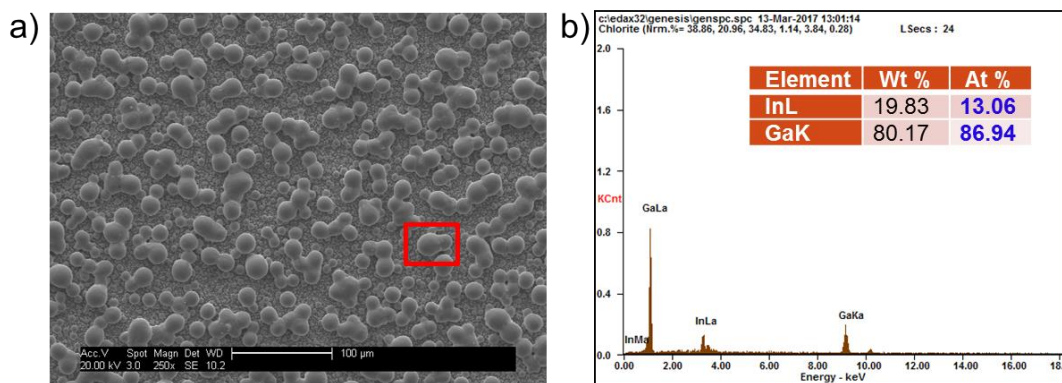
Figure 110. a) SEM image of the electrodeposited In-Ga film from a bath with $InCl_3$ to $GaCl_3$ molar ratio of 1 to 5. b) EDS spot analysis of spherical feature shown in in red rectangle.

It was further noticed that the electroplated sample with different size distribution for different spheres shows different composition with respect to the size of the spheres. The

Fig. 111 shows the SEM image of the sample electroplated on a p^+-Si at 6V for 10 seconds at 1.5 °C from a bath of 5:3 $InCl_3$ to $GaCl_3$ precursor ratio. This is performed with an aim towards making $In_{0.5}Ga_{0.5}P$ as one of the subcells for LAMB cells by phosphorization of the electroplated $In_{0.5}Ga_{0.5}$.

Element	Wt %	At %
InL	67.91	56.24
GaK	32.09	43.76

Element	Wt %	At %
InL	76.29	66.14
GaK	23.71	33.86
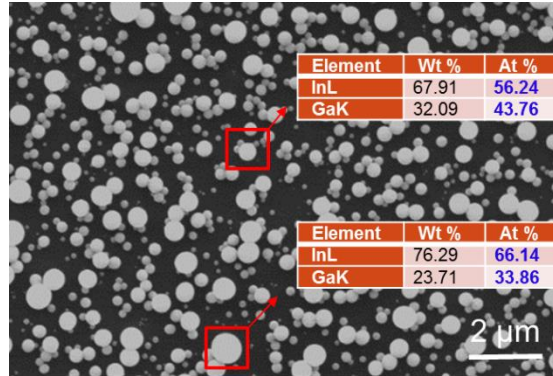
Figure 111. SEM image of the electrodeposited In-Ga film on p^+-Si substrate from a bath with $InCl_3$ to $GaCl_3$ molar ratio of 5 to 3 at 6V for 10 sec. The EDS results are obtained from the In-Ga spheres representing their composition.

It turns out that the spheres with smaller size have less In content and we have seen this for other samples as well, independent of the plating voltage varying between 5-10 V. This provides us with a hint that there are so many parameters to be optimized for successful control of the composition of the electroplated In-Ga alloys since it is critically importance before forward with the growth under phosphorus or arsenic flux.

7.6 Growth of InP via Phosphorization of Metal-Plated Template

Here we aim to produce a high quality InP film with various alloy composition, x, through a unique phosphorization process. This process starts with an electroplating of In film on various conducting substrates. The phosphorization of the metal layers of 1-2 microns thick in a chemical vapor deposition (CVD) reactor would produce a high-quality film with a quality comparable to those produced through a typical standard film

deposition [149].The attractive features of this approach compared to epitaxial growth of III-V alloy semiconductors can be expressed as; a) no expensive metal-organic precursors or epitaxial equipment such as MOCVD or MBE is required; b) no epitaxial-ready single crystal substrate is needed; c) The metal-catalyzed phosphorization process would produce a material quality comparable to thin-film deposition obtained by other techniques giving rise to polycrystalline films. So far, we have successfully electroplated In with 100% filling ratio across the template and as the second step we have performed the phosphorization of the In-plated templates as follows; To prevent dewetting of the In with fairly low melting point of 157 (or 30) $^{\circ}$C, a thin layer (50-100 nm) of SiO_2 is grown on electro-plated metal layer using Plasma-Enhanced Chemical Vapor Deposition (PECVD). The phosphorization is performed at ambient pressure in a consistently pumped low pressure chemical vapor deposition (LPCVD) reactor (see Fig. 112a). The substrate is loaded in the downstream of the LPCVD reactor at an appropriate optimized temperature under the P flux for a long- enough time until complete conversion of In to InP (see Fig. 112b for schematic).
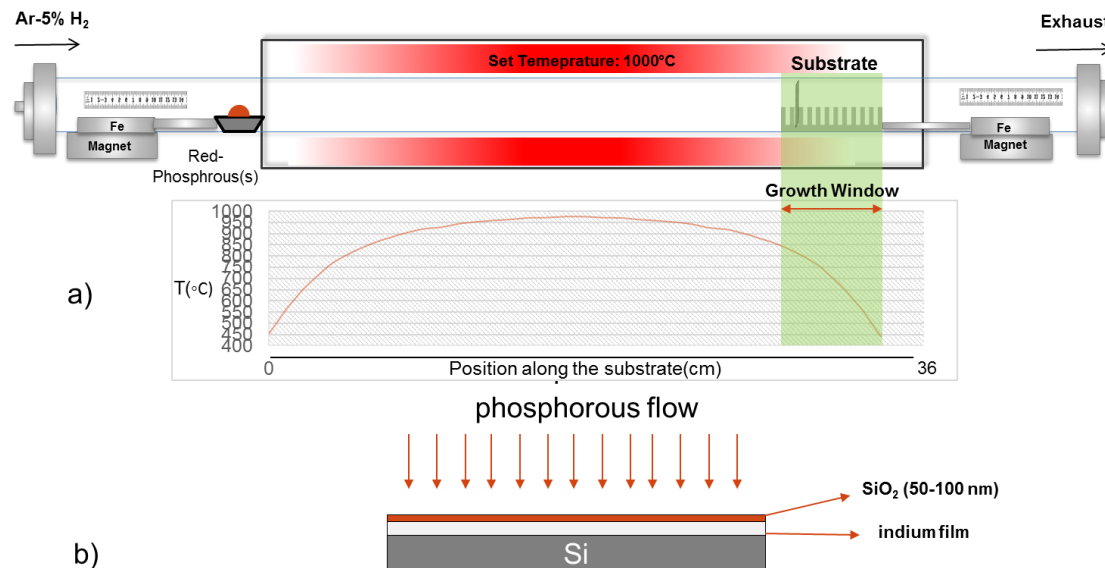
Figure 112. a) Schematic of phosphorization growth setup with two different magnetic manipulators for rapid cooling of the sample and control over the P flux, b) Schematic of phosphorization for SiO2-capped metal In layer.

The growth window primarily includes the reaction temperature and time which are key influencing parameters to be optimized to assure the complete conversation of In to InP. Detailed phase diagram of solid solutions of binary In-P is utilized to guide the process to achieve stoichiometry between In and P. At the end of the phosporization, the substrate is quenched or rapid cooled to prevent phase segregation into second phases such as In droplets, etc. The capping layer of SiO_2 is subsequently removed with dilute 2% hydrofluoric (HF) acid (for 5 min). Fig. 113a shows a representative SEM image of stoichiometric InP film grown on InP substrate by phosphorization of In film with a thickness of 1.2 μm thickness at 720 ∘C and pressure of ~700 Torr.
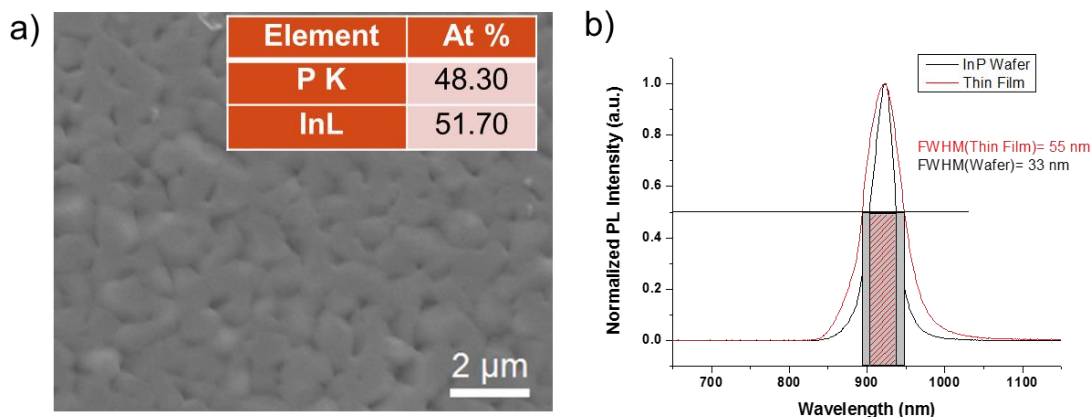
Figure 113. a) SEM micrograph of InP thin film samples obtained by phosphorization. b) PL spectra for as grown InP sample and wafer.

As shown in the inset of Fig. 113a, the obtained polycrystalline InP film is highly stoichiometric with an P/In of 48.3 to 51.7. The PL spectrum (Fig. 113b) shows main features very similar to those of a commercial wafer, with linewidth (55 nm) somewhat broader than that of single crystal wafer at 35 nm, indicating possible defects and surface states contributions. All these can be minimized through an optimization of phosphorization process and through an eventual surface treatment. The same strategy was implemented to grow the InP pillars through phosphorization of In-plated template. The SEM image of the sample of before and after phosphorization is shown in Fig. 114a and 114b. The electroplating was performed on a sample with an average pore size ~550 nm for 1 min and applied voltage of 5V. Subsequently, the optimum phosphorization was achieved at the temperature of 400 ∘C and pressure of ~700 Torr for 45 min.

The sample was then polished using the Allied Polishing System. Fig. 114b shows the SEM image of the sample after polishing with the corresponding PL spectrum with a narrow bandwidth of ~40 nm measured under optical pumping of an Nd:YLF laser

$(\lambda = 349\ nm)$ indicating a high quality of the grown InP obtained by phosphorization.bThe emission wavelength of the InP is around 926nm that matches with that of ZB InP. The EDS elemental analysis also shows a good stoichiometric ratio between In and P for the templated InP NPs.
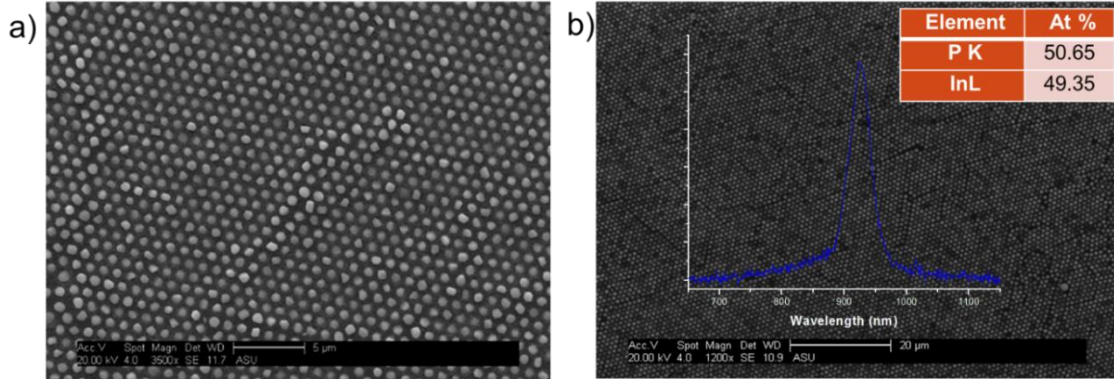
Figure 114. SEM micrograph of In-plated template before and after phosphorization (a). Templated InP pillars obtained by phosphorization after polishing. Embedded PL shows narrow bandwidth of the obtained InP. Top right inset is the elemental spot analysis of one the pores containing InP crystal (b).

7.7 Summary

A universal template with pore arrays fabricated based on SiO_2 coated Si substrate was established. The aim was to develop a templated substrate that can be used to grow a wide range of alloy NP materials, without being limited by typical lattice mismatch, providing a low cost universal platform for future PV. A facile recipe for electroplating metals such as Au, In and Ga into the pores of template was introduced. Subsequently, the growth of InP pillars through both Au-catalyzed VLS growth and phosphorization of In-plated template was demonstrated. It is believed, lowering the cost as a critical issue in fabrication of solar cells can be addressed by further development of such technology in combination with LAMB cells towards making highly efficient solar cell.

8 CONCLUSIONS AND RECOMMENDATIONS FOR FUTURE

This dissertation explored the growth of InGaAsP alloys using a low-cost method that could be potentially important especially for III-V NW-based solar cells. The NWs were grown by Vapor-Liquid-Solid (VLS) and Vapor-Solid (VS) mechanisms using a Low-Pressure Chemical Vapor Deposition (LPCVD) technique, without requiring the use of lattice-matched single crystal substrates. The concept of supersaturation was employed to control the morphology of NWs through the interplay between VLS and VS growth mechanisms. Comprehensive optical and material characterizations were carried out to evaluate the quality of the grown materials. Concluding remarks on the obtained key results are summarized below.

8.1 Conclusion

A simple, but successful strategy for growth of highly stoichiometric InP nanostructures was presented. Since non-stoichiometric materials are often accompanied by defect emission or less efficient bandedge emission, the presented method in chapter 3 for growth of InP could be potentially important for demonstration of the highly efficient InP-base photonic devices. The growth mechanism of InP NWs was explained by an interplay between VLS and VS growth. The optical properties of InP nanostructures such as NWs, NBs and microdisks showed that all the as grown nanostructures support lasing under high optical pumping conditions.

An Au-catalyzed VLS growth of highly stoichiometric ZB GaP NWs on Si substrates was introduced in chapter 4. It was found that providing the excess P precursor is necessary to replenish the deficiency of P exerted by sublimation of P above the

congruent sublimation temperature of GaP binary source. It was shown that GaP NWs grown under excess P condition result in better stoichiometry and optical properties. From a comprehensive PL study of synthesized NWs using different precursors of GaP and under different growth conditions, NWs grown using GaP and P source material exhibited strong BE emission with a relatively weak DE emission intensity. Furthermore, with a plausible set of data obtained from EDS and BE/DE ratio from PL, a correlation between stoichiometry and concentration of the minority defects was established. Formation of a large enough concentration of such defects during the growth of GaP NWs may preclude them to be used for making the optoelectronic devices. It is therefore imperative to study the crucial role that the growth parameters play in their optical properties. However, there are more aspects of such growth yet to be explored in context of both optical and structural properties. In addition, the versatility of the GaP growth was shown by bandgap tuning of its alloys such as InGaP and GaAsP NWs, simply by adding the As or In source into the growth medium.

Growth of high quality III-V such as InP films using the inexpensive approaches is critical in lowering the cost of solar energy. So far, InP films have been mostly produced using the high-cost precursors using the single-crystal substrates in the case of epitaxial growth. In chapter 5, a low-cost growth of high quality polycrystalline InP thin film and nano-networks using a direct co-evaporation of single elemental In and P precursors via a chemical vapor deposition technique was demonstrated for solar cell applications. A very small deviation from the perfect stoichiometry for the films grown at a wide temperature range of 560 ∘C to 720 ∘C was observed. The proposed method was

shown to be largely independent of type of substrate for both Au and self- (In-) catalyzed growth indicating the versatility of the growth approach. The underlying growth mechanism of nano-networks and coalesced thin films was explained via interplay between VLS and VS regimes. The key role that Au catalyst plays in the promotion of transverse growth was well defined. The grains size and spatial pore filling as well as the thickness of InP film was shown to be controllable by changing the growth parameters. Structural, optical and electrical properties of the grown films were investigated and eventually the preliminary solar cell devices were fabricated on a p-type silicon with an ITO contact layer. It is believed that our growth strategy provides a simpler approach for producing the high quality InP thin films to be used for fabrication of high efficiency solar cells, while lowering the cost for both precursors and growth substrate.

In chapter 6, growth of spatially composition-graded InGaAsP alloy NWs with a widely tunable bandgap on the single substrates was shown. The low-cost dual gradient method in combination with metal-catalyzed VLS approach was utilized to provide both source material dispersion and temperature gradient across the length of the substrate to grow InGaP, InGaAs, and GaAsP alloys with spatially-graded bandgaps. A series of different growth experiments were performed in our homemade CVD setup to find the optimum growth parameters and more specifically the growth window of such materials. Further extension of the range of achievable alloy composition and the associated alloy uniformity is the goal of future investigation. Such unique material capability provides a III-V platform for application in a wide range of novel devices from full spectrum solar cells, multispectral detector, tunable nanolasers, and spectrometer on a chip.

Finally, fabrication of a universal template with uniform pore arrays based on SiO$_2$ coated Si substrate was established. The aim was to develop a templated substrate that can be used to grow a wide range of alloy NP materials, without being limited by typical lattice mismatch, providing a low cost universal platform for future PV. A facile recipe for electroplating metals such as Au, In and Ga into the pores of template was introduced. Subsequently, the growth of InP pillars through both Au-catalyzed VLS growth and phosphorization of In-plated template was demonstrated. It is believed that lowering the cost as a critical issue in fabrication of solar cells can be addressed by further development of such technology in combination with LAMB cells towards making highly efficient solar cell.

8.1 Future Work

Despite the extensive effort made to grow different binaries and associated ternary alloys of InGaAsP, it is still important to push the boundaries of this exploration by further improving the morphology, optical quality and more in-depth structural studies of the grown structures as follows:

For instance, Growth of the InP NWs can be further studied by optimizing the different parameters of growth and controlling the morphology of different nanostructure such as NWs, NBs and nanosheets. Structural phase and crystal quality of InP micropillar should be further studied using HRTEM for study of the WZ/ZB polytypism and stacking faults.

One of the challenging tasks to accomplish is to grow hexagonal wurtzite GaP NWs with direct band gap. With the PL emission falling in the green portion of the

spectrum, direct gap GaP can be used for making the highly efficient LEDs and solar cells.

Growth of monolithic InGaAsP nanobelts can be achieved using a novel growth methodology based on dual ion exchange mechanism similar to our previous work [187] based on II-VI material.

We have, so far, achieved a continuous spatial grading for $In_xGa_{1-x}P$, $In_xGa_{1-x}As$ and $GaAs_xP_{1-x}$ alloys on a single Si substrate. Further extension of the range of achievable alloy composition and the associated alloy uniformity is under investigation. As a near-term future work, the preliminary 3-LAMB solar cell will be demonstrated. It is believed this methodology, the dual gradient method, for bandgap engineering can be extended more generally to other ternary and quaternary alloy systems such as perovskites with wide range of emission wavelengths on a single substrate.

The electroplating recipe developed in the current PhD dissertation can be further extended by electroplating of In-Ga alloys into pore array of template for subsequent growth of ternary InGaP alloy NPs under phosphorization. While the key principle of similar phosphorization process has been explored in the case of InP with high material quality, similar approach to produce III-V NPs has not been demonstrated. It is believed that an in-depth study on both tuning the composition of electroplated In_xGa_{1-x} metal film and subsequent phosphorizarion (arsenidation) process is required. This can raise the hope for making InGaAsP with a high quality using the similar low-cost approach. With no need for using the expensive metal-organic precursors or epitaxial equipment such as MOCVD or MBE and single crystal substrate this method seems very promising as it

REFERENCES

1. http://pveducation.org/pvcdrom/semiconductor-materials

2. Mino, L., Agostini, G., Borfecchia, E., Gianolio, D., Piovano, A., Gallo, E. and Lamberti, C., 2013. Low-dimensional systems investigated by x-ray absorption spectroscopy: a selection of 2D, 1D and 0D cases. Journal of Physics D: Applied Physics, 46(42), p.423001.

3. Van Zeghbroeck, B.J., 1996. Temperature dependence of the energy bandgap. ecee. colorado. edu.

4. Fang, M., Han, N., Wang, F., Yang, Z.X., Yip, S., Dong, G., Hou, J.J., Chueh, Y. and Ho, J.C., 2014. III–V Nanowires: Synthesis, property manipulations, and device applications. Journal of Nanomaterials, 2014, p.4.

5. Joyce, H.J., Gao, Q., Tan, H.H., Jagadish, C., Kim, Y., Zou, J., Smith, L.M., Jackson, H.E., Yarrison-Rice, J.M., Parkinson, P. and Johnston, M.B., 2011. III–V semiconductor nanowires for optoelectronic device applications. Progress in Quantum Electronics, 35(2), pp.23-75.

6. Kavanagh, K.L., 2010. Misfit dislocations in nanowire heterostructures. Semiconductor Science and Technology, 25(2), p.024006.

7. Chuang, L.C., Moewe, M., Chase, C., Kobayashi, N.P., Chang-Hasnain, C. and Crankshaw, S., 2007. Critical diameter for III-V nanowires grown on lattice-mismatched substrates. Applied Physics Letters, 90(4), p.043115.

8. Sarkar, A.R., Kimukin, I., Edgar, C.W., Yi, S.S. and Islam, M.S., 2008. Heteroepitaxial growth dynamics of InP nanowires on silicon. Journal of Nanophotonics, 2(1), p.021775.

9. Garnett, E.C., Brongersma, M.L., Cui, Y. and McGehee, M.D., 2011. Nanowire solar cells. Annual Review of Materials Research, 41, pp.269-295.

10. Krogstrup, P., Jørgensen, H.I., Heiss, M., Demichel, O., Holm, J.V., Aagesen, M., Nygard, J. and i Morral, A.F., 2013. Single-nanowire solar cells beyond the Shockley-Queisser limit. Nature Photonics, 7(4), pp.306-310.

11. Pan, A., Zhou, W., Leong, E.S., Liu, R., Chin, A.H., Zou, B. and Ning, C.Z., 2009. Continuous alloy-composition spatial grading and superbroad wavelength-tunable nanowire lasers on a single chip. Nano letters, 9(2), pp.784-788.

12. Takahashi, T., Nichols, P., Takei, K., Ford, A.C., Jamshidi, A., Wu, M.C., Ning, C.Z. and Javey, A., 2012. Contact printing of compositionally graded CdS_xSe_{1-x} nanowire parallel arrays for tunable photodetectors. Nanotechnology, 23(4), p.045201.

13. Fan, F., Turkdogan, S., Liu, Z., Shelhammer, D. and Ning, C.Z., 2015. A monolithic white laser. Nature nanotechnology, 10(9), pp.796-803.

14. Pan, A., Liu, R., Sun, M. and Ning, C.Z., 2010. Spatial composition grading of quaternary ZnCdSSe alloy nanowires with tunable light emission between 350 and 710 nm on a single substrate. ACS nano, 4(2), pp.671-680.

15. Caselli, D., Liu, Z., Shelhammer, D. and Ning, C.Z., 2014. Composition-graded nanowire solar cells fabricated in a single process for spectrum-splitting photovoltaic systems. Nano letters, 14(10), pp.5772-5779.

16. Zhuang, X., Ning, C.Z. and Pan, A., 2012. Composition and Bandgap-Graded Semiconductor Alloy Nanowires. Advanced Materials, 24(1), pp.13-33.

17. Hoffmann, B., Sivakov, V., Schmitt, S.W., Bashouti, M.Y., Latzel, M., Dluhoš, J., Jiruse, J. and Christiansen, S., 2012. Wet–chemically etched silicon nanowire solar cells: fabrication and advanced characterization. In Nanowires-Recent Advances. InTech.

18. Wagner, R.S. and Ellis, W.C., 1964. Vapor-liquid-solid mechanism of single crystal growth. Applied Physics Letters, 4(5), pp.89-90.

19. Choi, H.J., 2012. Vapor–liquid–solid growth of semiconductor nanowires. In Semiconductor Nanostructures for Optoelectronic Devices (pp. 1-36). Springer Berlin Heidelberg.

20. Chen, L., Lu, W. and Lieber, C.M., 2014, Semiconductor Nanowire Growth and Integration, pp.1-53.

21. Wood, C.E.C., Singer, K., Ohashi, T., Dawson, L.R. and Noreika, A.J., 1983. A pragmatic approach to adatom-induced surface reconstruction of III-V compounds. Journal of Applied Physics, 54(5), pp.2732-2737.

22. Han, N., Wang, F., Hui, A.T., Hou, J.J., Shan, G., Xiu, F., Hung, T. and Ho, J.C., 2011. Facile synthesis and growth mechanism of Ni-catalyzed GaAs nanowires on non-crystalline substrates. Nanotechnology, 22(28), p.285607.

23. Chatillon, C. and Chatain, D., 1995. Congruent vaporization of GaAs (s) and stability of Ga (l) droplets at the GaAs (s) surface. Journal of crystal growth, 151(1-2), pp.91-101.

24. Schmidt, P., Binnewies, M., Glaum, R. and Schmidt, M., 2013. Chemical Vapor Transport Reactions–Methods, Materials, Modeling. In Advanced Topics on Crystal Growth. InTech.

25. Goldstein, B., Szostak, D.J. and Ban, V.S., 1976. Langmuir evaporation from the (100),(111A), and (111B) faces of GaAs. Surface Science, 57(2), pp.733-740.

26. Zi, Y., Jung, K., Zakharov, D. and Yang, C., 2013. Understanding self-aligned planar growth of InAs nanowires. Nano letters.

27. Zhou, Z.Y., Zheng, C.X., Tang, W.X., Jesson, D.E. and Tersoff, J., 2010. Congruent evaporation temperature of GaAs (001) controlled by As flux. Applied Physics Letters, 97(12), p.121912.

28. Philipps, S.P., Bett, A.W., Horowitz, K. and Kurtz, S., 2015. Current status of concentrator photovoltaic (CPV) technology (No. NREL/TP-5J00-65130). NREL (National Renewable Energy Laboratory (NREL), Golden, CO (United States)).

29. Sasaki, K., Agui, T., Nakaido, K., Takahashi, N., Onitsuka, R. and Takamoto, T., 2013, September. Development of InGaP/GaAs/InGaAs inverted triple junction concentrator solar cells. In AIP Conference Proceedings (Vol. 1556, No. 1, pp. 22-25). AIP.

30. Fraunhofer ISE, New world record for solar cell efficiency at 46%, http://www.ise.fraunhofer.de/en/press-and-media/press-releases/pressreleases-2014/new-world-record-for-solar-cell-efficiency-at-46-percent (2014).

31. Caselli, D. A., and C. Z. Ning. "High-performance laterally-arranged multiple-bandgap solar cells using spatially composition-graded $Cd_xPb_{1-x}S$ nanowires on a single substrate: a design study." Optics express 19.104 (2011): A686-A694.

32. Arthur, J.R., 1967. Vapor pressures and phase equilibria in the GaAs system. Journal of Physics and Chemistry of Solids, 28(11), pp.2257-2267.

33. Tatsumi, M., Y. Hosokawa, T. Iwasaki, N. Toyoda, and K. Fujita. "Growth and characterization of III–V materials grown by vapor-pressure-controlled Czochralski method: comparison with standard liquid-encapsulated Czochralski materials." Materials Science and Engineering: B 28, no. 1-3 (1994): 65-71

34. https://www.crystec.com/klllpcvde.htm

35. Hoffman, D. M.; Singh, B.; Thomas, J. H. Handbook of Vacuum Science and Technology; Academic Press: San Diego, 1998; pp 17-29.

36. Blocher Jr, J.M., 1974. Structure/property/process relationships in chemical vapor deposition CVD. Journal of Vacuum Science and Technology, 11(4), pp.680-686.

37. Chen, X., Lenhert, S., Hirtz, M., Lu, N., Fuchs, H. and Chi, L., 2007. Langmuir–Blodgett patterning: a bottom–up way to build mesostructures over large areas. Accounts of chemical research, 40(6), pp.393-401.

38. Lee, S., Teshima, K., Fujisawa, M., Fujii, S., Endo, M. and Oishi, S., 2009. Fabrication of highly ordered, macroporous $Na_2W_4O_{13}$ arrays by spray pyrolysis using polystyrene colloidal crystals as templates. Physical Chemistry Chemical Physics, 11(19), pp.3628-3633.

39. Dai, Z., Li, Y., Duan, G., Jia, L. and Cai, W., 2012. Phase diagram, design of monolayer binary colloidal crystals, and their fabrication based on ethanol-assisted self-assembly at the air/water interface. Acs Nano, 6(8), pp.6706-6716.

40. https://www.oxford-instruments.com/products/etching-deposition-and-growth/plasma-etch-deposition/pecvd

41. Joyce, Hannah Jane. Growth and Characterization of III-V Semiconductor Nanowires for Optoelectronic Device Applications. Australian National University, 2009.

42. Williams, David B., and C. Barry Carter. The Transmission Electron Microscope. Springer Us, 1996.].

43. Bell, D.C., Wu, Y., Barrelet, C.J., Gradečak, S., Xiang, J., Timko, B.P. and Lieber, C.M., 2004. Imaging and analysis of nanowires. Microscopy research and technique, 64(5-6), pp.373-389

44. Gilliland, G.D., 1997. Photoluminescence spectroscopy of crystalline semiconductors. Materials Science and Engineering: R: Reports, 18(3-6), pp.99-399.

45. Turkdogan, S., 2015. Growth and Characterization of Multisegment Chalcogenide Alloy Nanostructures for Photonic Applications in a Wide Spectral Range. Arizona State University.

46. http://www.horiba.com/fileadmin/uploads/Scientific/Documents/Fluorescence/Tech_Note1_-_Lifetime_measurements.pdf

47. W. Becker, The bh TCSPC handbook, 2nd Ed. (Becker & Hickl GmbH, 2006).

48. Yin, L., 2013. Synthesis and Characterization of Erbium Compound Nanowires as High Gain Optical Materials. Arizona State University.

49. Raman, C.V. and Krishnan, K.S., 1928. A new type of secondary radiation. Nature, 121(3048), pp.501-502.

50. Wang, J.B., Li, Z.F., Chen, P.P., Lu, W. and Yao, T., 2007. Raman study of gap mode and lattice disorder effect in InN films prepared by plasma-assisted molecular beam epitaxy. *Acta materialia*, *55*(1), pp.183-187.

51. https://en.wikipedia.org/wiki/Raman_spectroscopy

52. Denton, Alan R., and Neil W. Ashcroft. "Vegard's law." Physical review A 43.6 (1991): 3161.

53. https://commons.wikimedia.org/wiki/File:EDX-scheme.svg

54. http://web.mit.edu/magzpavz/www/Fall%202014/8.13-3rdpaper-XRayPhysics.pdf

55. https://www.mccrone.com/mm/low-voltage-microanalysis/

56. Nichols, Patricia, Growth and Characterization of Chalcogenide Alloy Nanowires with Controlled Spatial Composition Variation for Optoelectronic Applications, 2012.

57. Edwin Hall (1879). "On a New Action of the Magnet on Electric Currents". American Journal of Mathematics. 2 (3): 287–92.

58. "The Hall Effect". NIST. Retrieved 2008-02-28

59. Green, R., 2011. Hall Effect Measurements in Materials Characterization. White paper, (3111).

60. Lindholm, F. A., J. G. Fossum, and E. L. Burgess, "Application of the superposition principle to solar-cell analysis", IEEE Transactions on Electron Devices, vol. 26, no. 3, pp. 165–171, 1979.

61. Li, K., Ng, K.W., Tran, T.T.D., Sun, H., Lu, F. and Chang-Hasnain, C.J., 2015. Wurtzite-phased InP micropillars grown on silicon with low surface recombination velocity. Nano letters, 15(11), pp.7189-7198.

62. Gao, Q., Saxena, D., Wang, F., Fu, L., Mokkapati, S., Guo, Y., Li, L., Wong-Leung, J., Caroff, P., Tan, H.H. and Jagadish, C., 2014. Selective-area epitaxy of pure wurtzite InP nanowires: high quantum efficiency and room-temperature lasing. Nano letters, 14(9), pp.5206-5211.

63. Amiri, S.E.H., Turkdogan, S., Fan, F., Yu, Y., Ranga, P. and Ning, C.Z., 2016, June. Growth of stoichiometric InP nanowires/nanobelts by a facile vapor transport method. In CLEO: Science and Innovations (pp. SM1R-6). Optical Society of America.

64. Hiruma, K.; Yazawa, M.; Katsuyama, T.; Ogawa, K.; Haraguchi, K.; Koguchi, M.; Kakibayashi, H. J. Appl. Phys. 1995, 77 (2), 447–462.

65. Fortuna, S.A., Wen, J., Chun, I.S. and Li, X., 2008. Planar GaAs nanowires on GaAs (100) substrates: self-aligned, nearly twin-defect free, and transfer-printable. Nano Letters, 8(12), pp.4421-4427.

66. Wu, Z.H., Mei, X., Kim, D., Blumin, M., Ruda, H.E., Liu, J.Q. and Kavanagh, K.L., 2003. Growth, branching, and kinking of molecular-beam epitaxial< 110> GaAs nanowires. Applied physics letters, 83(16), pp.3368-3370.

67. Krishnamachari, U., Borgstrom, M., Ohlsson, B.J., Panev, N., Samuelson, L., Seifert, W., Larsson, M.W. and Wallenberg, L.R., 2004. Defect-free InP nanowires grown in [001] direction on InP (001). Applied Physics Letters, 85(11), pp.2077-2079.

68. Mikkelsen, A., Eriksson, J., Lundgren, E., Andersen, J.N., Weissenrieder, J. and Seifert, W., 2005. The influence of lysine on InP (001) surface ordering and nanowire growth. Nanotechnology, 16(10), p.2354.

69. Fonseka, H.A., Caroff, P., Wong-Leung, J., Ameruddin, A.S., Tan, H.H. and Jagadish, C., 2014. Nanowires grown on InP (100): growth directions, facets, crystal structures, and relative yield control. ACS nano, 8(7), pp.6945-6954.

70. Wan J, Plissard S R, Verheijen M A, Feiner L-F, Cavalli A and Bakkers E P A M 2013 Reversible switching of InP nanowire growth direction by catalyst engineering Nano Lett. 13 3802

71. Watson, D.C., Martinez, R.V., Fontana, Y., Russo-Averchi, E., Heiss, M., Fontcuberta i Morral, A., Whitesides, G.M. and Lončar, M., 2014. Nanoskiving Core–Shell Nanowires: A New Fabrication Method for Nano-optics. Nano letters, 14(2), pp.524-531.

72. Chen, C.; Plante, M. C.; Fradin, C. & LaPierre, R. R. (2006). Layer-by-layer and step-flow growth mechanisms in GaAsP/GaP nanowire heterostructures, J. Mat. Res., 21, 2801-2809.

73. Dayeh, Shadi A., Edward T. Yu, and Deli Wang. "III-V nanowire growth mechanism: V/III ratio and temperature effects." Nano letters 7.8 (2007): 2486-2490.

74. Fonseka, H. A., et al. "High vertical yield InP nanowire growth on Si (111) using a thin buffer layer." Nanotechnology 24.46 (2013): 465602.

75. Du, L. and Lei, Y., 2013. Synthesis of high-quality Cl-doped CdSe nanobelts and their application in nanodevices. Materials Letters, 106, pp.100-103

76. Siu, Chun Kit, Junqian Zhao, Yunfeng Wang, Decheng Yang, Xuhui Xu, Shusheng Pan, and Siu Fung Yu. "Lasing characteristics of single-crystalline CsPbCl$_3$ perovskite microcavities under multiphoton excitation., J. Phys. D: Appl. Phys. 50 (2017) 225101 (6pp)

77. Yan, Ruoxue, Daniel Gargas, and Peidong Yang. "Nanowire photonics." Nature Photonics 3.10 (2009): 569-576.

78. Zimmler, Mariano A., et al. "Optically pumped nanowire lasers: invited review." Semiconductor Science and Technology 25.2 (2010): 024001.

79. Patzke, G.R., Kontic, R., Shiolashvili, Z., Makhatadze, N. and Jishiashvili, D., 2012. Hydrazine-assisted formation of Indium Phosphide (InP)-based nanowires and core-shell composites. Materials, 6(1), pp.85-100.

80. Craford, M.G., Dupuis, R.D., Feng, M., Kish, F.A. and Laskar, J., 2013. 50th anniversary of the light-emitting diode (LED): An ultimate lamp [scanning the issue]. Proceedings of the IEEE, 101(10), pp.2154-2157.

81. Feifel, M., Rachow, T., Benick, J., Ohlmann, J., Janz, S., Hermle, M., Dimroth, F. and Lackner, D., 2016. Gallium phosphide window layer for silicon solar cells. IEEE Journal of Photovoltaics, 6(1), pp.384-390.

82. Standing, A., Assali, S., Gao, L., Verheijen, M.A., Van Dam, D., Cui, Y., Notten, P.H., Haverkort, J.E. and Bakkers, E.P., 2015. Efficient water reduction with gallium phosphide nanowires. Nature communications, 6.

83. Tietjen, J. J. & Amick, J. A. The preparation and properties of vapor-deposited epitaxial GaAs$_{1-x}$P$_x$ using arsine and phosphine. J. Electrochem. Soc. 113, 724–728 (1966).

84. Kornienko, N., Whitmore, D.D., Yu, Y., Leone, S.R. and Yang, P., 2015. Solution phase synthesis of indium gallium phosphide alloy nanowires. ACS nano, 9(4), pp.3951-3960.

85. Amiri, S.E.H., Ranga, P., Li, D. and Ning, C.Z., 2017, May. Growth of InGaP Alloy Nanowires with Widely Tunable Bandgaps on Silicon Substrates. In CLEO: Science and Innovations (pp. STh3I-4). Optical Society of America.

86. Shi, W.S., Zheng, Y.F., Wang, N., Lee, C.S. and Lee, S.T., 2001. Synthesis and microstructure of gallium phosphide nanowires. Journal of Vacuum Science & Technology B: Microelectronics and Nanometer Structures Processing, Measurement, and Phenomena, 19(4), pp.1115-1118.

87. Assali, S., Zardo, I., Plissard, S., Kriegner, D., Verheijen, M.A., Bauer, G., Meijerink, A., Belabbes, A., Bechstedt, F., Haverkort, J.E.M. and Bakkers, E.P.A.M., 2013. Direct band gap wurtzite gallium phosphide nanowires. Nano letters, 13(4), p.1559.

88. Boulanger, J. P., and R. R. Lapierre. "Patterned gold-assisted growth of GaP nanowires on Si." Semiconductor Science and Technology 27.3 (2012): 035002.

89. Liu, C., Sun, J., Tang, J. and Yang, P., 2012. Zn-doped p-type gallium phosphide nanowire photocathodes from a surfactant-free solution synthesis. Nano letters, 12(10), pp.5407-5411.

90. Gu, Zhanjun, M. Parans Paranthaman, and Zhengwei Pan. "Vapor-phase synthesis of gallium phosphide nanowires." Crystal Growth and Design 9.1 (2008): 525-527.

91. Seo, H.W., Bae, S.Y., Park, J., Yang, H. and Kim, S., 2002. Synthesis of gallium phosphide nanowires via sublimation method. Chemical Communications, (21), pp.2564-2565.

92. Shen, G., Bando, Y. and Golberg, D., 2007. InP-GaP Bi-Coaxial Nanowires and Amorphous GaP Nanotubes. The Journal of Physical Chemistry C, 111(9), pp.3665-3668.

93. Lyu, S.C., Zhang, Y., Ruh, H., Lee, H.J. and Lee, C.J., 2003. Synthesis of high-purity GaP nanowires using a vapor deposition method. Chemical physics letters, 367(5-6), pp.717-722.

94. Craford, M. George, and W. O. Groves. "Vapor phase epitaxial materials for LED applications." Proceedings of the IEEE 61.7 (1973): 862-880.

95. Tahini, H.A., Chroneos, A., Murphy, S.T., Schwingenschlögl, U. and Grimes, R.W., 2013. Vacancies and defect levels in III–V semiconductors. Journal of Applied Physics, 114(6), p.063517.

96. Fazzio, A., L. M. Brescansin, and J. R. Leite. "Electronic structure of neutral and negatively charged gallium vacancies in GaP." Journal of Physics C: Solid State Physics 15.2 (1982): L1.

97. Wang, L., Wolk, J.A., Hsu, L., Haller, E.E., Erickson, J.W., Cardona, M., Ruf, T., Silveira, J.P. and Briones, F., 1997. Gallium self-diffusion in gallium phosphide. Applied physics letters, 70(14), pp.1831-1833.

98. Jordan, A.S., Caruso, R., Von Neida, A.R. and Weiner, M.E., 1974. Solid composition and gallium and phosphorus vacancy concentration isobars for GaP. Journal of Applied Physics, 45(8), pp.3472-3476.

99. Höglund, A., Castleton, C.W. and Mirbt, S., 2005. Relative concentration and structure of native defects in GaP. Physical Review B, 72(19), p.195213.

100. Sheetz, R.M., Ponomareva, I., Richter, E., Andriotis, A.N. and Menon, M., 2009. Defect-induced optical absorption in the visible range in ZnO nanowires. Physical Review B, 80(19), p.195314.

101. Philipose, U., Xu, T., Yang, S., Sun, P., Ruda, H.E., Wang, Y.Q. and Kavanagh, K.L., 2006. Enhancement of band edge luminescence in ZnSe nanowires. Journal of applied physics, 100(8), p.084316.

102. Mori, H., M. Ogasawara, M. Yamamoto, and M. Tachikawa. "New hydride vapor phase epitaxy for GaP growth on Si." Applied physics letters 51, no. 16 (1987): 1245-1247.

103. Ledentsov, Nikolai N. Growth processes and surface phase equilibria in molecular beam epitaxy. Vol. 156. Springer Science & Business Media, 1999

104. Rinaldi, Fernando. "Basics of molecular beam epitaxy (MBE)." Annual Report (2002): 1-8.

105. Mondry, M. J., E. J. Caine, and H. Kroemer. "A GaP decomposition source for producing a dimer phosphorus molecular beam free of gallium and tetramer phosphorus." Journal of Vacuum Science & Technology A: Vacuum, Surfaces, and Films 3.2 (1985): 316-318.

106. Ledentsov, N.N., 1999. Growth processes and surface phase equilibria in molecular beam epitaxy (Vol. 156). Springer Science & Business Media.

107. Wang, J.B., Li, Z.F., Chen, P.P., Lu, W. and Yao, T., 2007. Raman study of gap mode and lattice disorder effect in InN films prepared by plasma-assisted molecular beam epitaxy. Acta materialia, 55(1), pp.183-187.

108. Nasibov, A.S., Mel'nik, N.N., Ponomarev, I.V., Romanko, S.V., Topchii, S.B., Obraztsov, A.N., Bashtanov, M.Y. and Krasnovskii, A.A., 1998. Copper and gold vapour lasers for spectroscopy. Quantum electronics, 28(5), p.403.

109. He, Y., El-Masry, N.A., Ramdani, J., Bedair, S.M., McCormick, T.L., Nemanich, R.J. and Weber, E.R., 1994. Determination of excess phosphorus in low-temperature GaP grown by gas source molecular beam epitaxy. Applied physics letters, 65(13), pp.1671-1673.

110.   Kuriyama, K., Y. Miyamoto, and M. Okada. "Redshift of the longitudinal optical phonon in neutron irradiated GaP." Journal of applied physics 85.7 (1999): 3499-3502.

111.   Lewis, I.R. and Edwards, H., 2001. Handbook of Raman spectroscopy: from the research laboratory to the process line. CRC Press.

112.   109. Cantarero, A., 2013. Review on Raman scattering in semiconductor nanowires: I. theory. Journal of Nanophotonics, 7(1), pp.071598-071598.

113.   110. de la Chapelle, M. Lamy, H. X. Han, and C. C. Tang. "Raman scattering from GaP nanowires." The European Physical Journal B-Condensed Matter and Complex Systems 46.4 (2005): 507-513.

114.   111. Wu, J., Zhang, D., Lu, Q., Gutierrez, H.R. and Eklund, P.C., 2010. Polarized Raman scattering from single GaP nanowires. Physical Review B, 81(16), p.165415.

115.   112. Gupta, R., Xiong, Q., Mahan, G.D. and Eklund, P.C., 2003. Surface optical phonons in gallium phosphide nanowires. Nano Letters, 3(12), pp.1745-1750.

116.   113. Adu, K.W., Xiong, Q., Gutierrez, H.R., Chen, G. and Eklund, P.C., 2006. Raman scattering as a probe of phonon confinement and surface optical modes in semiconducting nanowires. Applied Physics A, 85(3), p.287.

117.   114. Zardo, I., Conesa-Boj, S., Peiro, F., Morante, J.R., Arbiol, J., Uccelli, E., Abstreiter, G. and i Morral, A.F., 2009. Raman spectroscopy of wurtzite and zinc-blende GaAs nanowires: polarization dependence, selection rules, and strain effects. Physical review B, 80(24), p.245324.

118.   115. Xiong, Qihua, J. Wang, and P. C. Eklund. "Coherent twinning phenomena: Towards twinning superlattices in III-V semiconducting nanowires." Nano letters 6.12 (2006): 2736-2742.

119.   116. Caroff, P., Dick, K.A., Johansson, J., Messing, M.E., Deppert, K. and Samuelson, L., 2009. Controlled polytypic and twin-plane superlattices in III–V nanowires. Nature nanotechnology, 4(1), pp.50-55.

120.   117. Ikonic, Z., G. P. Srivastava, and J. C. Inkson. "Optical properties of twinning superlattices in diamond-type and zinc-blende-type semiconductors." Physical Review B 52.19 (1995): 14078.

121.   118. Stiltz, S., "Au-Ga-P Ternary Phase Diagram Evaluation", in MSI Eureka, Effenberg, G. (Ed.), MSI, Materials Science International Services GmbH, Stuttgart (1995), Document ID: 10.21427.1.1 (Crys. Structure, Phase Diagram, Phase Relations, Assessment, 4)

122.   119. Harmand, J.C., Patriarche, G., Péré-Laperne, N., Merat-Combes, M.N., Travers, L. and Glas, F., 2005. Analysis of vapor-liquid-solid mechanism in Au-assisted GaAs nanowire growth. Applied Physics Letters, 87(20), p.203101.

123.   120. Persson, A.I., Larsson, M.W., Stenström, S., Ohlsson, B.J., Samuelson, L. and Wallenberg, L.R., 2004. Solid-phase diffusion mechanism for GaAs nanowire growth. Nature materials, 3(10), pp.677-681.

124.   Gu, Qilin, and B. Wang. "Correlation between structural defects and optical properties of Cu_2O nanowires grown by thermal oxidation." arXiv preprint arXiv:1012.5338 (2010).

125.   Lähnemann, Jonas, Uwe Jahn, Oliver Brandt, Timur Flissikowski, Pinar Dogan, and Holger T. Grahn. "Luminescence associated with stacking faults in GaN." Journal of Physics D: Applied Physics 47, no. 42 (2014): 423001.

126.   Philipose, U., Yang, S., Xu, T. and Ruda, H.E., 2007, Origin of the red luminescence band in photoluminescence spectra of ZnSe nanowires. Applied physics letters, 90(6), p.063103.

127.   Scheffler, Matthias, J. Bernholc, N. O. Lipari, and Sokrates T. Pantelides. "Electronic structure and identification of deep defects in GaP." Physical Review B 29, no. 6 (1984): 3269.

128.   Kohn, Walter, and Lu Jeu Sham. "Self-consistent equations including exchange and correlation effects." Physical review 140.4A (1965): A1133.

129.   Scheffler, M., Bernholc, J., Lipari, N.O. and Pantelides, S.T., 1984. Electronic structure and identification of deep defects in GaP. Physical Review B, 29(6), p.3269.

130.   Yin, X., Battaglia, C., Lin, Y., Chen, K., Hettick, M., Zheng, M., Chen, C.Y., Kiriya, D. and Javey, A., 2014. 19.2% Efficient InP heterojunction solar cell with electron-selective TiO2 contact. ACS photonics, 1(12), p.1245.

131.   Wallentin, J., Anttu, N., Asoli, D., Huffman, M., Åberg, I., Magnusson, M.H., Siefer, G., Fuss-Kailuweit, P., Dimroth, F., Witzigmann, B. and Xu, H.Q., 2013. InP nanowire array solar cells achieving 13.8% efficiency by exceeding the ray optics limit. Science, 339(6123), pp.1057-1060.

132.   Li, N., Lee, K., Renshaw, C.K., Xiao, X. and Forrest, S.R., 2011. Improved power conversion efficiency of InP solar cells using organic window layers. Applied Physics Letters, 98(5), p.053504.

133. Cotal, H., Fetzer, C., Boisvert, J., Kinsey, G., King, R., Hebert, P., Yoon, H. and Karam, N., 2009. III–V multijunction solar cells for concentrating photovoltaics. Energy & Environmental Science, 2(2), pp.174-192.

134. Akahori, K., Wang, G., Okumura, K., Soga, T., Jimbo, T. and Umeno, M., 2001. Improvement of the MOCVD-grown InGaP-on-Si towards high-efficiency solar cell application. Solar energy materials and solar cells, 66(1), pp.593-598.

135. Fairhurst, K., Lee, D., Robertson, D.S., Parfitt, H.T. and Wilgoss, W.H.E., 1981. A study of vapour phase epitaxy of indium phosphide. Journal of Materials Science, 16(4), pp.1013-1022.

136. Zhu, L.D., Chan, K.T. and Ballantyne, J.M., 1985. Very high mobility InP grown by low pressure metalorganic vapor phase epitaxy using solid trimethylindium source. Applied Physics Letters, 47(1), pp.47-48.

137. Sze, Simon M., and Kwok K. Ng. Physics of semiconductor devices. John wiley & sons, 2006

138. Nakamura, T. and Katoda, T., 1984. Effects of optically excited carriers on Raman spectra from InP. Journal of applied physics, 55(8), pp.3064-3067.

139. Rosenwaks, Y., Shapira, Y. and Huppert, D., 1992. Picosecond time-resolved luminescence studies of surface and bulk recombination processes in InP. Physical Review B, 45(16), p.9108.

140. Jastrzebski, L., Lagowski, J. and Gatos, H.C., 1975. Application of scanning electron microscopy to determination of surface recombination velocity: GaAs. Applied Physics Letters, 27(10), pp.537-539.

141. Nolte, D.D., 1990. Surface recombination, free-carrier saturation, and dangling bonds in InP and GaAs. Solid-state electronics, 33(2), pp.295-298.

142. Lloyd-Hughes, J., Merchant, S.K.E., Fu, L., Tan, H.H., Jagadish, C., Castro-Camus, E. and Johnston, M.B., 2006. Influence of surface passivation on ultrafast carrier dynamics and terahertz radiation generation in GaAs. Applied physics letters, 89(23), p.232102.

143. Mertens, Konrad. Photovoltaics: fundamentals, technology and practice. John Wiley & Sons, 2013.

144. Turner, W.J., Reese, W.E. and Pettit, G.D., 1964. Exciton absorption and emission in InP. Physical Review, 136(5A), p.A1467.

145. Zheng, M., Horowitz, K., Woodhouse, M., Battaglia, C., Kapadia, R. and Javey, A., 2016. III-Vs at scale: a PV manufacturing cost analysis of the thin film vapor–liquid–solid growth mode. Progress in Photovoltaics: Research and Applications, 24(6), pp.871-878.

146. Yamaguchi, M., Yamamoto, A., Uchida, N. and Uemura, C., 1986. A new approach for thin film InP solar cells. Solar Cells, 19(1), pp.85-96.

147. Zheng, M., Yu, Z., Joon Seok, T., Chen, Y.Z., Kapadia, R., Takei, K., Aloni, S., Ager, J.W., Wu, M., Chueh, Y.L. and Javey, A., 2012. High optical quality polycrystalline indium phosphide grown on metal substrates by metalorganic chemical vapor deposition. Journal of Applied Physics, 111(12), p.123112.

148. Morales, F.M., García, R., Molina, S.I., Aouni, A., Postigo, P.A. and Fonstad, C.G., 2009. Microstructural improvements of InP on GaAs (001) grown by molecular beam epitaxy by in situ hydrogenation and postgrowth annealing. Applied Physics Letters, 94(4), p.041919.

149. Kapadia, R., Yu, Z., Wang, H.H.H., Zheng, M., Battaglia, C., Hettick, M., Kiriya, D., Takei, K., Lobaccaro, P., Beeman, J.W. and Ager, J.W., 2013. A direct thin-film path towards low-cost large-area III-V photovoltaics. Scientific reports, 3, p.srep02275.

150. Kiriya, D., Zheng, M., Kapadia, R., Zhang, J., Hettick, M., Yu, Z., Takei, K., Hank Wang, H.H., Lobaccaro, P. and Javey, A., 2012. Morphological and spatial control of InP growth using closed-space sublimation. Journal of Applied Physics, 112(12), p.123102.

151. Paiman, S., Gao, Q., Joyce, H.J., Kim, Y., Tan, H.H., Jagadish, C., Zhang, X., Guo, Y. and Zou, J., 2010. Growth temperature and V/III ratio effects on the morphology and crystal structure of InP nanowires. Journal of Physics D: Applied Physics, 43(44), p.445402.

152. Palisaitis, J. and Vasiliauskas, R., 2008. Epitaxial growth of thin films. Physics of Advanced Materials Winter School, pp.1-16.

153. Cverna, F. ed., 2002. ASM ready reference: thermal properties of metals. ASM International.

154. Chen, Lin, Wei Lu, and Charles M. Lieber. "Semiconductor Nanowire Growth and Integration." (2014): 1-53.

155. Dubrovskii, V. G., et al. "Length distributions of Au-catalyzed and In-catalyzed InAs nanowires." Nanotechnology 27.37 (2016): 375602.

156.   ICDD PDF-2, Entry 00–010-0216, 2003.

157.   Artús, L., et al. "Up to fifth-order Raman scattering of InP under nonresonant conditions." Physical Review B 50.16 (1994): 11552.

158.   Alfrey, G. F., and P. H. Borcherds. "Phonon frequencies from the Raman spectrum of indium phosphide." Journal of Physics C: Solid State Physics 5.20 (1972): L275.

159.   Schmidt, T., K. Lischka, and W. Zulehner. "Excitation-power dependence of the near-band-edge photoluminescence of semiconductors." Physical Review B 45.16 (1992): 8989.

160.   Mao, L., Sun, N., Zhou, X., Wu, X., Guo, W., Hu, M., Li, L., Xiao, M., Fu, J., Yao, Z. and Zhao, Y., 2004, September. Character of non-stoichiometric InP bulk crystal. In Semiconducting and Insulating Materials, 2004. SIMC-XIII-2004. 13th International Conference on (pp. 19-22). IEEE.

161.   Chen, X.D., Sun, N.F., Sun, T.N., Liu, S.L., Yang, G.Y., Zhao, Y.W., Xu, X.L., Beling, C.D. and Fung, S., 1998, May. Electrical and FT-IR measurements of undoped n-type InP materials grown from various stoichiometric melts. In Indium Phosphide and Related Materials, 1998 International Conference on (pp. 42-44). IEEE.

162.   Roy, J. N., S. Basu, and D. N. Bose. "Grain size dependence of mobility in polycrystalline n-indium phosphide." Journal of applied physics 54.2 (1983): 847-852.

163.   Anderson, D.A., Apsley, N., Davies, P. and Giles, P.L., 1985. Compensation in heavily doped n-type InP and GaAs. Journal of applied physics, 58(8), pp.3059-3067.

164.   Parguel, V., Favennec, P.N., Gauneau, M., Rihet, Y., Chaplain, R., L'Haridon, H. and Vaudry, C., 1987. Gold diffusion in InP. Journal of applied physics, 62(3), pp.824-827.

165.   Breuer, S., Pfüller, C., Flissikowski, T., Brandt, O., Grahn, H.T., Geelhaar, L. and Riechert, H., 2011. Suitability of Au-and self-assisted GaAs nanowires for optoelectronic applications. Nano letters, 11(3), pp.1276-1279.

166.   Jiang, N., Parkinson, P., Gao, Q., Breuer, S., Tan, H.H., Wong-Leung, J. and Jagadish, C., 2012. Long minority carrier lifetime in Au-catalyzed GaAs/AlxGa1−xAs core-shell nanowires. Applied Physics Letters, 101(2), p.023111.

167.   Tambe, M.J., Ren, S. and Gradecak, S., 2010. Effects of gold diffusion on n-type doping of GaAs nanowires. Nano letters, 10(11), pp.4584-4589.

168. Lin, Q., Sarkar, D., Lin, Y., Yeung, M., Blankemeier, L., Hazra, J., Wang, W., Niu, S., Ravichandran, J., Fan, Z. and Kapadia, R., 2017. Scalable Indium Phosphide Thin-Film Nanophotonics Platform for Photovoltaic and Photoelectrochemical Devices. ACS nano.

169. Metaferia, W., Sun, Y.T., Pietralunga, S.M., Zani, M., Tagliaferri, A. and Lourdudoss, S., 2014. Polycrystalline indium phosphide on silicon by indium assisted growth in hydride vapor phase epitaxy. Journal of Applied Physics, 116(3), p.033519.

170. Gayen, R. N., Das, S. N., Dalui, S., Paul, R., Bhar, R., & Pal, A. K. (2010)., Thin Solid Films, 518(14), 3595-3603.

171. Iribarren, A., Castro-Rodríguez, R., Ponce-Cabrera, L., & Peña, J. L. (2006)., Thin solid films, 510(1), 134-137.

172. Chandra, G. H., de la Cruz, J. P., & Ventura, J. (2011)., Semiconductor Science and Technology, 26(7), 075017.

173. Öztaş, M., Bedir, M., Kayalı, R., & Aksoy, F. (2006)., Journal of Materials Science: Materials in Electronics, 17(10), 841-845.

174. Sanatinia, R., Berrier, A., Dhaka, V., Perros, A.P., Huhtio, T., Lipsanen, H. and Anand, S., 2015. Wafer-scale self-organized InP nanopillars with controlled orientation for photovoltaic devices. Nanotechnology, 26(41), p.415304.

175. Cui, Y., Wang, J., Plissard, S.R., Cavalli, A., Vu, T.T., van Veldhoven, R.P., Gao, L., Trainor, M., Verheijen, M.A., Haverkort, J.E. and Bakkers, E.P., 2013. Efficiency enhancement of InP nanowire solar cells by surface cleaning. Nano letters, 13(9), pp.4113-4117.

176. Nagel, James R., and Michael A. Scarpulla. "Enhanced absorption in optically thin solar cells by scattering from embedded dielectric nanoparticles." Optics express 18.102 (2010): A139-A146.

177. West, B.M., Stuckelberger, M., Guthrey, H., Chen, L., Lai, B., Maser, J., Rose, V., Shafarman, W., Al-Jassim, M. and Bertoni, M.I., 2017. Grain engineering: How nanoscale inhomogeneities can control charge collection in solar cells. Nano Energy, 32, pp.488-493.

178. Bhandari, K.P., Collier, J.M., Ellingson, R.J. and Apul, D.S., 2015. Energy payback time (EPBT) and energy return on energy invested (EROI) of solar photovoltaic systems: A systematic review and meta-analysis. Renewable and Sustainable Energy Reviews, 47, pp.133-141.

179. Mårtensson, Thomas, C. Patrik T. Svensson, Brent A. Wacaser, Magnus W. Larsson, Werner Seifert, Knut Deppert, Anders Gustafsson, L. Reine Wallenberg, and Lars Samuelson. "Epitaxial III− V nanowires on silicon." Nano Letters 4, no. 10 (2004): 1987-1990.

180. Kuykendall, T., Ulrich, P., Aloni, S. and Yang, P., 2007. Complete composition tunability of InGaN nanowires using a combinatorial approach. Nature materials, 6(12), pp.951-956.

181. Jung, C.S., Kim, H.S., Jung, G.B., Gong, K.J., Cho, Y.J., Jang, S.Y., Kim, C.H., Lee, C.W. and Park, J., 2011. Composition and phase tuned InGaAs alloy nanowires. The Journal of Physical Chemistry C, 115(16), pp.7843-7850.

182. Im, H.S., Jung, C.S., Park, K., Jang, D.M., Lim, Y.R. and Park, J., 2014. Band gap tuning of twinned GaAsP ternary nanowires. The Journal of Physical Chemistry C, 118(8), pp.4546-4552.

183. Caselli, D. and Ning, C.Z., 2015. Monolithically-integrated laterally-arrayed multiple bandgap solar cells for spectrum-splitting photovoltaic systems. Progress in Quantum Electronics, 39, pp.24-70.

184. Berg, A., Caroff, P., Shahid, N., Lockrey, M.N., Yuan, X., Borgström, M.T., Tan, H.H. and Jagadish, C., 2017. Growth and optical properties of $In_xGa_{1−x}P$ nanowires synthesized by selective-area epitaxy. Nano Research, 10(2), pp.672-682.

185. Gagliano, L., Belabbes, A., Albani, M., Assali, S., Verheijen, M.A., Miglio, L., Bechstedt, F., Haverkort, J.E.M. and Bakkers, E.P.A.M., 2016. Pseudodirect to Direct Compositional Crossover in Wurtzite $GaP/In_xGa_{1−x}P$ Core–Shell Nanowires. Nano letters, 16(12), pp.7930-7936.

186. Jacobsson, D., Persson, J.M., Kriegner, D., Etzelstorfer, T., Wallentin, J., Wagner, J.B., Stangl, J., Samuelson, L., Deppert, K. and Borgström, M.T., 2012. Particle-assisted $Ga_xIn_{1−x}P$ nanowire growth for designed bandgap structures. Nanotechnology, 23(24), p.245601.

187. Turkdogan, S., Amiri, S.E.H. and Ning, C.Z., 2017. Simultaneous anion and cation exchange processes for the growth of novel optoelectronic structures. Journal of Alloys and Compounds, 724, pp.29-33.

188. A. Zunger and S. Mahajan, in Handbook on Semiconductors, edited by S. Mahajan ~North-Holland, Amsterdam, 1994, Vol. 3.

189.   Stringfellow, G. B. "Miscibility gaps in quaternary III/V alloys." Journal of Crystal Growth 58, no. 1 (1982): 194-202.

190.   Panish, M. B., M. Ilegems, H. Reiss, and J. O. McCaldin. "Progress in solid state chemistry, Vol. 7." (1972): 39.

191.   Segura-Ruiz, J., Martínez-Criado, G., Denker, C., Malindretos, J. and Rizzi, A., 2014. Phase Separation in Single $In_xGa_{1-x}N$ Nanowires Revealed through a Hard X-ray Synchrotron Nanoprobe. Nano letters, 14(3), pp.1300-1305.

192.   Guo, Ya-Nan, Hong-Yi Xu, Graeme J. Auchterlonie, Tim Burgess, Hannah J. Joyce, Qiang Gao, Hark Hoe Tan et al. "Phase separation induced by Au catalysts in ternary InGaAs nanowires." Nano letters 13, no. 2 (2013): 643-650.

193.   Sköld, N., Wagner, J.B., Karlsson, G., Hernán, T., Seifert, W., Pistol, M.E. and Samuelson, L., 2006. Phase segregation in AlInP shells on GaAs nanowires. Nano letters, 6(12), pp.2743-2747.

194.   Nichols, P.L., Liu, Z., Yin, L., Turkdogan, S., Fan, F. and Ning, C.Z., 2015. $Cd_xPb_{1-x}S$ Alloy Nanowires and Heterostructures with Simultaneous Emission in Mid-Infrared and Visible Wavelengths. Nano letters, 15(2), pp.909-916.

195.   Paladugu, M., Zou, J., Guo, Y.N., Zhang, X., Kim, Y., Joyce, H.J., Gao, Q., Tan, H.H. and Jagadish, C., 2008. Nature of heterointerfaces in GaAs/InAs and InAs/GaAs axial nanowire heterostructures. Applied Physics Letters, 93(10), p.101911.

196.   Yang, L., Motohisa, J., Tomioka, K., Takeda, J., Fukui, T., Geng, M.M., Jia, L.X., Zhang, L. and Liu, Y.L., 2008. Fabrication and excitation-power-density-dependent micro-photoluminescence of hexagonal nanopillars with a single InGaAs/GaAs quantum well. Nanotechnology, 19(27), p.275304.

197.   Treu, J., Speckbacher, M., Saller, K., Morkötter, S., Döblinger, M., Xu, X., Riedl, H., Abstreiter, G., Finley, J.J. and Koblmüller, G., 2016. Widely tunable alloy composition and crystal structure in catalyst-free InGaAs nanowire arrays grown by selective area molecular beam epitaxy. Applied Physics Letters, 108(5), p.053110.

198.   Moratis, K., Tan, S.L., Germanis, S., Katsidis, C., Androulidaki, M., Tsagaraki, K., Hatzopoulos, Z., Donatini, F., Cibert, J., Niquet, Y.M. and Mariette, H., 2016. Strained GaAs/InGaAs Core-Shell Nanowires for Photovoltaic Applications. Nanoscale research letters, 11(1), p.176.

199.   Hou, J.J., Wang, F., Han, N., Xiu, F., Yip, S., Fang, M., Lin, H., Hung, T.F. and Ho, J.C., 2012. Stoichiometric Effect on Electrical, Optical, and Structural Properties of Composition-Tunable $In_xGa_{1-x}As$ Nanowires. ACS nano, 6(10), pp.9320-9325.

200. Demichel, O., Heiss, M., Bleuse, J., Mariette, H. and Fontcuberta i Morral, A., 2010. Impact of surfaces on the optical properties of GaAs nanowires. Applied Physics Letters, 97(20), p.201907.

201. Sun, M. H., Leong, E. S. P., Chin, A. H., Ning, C. Z., Cirlin, G. E., Samsonenko, Y. B., Dubrovskii, V. G., Chuang, L. and Chang-Hasnain, C., 2010. Photoluminescence properties of InAs nanowires grown on GaAs and Si substrates. Nanotechnology, 21(33), p.335705.

202. Sun, M.H., Joyce, H.J., Gao, Q., Tan, H.H., Jagadish, C. and Ning, C.Z., 2012. Removal of surface states and recovery of band-edge emission in InAs nanowires through surface passivation. Nano letters, 12(7), pp.3378-3384.

203. Westwater, J., Gosain, D.P. and Usui, S., 1997. Control of the size and position of silicon nanowires grown via the vapor-liquid-solid technique. Japanese journal of applied physics, 36(10R), p.6204.

204. Mårtensson, T., Borgström, M., Seifert, W., Ohlsson, B.J. and Samuelson, L., 2003. Fabrication of individually seeded nanowire arrays by vapour–liquid–solid growth. Nanotechnology, 14(12), p.1255.

205. Kuykendall, T.R., Altoe, M.V.P., Ogletree, D.F. and Aloni, S., 2014. Catalyst-directed crystallographic orientation control of GaN nanowire growth. Nano letters, 14(12), pp.6767-6773.

206. Cho, J.H. and Picraux, S.T., 2013. Enhanced lithium ion battery cycling of silicon nanowire anodes by template growth to eliminate silicon underlayer islands. Nano letters, 13(11), pp.5740-5747.

207. Byun, J., Lee, J.I., Kwon, S., Jeon, G. and Kim, J.K., 2010. Highly Ordered Nanoporous Alumina on Conducting Substrates with Adhesion Enhanced by Surface Modification: Universal Templates for Ultrahigh-Density Arrays of Nanorods. Advanced Materials, 22(18), pp.2028-2032.

208. Zhang, Z., Shimizu, T., Senz, S. and Gösele, U., 2009. Ordered High-Density Si [100] Nanowire Arrays Epitaxially Grown by Bottom Imprint Method. Advanced Materials, 21(27), pp.2824-2828.

209. Shimizu, T., Xie, T., Nishikawa, J., Shingubara, S., Senz, S. and Gösele, U., 2007. Synthesis of Vertical High-Density Epitaxial Si (100) Nanowire Arrays on a Si (100) Substrate Using an Anodic Aluminum Oxide Template. Advanced Materials, 19(7), pp.917-920.

210. (Xu, D., Chen, D., Xu, Y., Shi, X., Guo, G., Gui, L. and Tang, Y., 2000. Preparation of II-VI group semiconductor nanowire arrays by dc electrochemical

deposition in porous aluminum oxide templates. Pure and applied chemistry, 72(1-2), pp.127-135.

211.   Fan, Z., Razavi, H., Do, J.W., Moriwaki, A., Ergen, O., Chueh, Y.L., Leu, P.W., Ho, J.C., Takahashi, T., Reichertz, L.A. and Neale, S., 2009. Three-dimensional nanopillar-array photovoltaics on low-cost and flexible substrates. Nature materials, 8(8), p.648.

212.   Ding, J.X., Zapien, J.A., Chen, W.W., Lifshitz, Y., Lee, S.T. and Meng, X.M., 2004. Lasing in ZnS nanowires grown on anodic aluminum oxide templates. Applied physics letters, 85(12), pp.2361-2363.),

213.   Ashley, M.J., O'Brien, M.N., Hedderick, K.R., Mason, J.A., Ross, M.B. and Mirkin, C.A., 2016. Templated synthesis of uniform perovskite nanowire arrays. Journal of the American Chemical Society, 138(32), pp.10096-10099.

214.   Huang, Z., Geyer, N., Werner, P., De Boor, J. and Gösele, U., 2011. Metal-assisted chemical etching of silicon: a review. Advanced materials, 23(2), pp.285-308.

215.   Peng, K., Zhang, M., Lu, A., Wong, N.B., Zhang, R. and Lee, S.T., 2007. Ordered silicon nanowire arrays via nanosphere lithography and metal-induced etching. Applied physics letters, 90(16), p.163123.

216.   Chen, K., Kapadia, R., Harker, A., Desai, S., Kang, J.S., Chuang, S., Tosun, M., Sutter-Fella, C.M., Tsang, M., Zeng, Y. and Kiriya, D., 2016. Direct growth of single-crystalline III–V semiconductors on amorphous substrates. Nature communications, 7, p.10502.

217.   Schmid, H., Borg, M., Moselund, K., Gignac, L., Breslin, C.M., Bruley, J., Cutaia, D. and Riel, H., 2015. Template-assisted selective epitaxy of III–V nanoscale devices for co-planar heterogeneous integration with Si. Applied Physics Letters, 106(23), p.233101.

218.   Michaelis, S., Timme, H.J., Wycisk, M. and Binder, J., 2000. Additive electroplating technology as a post-CMOS process for the production of MEMS acceleration-threshold switches for transportation applications. Journal of Micromechanics and Microengineering, 10(2), p.120.

219.   Fujita, T., Nakamichi, S., Ioku, S., Maenaka, K. and Takayama, Y., 2007. Seedlayer-less gold electroplating on silicon surface for MEMS applications. Sensors and Actuators A: Physical, 135(1), pp.50-57.].

220. Buttard, D., Oelher, F. and David, T., 2011. Gold colloidal nanoparticle electrodeposition on a silicon surface in a uniform electric field. Nanoscale research letters, 6(1), p.580.

221. Bhattacharya, R.N., 2010. Electrodeposited two-layer Cu–In–Ga–Se/In–Se thin films. Journal of The Electrochemical Society, 157(7), pp.D406-D410.

222. Aksu, S., Wang, J. and Basol, B.M., Solopower, Inc., 2009. Efficient gallium thin film electroplating methods and chemistries. U.S. Patent 7,507,321.

223. Lobaccaro, P., Raygani, A., Oriani, A., Miani, N., Piotto, A., Kapadia, R., Zheng, M., Yu, Z., Magagnin, L., Chrzan, D.C. and Maboudian, R., 2014. Electrodeposition of high-purity indium thin films and its application to indium phosphide solar cells. Journal of The Electrochemical Society, 161(14), pp.D794-D800.

224. Aksu, S., Pethe, S., Kleiman-Shwarsctein, A., Kundu, S. and Pinarbasi, M., 2012, June. Recent advances in electroplating based CIGS solar cell fabrication. In Photovoltaic Specialists Conference (PVSC), 2012 38th IEEE (pp. 003092-003097). IEEE.